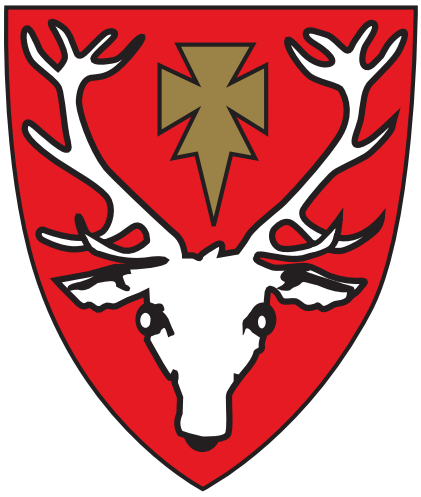
A micromechanical investigation of proton irradiated oxide dispersion strengthened steels





Christopher A. Jones

Hertford College, University of Oxford

A thesis submitted for the degree of

Doctor of Philosophy

Michaelmas term 2016

This thesis is dedicated to my wife, Bailey.

Thank you for your unwavering support.

Preface

The work presented in this doctoral thesis has been carried out at the Department of Materials, University of Oxford from October 2011 to July 2016, under the supervision of Prof. S. G. Roberts, Dr. D. E. J. Armstrong (2013 - 2016) and Dr T. B. Britton (2011-2013). All of the research carried out for this thesis is original, and where the work of others has been included it has been clearly referenced and acknowledged. All figures and tables reproduced from journal articles and books have been used with permission from the respective copyright owner. A list of references is given at the end of the thesis. No part of this thesis has been submitted for a degree at this, or any other university.

Abstract

This thesis was most concerned with the mechanical response to irradiation of two in-house produced oxide dispersion strengthened (ODS) steels and two non-ODS counterparts. The steels, manufactured by Dr. M. J. Gorley (University of Oxford), were mechanically alloyed from gas-atomised Fe-14Cr-3W-0.2Ti, with the addition of $0.25Y_2O_3$ powder in the case of the ODS variants. The powders were hot isostatic pressed at consolidation temperatures of 950 $^{\circ}C$ and 1150 $^{\circ}C$. The four steels were designated 14WT 950 (non-ODS), 14YWT 950 (ODS), 14WT 1150 (non-ODS) and 14YWT 1150 (ODS), and were used in the as-produced condition.

Initially, the macroscale elastic modulus and yield stress were determined using a four-point flexure test, employing digital image correlation (DIC) as a strain gauge. The microcantilever size effects were then characterised, and it was determined that the yield stress significantly diverged from macroscale values at microcantilever beam depths of < 4.5 μm. Using knowledge of this, the in-house produced alloys were irradiated with 2 MeV protons at the Surrey Ion Beam Centre (University of Surrey, UK) to a displacement damage of ~ 0.02 dpa and 0.2 dpa (Bragg peak). This was to produce a deep irradiated layer for the fabrication of large microcantilevers with reduced size effects.

The cross-sectional surface of the irradiated layer was then exposed and inclined linear arrays of 250 nm deep indents were placed across the damage profile. 14WT 1150 (non-ODS) revealed a clear proton damage profile in plots of hardness against irradiation depth, 14WT 950 (non-ODS) also showed modest hardening in the region of the Bragg peak. No appreciable hardening was observed in either 14YWT specimens, attributed to the fine dispersion of nanoscale oxides providing a high number density of defect sink sites. However, a large bimodal variation in hardness was measured in both ODS variants. This was investigated using EBSD and EDX, and was determined to be caused by a pronounced heterogeneity of the microstructure. While Hall-Petch strengthening and changes in the local chemistry had some effect on the measured hardness, the most likely cause of the large variation in local hardness was heterogeneity in the nanoscale oxide population.

Microcantilevers were fabricated out of the irradiated layer cross-section in 14WT 1150 and 14YWT 1150. Larger microcantilevers, with ~ 5 μm beam depth, were placed with their beam centre at ~ 0.026 dpa. Smaller microcantilevers, with ~ 1.5 μm beam depth, were placed with their beam centre at the Bragg peak, 0.2 dpa. Both the large and the small microcantilevers fabricated in 14WT 1150 (non-ODS) displayed significant irradiation hardening. In the ODS variant, 14YWT 1150, irradiation hardening

appeared to be reduced. The work in this thesis successfully showed that it was possible to extract a close approximation of the macroscale yield stress from shallow irradiated layers, providing that the irradiation condition is carefully chosen in response to known size dependent behaviour.

This thesis also investigated the size dependent behaviour of microcantilevers using a lengthscale dependent crystal plasticity UMAT, developed by Dunne et al. and implemented within ABAQUS 6.14-2 commercially available finite element software. The simulation of the GND density evolution with increasing plastic strain allowed their contribution to the microcantilever size effect, through mobile dislocation pinning, to be determined. This novel approach to modelling size effects in three dimensional finite element microcantilever models demonstrated that while it was possible to simulate a lengthscale-dependent response in finite element microcantilever models, the constitutive equation for the plastic velocity gradient needs to be more physically based in order the match the experimentally derived results; for example, a lengthscale-dependent term relating to the dislocation source density of the material.

Although the apparent reduction of irradiation hardening in ODS in-house produced alloys showed great promise, these alloys also displayed a large amount of scatter in measured hardness and yield stress, attributed to the pronounced heterogeneity in the microstructure. Alloys with such significant microstructural heterogeneity are not suitable for engineering or commercial use.

Acknowledgments

Firstly, I would like to offer particular thanks to my supervisors, Prof. Steve Roberts and Dr. Dave Armstrong. In no uncertain terms, this thesis is presented due to their immense support and guidance, and for that, I am incredibly grateful. Special thanks also goes to my adopted supervisor, Dr. Ed Tarleton, who had the particular pleasure of teaching computational plasticity to an experimentalist, and for that, I apologise. I would like to also acknowledge the support given by Dr. Ben Britton, his excellent practical advice early on was always very useful, even in the latter stages of my project.

I would like to thank all of my past and present colleagues in the Materials for Fusion & Fission Power group for their help and friendship. Particularly, Dr. Ele Grieveson, Dr. Anna Kareer and Dr. Andy London. A special mention goes to the chaps in the small office: Kris, Junnan, Bo, Luke, Dr. Yevhen and Tomo for providing the laughs that made the last couple of years much more bearable.

Thanks goes to the Oxford Materials TSG for keeping the microscopes online for as much time as possible. Particularly Mrs G. Chapman, Dr. G. Hughes and Mr. S. Lett for microscope training and their much appreciated advice.

Thanks also goes to Dr. Mike Gorley for providing the materials used in this thesis, and Dr. Chris Hardie whose Matlab script has saved many hours of analytical work.

The members and alumni of Hertford College Boat Club, to whom I owe my sanity. With your help, I have thoroughly enjoyed my past five years in Oxford and hope to enjoy many more years as an alumnus.

Mum, Dad, Alison and Mark for all your love, support and encouragement, even when I told you I was going be a student for a little while longer.

Dr. Dan Thompson, who has been a friend for life ever since that entertaining and eventful week in a York Travelodge.

Lastly, my wife Bailey. Your continued love and support over the past five years means the world to me and I would have never have achieved this without you. I'm sure you'll miss the FIB as much as I will!

Contents

1 Introduction **1**

1.1 Research objectives 2

1.2 Thesis outline 3

2 Literature review of ODS steels and micromechanics **4**

2.1 Introduction to materials for fusion reactors 4

2.1.1 Engineering challenges for plasma facing materials 8

2.2 Mechanisms and effects of irradiation damage 10

2.2.1 Neutron bombardment and the damage cascade 10

2.2.2 Defect accumulation and transport in iron-based alloys 16

2.3 Engineering irradiation resistance 18

2.3.1 Introduction 18

2.3.2 Development of reduced activation steels 22

2.4 Mechanical properties of irradiated RAFM steels 27

2.5 Oxide dispersion strengthened steels 35

2.5.1 Introduction 35

2.5.2 Fabrication 35

2.5.3 Mechanical properties of ODS steels 39

2.5.4 Main concerns regarding the further development of ODS steels . 50

2.6 Micromechanical testing 51

2.6.1 Nanoindentation 52

2.6.2 Continuous stiffness measurement (CSM) 57

2.6.3 Nanoindentation of proton irradiated steels 58

2.6.4 Summary of nanoindentation 64

2.6.5 FIB prepared microcantilever test specimens 65

2.6.6 Microcantilever summary 72

2.6.7 Micromechanical size effects 72
2.6.8 Size effects in irradiated micromechanical test specimens 83
2.6.9 Micromechanical size effect summary 88
2.6.10 Microcantilevers in self-ion irradiated Fe-Cr alloys 89

3 Characterisation of materials **95**

3.1 Research materials 95
3.2 EBSD crystallography characterisation 102
3.2.1 Scanning electron microscopy 102
3.2.2 Sample preparation 103
3.2.3 EBSD mapping of research materials 104
3.2.4 Discussion of microstructure characterisation 109
3.2.5 Summary of EBSD characterisation 111
3.3 Determination of macroscale mechanical properties 111
3.3.1 Strain measurements using digital image correlation 111
3.3.2 Determining elastic modulus and yield stress from stress-strain curves 122
3.3.3 Four-point flexural test results 124
3.3.4 Discussion of four-point flexural test results 127
3.3.5 Summary of macroscale mechanical behaviour 130
3.4 Characterisation of the microcantilever size effect in ODS steels 131
3.4.1 Focused ion beam (FIB) 131
3.4.2 Microcantilever manufacture 132
3.4.3 Microcantilever testing 132
3.4.4 Microcantilever analysis 135
3.4.5 Microcantilever size effect results 142
3.4.6 Summary of microcantilever size effects 148

4 Computational plasticity study of the microcantilever size effect 150

4.1 Introduction to computational plasticity 150

4.2 Computational plasticity theory 153

4.2.1 Introduction 153

4.2.2 The deformation gradient 154

4.2.3 Implicit integration implementation 163

4.2.4 UMAT implementation of the GND density calculation 167

4.2.5 Crystal plasticity UMAT implementation summary 168

4.3 UMAT code check and model optimisation 172

4.3.1 Introduction 172

4.3.2 Identification of UMAT constants 172

4.3.3 Mesh convergence 173

4.3.4 GND check 179

4.3.5 Meshing techniques 186

4.3.6 UMAT check and model optimisation summary 211

4.4 Modelling of the GND contribution to microcantilever size effects . . . 212

4.4.1 Introduction 212

4.4.2 Simulation details 213

4.4.3 Results and discussion 214

4.4.4 CP microcantilever size effect summary 226

4.5 Computational plasticity study conclusion 228

5 Micromechanical study of proton irradiated ODS steels 229

5.1 Introducing damage 229

5.1.1 Proton irradiation at Surrey Ion Beam Centre 230

5.2 Nanoindentation normal to irradiated layer 235

5.2.1 Results for indentation normal to irradiated layer 236

5.2.2 Result summary for indents normal to irradiated layer 238

5.3 Nanoindentation across irradiated layer 240
5.3.1 Method for nanoindentation of irradiated layer cross-section . . . 240
5.3.2 Results for nanoindentation of irradiated layer cross-sections . . 243
5.3.3 Discussion for nanoindentation of irradiated layer cross-section . 246
5.3.4 Investigation of bimodal nanoindentation hardness in ODS 14YWT 249
5.3.5 Summary of nanoindentation in the irradiated layer cross-section 262
5.4 Microcantilevers in irradiated 14WT 1150 and 14YWT 1150 265
5.4.1 Method used for the placement of microcantilevers in the irradiated layer 266
5.4.2 Results for irradiated microcantilevers 268
5.4.3 Discussion of irradiated microcantilevers 273
5.4.4 Summary for irradiated microcantilevers 279

6 Summary, conclusions and further work 281
6.1 Thesis aims 281
6.2 Summary of experimental chapters 281
6.3 Thesis conclusion 286
6.4 Further work 286

Common abbreviations

ODS	Oxide dispersion strengthened
RAF/M	Reduced activation ferritic/martensitic
RAF	Reduced activation ferritic
GND	Geometrically necessary dislocations
SSD	Statistically stored dislocations
ITER	International thermonuclear experimental reactor
DEMO	Demonstration reactor
PFMs	Plasma facing materials
RIS	Radiation induced segregation
RIP	Radiation induced precipitation
DBTT	Ductile to brittle transition temperature
PKA	Primary knock on atom
SIA	Self interstitial atom
dpa	Displacement per atom
BCC	Body centred cubic
FCC	Face centred cubic
SEM	Scanning electron microscope
TEM	Transmission electron microscope
APT	Atom probe tomography

AFM	Atomic force microscope
EBSD	Electron backscattered diffraction
EDX	Energy dispersive x-ray spectroscopy
HIP	Hot isostatic press
CP	Crystal plasticity
FEM	Finite element modelling
FE	Finite element
FEA	Finite element analysis
UMAT	User defined material
RSS	Resolved shear stress
CRSS	Critically resolved shear stress
DIC	Digital image correlation
CCD	Charged-coupled device
SRIM	Stopping range of ions in matter

Chapter 1

1 Introduction

"There's one issue that will define the contours of this century more dramatically than any other, and that is the urgent threat of a changing climate" U.S. president, Barack Obama, at the U.N. Climate Change Summit (2014).

Our generation's struggle to curb the potentially catastrophic effects of climate change is set to define the 21st century. The fifth assessment report by the Intergovernmental Panel on Climate Change (IPCC) in 2013, projects that the global mean surface temperatures will increase between 1 °C and 4 °C by the year 2100, depending on a range of emission scenarios [1]. The scientific evidence that human activity is the dominant cause of the observed changes in climate has only become stronger since the first assessment report was presented in 1990. Yet, international commitments to reduce carbon emissions have been far below that recommended by the scientific community; data from the World bank showed that in 2013 OECD (The Organisation for Economic Co-operation and Development) countries still derived 80.7 % of their total energy consumption from hydrocarbon based fuels [2].

Mounting international pressure on developed countries to implement changes to their energy consumption, alongside national interests to switch to more secure, stable energy sources, has renewed research into advanced nuclear power concepts. Any future energy source will need to decrease worldwide carbon emissions, and substantially reduce reliance on hydrocarbons [3, 4]. Advance nuclear reactors such as Generation IV (GenIV) fission reactors and future fusion reactors are some of the foremost technologies capable of achieving these demands, but their success as a viable energy source depends on the development of new materials capable of enduring the extremely hostile working conditions that will be seen during the lifetime of the reactors [5, 6, 7].

The structural materials for GenIV fission and future fusion reactors will experience higher temperatures and more severe radiation exposure when compared to current reactors operating today. Oxide dispersion strengthened (ODS) steels are one of the most promising candidate materials for fuel cladding tubes, in GenIV reactors, and plasma facing components for tritium breeding blankets in fusion reactors [8]. Although first developed during the 1960's, recent research has demonstrated an improved high temperature strength and irradiation resistance over the more conventional high chromium reduced activation ferritic/martensitic (RAF/M) steels. This improved performance is obtained through microstructures that contain a high density of insoluble nanoscale oxides dispersed in the ferrite matrix. However, concerns remain over their use in future nuclear applications; not only are the current operating temperatures for ODS steels below that needed to optimise reactor efficiency, but our knowledge of their behaviour when subjected to radiation damage is incomplete. This thesis aims to extend our knowledge of the mechanical behaviour of ODS EUROFER and in-house produced ODS alloy, Fe-14Cr-3W-0.2Ti-0.25Y_2O_3, and their non-ODS counterparts, by employing macro and micromechanical testing methods on both as-produced and proton irradiated samples.

1.1 Research objectives

The key objectives of the research in this thesis are:

- Develop a method for extracting yield stress and elastic modulus data from shallow irradiated layers that closely estimates macroscale values.
- To investigate the extent of the microcantilever size effect in ODS steels.
- To establish a method for using digital image correlation (DIC) as strain gauge in macroscale four-point flexure tests.
- To investigate the contribution geometrically necessary dislocation (GND) densities have to the microcantilever size effect, using a lengthscale-dependent finite

element crystal plasticity model.

- To investigate the mechanical behaviour of two in-house produced ODS ferritic alloys after being subjected to 2 MeV proton irradiation at 300°C, by using micromechanical testing methods.

1.2 Thesis outline

The structure of the thesis is as follows:

Chapter 2 Describes and summarises the relevant literature and theory surrounding future fusion reactor systems, the causes and consequences of irradiation damage in metallic microstructures, engineering irradiation resistance in alloys, and methods of examining mechanical properties on the microscale.

Chapter 3 Introduces and characterises the materials investigated within the project. The macromechanical properties are determined using four-point flexure with strain measured using digital image correlation. Lastly, the microcantilever size effect is investigated and characterised for the material array.

Chapter 4 Uses a lengthscale-dependent crystal plasticity model to investigate the contribution GND densities have to the microcantilever size effect.

Chapter 5 Probes the mechanical response of ODS steels to proton irradiation using nanoindentation and microcantilever testing methods.

Chapter 6 Provides a project conclusion, and suggests ways in which the work presented could be built upon.

Chapter 2

2 Literature review of ODS steels and micromechanics

This review is divided into two parts. The first part serves as an introduction to oxide dispersion strengthened steels, and discusses why they are of interest to the scientific community for future use in advanced nuclear reactor applications. The second part discusses the use of micromechanics as a method of extracting mechanical behaviour from small sample volumes. Literature relating to key points will be cited to help support our discussion. First however, we will begin by discussing the extreme environment that materials will have to face in future nuclear reactors.

2.1 Introduction to materials for fusion reactors

Fusion and Gen IV fission reactors are currently under intensive research and development worldwide. Both reactor technologies share the common goals of providing safer and cleaner energy whilst reducing the risk of nuclear proliferation. The lifetime, performance and consequently the economic viability of these technologies, is largely dictated by the operational limitations of structural materials [9, 10]. Although these technologies utilise different nuclear reactions to produce heat, they share many of the same engineering challenges, namely high operating temperatures and an intense neutron flux. Figure 2.1 provides an overview of the typical operating conditions for structural materials in current generation II and III reactors, alongside the proposed Gen IV and fusion systems.

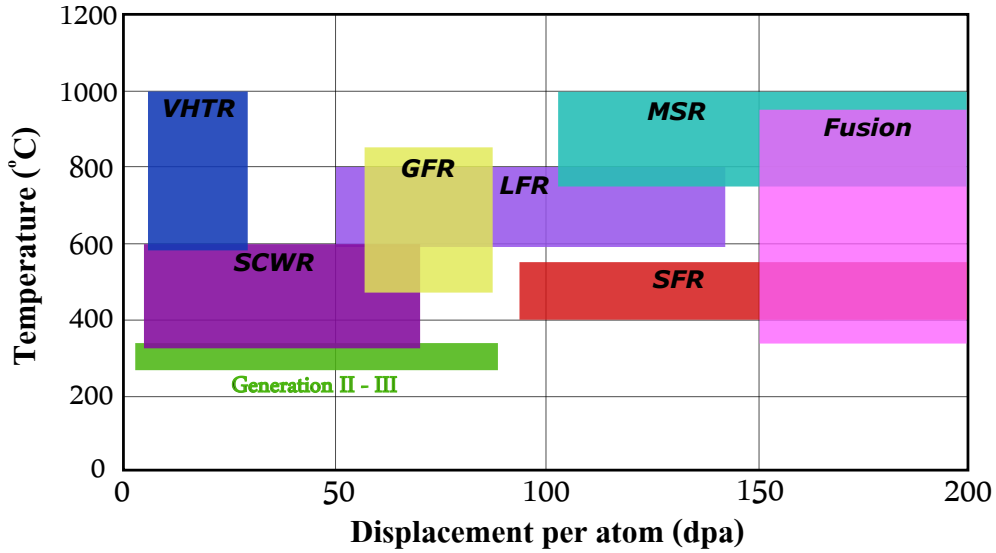


Figure 2.1: An overview of the operating conditions an in-core structural material will face in proposed advanced nuclear reactors. Included are the current generation II-III reactors, the six proposed Gen IV reactor concepts, and fusion energy systems. The six proposed Gen IV reactor concepts include; the very-high temperature reactor (VHTR); the super-critical water-cooled reactor (SCWR); the gas fast reactor (GFR); the lead fast reactor (LFR); the molten salt reactor (MSR) and the sodium fast reactor (SFR). Figure redrawn from [10].

High performance structural materials designated for use in fusion environments will arguably have to overcome the most extreme conditions in future reactor designs. Not only are the steady state heat fluxes for the first wall and divertor components projected to be in the region of 1-10 $\mathrm{MWm^{-2}}$ ($\sim 1\,\mathrm{MWm^{-2}}$ in Gen IV), but the anticipated radiation dosage over the course of the component's lifetime is approximately five times higher than the core internal structures for existing fission reactors [11]. Additionally, the average neutron energy associated with a deuterium-tritium (D-T) reaction is substantially higher than that produced by a fission reaction. An increase in incident neutron energy tends to lead to much higher levels of transmutant solutes, such as hydrogen and helium, within the structural medium which generally exasperates radiation induced degradation [11].

However, after sustained research over several decades, the scientific community is

on the brink of demonstrating the plasma physics feasibility of a magnetically confined fusion reactor. The material challenge is now becoming the limiting factor to making these proposed designs a reality. If successful, fusion could make the future of nuclear power more efficient, fuel abundant, intrinsically meltdown and proliferation proof, as well as vastly reducing nuclear waste production rates. For this reason, this review will now focus on the development of materials specifically for blanket applications in magnetically confined fusion reactors.

The primary aim for research and development in magnetically confined fusion rectors is to build a demonstration reactor (DEMO), to prove its viability as an energy source. Before we can achieve such a reactor, engineering, plasma physics and material challenges have to be overcome. To help solve these problems, construction has begun on the International Thermonuclear Experimental Reactor (ITER) which will serve as a testing ground for components to be used in a DEMO reactor. A schematic diagram of ITER is shown in figure 2.2(a).

Magnetic confinement fusion reactors are generally designed around the tokamak design. They contain powerful toroidal and poloidal field magnets around a vacuum vessel, in which an ionised D-T plasma is confined. The plasma in a tokamak is heated until the coulomb barrier is overcome and fusion can occur. A single D-T fusion reaction produces a 3.5 MeV He^4 and a 14.1 MeV neutron, a percentage of the heat, helium and neutrons are absorbed by the surrounding first wall, divertor, and internal blanket components [12, 13], shown in figure 2.2(c), (b), and (c) respectively.

This project is concerned with the candidate materials for the first wall and structural components in the breeder blanket. The major functions of the breeder blanket are to absorb the heat and neutrons produced by the D-T reaction and efficiently transfer the energy to a coolant for the production of electricity, as well as producing a constant supply of tritium fuel via transmutation of lithium caused by incident neutrons [17, 18].

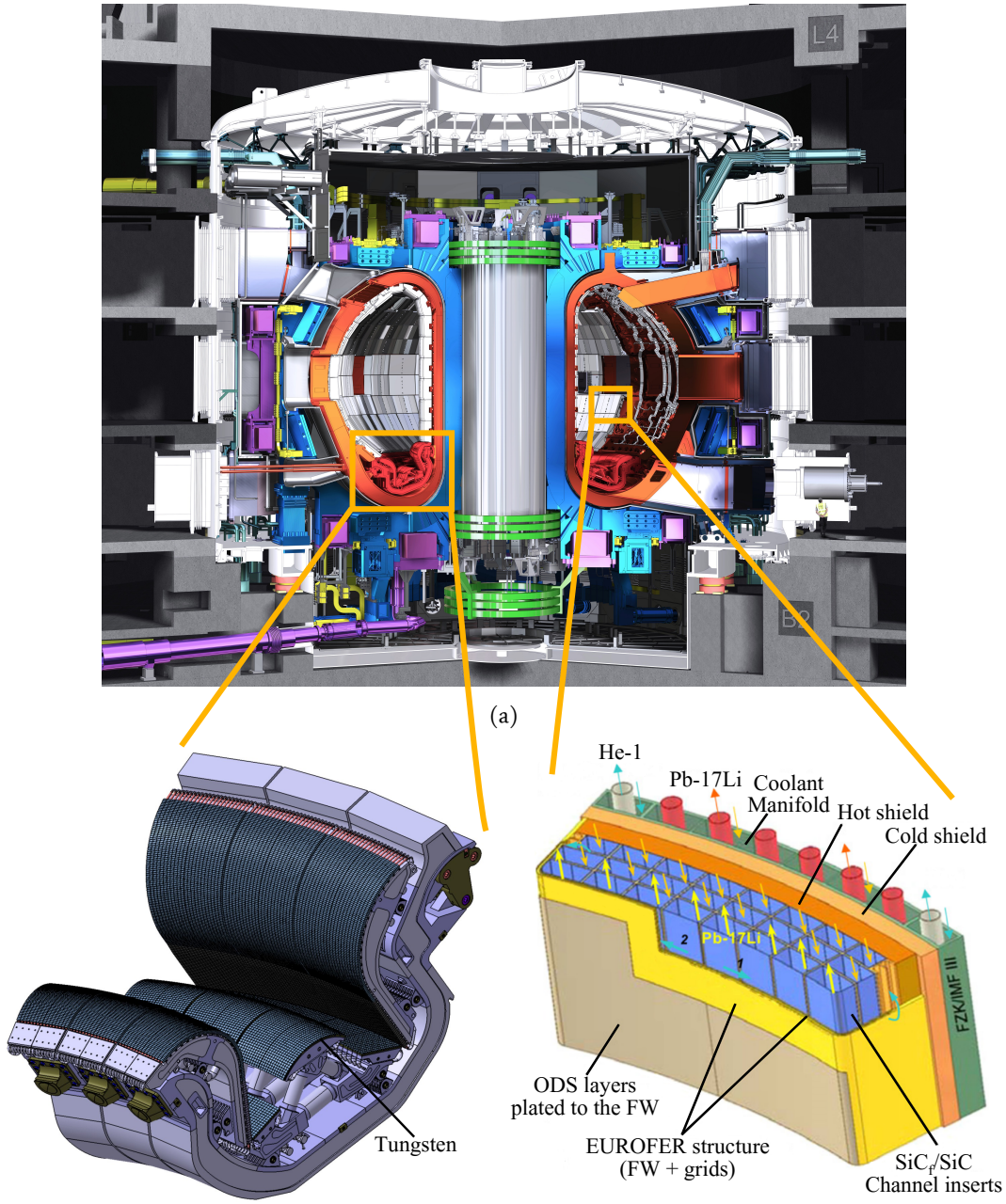


Figure 2.2: (a) A schematic diagram of ITER [14]. (b) The ITER divertor [14]. (c) An example of a duel-coolant lead-lithium (DCLL) blanket concept [15, 16].

2.1.1 Engineering challenges for plasma facing materials

Typical first wall plasma facing materials (PFMs) in must withstand a combination of; elevated temperatures of up to 700 °C; large time-varying stresses; hydrogen and helium deposition; cyclical thermals stresses and intense neutron fluences [19, 20]. After an expected working life cycle of five years, PFMs in certain applications are predicted to receive an atomic displacement damage of approximately 150 - 200 dpa (displacements per atom) [4, 12, 21, 8], creating excess concentrations (with respect to the thermodynamic equilibrium) of vacancy and self interstitial atom (SIA) defects [22, 23, 24]. Highly localised defect populations are responsible for a number of important processes, often leading to the hardening and embitterment of the irradiated material. Localised concentrations of defects may lead to the nucleation of voids and gas-filled bubbles, and the formation of a dense dislocation network [25]. Long range diffusion of defects to sink sites may lead to radiation induced segregation (RIS) of solutes and impurities, which subsequently can lead to radiation induced precipitation (RIP) at these sites [25, 26, 27].

The effect of irradiation on the tensile behaviour of RAF/M steel is directly dependent on temperature [5]. Hardening, as seen by a loss of ductility and an increase in yield strength and ultimate tensile strength, occurs at irradiation temperatures up to approximately 0.35 T_m (melting temperature), approximately 500 °C [28, 29]. This would be a huge risk to the integrity of the vessel during cool down phases. Hardening effects saturate with increasing fluence; saturation for most compositions is observed at between 10 to 20 dpa [28, 30]. For irradiation temperatures above 0.35 T_m, properties are largely unchanged, although radiation enhanced softening may occur in certain steels depending on temperature and fluence [9].

Irradiation compromises other mechanical properties, such as fatigue and fracture toughness. The latter is one of the greatest concerns for RAF/M steels for fusion and fission applications [31]. The effect on fracture toughness is observed as an increase in ductile to brittle transition temperature (DBTT) and a decrease in upper-self energy

(USE) [32, 30]. In a manner similar to the hardening effect seen in tensile tests, the shift in the DBTT starts to saturate at around 10-17 dpa[30, 32].

Furthermore, the accumulation of helium is approximately two orders of magnitude above that seen in current fission reactors [8]. Helium, accumulated from exhaust gases and the decay of transmutant elements, plays a crucial role in the evolution of the microstructure [33, 34, 35] and has a particularly low solubility in the iron lattice; even small concentrations may precipitate out to form bubbles [25]. These bubbles often form around microstructural features such as, dislocations, grain boundaries, and precipitate interfaces. Bubbles produced during this process form preferential sites for void swelling and grain boundary creep cavities [25, 23, 36, 37, 38, 39, 40].

As well as the production of He, neutron induced transmutations can cause the accumulation of long half-life radionuclides within material components [41, 42]. Candidate structural materials and candidate PFMs will need to have a chemical composition that is based on 'reduced activation' chemical elements (Fe, Cr, Mn, V, Ti, W, Ta, Si, C, O) [43, 32, 44, 45]. Alloys utilising these elements will help reduce radioactive waste inventory throughout the life of the reactor (see section 2.3.2).

The material challenges are truly daunting when the severe loss of fracture toughness and uniform tensile ductility, are combined with irradiation creep, void swelling, and the extreme thermomechanical conditions. This emphasises the necessity for the research into fusion-specific materials that have the superior mechanical, physical and radiological capabilities necessary for a viable fusion reactor.

In order to effectively communicate this research, we must first detail the recent progress made towards developing new iron-based alloys. Important factors to this discussion are the mechanisms and effects of irradiation damage, the history of radiation resistance, and the reasons that have necessitated the evolution of the alloys to where they are today. This will lead to a discussion of oxide dispersion strengthened (ODS) steels, which have greatly improved thermal and irradiation resistant properties when

compared against RAF/M predecessors. Lastly, the focus will turn to the discussion of micromechanical testing as a way of examining mechanical properties of microscale irradiated layers.

2.2 Mechanisms and effects of irradiation damage

This section summarises the causes and consequences of the inevitable radiation damage a first wall structural material will receive. Learning to correctly manage the microstructural evolution to minimise or manipulate damage accumulation is vital when attempting to decrease mechanical degradation. However, defect production and the effect their diffusion has on the material microstructure must be first be explored before considering the dependence mechanical properties have on this altered microstructure.

2.2.1 Neutron bombardment and the damage cascade

Nuclear fusion D-T reactions produce a high-energy neutron flux. As they are neutrally charged, an incident neutron entering a material matrix may elastically scatter off of an atom in the lattice. If the transfer of energy is above a thereshold displacement energy, E_d, then the lattice atom, known as the primary knock-on atom (PKA), will be displaced from its lattice site. If the PKA has sufficient energy it will go on to displace neighbouring atoms from their equilibrium lattice sites until the energy has dissipated to below E_d [25]. In this way, a single neutron-nucleus interaction can cause multiple displacements of lattice atoms, this is known as a damage cascade. This cascade effect produces vacancy and self interstitial atom (SIA) point defects, known as a Frenkel pair, in equal numbers. The spatial distribution of the damage cascade region is notably heterogeneous, as initially it consists of highly localised regions of defects with vacancy enriched cores and interstitial shells at the end of each PKA track [24]. This is illustrated in figure 2.3.

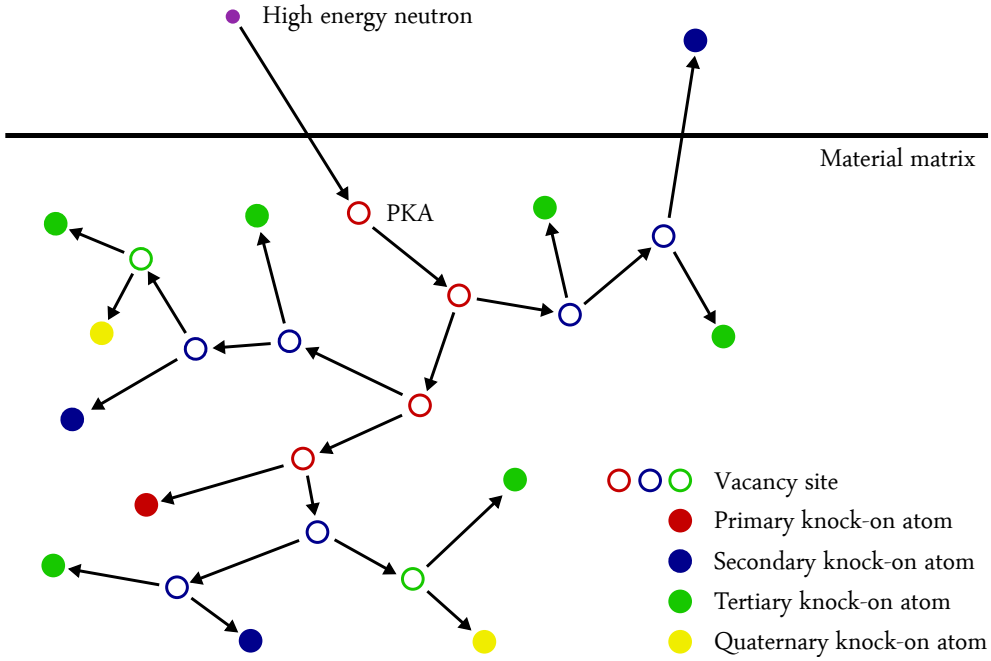


Figure 2.3: Neutron damage cascade.

To evaluate radiation damage, a parameter that characterises lattice displacement events is required. The international standard measurement is the 'displacements per atom' or dpa. A damage of 1 dpa corresponds to a displacement of every atom from its original lattice site [11]. To quantify displacement damage, a solution is needed for the damage rate, R_d, given by the following equation [25],

$$R_d = N \int_{\check{E}}^{\hat{E}} \phi(E_i)\sigma_D(E_i)dE_i \tag{2.1}$$

where N is the atomic density, $\phi(E_i)$ is the particle flux as a function of incoming particle energy, E_i, $\sigma_D(E_i)$ is the displacement cross-section as a function of incoming particle energy, E_i. In physical terms, the displacement cross section is the probability for the displacement of atoms in the lattice by incident particles, and is given by the equation,

$$\sigma_D(E_i) = \int_{\check{T}}^{\hat{T}} \sigma(E_i, T)v(T)dT \tag{2.2}$$

where $\sigma(E_i, T)$ is the probability that a particle of energy E_i will impart a recoil energy, T, to an atom in the lattice, and the limits of T between which displacements occur. $v(T)$ is the number of displaced atoms resulting from a displacement collision, otherwise put, the total number of stable Frenkel pairs produced by an incident particle. The value of $v(T)$ is predicted by several models, but the most widely cited model is that that presented by Kinchin and Pease (1955) [46], otherwise known as the K-P model. The full K-P result for $v(T)$ is,

$$v(T) = \begin{cases} 0 \text{ for } T < E_d \\ 1 \text{ for } E_d < T < 2E_d \\ \dfrac{T}{2E_d} \text{ for } 2E_d < T < E_c \\ \dfrac{E_c}{2E_d} \text{ for } T \geq E_c \end{cases} \tag{2.3}$$

The K-P model assumes the cascade is created by elastic collisions with no energy loss to the surroundings, so that the number of atoms displaced sharply increases to 1 for PKA energies, $E_d < T < 2E_d$. It is also assumed that number of displaced atoms increases linearly from $2E_d$ to a saturation/cut-off point, E_c. PKAs with energy $> E_c$ are assumed to have their energy reduced to E_c due to electronic stopping via Bremsstrahlung radiation [47]. The K-P model is represented graphically in figure 2.4.

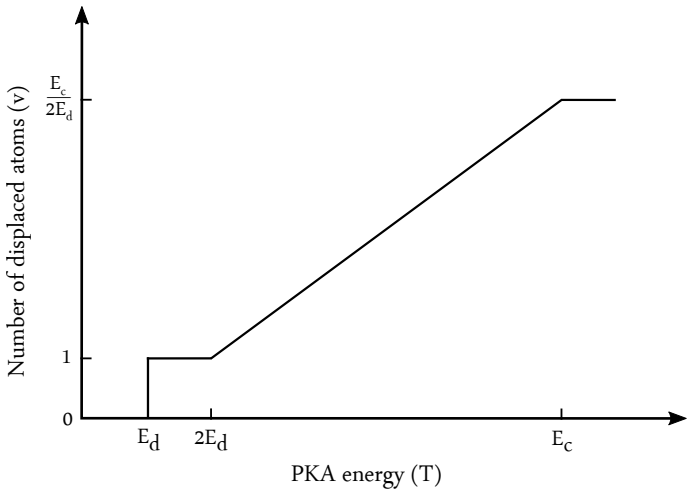


Figure 2.4: Number of displaced atoms in the cascade as a function of the PKA energy according to the model of Kinchin and Pease. [25]

Building on the work of Kinchin and Pease, Norgett, Robinson, and Torrens (NRT) (1975) [48] developed a model for calculating $v(T)$ that has been widely adopted by the radiation effects community [49, 47]. The NRT displacement model gives the total number of atomic displaced atoms/stable Frenkel pairs produced by PKA with energy E_{PKA} as,

$$V_{NRT} = \frac{0.8T_{dam}(E_{PKA})}{2E_d} \tag{2.4}$$

where $T_{dam}(E_{PKA})$ represents the damage energy, and is a function of the PKA energy. Physically, it represents the energy available to generate atomic displacement by elastic collisions [48]. As PKA energy increases a larger percentage of the total energy is dissipated via electron stopping, so a smaller portion of the total energy is imparted to atoms in the lattice, and number of Frankel pairs created begins to saturate. Since the total displacement energy is explicitly accounted for, the NRT model can be used to calculate displacement damage obtained via different irradiation sources, e.g. a range of neutron energy spectra, ion or electron radiation [47].

It is important to note that it is not possible to calculate the number of Frankel

pairs created for a given PKA energy in any absolute sense using these models. Their strength does not necessarily lie with their accuracy but as standard reference values for the scientific community. The Monte Carlo simulation code, Stopping of Ions in Matter (SRIM), uses such models to simulate the displacement damage in a material when exposed to ion irradiation [50]. Due to its ease of use, it has become one of the most popular tools to determine the dpa associated with a particular experimental ion irradiation. SRIM gives the user the option of computing radiation damage production using a 'Quick K-P calculation' or a 'Full Casacade'. Stoller et al. (2013) [47] highlighted a coding error in the 'Full Cascade' option that gave displacement values approximately double that predicted by the NRT model, instead the author recommends the use of the quick K-P damage energy calculation. For the damage calculation in this project, SRIM was run using the 'Quick K-P' option with a displacement threshold energy, E_d, of 40 eV and a lattice binding energy of 0 eV, as recommended for iron-based alloys by Stoller et al. (2013) [47].

Both the K-P and NRT models simplify the calculations of irradiation damage in materials by ignoring variables such as; temperature, known to have a modest impact on point defect production through molecular dynamics simulations; impurity atoms and crystallographic orientation, that both give a spread in the threshold displacement energy, E_d; inelastic scattering; the neutron absorption cross-section and defect annihilation and recombination.

The neutron absorption cross-section represents the probability that a neutron will be absorbed by a target nucleus. This can result in a number of transmutations in PFMs producing both solid and gaseous products, such as Mn from Fe and large amounts of H and He [51]. Of these, helium is arguably the most relevant to mechanical properties, as compositional changes in a ferritic based alloy in a fusion system are generally minimal and hydrogen is able to diffuse rapidly to reach equilibrium with the environment. Helium production increases with increasing incident energy and flux, fusion

helium accumulation is approximately two orders of magnitude above that of current fission reactors [8]. Figure 2.5 provides a comparison of helium accumulation verses displacement per atom (dpa) between current fission reactors, current neutron sources, proposed neutron sources and a proposed DEMO fusion reactor.

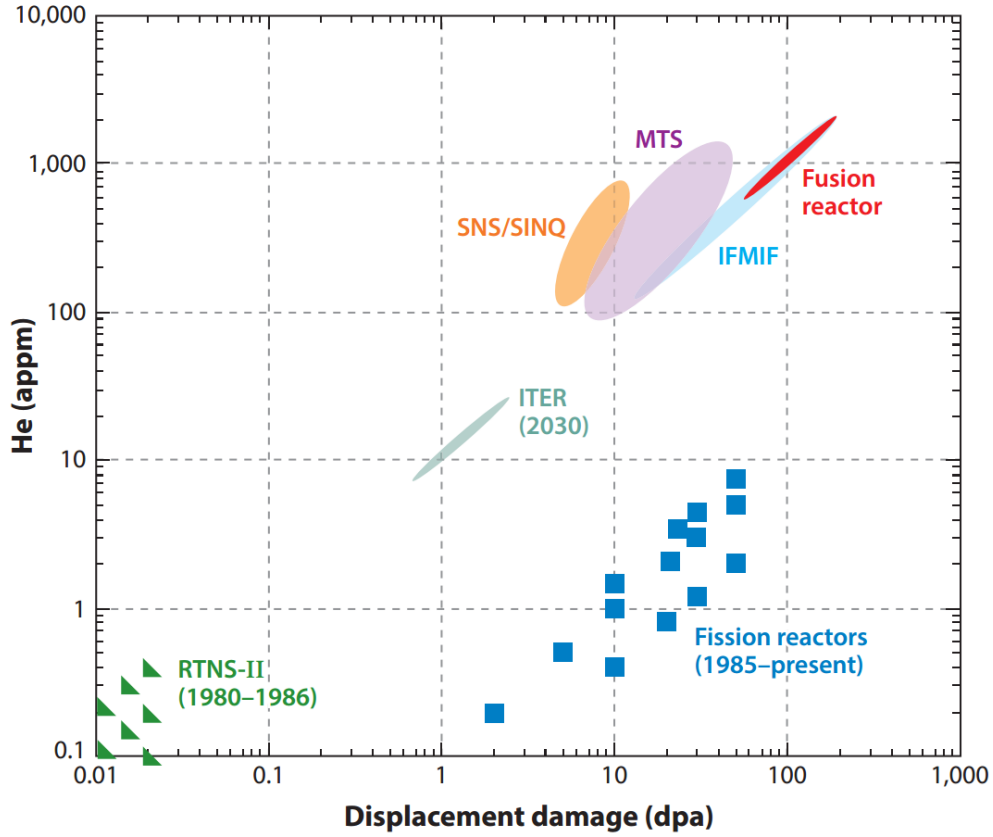


Figure 2.5: Helium accumulation with increasing irradiation damage, from a summary by Zinkle and Snead (2014) [8] of the RAFM steels experimental data base. Abbreviations include: RTNS, rotating target neutron source; IFMIF, proposed D-Li International Fusion Materials Irradiation Facility; SINQ, Swiss Spallation Source; SNS, Spallation Neutron Source; MTS, proposed Materials Test Station spallation source.

2.2.2 Defect accumulation and transport in iron-based alloys

As discussed, energetic neutrons from D-T reactions induce significant atomic displacements within the material matrix, producing vacancy and interstitial point defects in equal numbers. Due to their high mobility and instability, particularly at reactor relevant temperatures, a large majority ($\sim$ 99.7 % [52]) of these point defects recombine and annihilate, the fraction that remain can migrate and interact to form more stable structures such as, diffuse vacancy clusters, dislocation loops and microvoids, or they can be involved in long range diffusion, causing radiation induced segregation (RIS) and precipitation (RIP), void swelling and grain boundary cavity growth [53, 8, 54, 11]. Generally, the transition between each of these microstructural regimes is dictated by the irradiation temperature, T, although other variables such as PKA energy, radiation dose, dose rate, crystal structure, and products from transmutation reactions, e.g. H and He, can also effect the extent of the microstructural evolution [8]. The exact temperature at which the transition between each regime occurs is material dependent. However, these transition temperatures can be approximated by using the homologous irradiation temperature, ($^{T}/_{T_m}$), since the migration of interstitial and vacancy defects, vacancy cluster binding and dissociation energy, and the helium bubble migration energy are approximately proportional to the melting temperature of the material, T_m [8].

At low temperatures, e.g. 0 - 50 K, diffuse point defect clusters are formed, since the migration of point defects is minimal [55, 25]. As the irradiation temperature increases, long range interstitial migration is initiated, this allows interstitial dislocation loops and large defect clusters to form. Interstitial migration defines the type of defect structures seen until temperatures are high enough to allow significant vacancy migration, which occurs at around 0.3 T_m [8, 11, 56, 57]. Vacancy accumulation leads to void swelling and grain boundary embrittlement. At elevated temperatures defect fluxes in the material matrix increase; this can lead to the promotion of phenomena such as RIS and RIP [25].

As the irradiation temperature is further increased, $> 0.5\ T_m$, vacancy clusters start to dissociate, and are eventually annihilated until all the damage is removed [25, 58]. However, at these temperatures, stress-assisted helium migration to grain boundaries can cause cavities, leading to grain boundary embrittlement and a dramatic loss in fracture toughness [59].

The five main phenomena produced by defect accumulation and migration at varying damage dose and temperature are summarised in table 2.1.

Phenomena	T_m	T_m^{iron} /$^\circ C$	Damage/ dpa
Radiation hardening and embrittlement	< 0.4	< 600	> 0.01
Volumetric swelling	0.3 - 0.6	450 - 900	> 10
RIP and RIS	0.3 - 0.6	450 - 900	> 10
Irradiation Creep	> 0.45	> 675	> 10
High temperature He embrittlement	> 0.5	> 750	> 10

Table 2.1: Summary of the five main phenomena seen in irradiated materials, controlled by temperature and radiation dose. Data from Zinkle and Busby (2009) [11].

The material challenges summarised in table 2.1 must be considered in the development of structural and plasma facing materials for advanced nuclear reactors, however some of these will feature more strongly than others depending on the susceptibility of particular alloys. An outline of the theoretical framework dictating the microstructural evolution of irradiated metals is given in Mansur (1994) [22]. For a more comprehensive explanation of the theory surrounding each phenomena and their subsequent consequences on the mechanical behaviour of steels, see Was (2007) [25].

Since the irradiation temperature and dose used in the work presented in thesis was quite low, 300 $^\circ C$ and 0.01 - 0.2 dpa respectively, irradiation hardening was of primary concern. At these temperatures and doses, significant volumetric swelling and radiation induced diffusion were not expected, and fracture and creep tests were beyond the scope

of the mechanical tests performed.

The following section will first detail the development of RAF/M steels for fusion applications, and then finish by explaining why the introduction of a fine dispersion of oxides into the matrix was necessary to further increase radiation and high temperature resistance of candidate steels.

2.3 Engineering irradiation resistance

2.3.1 Introduction

Until the 1970s, austenitic stainless steels were the primary structural material for fast reactors, and are still used for certain components, such as fuel cladding, in the current Gen III reactors [60]. This was largely due to their popularity as an engineering material, superior corrosion resistant properties and ability to maintain mechanical integrity when subjected to relatively high temperatures. However, to improve reactor efficiency and to increase the operating lifetime, research into new steels alloys with increased radiation resistance was necessary. Ferritic/martensitic (F/M) steels, such as Sandvik HT-9, became an attractive candidate for such roles, owing to its excellent thermal properties and reduced swelling when compared to austenitic stainless steels [61].

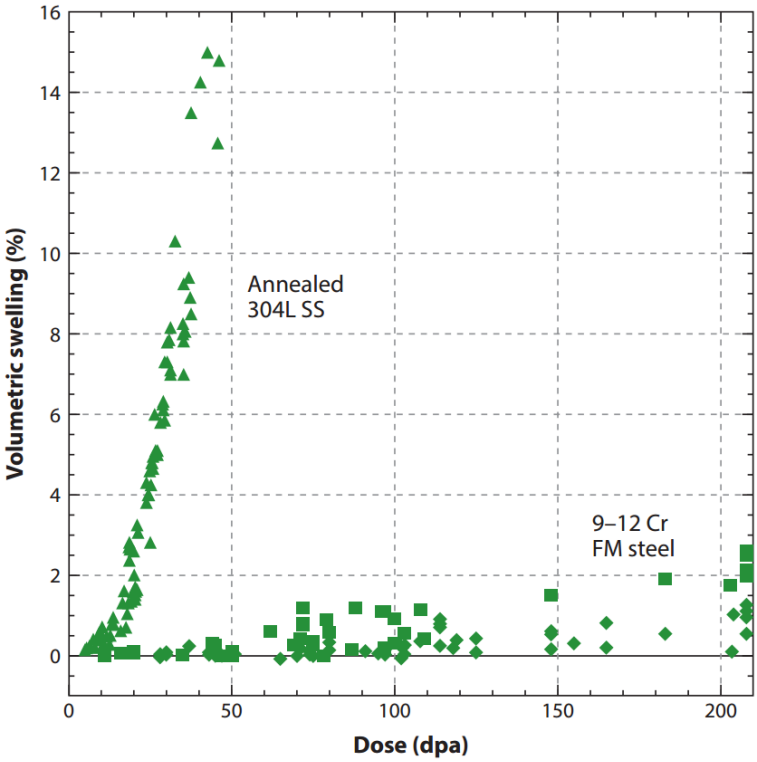


Figure 2.6: Comparison of void swelling in neutron irradiated 304L austenitic stainless steel and 9-12 % Cr ferritic-martensitic steel, such as HT9 (Fe-12Cr-1Mo-V-W-Ni), irradiated at 400-550 $°C$. Figure from [8].

A lower swelling response of body centred cubic (BCC) compared to face centred cubic (FCC) lattice types is primarily a result of the way the different lattices respond to both defect types. Krivit et al. (2011) [62] and Klueh and Harries (2001) [63] identify the following mechanisms to explain the origin the superior swelling resistance experimentally observed in ferritic steels:

1. The difference between the interstitial and vacancy relaxation volume is smaller in BCC than FCC lattice structures. This smaller divergence of the strain fields surrounding point defects in the BCC lattice decreases the bias towards accommodating interstitials. This leaves a greater number of 'free' interstitials in the BCC lattice than an FCC lattice, increasing the recombination probability with vacancies greatly. As a consequence, more displacement damage is needed to achieve a

supersaturation of vacancies, thus the transient swelling regime is extended and steady-state swelling is reduced [64, 65].

2. The vacancy migration energy in ferritic iron is lower than that of austenite. The increased vacancy mobility in BCC iron promotes recombination, thus reducing the vacancy number density, leading to a decrease in swelling. Additionally, the interstitial solutes (C and N), found in relatively large quantities in BCC steels, have a high binding energy with vacancy defects; this acts to reduce vacancy clustering and enhance defect recombination.

3. A strong interaction between dislocations and interstitial solutes in BCC iron causes a solute atmosphere around dislocations, reducing the interstitial dislocation bias. The solute atmosphere also inhibits glide and climb, allowing dislocations to remain as sinks for excess interstitials.

4. Sub-grain and lath interfaces in ferritic-martensitic (FM) steels serve as point defect sinks, that further enhance defect recombination and help suppress void swelling.

Although BCC alloys show an improved swelling resistance, they are not completely immune to void growth. Garner et al. (2000) [64] suggests that BCC alloys have extended transient regimes prior to the onset steady-state swelling, especially when irradiated under higher temperatures. Since the resistance to swelling depends primarily on void nucleation during the transient regime, the onset of this swelling maybe highly sensitive to dose rate and transmutant gas. The latter two effects are largely unexplored in literature, as the majority of high fluence data on swelling in BCC iron has been carried out using fast reactors with significantly lower dose rates and helium production than found with fusion relevant irradiation. More data needs to be gathered in order to fully understand the processes involved.

Since it is impossible to prevent cascade defect production from occurring, radiation resistance in steels must be engineered through alternative routes. Resistance can be built into a material by altering various aspects of the material such as the composition and microstructure, through the use of novel processing routes and thermo-mechanical treatments.

One fundamental compositional change is to eliminate nickel, which has a much higher neutron interaction cross-section than iron or chromium. Hence, reduced nickel steel alloys would be expected to produce lower concentrations of helium transmutations, thus reducing helium's detrimental effects on the microstructure [66, 67]. Additionally, the removal of nickel helps to reduce the activation of the material after decommissioning, discussed further in section 2.3.2. TEM analysis by Kasada et al. (2000) [68] revealed that irradiated steels alloyed with nickel produced dislocation loops that had a decreased size and increased number density compared with steels alloyed without. This had the effect of increasing the radiation hardening four-fold in the nickel alloyed steels.

Probably the most prominent effort to install radiation resistance in materials is based on the introduction of a high density of sink sites to control the fate of Frankel defects. They act to promote defect recombination [69, 70] and reduce related phenomena such as void swelling, RIS, irradiation hardening and creep. Sink sites can be introduced via high density of stable dislocations, grain boundaries or finely dispersed precipitates [24]. Odette and Hoelzer (2010) [23] suggest that high concentrations of subcritical bubbles can provide significant radiation protection. The authors suggest that a protection of > 400 dpa can theoretically be achieved by introducing a surplus of fine bubbles acting as deep helium traps, limiting the quantity of bubbles reaching bias driven growth. Granular and intergranular bubbles may also help to mitigate the accumulation of bias-driven cavities on grain boundaries, reducing high temperature helium embrittlement and low temperature DBTT shifts. However, the authors do warn

that the positive effects of subcritical helium bubbles can be completely reversed at high temperatures if they are not kept stable. Higher temperatures increase the He diffusion coefficient, greatly reducing the number of intergranular helium bubbles and increasing the amount trapped at grain boundaries. The authors propose that stable bubble densities can be achieved by trapping helium on the dislocation-matrix interface and fine scale thermally stable precipitates. Nanoscale precipitates also help to slow dislocation recovery at high temperatures, providing improved yield and creep strength [66, 23, 71, 72]. Section 2.5 discusses this in greater detail.

2.3.2 Development of reduced activation steels

In the mid 1980s, fusion materials programs worldwide began to develop reduced activation (RA) steels. The objective was to reduce the radioactivity of reactor materials, so as to improve worker and public safety whilst carrying out maintenance and the decommissioning of reactor components. To achieve this, certain traditional alloying elements, which when activated by high energy neutrons produce long half-life transmutation products, needed to be replaced. From nuclear calculations, elements such as Mo, Nb, Ni, Cu, Co, Ag, Al and N needed to be minimised or ideally completely eliminated. Molybdenum, for solid solution strengthening, was replaced by tungsten; vanadium and niobium, for fine carbide formation, was replaced with the chemically similar tantalum [60, 73].

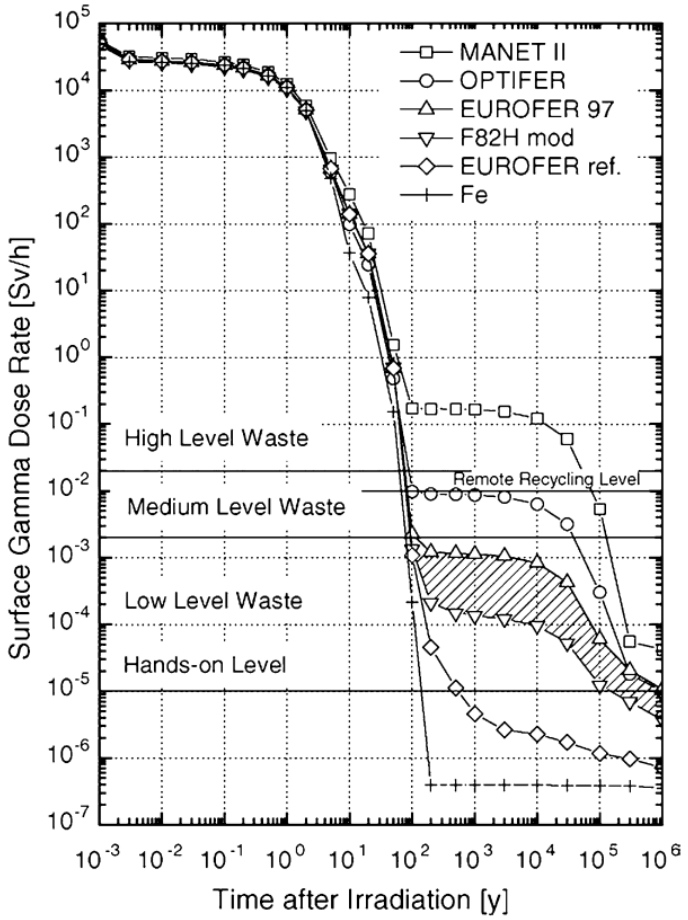


Figure 2.7: Calculated decay of γ-surface dose rate in pure iron and ferritic-martensitic steels after a simulated irradiation of 12.5MW year/m^2(up to 115 dpa) equivalent to conditions expected in a DEMO reactor first wall. Graph from [74].

Co-operation by the US, Japan and the EU, brought about by an IEA agreement, saw the joint research to develop an F/M steel that would keep activation levels to a minimum, whilst at same time resist radiation induced embrittlement, particularly at temperatures below 700 K. This was achieved by evolving more established F/M steels, such as HT9 and MANET II. Early examples of this approach are the Japanese produced reduced activation ferritic-martensitic (RAF/M) steel, F82H, and the OPTIFER RAF/M steel, produced at FZK (now KIT) in Germany [75, 76]. By the mid 90s, RAF/M steels were considered to have the most potential for fusion blanket applica-

tions. The research provided by F82H and OPTIFER, among others, paved the way for the production of a slightly modified RAF/M steel, EUROFER97, commissioned by the EU and designated to be tested in ITER blanket modules [75, 76]. The compositions of each of these steels are given in table 2.2.

The radioactivity level of RAF/M steels after service in DEMO is calculated by Enlich et al. (1996) [74] and demonstrated in figure 2.7. All RAF/M steels showed a reduction of activity over time when compared with the FM steel, MANET II. However, EUROFER97 (as measured) could not reach the desired low activation levels within 100 years for either shallow land burial (low level waste) or the hands-on recycling limit of 25 μSvh^{-1} [77, 41]. This was due to the relatively high levels of undesired impurities introduced during the fabrication process, either from raw materials that did not satisfy the specified impurity tolerance, or from residues left in equipment used for producing conventional alloys. Van der Schaaf et al. (2003) [75] suggests that hands-on activity levels within 100 years can feasibly be achieved with more control over the raw material feedstock and if dedicated production lines are used.

Material	Desired /%wt	Fe	Cr	W	Mn	V	Ta	C	Undesired /ppm	Nb	Mo	Ni	Cu	Al	Co
EUROFER (ref) specified tol		Bal.	8.5 to 9.5	1.0 to 1.2	0.20 to 0.60	0.15 to 0.25	0.10 to 0.14	0.09 to 0.12		< 10 [<0.01]	< 50 [< 1]	< 50 [< 10]	< 50 [< 10]	< 100 [< 1]	< 50 [< 10]
EUROFER97 as measured		Bal.	8.84	1.11	0.43	0.19	0.14	0.12		5	21	175	118	75	50
F82Hmod		Bal.	7.7	1.94	0.16	0.16	0.02	0.09		1	30	200	100	30	50
OPTIFER V		Bal.	9.48	0.99	0.39	0.25	0.06	0.12		70	50	50	50	70	-
MANET II		Bal.	10.3	-	0.78	0.2	-	0.11		1400	6100	6800	100	40	-

Table 2.2: Chemical composition of EUROFER97 compared to F82Hmod, OPTIFER V and MANET II. Square brackets represents ideal quantities for EUROFER(ref). Data from [76].

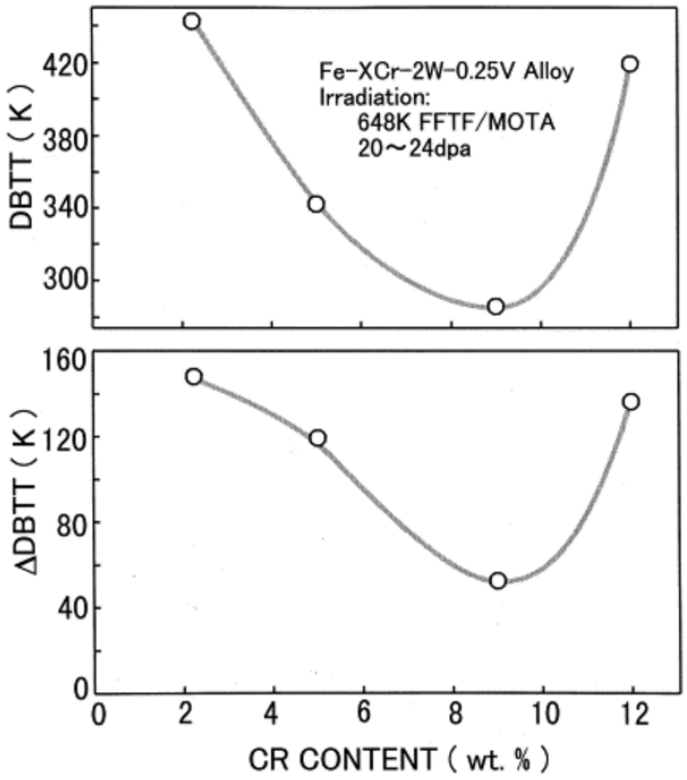


Figure 2.8: Chromium content dependence of the DBTT and the DBTT shift (ΔDBTT) for RAFM alloys after neutron irradiation. Figure from [44].

When considering the compositions of RAFM structural candidates, steels with 7 - 9 % Cr were favoured over those with 12 % Cr [37]. This was because of the difficulty with eliminating the δ-ferrite phase, causing reduced toughness, in 12 % Cr steels without the austenitic stabilisation by an increased carbon or manganese content [60]. Furthermore, figure 2.8 shows that ΔDBTT and DBTT was minimised at approximately 9 %wt Cr.

This led to the preference of 9 %wt Cr steel when choosing alloy compositions for candidate structural materials such as EUROFER97. In addition, tantalum was chosen to stabalise the grain size via fine carbide formation and improved the DBTT and strength. Tungsten also improves the DBTT and strength, additionally, it was also seen to improve ductility and creep strength. However, it is necessary to keep the tungsten content low, $\backsim$ 1 %wt, as the tritium breeding ratio is higher for a lower W content [76].

2.4 Mechanical properties of irradiated RAFM steels

The low swelling character of tempered ferritic-martensitic steels has been demonstrated during irradiations of over 200 dpa at 400 $°C$ performed at the Fast Flux Test Facility (FFTF), the majority of steels irradiated showed swelling of < 3 %, with the maximum swelling observed in an alloy of 9Cr-2Mn-1WV, for which swelling still remained < 5 % [78, 79]. Although radiation induced swelling in RAF/M steel is largely suppressed, displacement damage from high energy neutron irradiation can have significant negative effects on the mechanical properties. Radiation hardening caused by the evolution of the microstructure via the agglomeration of point defects can reduce ductility, increase DBTT and reduce the upper shelf energy (USE), which raises the lower bound of the operating temperature window. RAF/M steels are also prone to a dramatic loss in tensile and creep strength at temperatures above $\backsim$ 500 $°C$, the latter of which is only further exacerbated by irradiation.

Irradiation hardening

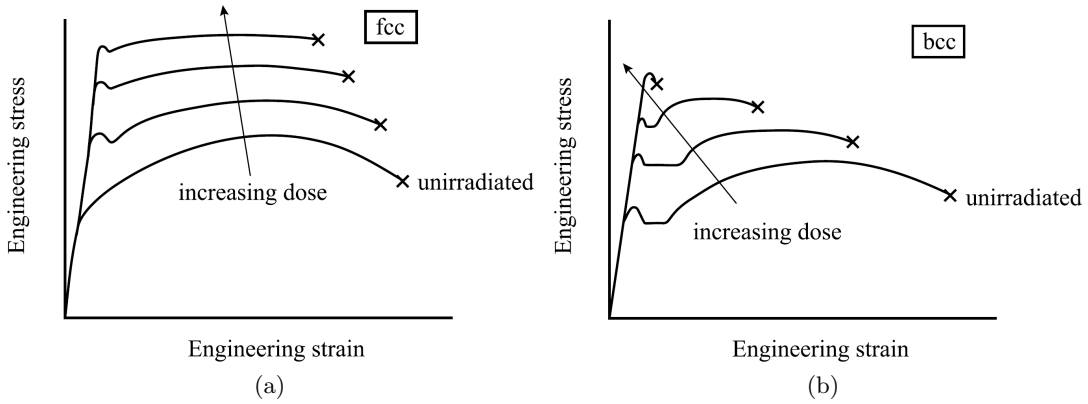


Figure 2.9: Effect of irradiation damage on the uniaxial tenisle behaviour in, (a) an FCC austenitic steel, and (b) a BCC ferritic steel. Figure from Was (2007) [25]

The stress required to initiate and maintain plastic flow in metals may be increased via two mechanisms, source hardening and friction hardening. Source hardening is the

increase in stress needed to unlock a pinned dislocation and allow it to move on its glide plane, this effect is significant when a clear upper and lower yield point is observed in a uniaxial tensile test [80, 81]. Source hardening is particularly prevalent in BCC metals with high levels of free interstitial impurity atoms such as carbon and nitrogen [82, 83], but is also present in irradiated FCC metals (represented in figure 2.9) where defect clusters local to Frank-Read sources increases the stress needed to expand the loops [25, 84]. Conversely, source hardening in BCC metals is seen to decrease with increasing fluence, this has been attributed to interstitial solute trapping by individual point defects or defect aggregates [82, 83].

Since source hardening decreases with increasing fluence, the majority of radiation hardening in BCC metals stems from the increase in stress needed for dislocations to overcome obstacles, otherwise known as friction hardening. Friction hardening can occur via long range or short range stress fields. This can arise from mobile dislocation interaction with the dislocation network, or obstacles such as defect clusters, loops, precipitates, voids, grain boundaries, etc [25]. When dislocations interact with components of the dislocation network they exert forces on each other due to their associated stress fields, additional stress is needed to overcome these forces [84].

Even quite modest displacement damage levels can lead to significant hardening, this is demonstrated in figure 2.10, where the yield stress in RAFM steels, EUROFER97 and F92H, increases rapidly from 0 to 5 dpa.

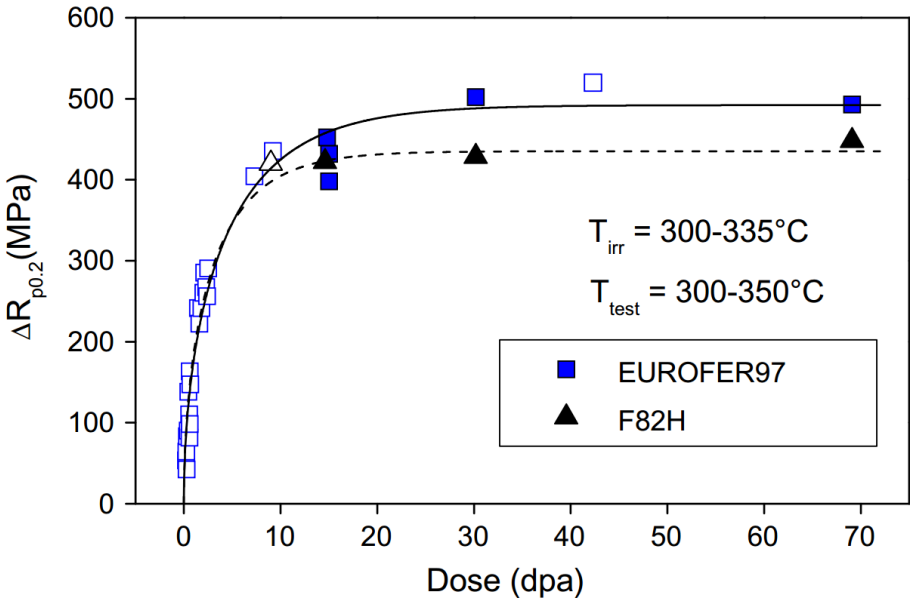


Figure 2.10: Saturation of irradiation hardening for RAFM steels, EUROFER97 and F82H. Solid symbols represent data from KIT, irradiated in BOR-60 at 300-335 $°C$ [85]. Open symbols represents data from [86, 87, 88]. Figure from [89]

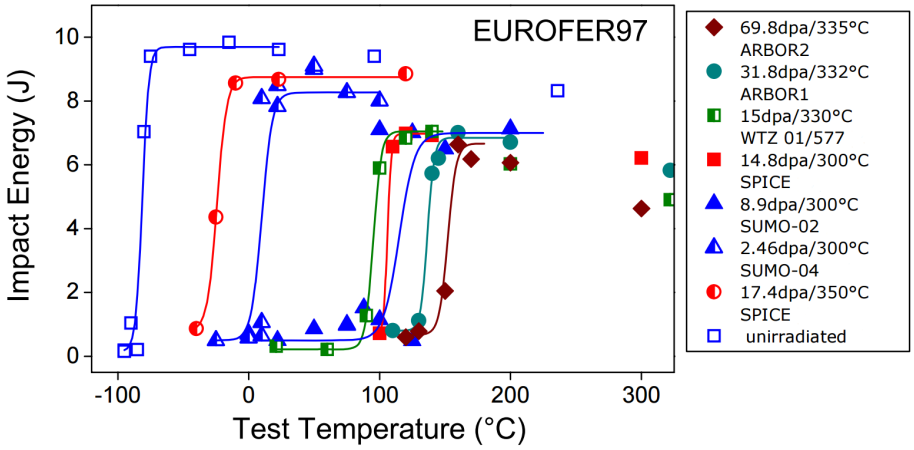
Radiation hardening is shown to saturate with increasing fluence; results summarised by Giganidze et al. (2011) [85] found that the saturation point occurred at approximately 10 dpa at an irradiation temperature of $\backsim$ 300 $°C$, with no significant change in yield stress past 40 dpa [90, 91]. This is because at low doses, hardening is dominated by defect clusters and small loops, as the dose increases, loops expand and become part of the dislocation network, saturating the hardening [92].

As the temperature is increased to around 300 - 400 $°C$, vacancies have enough energy to migrate and form voids and bubbles that contribute to the hardening. As the temperature is increased to $\backsim$ 600 $°C$, hardening is dominated by network dislocations, although radiation hardening is generally suppressed due to lattice recovery and reduced void growth. However at high doses, void growth can become significant. As temperature increased further, radiation damage from point defect creation completely anneals, although at extreme temperatures, cavity grow caused by stress assisted helium migration may become relevant to material degradation.

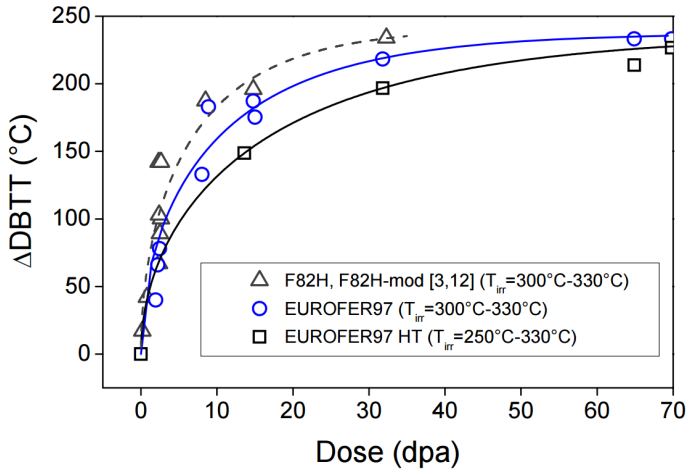
It is generally accepted that hardening is maximised at approximately 300 $^{\circ}C$ and at doses of 20 - 30 dpa. At this temperature the combined contribution to hardening from of defect clusters, dislocation loops/network, voids and helium bubbles is greatest[25].

Impact and fracture toughness

Matrix hardening is often accompanied by a substantial loss in ductility and work hardening capability, and can induce a decrease in fracture toughness, manifesting in an increase of the ductile to brittle transition temperature (DBTT) and a reduction in upper-self energy (USE) [93, 94, 24]. A brittle fracture is characterised by a rapid crack propagation across the entire specimen, without any appreciable plastic deformation prior to fracture [25]. Whereas if the material undergoes plastic deformation prior to and during crack propagation, then it can be described as a ductile fracture [95]. Initially, the shift in DBTT and magnitude the embrittlement increases rapidly with radiation dose (below $\backsim$ 10 dpa), after which the effect is seen to saturate [96].



(a)



(b)

Figure 2.11: (a) DBTT of EUROFER97 in unirradiated condition, and after neutron irradiation in different European irradiation programs. Data summarised by [89]. Unirradiated data and SPICE data from [97], SUMO data from [88], WTZ data from [98], ARBOR1 data from [99], and ARBOR2 data from [89]. (b) The change in DBTT (ΔDBTT) saturating with increasing displacement damage [89].

Data summarised by Giganidze et al. (2008) [89] in figure 2.11 display a large increase in the DBTT of EUROFER97, $\backsim 250\ °C$ at 70 dpa and an irradiation temperature of $\backsim 300\ °C$. These conditions also cause a drop in the USE by almost a third. The dramatic reduction in USE and the increase of the DBTT from cryogenic temperatures to above room temperature is reported by many authors for RAF/M steels [60, 41, 76, 96]

and presents a serious problem for nuclear engineers. Reactor vessels using EUROFER, or other RAF/M steels, as structural materials run a severe risk of fracture during cool down periods if irradiated at this temperature. Similar to the observed saturation in tensile tests, the ΔDBTT begins to saturate with increasing fluence at approximately 20 - 40 dpa for irradiation temperatures of approximately 300 $^{\circ}C$, shown in figure 2.11(b).

The increase in DBTT and decrease in USE at these irradiation temperatures puts a lower bound to the safe operating window of RAF/M steels. Radiation induced fracture toughness can be suppressed by increasing the irradiation temperature, however as the temperature increased past $\backsim$ 500 $^{\circ}C$ RAF/M steels experience a large reduction in strength and increase in creep strain.

Temperature dependence of strength

Obstacle strength and density determine the average glide velocity of dislocations and so determines the work hardening behaviour. An activation energy is needed for a dislocation to overcome an obstacle, the energy available to a dislocation is a summation of the thermal energy and the energy provided by the stress field. If the thermal energy/temperature is increased, less stress is needed for the dislocation to overcome the obstacle, and the material softens.

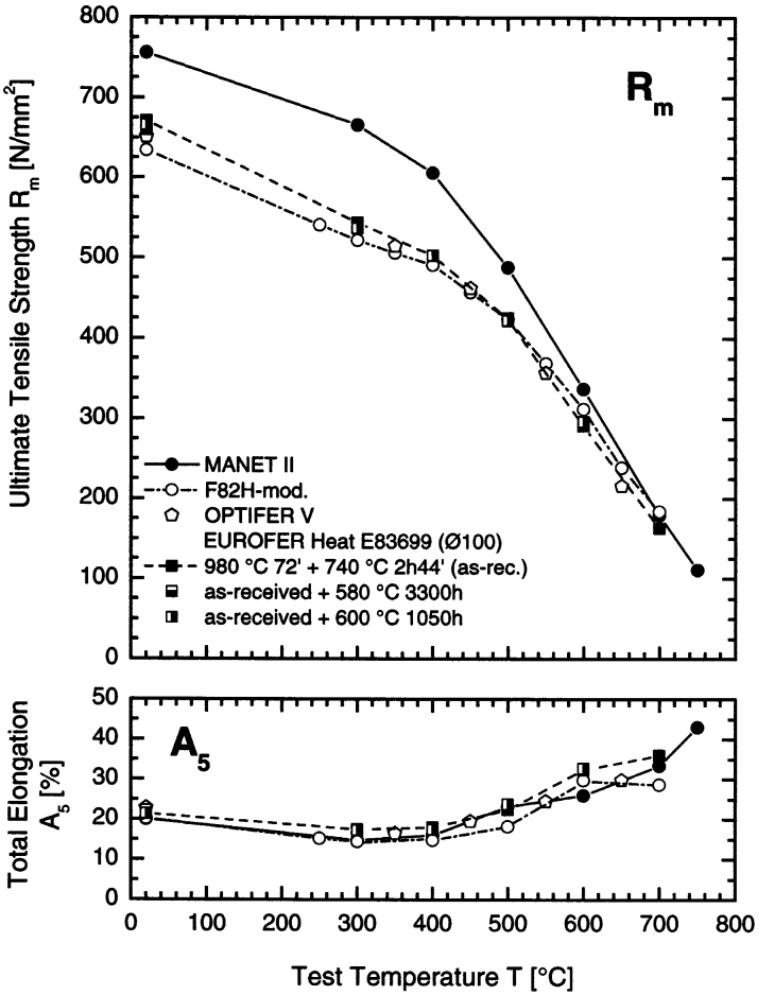


Figure 2.12: Strength and elongation dependence on temperature for various unirradiated RAF/M steels. Figure from [100].

For fusion power to be a viable energy source, first wall structural materials will need to have operating temperatures well beyond those used in previous reactor concepts. One of the critical issues surrounding the use of RAF/M steels for fusion applications is their thermo-mechanical response. Figure 2.12 shows the deterioration of strength with increasing temperature for different RAF/M steels. This is often characterised by a rapid loss in yield and UTS and an increase in ductility after $\backsim$ 500 $°C$, attributed to lattice recovery, grain growth, decrease in stress needed for dislocation sources to overcome obstacles, etc. More specifically to RAF/M steels, fine carbides, such as

($M_{23}C_6$), which decorate and protect lath boundaries from disintegration, are found to coarsen above 450 $°C$ [101, 102]. This precipitate coarsening and loss of lath boundary protection at high temperatures could also help to explain the reduction of UTS and increase in ductility with temperature. Although carbides help to maintain tensile strength when under cyclic strains, the precipitation of carbide phases have also been shown significant degrade tensile ductility and impact properties [103].

Summary

Currently the major areas of concern in RAF/M alloys are their upper temperature limit, irradiation induced hardening, and the embrittlement effects of high concentrations of hydrogen and helium [12]. RAF/M alloys demonstrate an increase in yield stress and embrittlement at irradiation temperatures lower than 400 $°C$. As irradiation temperature increases, the effects of irradiation hardening start to diminish, becoming negligible past 500 $°C$. However, above 500 - 550 $°C$, softening can occur, leading to drop in tensile strength and a strong reduction in creep strength [104]. The target operating temperature for a first wall structural material in a prototype fusion reactor is approximately 600 - 800 $°C$. If the temperature limit of RAF/M steels can be increased to 600 - 650 $°C$, then liquid metal cooling systems could be employed to keep the temperature within safe limits [7, 105]. Current research is aimed at enhancing the upper operating limit and suppressing helium embrittlement by introducing a high density of fine oxide dispersants within the RAF/M, more recently reduced activation ferritic (RAF), alloy matrix.

2.5 Oxide dispersion strengthened steels

2.5.1 Introduction

By introducing a fine dispersion of stable nanoscale oxides into the material matrix, both the radiation and high temperature resistant properties developed in RAF/M steels may be improved upon. A high density of these nanoscale particles provide numerous oxide-matrix interfaces which act as sink sites for point defects, promoting their recombination [69, 70]. While the underlying mechanisms are still in contention, it is thought that the superimposed network of interface dislocations accommodating coherency strains between two adjacent crystal lattices and their intersections (referred to as nodes), can act as sink sites and sources of point defects due to the low point defect formation energy at these points [106, 107].

Point defect recombination helps to alleviate irradiation induced microstructural changes. In turn, reducing effects such as irradiation hardening and embrittlement, void growth, RIS and RIP, and irradiation creep [24, 12]. Fine scaled particles can also reduce the creep strain rate and increase strength at elevated temperatures through precipitate/dispersion hardening. They also serve as nucleation sites for helium bubbles, which can act as additional sink sites, and prevents bubbles from coalescing at grain boundaries, suppressing helium induced embrittlement [23, 12]. To achieve success, ODS alloys will have to find a suitable compromise between improved high temperature strength, and reduced ductility, fracture and impact toughness [108, 109, 110].

2.5.2 Fabrication

In the late 1960's J.S Benjamin and his colleagues at the Paul D. Merica Research Laboratory of the International Nickel Company (INCO) developed a cold welding and powder refinement process, later known as mechanical alloying, that involved the creation of an alloy by using intense mechanical deformation to bind mixtures of elemental or master alloy powders [111, 112]. Using this process, the usual limits of solubility

imposed by solidification may be exceeded and dispersoid particles, commonly yttrium oxides, may be uniformly incorporated into the bulk material [113]. Figure 2.13 shows a schematic diagram that describes the basic fabrication process for ODS alloys.

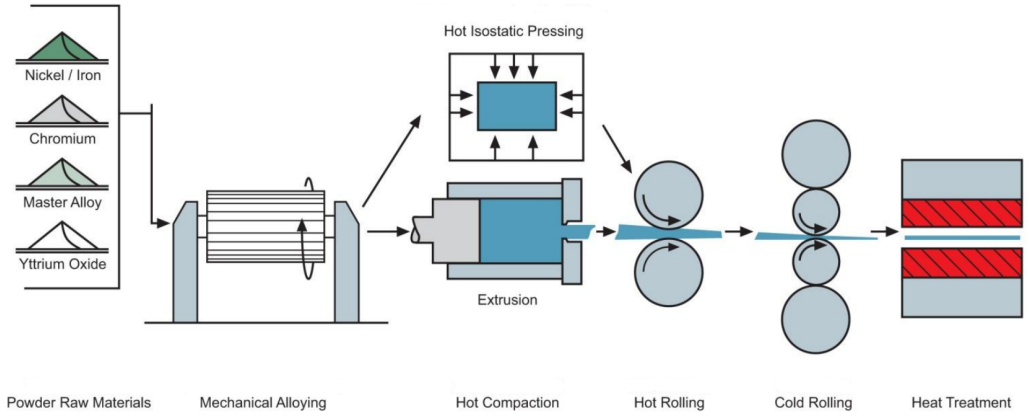


Figure 2.13: Schematic of the ODS fabrication process showing the mechanical alloying of elemental powders, followed by the consolidation stage that ultilises either HIP or extrusion. After this, optional post processing treatments can be applied, depending on consolidation technique and material purpose. Figure from [114].

Due to the relatively low levels of deformation in the starting powder, particle size increases during the initial stages of mechanical alloying via the cold welding process. As the powder becomes increasingly work hardened and the grain structure refined, particle fracture starts to increase leading to an overall reduction in their size [113]. Eventually, cold welding and fracture balance, and particle size tends to a specific value as milling time is increased [115]. Milling occurs in an inert atmosphere over the course of tens of hours, depending on the milling method used [116]. Both a high concentration of defects and an increased local temperature contribute to the diffusion of powder constituents, for example solute into the matrix. Ideally the particle composition reaches a steady state, where every particle contains the same compositional proportions as the starting powder [116]. Once a compositional steady state is achieved, usually determined using techniques such as X-ray diffraction (XRD), the mechanically alloyed powder is vacuum degassed, placed into a mild steel container and consolidated using hot-isostatic pressing

(HIPing) or hot extrusion.

The method of consolidation directly effects the microstructure; hot extrusion typically produces grains that are elongated in the extruded direction with a diameter/length ratio of approximately 1/10, with a (110)-fibre texture. [24, 117]. Odette et al. (2008) [24] reports that extruded ODS cladding tubes typically have half the creep strength in the hoop direction compared to the axial direction. Grain elongation and texturing also produces a low toughness for cracks propagating in the axial direction. Because of this, powders consolidated via extrusion are often subjected to thermal recrystallisation to reduce the anisotropic mechanical properties [118, 119, 24]. In contrast, powder consolidated in a HIP has the advantage of producing ODS material with an equiaxed grain structure, thus heat treatments are not essential, and the post processed microstructure can be retained. However, the geometry of the material produced is not very practical for commercial use.

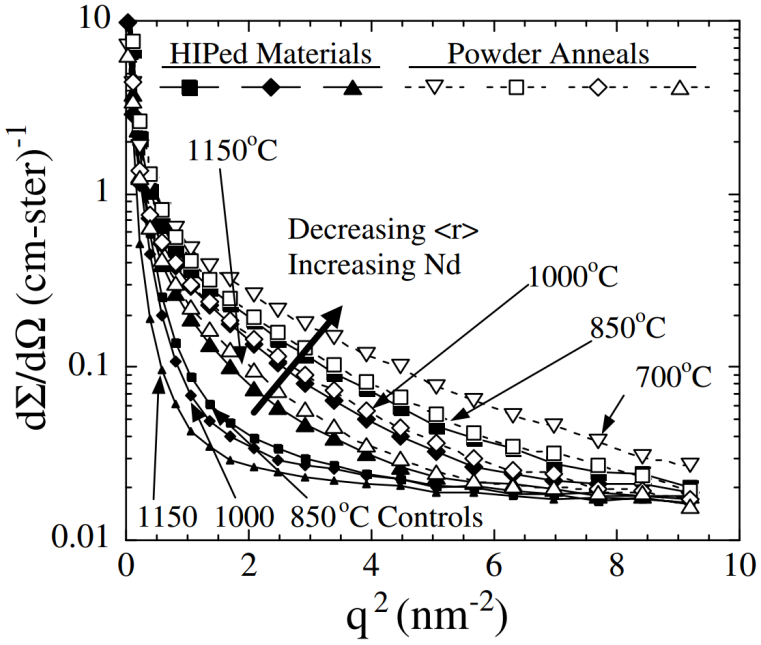


Figure 2.14: The effect of HIP consolidation (closed symbols) and powder annealing (open symbols) temperatures on the nanocluster formation in 14YWT (Fe-14Cr-3W-0.4Ti-0.25Y_2O_3). The controls are of the same composition but without yttrium. Figure from [120].

Consolidation temperature can also have a significant effect on the mechanical properties of ODS steels. Using small-angle neutron scattering (SANS), Alinger et al. (2004) [120] investigated the effect of HIP and powder annealing temperature on the nanocluster dispersion radius, number density and volume fraction in 14YWT (Fe-14Cr-3W-0.4Ti-0.25Y_2O_3) . The total neutron scattering cross section (nuclear and magnetic), $\frac{d\Sigma}{d\Omega}(q,\phi)$, was plotted against the square of maximum scattering vector, q^2, results are presented in figure 2.14. The shallow slope of the non-yttriated 14WT control specimens in the range of $> q^2$ indicates that nanocluster dispersants are not present. The corresponding $\frac{d\Sigma}{d\Omega}$ curve for each 14YWT of HIPing temperatures, 1150 $^\circ C$, 1000 $^\circ C$ and 850 $^\circ C$, indicates the presence of nanocluster dispersants, the increasing scattering cross-section suggests the decrease in cluster radius and increase in cluster number density with decreasing HIPing temperature.

The exact mechanisms responsible for the introduction of oxides into the matrix are still under contention. The general consensus of the literature is that the thermally stable Y_2O_3 powder particles decompose into yttrium and oxygen atoms during high energy mechanical alloying, evidenced by a reduction in the intensity of Y_2O_3 peaks in XRD and SANS with increasing milling time. Using the example of ODS ferritic alloys, the yttrium and oxygen then dissolves into the ferritic steel matrix, and following consolidation at $> 1000\ ^\circ K$ is then precipitated out as stable nanoscale oxide particles [53, 121, 122, 123, 124, 125]. However, the work of Hilger et al. (2014) [126] refutes this, since dissolution would change the lattice parameter of the iron matrix, which was not observed in XRD measurements. There is increasing evidence that the Y-O bonds remain intact after milling, and the reduction of the Y_2O_3 peak is due to the severe fragmentation of the initial cubic yttrium oxide powder into an X-ray amorphous sub-nanocrystalline phase [127, 128, 126]. Subsequent thermal consolidation then leads to Ostwald ripening of the oxides, after which the nanoparticles can be resolved in XRD. Further investigation is necessary as this model cannot easily explain how more

complex structures, such as the Y-Ti-O oxides that are widely reported in the literature, are formed.

2.5.3 Mechanical properties of ODS steels

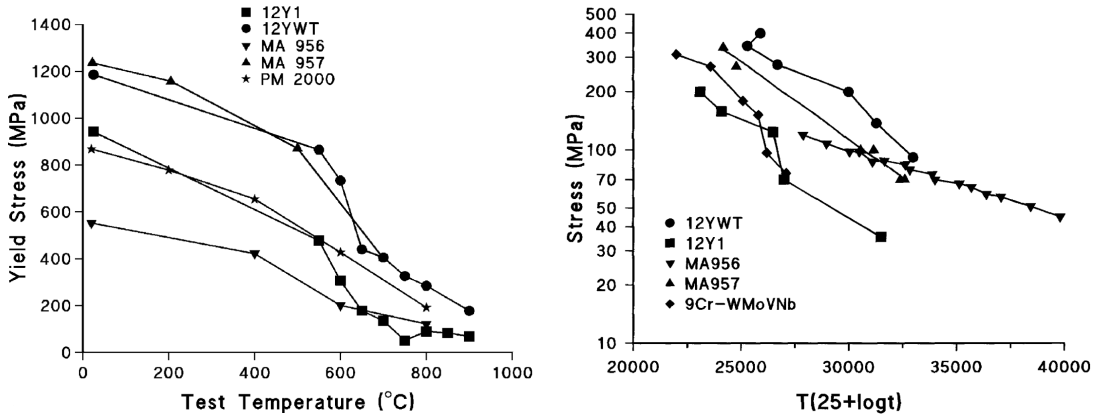
Early commercial ODS steel variants such as MA956 and PM 2000, developed by the International Nickel Company (INCO) and Metallwerk Plansee GmbH respectively, were alloyed with aluminium alongside chromium. Although they showed improved high temperature and creep strength when compared to their non ODS counterparts, they suffered from coarse microstructures dominated by relatively large Y-Al-O oxide particles [129, 130]. Klueh et al. (2005) [129] compared the mechanical behaviour and microstructure of these early commercial ODS steels with an other INCOloy, MA957, and two experimental ODS steels from Oak Ridge National Laboratory (ORNL), designated 12YWT and 12Y1. The compositions of each ODS steel are given in table 2.3.

	Fe	Cr	W	Ti	Al	Ni	Mn	Mo	Si	Y	O	C
PM 2000	Bal.	18.9	0.04	0.45	5.10	0.01	0.11	0.01	0.04	0.37	0.25	0.01
MA956	Bal.	21.7	-	0.33	5.77	0.11	0.06	<0.05	0.05	0.38	0.28	0.03
MA957	Bal.	13.7	-	0.98	0.03	0.13	0.09	0.30	0.04	0.28	0.21	0.03
12YWT	Bal.	12.6	2.44	0.35	-	0.27	0.60	0.02	0.18	0.16	0.16	0.05
12Y1	Bal.	12.9	<0.01	0.003	0.007	0.24	0.04	0.03	0.03	0.20	0.15	0.045

Table 2.3: Chemical compositions of five ODS steels investigated by Kleuh et al. (2005) [129].

Using a combination of optical microscopy, transmission electron microscopy (TEM) and atom probe tomography (APT) multiple authors have determined that the addition of titanium and the removal of aluminium vastly altered the size, number density and composition of the oxide dispersants [131, 132, 133, 134]. For 12Y1, the dispersant diameter was found to be between 10 - 40 nm at a number density of 10^{20} - 10^{21}

m^{-3}, with diffraction studies indicating the particles were essentially unaltered pure crystalline Y_2O_3. Whereas with the addition of titanium and tungsten, the dispersant diameter and number density was found to be 3 - 5 nm, and 1 - 2 x10^{23} m^{-3} respectively. APT revealed that these dispersants were compositionally distinct nano-sized clusters enriched in yttrium, titanium and oxygen (Y-Ti-O), slightly enriched in chromium and slightly depleted in iron and tungsten [129]. A similar difference in dispersant composition, size and number density are also present in the PM 2000 and INCOly steels, with the aluminium depleted MA957 steel showing a high number density of < 5 nm Y-Ti-O clusters. Whereas the steels alloyed with aluminium, MA956 and PM 2000, demonstrated a decomposition of Y_2O_3 into $Y_4Al_2O_9$ complex oxides, which were of a larger size and smaller number density than the respective Y-Ti-O clusters found in MA957 [135, 136, 129]. Mechanical data, presented by Klueh et al. (2005) [129], suggest that a high number density of the fine Y-Ti-O dispersions results in a greatly improved mechanical response, particularly at elevated temperatures. The supporting data carried out by the author on the materials stated in table 2.3 is given in figure 2.15.



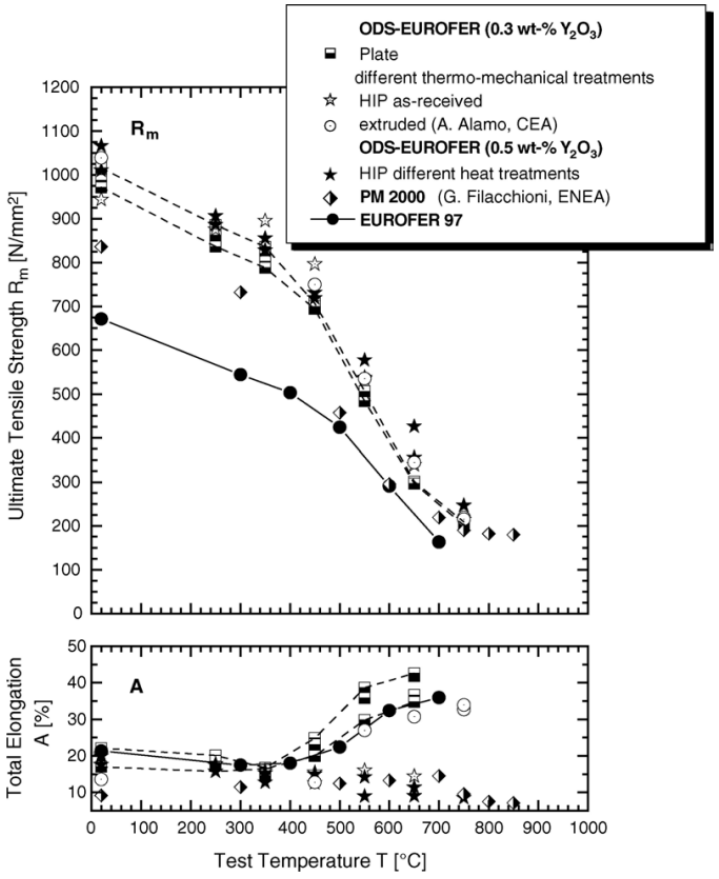
(a) (b)

Figure 2.15: A comparison of mechanical data from the materials presented in table 2.3. (a) Yield stress dependence on temperature. (b) Rupture stress vs. Larson-Miller parameter, including an FM steel. Figures from [129].

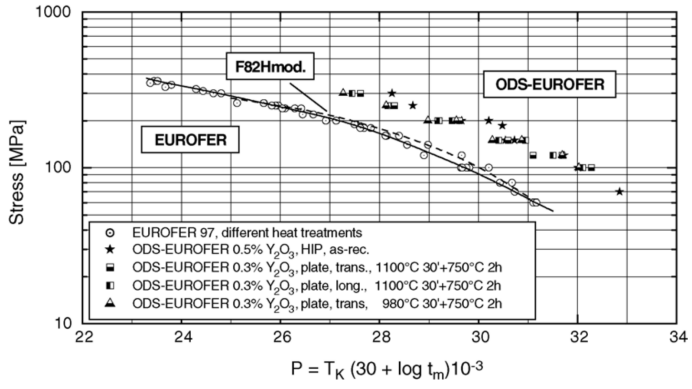
The differences in the microstructure were reflected in the differences in mechanical properties. Figure 2.15(a) shows a significant variation in the yield stress of the different steel compositions from room temperature to 800 $°C$, although all steels showed decrease in yield stress with increasing temperature. The yield stress of 12YWT is much higher than 12Y1, as was MA957 compared to MA956. The 12YWT and MA957 alloys had a very similar mechanical response to tensile testing. The yield strength properties of all steels appeared to converge for extrapolations of temperatures > 850 $°C$.

The creep-rupture properties were compared using a Larson-Miller parameter with a constant of 25, and are shown in figure 2.15(b). The Larson-Miller parameter allows the relation of creep rupture time and temperature to a given applied stress, where T is the test temperature and t is the rupture time in hours for an isothermal condition.

The 12YWT alloy had greatly improved creep-rupture properties over the 12Y1 and the 9Cr FM alloy, and a modest improvement over the MA957 alloy for high stresses and low Larson-Miller values (e.g. lower temperature and rupture life). However, at Larson-Miller values of $\backsim$ 3.5 x10^4 there appeared to be a convergence of creep properties, with MA956 showing a resistance to rupture at extended Larson-Miller values. The similar tensile and creep properties of MA957 and 12YWT was concluded to be due to the fine distribution of < 5 nm sized oxide dispersions, and supports the present tendency of experimental ODS alloys to be composed of some variant of yttrium, tungsten and titanium (YWT), with best efforts to minimise aluminium.



(a)



(b)

Figure 2.16: The comparison of the mechanical behaviour of EUROFER and ODS EUROFER. The latter is subjected to various heat treatments after HIPing. (a) Ultimate tensile strength and total elongation dependence on temperature. (b) Rupture stress vs. Larson-Miller parameter with a constant of 30. Figure from [76].

The addition of yttrium oxide dispersions into the matrix of experimental RAFM steels, such as EUROFER97, has also been shown to improve their mechanical properties at elevated temperatures. ODS EUROFER is currently intended to be used as a plasma facing material plated to the EUROFER first wall of the candidate Pb-17Li blanket [76], shown in figure 2.2(c). Two different powder compositions were investigated by Lindau et al. (2005) [76], one contained 0.5 %wt Y_2O_3, and the other 0.3 %wt. The 0.5 %wt Y_2O_3 specimens were HIPed at four different temperatures and were tested in the 'as HIPed' condition, e.g. no thermo-mechanical treatments. The 0.3 %wt Y_2O_3 specimens were HIPed at one temperature (not specified by author) and subjected to hot rolling using the cross-rolling technique; with post-rolling heat treatments consisting of re-austenitisation and tempering, e.g. 30 mins at a varying temperature, water quenching, then 2 hours at 750 $^{\circ}C$. Figure 2.16(a) shows a large improvement in the ultimate tensile strength across all ODS EUROFER specimens compared to the more conventional EUROFER97. A similar result was found in creep-rupture tests where the author found all ODS EUROFER specimens showed similar creep strengths as RAFM EUROFER97 and F82H but at temperatures $\backsim$ 100 K higher.

However, the fabrication route and yttrium content affected the ductility of ODS EUROFER. The specimens from the production route that did not receive thermo-mechancial and post-rolling heat treatments, saw a reduction in total elongation for temperatures $>$ 400 $^{\circ}C$, indicating embrittlement. Whereas the speciemens that had been subjected to hot rolling and heat treatments, saw a notable increase in total elongation at temperatures $>$ 400 $^{\circ}C$, and was equal to, or even higher than the base material over the whole temperature range. Lindau et al. (2005) [76] also saw a similar variation in the impact behaviour of the ODS EUROFER specimens, results are displayed in figure.

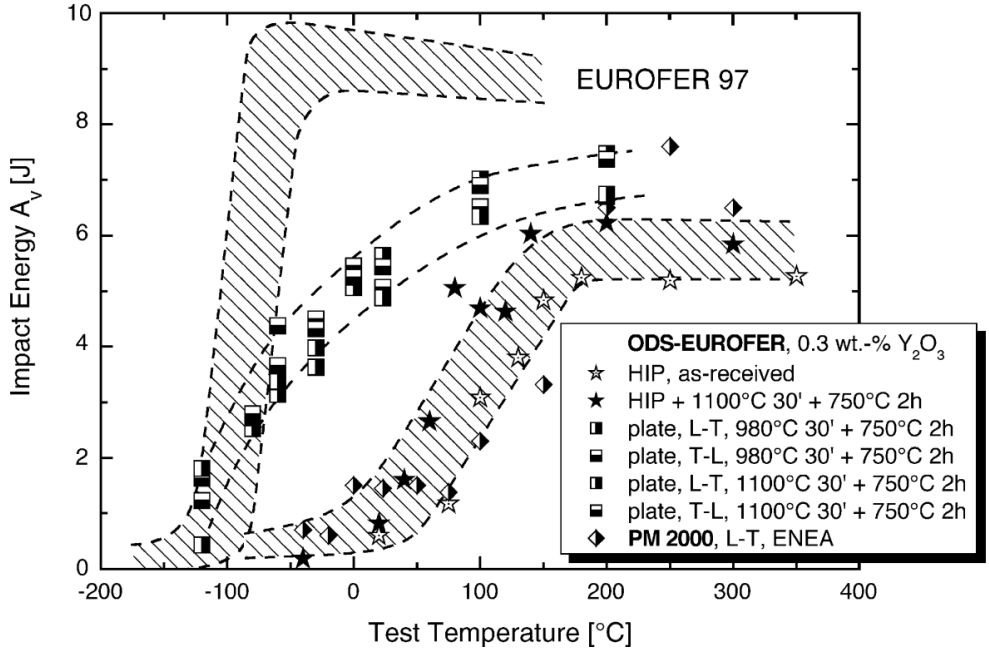
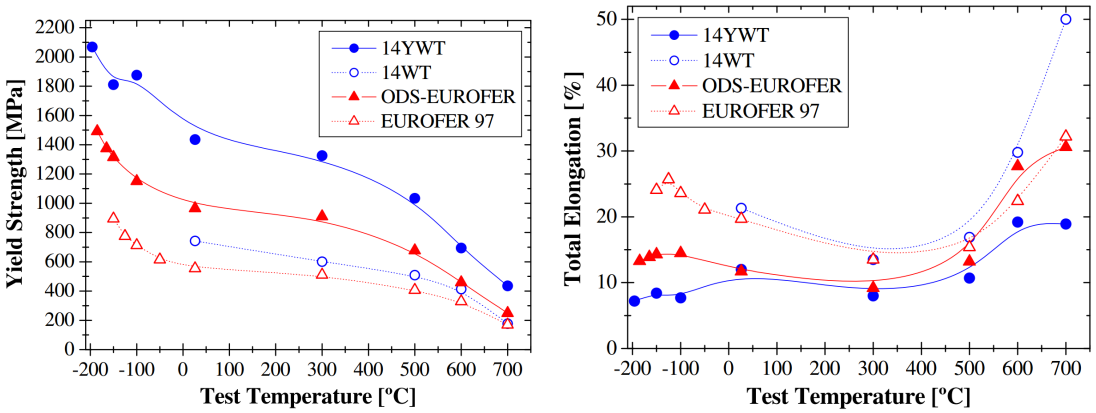


Figure 2.17: Temperature dependence of total absorbed energy of different ODS EUROFER steels in comparison with EUROFER97 and PM2000. L-T refers to fracture specimens fabricated with their long axis in the longitudinal direction, and T-L with their long axis in the transverse direction. Figure from [76].

Figure 2.17 demonstrates the shift of the DBTT from between +60 $^{\circ}C$ and +100 $^{\circ}C$ for the 'as-HIPed' and heat treatment only specimens, to approximately -40 $^{\circ}C$ and -80 $^{\circ}C$ for the specimens subjected to hot rolling and heat treatments. The author noted that due to the cross-rolling technique used to produce the plate specimens, there was no significant difference between samples taken from longitudinal and transverse direction. The USE was also increased by about 40 %. Klimiankou et al. (2007) [103] used evidence gained from TEM micrographs provide explanations as to why post-HIP thermomechanical treatments reduced the brittle behaviour of ODS EUROFER. The authors summerised that post-HIP treatments such as hot rolling and re-austinitisation and tempering, lead to: the dissolution of large embrittling chromium rich ($M_{23}C_6$) precipitates decorating grain boundaries; changes in the composition, size, shape and number density of intergranular precipitates; changes in the martensitic lath structures,

and general grain refinement. Therefore, all future ODS EUROFER manufactured was subject to hot rolling, as well as post-HIP heat treatments.

Although the formation of coarse $M_{23}C_6$ carbides in the final ODS material can be mitigated by post-HIP treatments, they can not be fully removed. These carbides only form in austenitic iron and since martensite is formed from the rapid quenching of austenite, a way to limit the formation of these carbides in to increase the chromium content of the initial alloying powders. At a chromium content of greater than $\backsim$ 12 - 13 %wt, iron is kept in an α-ferrite phase until melting temperature, and thus removes the martensitic phase introduced after quenching and the coarse carbides associated with it. Also, the martensitic phase itself can both suppress the favourable Y-Ti-O dispersions and increase embrittlement [137]. Due to this, reduced activation ferritic (RAF) steels, commonly using variations of 14Cr-Y-W-Ti, are currently favoured as iron-based candidate materials for advanced nuclear applications.



(a) (b)

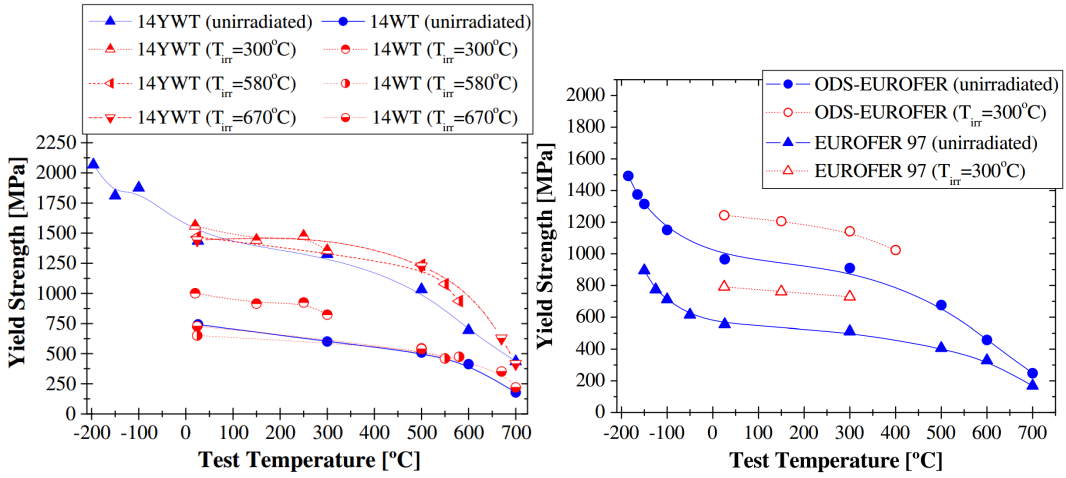
Figure 2.18: (a) Yield strength dependence on temperature. (b) Total elongation dependence on temperature. Figures from [138].

Although, early RAF steels such as the ORNL Fe-12Cr-3W-0.4Ti-0.25Y_2O_3 designated 12YWT (composition as measured is presented in table 2.3) were shown to have excellent tensile strengths compared to RAFM steels, they also revealed poor fracture toughness properties. Initial tests revealed a DBTT of approximately 75 $°C$ [139]. Mc-

Clintock et al. (2009) [138] aimed to improve upon the mechanical properties of 12YWT with another ORNL produced alloy of composition Fe-14Cr-3W-0.4Ti-0.3Y_2O_3 designated 14YWT. This composition slightly increased both the chromium and yttrium content and was extruded and hot rolled at 850 $°C$, decreased from 1150 $°C$ and 1050 $°C$ respectively for 12YWT. The decrease in consolidation and treatment temperature refined the grain structure, decreased the grain aspect ratio, and slightly increased the number density of fine Y-Ti-O dispersions. Mechanical data from McClintock et al. (2009) [138] in comparison to the RAF/M steel EUROFER and the ODS variant ODS EUROFER is presented in figure 2.18

Tensile data displayed in figure 2.18(a) shows a clear distinction between the magnitude of strengthening seen in the two ODS compositions. The ODS RAF alloy 14YWT measured a yield strength of $\backsim$ 1450 MPa at room temperature, compared to $\backsim$ 960 MPa for the RAFM alloy ODS-EUROFER. Excellent high temperature tensile properties are shown by ODS-EUROFER and 14YWT, but the latter outperforms ODS EUROFER and 12YWT considerably. 14YWT shows a yield strength of $\backsim$ 700 MPa at 600 $°C$ and $\backsim$ 420 MPa at 700 $°C$, approximately double that of ODS-EUROFER.

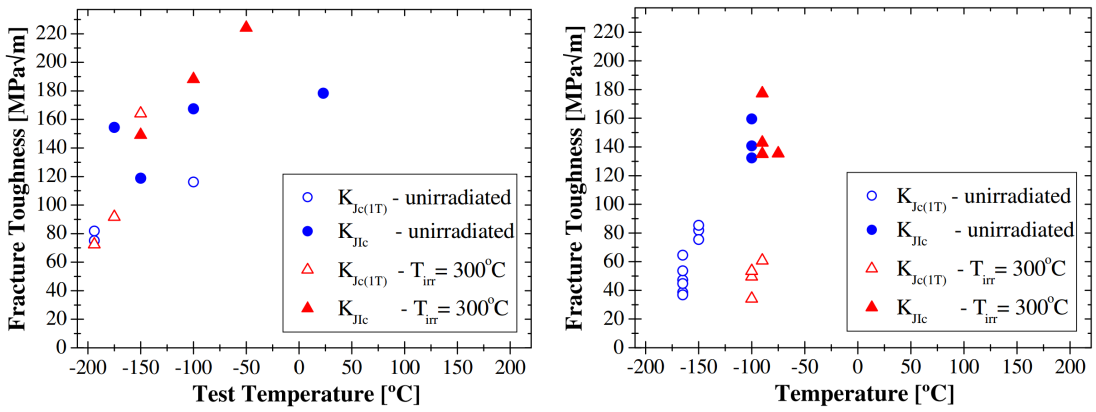
Although no Y_2O_3 was included during the mechanical alloying of 14WT, the alloy exhibited an improved room temperature yield strength over that of EUROFER. The author attributed this to the precipitation of 10 - 50 nm sized Ti rich oxide particles formed during mechanical alloying and extrusion. Figure 2.18(b) shows similar elongation profiles for all compositions, although the total elongation for the two ODS steels remain lower than their non-ODS counterparts at temperatures lower than 500 $°C$. At high temperatures, 14YWT showed a greatly reduced total elongation compared to the non ODS counterpart 14WT.



(a) (b)

Figure 2.19: Specimens neutron irradiated to 1.5 dpa at the HFIR in ORNL. (a) Yield strength dependence on temperature for 14YWT and 14WT in comparison to unirradiated specimens. (b) Yield strength dependence on temperature (up to 300 $°C$) for ODS EUROFER and EUROFER in comparison to unirradiated specimens. Figures from [138].

McClintock et al. (2009) [138] also neutron irradiated both 14YWT, ODS EUROFER and their non-ODS counterparts in the High Flux Isotope Reactor (HFIR) at ORNL to 1.5 dpa. The 14YWT and 14WT steels were irradiated at three different temperatures, 300 $°C$, 580 $°C$ and 670 $°C$, whereas the EUROFER based specimens were only irradiated at 300 $°C$. Figure 2.19(a) shows the yield dependence on temperature for irradiated 14YWT and 14WT, from room temperature to 300 $°C$. The addition of oxide dispersants significantly reduced the radiation-induced increase in yield stress. Interestingly however, 14YWT did show irradiation hardening of $\backsim$ 200 MPa at temperatures between 500 $°C$ and 600 $°C$, this was not seen in non-ODS 14WT. The introduction of yttrium oxide dispersants into the matrix of EUROFER did not reduce irradiation hardening, as yield stress increases of $\backsim$ 200 MPa were observed for both ODS and non-ODS specimens.



(a) (b)

Figure 2.20: (a) Fracture toughness stress intensity values of 14YWT – irradiated and unirradiated. (b) Fracture toughness stress intensity values for ODS-EUROFER – irradiated and unirradiated. Hollow shapes represent brittle fracture and filled represents ductile fracture. Figures from [138]

Both the 14YWT and ODS EUROFER demonstrate a low unirradiated DBTT temperature of $\backsim$ -175 $°C$ and $\backsim$ -125 $°C$ respectively, shown in figure 2.20. While neutron irradiation to 1.5 dpa had little affect on 14YWT, the DBTT of ODS EUROFER was increased, but not significantly enough to move the transition temperature from cryogenic temperatures.

The fracture toughness and DBTT temperature of 14YWT was greatly improved by McClintock et al. (2009) [138], however Byun et al. (2010) [140] found that the 14YWT steel examined by McClintock et al. (extruded and hot rolled at 850 $°C$) exhibited a dramatic drop in fracture toughness at relatively low temperatures, referred to as SM10 in figure 2.21. Hoelzer et al. (2016) [141], explored how mechanical alloying conditions, consolidation temperatures and post consolidation treatments could be utilsed to help mitigate this fracture toughness drop. The author varied extrusion temperature whilst keeping the post consolidation treatment conditions constant. The consolidation temperatures used were, 850 $°C$, 1000 $°C$, 1150 $°C$, whilst the post consolidation treatments were a 1h anneal at 1000 $°C$, hot rolled at 1000 $°C$, then a 1h anneal again at 1000 $°C$. The author used ball milling conditions that decreased the undesirable pickup of excess

O, C, N and also annealed the powder at 850 $°C$ prior to extrusion. Results are shown in figure 2.21.

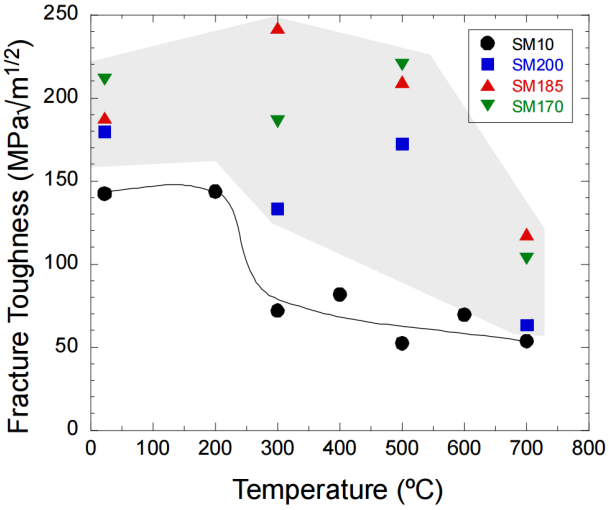


Figure 2.21: Comparison of the high-temperature fracture toughness between the different consolidation temperatures. SM10 - 850 $°C$ extrusion, annealed at 1000 $°C$ for 1h then hot rolled at 850 $°C$. Extrusion temperature for SM 170, SM 185, SM 200 was 850 $°C$, 1000 $°C$, 1150 $°C$ respectively, with SM 170, SM 185 and SM 200 each undergoing extrusion then annealing for 1h, hot rolling, then a final anneal at 1000 $°C$ for 1h. Figure from [141].

The ODS steels produced from the three consolidation temperatures, 850 $°C$, 1000 $°C$, 1150 $°C$, led to significant improvements in the fracture toughness at elevated temperatures, with the lower two temperature providing the most promising results. When compared to the earlier 14YWT steel (SM 10) the author reports a lower strength in the three new specimens but an increase in ductility over a temperature range of 25 $°C$ to 700 $°C$. The author attributes this to a decrease in Hall-Petch strengthening due to a increase in grain size. Analysis indicated that lowering the N and O levels reduced their segregation to grain boundaries enhancing cohesive strength, thus providing the most beneficial change for improving the high temperature fracture toughness. More research is needed to find out whether a further improved 14YWT can provide the tensile strength of the fine grained SM10 14YWT with the improved fracture toughness provided by the low N and O 14YWT variant (SM170 and SM185).

2.5.4 Main concerns regarding the further development of ODS steels

ODS steels are currently among the most favoured candidate materials for advanced nuclear, and particularly fusion, applications. Through the introduction of a fine dispersion of 2 - 5 nm Y-Ti-O type complex oxides, the operating temperature of reduced activation steels has been increased from around 550 $^{\circ}C$ to $>$ 650 $^{\circ}C$, thus are able operate at temperatures where displacement damage effects are minimal. The fine dispersions also act as excellent sink sites, promoting defect recombination, and helping to mitigate the negative effects of transmutant helium. Through careful control of the fabrication process, the fracture toughness and DBTT are now within acceptable limits, and the balance of mechanical properties is constantly improving. However, before ODS alloys can be utilised within practical engineering solutions significant challenges must be overcome, this includes, but not limited to:

- High cost of mechanically alloyed and powder consolidated materials compared with the more traditional melt processed alloys [24].
- Reduced strength and/or microstructural change of a weld [142].
- Fabrication of extruded and rolled product with isotropic microstructures and properties [141, 138].
- Alloy microstructural heterogeneity and batch to batch variability [24, 143].
- Full characterisation of the effects of irradiation, alongside high temperature thermomechanical service, on all performance sustaining properties for the lastest ODS steel evolutions [24].

The work in this thesis concerns the latter two points.

2.6 Micromechanical testing

Micro and nanoscale mechanical testing of irradiated materials is subject to a growing interest. This is because the irradiation of materials via high energy neutrons, can cause the build up of radioactive isotopes through transmutation reactions. The transport and storage of radioactive material is limited by stringent legislation [144], making the testing of large volumes of material difficult and time consuming. This also tends to make ion irradiation a preferred means of introducing damage within a specimen. However, the interaction cross-section for ion irradiation is much larger than that for neutron, limiting the damage layer to microscale thicknesses.

Since Gane and Bowden's pioneering work in 1968 [145], nanoindentation has been used to examine the mechanical properties of thin layers, and is increasingly being used as a method for determining the mechanical changes in shallow ion irradiated damage layers. While nanoindenation provides a useful quantitative comparison of the properties of microscale irradiated volumes, the complex stress state and ill defined deformation zone underneath the indenter tip make it difficult to determine more engineering relevant properties such as Young's modulus and yield stress.

The recent development of focused ion beam (FIB) microscopes have allowed the fabrication of a range of site-specific micro and nanoscale mechanical test specimens that includes, micropillar compression, microtensile and microcantilevers [146, 147, 148, 149, 150, 151]. These mechanical test specimens can be accurately positioned in areas of interest such as grain boundaries or damage layers, and have well defined geometries that make the extraction of engineering properties less complex.

Microscale mechanical testing reduces the quantities of active material that is necessary to be handled and stored, and allows the properties of shallow damage layers to be investigated. However, questions remain over exactly how well these microscale mechanical properties scale to the macroscale. This section aims to review the two main areas of micromechanical testing relevant to this project: Nanoindentation and

microcantilevers. Size effects in micropillars will briefly be discussed, but other test geometries such as microtensile tests are beyond the scope of this review.

2.6.1 Nanoindentation

Hardness testing, first proposed by Johan August Brinell in 1900 [152], uses the penetration of an indenter tip with a well defined geometry, and is still a widely used method of probing material properties. The Vicker's test, one of the most commonly used macroscale hardness tests, uses a diamond indenter tip with a square based pyramidal geometry. The advantage of this type of geometry is that is creates impressions that are geometrically similar, irrespective of indentation depth. Hardness is then calculated by dividing the applied load by the surface area of the indent. However, as the indentation size decreases, the measurement of the impression's surface area introduces a source of increasing uncertainty. Decrease indentation size further still and measurement of the surface area becomes impossible without the systematic and time-consuming imaging using microscopy techniques such as SEM and AFM, and subsequent post-processing [153].

Nevertheless, the advancement of technology and materials science necessitated the need to probe material properties on smaller and smaller lengthscales. Pethica et al. (1983) [154] calculated the Meyer hardness (defined as load divided by projected indent area) at lengthscales as low as 20 nm for nickel, gold and silicon. The author carried out the tests using a specialised microhardness tester that measured both the load and the indentation depth with applied load. However, this method still required labour intensive microscopy to estimate the true shape of the tip, achieved by comparing measured impression area with the penetration depth during unloading.

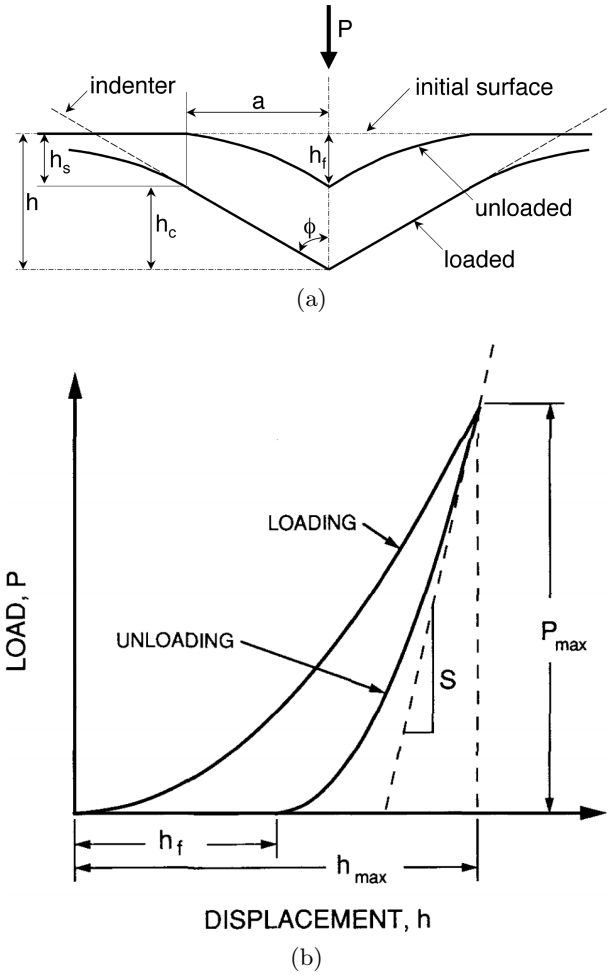


Figure 2.22: (a) A schematic representation of Berkovich indentation cross-section. (b) Schematic representation of a typical load displacement curve for a nanoindent. Figures from [155]

Oliver and Pharr (1992) [155] developed a method of determining the area function of the tip that did not require time intensive measurements of the indentation impression. The method was based on the assumption that the elastic modulus is independent of indentation depth, justification for this was also provided by the author using range of metallic and non-metallic materials. The procedure required the precise measurement of contact stiffness with varying indentation depths. To do this, it was necessary to first determine the load-frame compliance, accomplished by indenting into a mate-

rial in which very stiff contacts can be made at relatively low loads; the author chose well-annealed high purity aluminium due to its low hardness and near isotropic elastic behaviour. Modelling the load-frame and specimen compliance as two springs in series gives an expression for the total measured compliance, C, as

$$C = C_s + C_f \tag{2.5}$$

Where C_s and C_f are the compliance of the sample and load-frame respectively. Sample compliance, C_s, is given by the inverse of the stiffness, S, during elastic contact, calculated from the gradient, $^{dP}/_{dh}$, of the upper portion of the unloading curve, demonstrated in figure 2.22(b). Oliver and Pharr (1992) [155] provides an expression for C_s derived from elastic contact theory,

$$C_s = \frac{\sqrt{\pi}}{2E_r}\frac{1}{\sqrt{A}} \tag{2.6}$$

Where E_r is the reduced modulus and A is the area of contact between the indentation tip and the sample surface. E_r is called the 'reduced modulus' because the stiffness of the contact upon unloading has contributions from both the sample, E, and the diamond indenter tip, E_i. Thus, the effects of non-ridgid indenters on the load-displacement data can be found by defining E_r as,

$$\frac{1}{E_r} = \frac{(1-\nu^2)}{E} + \frac{(1-\nu_i^2)}{E_i} \tag{2.7}$$

Where ν and ν_i are the Poisson's ratio of the sample and diamond indenter tip respectively. Combining (2.6) with (2.5) gives,

$$C = C_f + \frac{\sqrt{\pi}}{2E_r}\frac{1}{\sqrt{A}} \tag{2.8}$$

Since the elastic modulus is constant with indentation depth, the plot of C vs. $A^{-\frac{1}{2}}$ is linear for a given material, with the y-axis intercept providing a measure of the load-

frame compliance. By making a series of indents of varying size in a material with known elastic constants using a Berkovich tip geometry, Oliver and Pharr estimated the area function of the larger indents to that of a perfect Berkvich indenter,

$$A(h_c) = 24.5h_c^2 \tag{2.9}$$

Where h_c is the contact depth and is derived from figure 2.22(a) as,

$$h_c = h_{(max)} - h_s \tag{2.10}$$

using h_s to represent the displacement of the surface.

Initial estimates of C_f and E_r could then be obtained by plotting C vs. $A^{-\frac{1}{2}}$. Using these values, the contact area for all indent depths were then found by rearranging (2.5) for A in terms of compliance,

$$A = \frac{\pi}{4}\frac{1}{E_r^2}\frac{1}{(C - C_f)} \tag{2.11}$$

An estimate of the area function could then be made by fitting the A vs. h_c data to the Taylor series,

$$A(h_c) = 24.5h_c^2 + C_1h_c + C_2h_c^{\frac{1}{2}} + C_3h_c^{\frac{1}{4}} + ... + C_8h_c^{\frac{1}{128}} \tag{2.12}$$

where C_1through C_8 are constants. The lead term of the series describes a perfect Berkovich indenter, whilst the following terms describe deviations from the Berkovich geometry due to imperfections and blunting. The exact form of the area function affects the values of C_f and E_r, so updated versions of the area function are iteratively calculated until a convergence is reached. Oliver and Pharr found that the use of aluminium for the calculation of the area function for small indents was limited by the load resolution on the indentation system, due to the low hardness of aluminium requiring low loads. The re-calibration of small indents in fused silica, a much harder isotropic material, improved area function accuracy and as such, was used for all area function calibrations in this thesis.

The area function for the calibrated tip can then be used to investigate an engineering material with unknown mechanical properties. Elastic modulus and hardness are the most common mechanical properties obtained from nanoindentation since they are closely related to Young's modulus and yield stress. Recalling that $S = 1/C$, the elastic reduced modulus can be found by rearranging (2.6),

$$E_r = \frac{S\sqrt{\pi}}{2\beta\sqrt{A}} \tag{2.13}$$

Where β is an indenter specific constant ≈ 1. While the specific values for this constant remain contentious, Oliver and Pharr (2004) [156] report that the range of β values for a Berkovich tip are $1.0226 \leq \beta \leq 1.0850$. Strader et al. (2006) [157] found that the best estimate of β for a Berkovich indentation of fused silica was 1.055 ± 0.021. The hardness, H, of the sample at an indent depth, h, is given by the relation,

$$H_h = \frac{P_h}{A_h} \tag{2.14}$$

Figure 2.22(a) shows a schematic cross-section the sample surface at peak load and after unloading. The sample surface under load demonstrates how the surrounding material can undergo elastic deformation. This phenomenon is known as 'sink-in' and may significantly reduce the contact area at a given displacement. The effect sink-in has on the stiffness measurement can be reduced by extrapolating the P-h gradient to the point of zero load, as shown in figure 2.22(b) and using the subsequent value for indentation depth when calculating the contact area using the derived area function.

Another limitation to the Oliver-Pharr method is that there is no account of soft pile-up around the indenter tip. As plastic deformation increases, ductile material can be forced upwards and around the indenter tip due to the work-hardening of surrounding bulk material. If this pile-up occurs, the contact area of the tip is larger than the apparent values, leading to an overestimate of the material stiffness. To account for soft pile-up, SEM, or AFM scanning, post-test analysis of each indent site is commonly

employed, however this can be quite time consuming. Beck et al. (2017) [158] used a priori knowledge of elastic properties from surface acoustic wave measurements to correct for pile-up in heavy-ion implanted tungsten-rhenium, allowing an accurate hardness measurement of the implanted material without the need for any further measurements. The Oliver-Pharr method also fails to account for elastic anisotropy, as seen in most real materials, so prediction of moduli can become quite complex.

2.6.2 Continuous stiffness measurement (CSM)

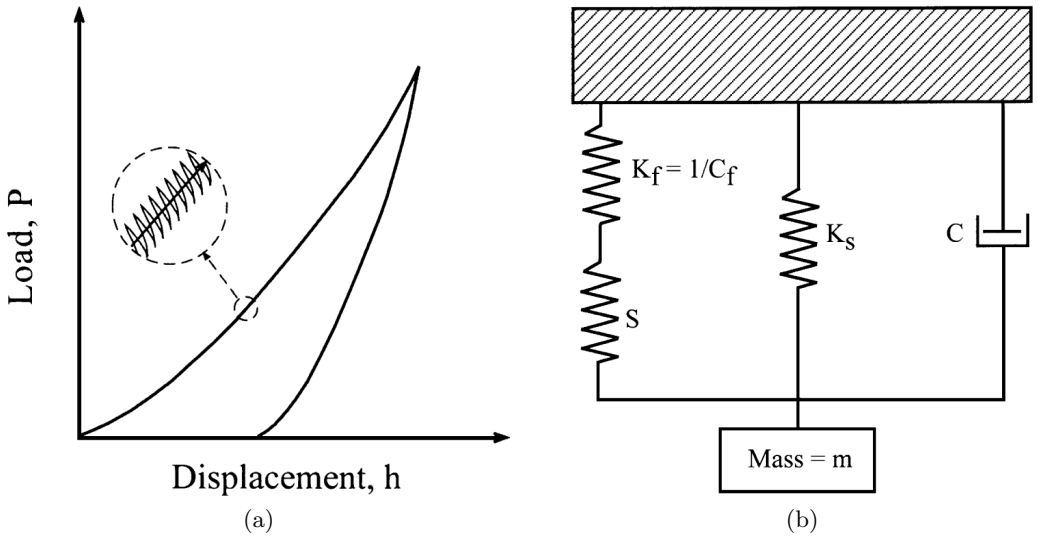


Figure 2.23: (a) Schematic of the CSM loading cycle. (b) Dynamic representation of the system. K_f and C_f are the frame stiffness and compliance, S is the contact stiffness, K_s is the spring constant of the indenter support leaf springs, C is the damping coefficient the displacement sensing capacitor plate, and m is the indenter mass. Figure from [159].

First introduced by Pethica and Oliver (1987) [160], CSM imposes a small oscillating force, $P = P_{os}\exp(i\omega t)$, added to the nominally increasing load, P, of the indenter, demonstrated in figure 2.23(a). The resultant displacement response of the indenter, $h(\omega) = h_0\exp(i\omega t + \phi)$, will have the same frequency of oscillation, ω, as the load but with a phase shift, ϕ. Relevant components contributing to the stiffness response of the indentation system are shown in figure 2.23(b); these combine with contact stiffness to

produce the overall dynamic response of the system. Contact stiffness, S, can either be calculated from the displacement signal using,

$$\left|\frac{P_{os}}{h(\omega)}\right| = \sqrt{\left(\left(S^{-1} + K_f^{-1}\right)^{-1} + K_s - m\omega^2\right)^2 + \omega^2 C^2} \tag{2.15}$$

or from the phase angle between the force and displacement signals using,

$$\tan(\phi) = \frac{\omega C}{\left(S^{-1} + K_f^{-1}\right)^{-1} + K_s - m\omega^2} \tag{2.16}$$

where P_{os} is the magnitude of the force oscillation and $h(\omega)$ is the magnitude of the resulting displacement oscillation, K_f is the load-frame stiffness, m is the mass of the indenter system and K_s is the spring constant of the supporting leaf springs of the indenter. From either (2.15) or (2.16), the stiffness can be calculated as a function of tip displacement, assuming a uniform material with constant elastic modulus. Using a known tip area function (using the Oliver-Pharr method), and contact stiffness as a function of tip displacement, both modulus and hardness may also be calculated as a function of tip displacement.

2.6.3 Nanoindentation of proton irradiated steels

Nanoindentation is a valuable tool when needing to rapidly assess the hardening produced by ion beam irradiation. However, it is rather difficult to extrapolate macroscopic mechanical properties, such as yield stress and work hardening, from the load-displacement data [161]. Particular care must be taken when interpreting data from irradiated layers for the following reasons:

- The size, shape and magnitude of the plastic zone under the indent is not well understood and can vary depending on local microstructure, crystallography and indenter geometry [162].
- The damage produced by ion irradiation is not constant with irradiation depth.

The depth of the plastic zone is generally much larger than the indent itself (assumed to be approximately five times the indentation depth [161]), suggesting that the mechanical properties measured by the indent is an average taken over a varying damage profile.

- The measured hardness increases with decreasing indentation depths, this is known as the indentation size effect. The indentation size effect depends on the defect and dislocation source density, so cross comparison between materials can be problematic [161]. Therefore, it is important to perform indents with a depth controlled method, as opposed to load controlled, since indents set to the same load but performed in different materials will have varying indent depths.

- Even though most irradiation is performed in a vacuum, oxidation of the surface can occur, particularly when irradiating at high temperatures. A thin layer of surface oxide is negligible during microindentation, but as indentation depths are decreased to the nanoscale, there is a risk of it significantly altering the measured data. To mitigate this, indents should be made as large as possible (within the confines of the experiment).

- Bubbles may form if irradiating with insoluble gasses. An indent performed through the ion stopping region may sample areas where bubbles are present. If present, these could contribute to the hardness measured, leading to a different interpretation of mechanical response compared to that from the dose alone. However, the stopping peak is very narrow and the formation of bubbles is dependent on the irradiating ion, target material and fluence used.

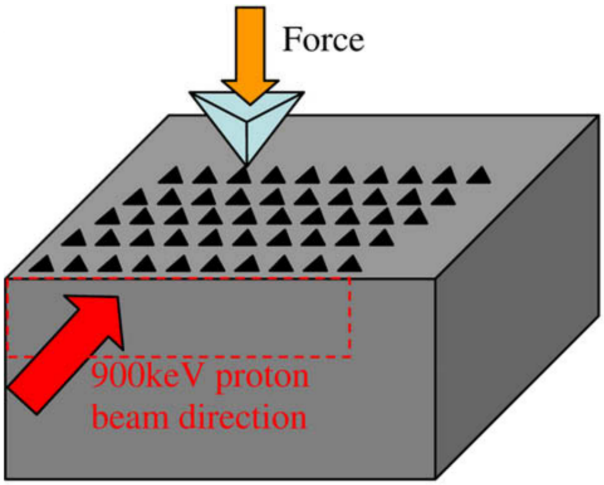


Figure 2.24: Schematic diagram of nanoindents placed in the cross-section of the proton irradiated layer by Hosemann et al. (2009). Figure from [163].

Hosemann et al. (2009) [163] investigated the susceptibility of the ferritic-martensitic steel, HT-9-M, to radiation hardening compared to the purely ferritic variant, HT-9-F. 900 keV proton irradiation was carried out at varying temperatures in the NEC 9SDH-2 particle accelerator at the Ion Beam Materials Laboratory, Los Alamos National Laboratory, USA. A total fluence of 7.5 x10^{17} ions/cm^2 was recorded after an irradiation time of 30 hours. The subsequent damage profile was calculated in SRIM 2006, however the particular damage calculation used was not specified. Berkovich indents, approximately 200 nm deep and each with 4 μm of separation, were placed in the cross-section of the proton irradiated layer, as depicted in figure 2.24. Results of the hardness with respect to the irradiation depth are shown in figure 2.25.

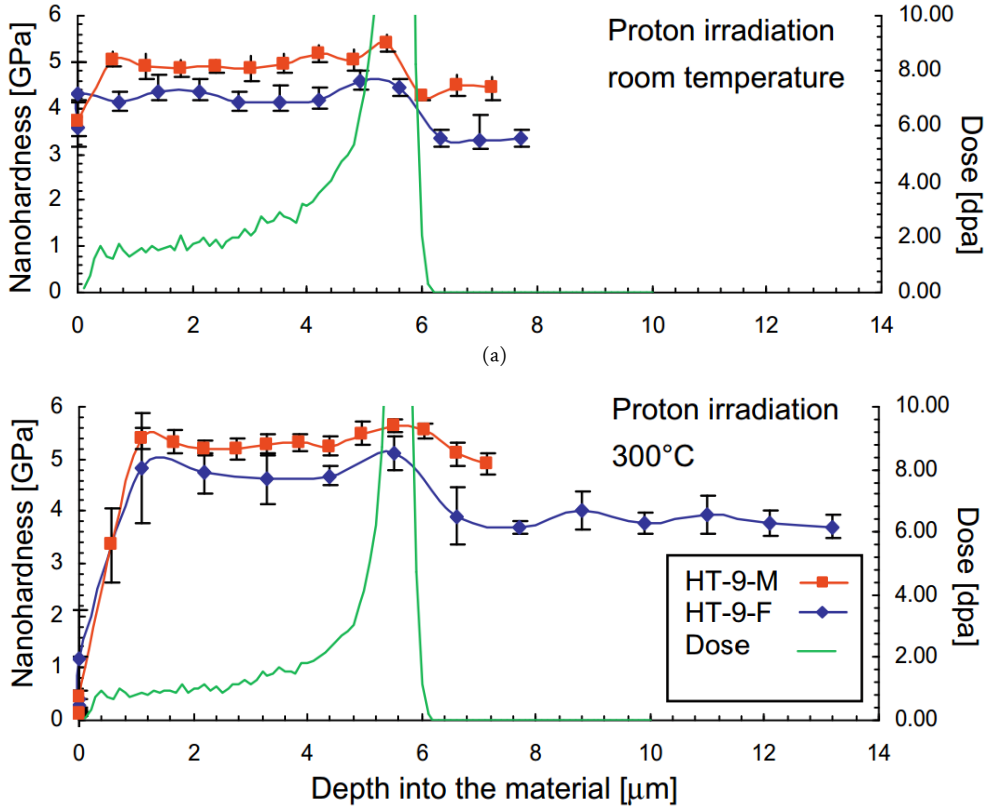


Figure 2.25: Hardness data from HT-9-M and HT-9-F, nanoindents in the cross-section of proton irradiated layer. Overlaid in green is the SRIM calculation of the damage profile. (a) Irradiation at room temperature. (b) Irradiation at 300 $°C$. Figure from [163].

The hardness with respect to cross-sectional depth into material for proton irradiation at room temperature is shown in figure 2.25(a). The region with an approximately flat damage profile (damage $\sim$ 1 dpa) shows a clear hardness increase of 12 % for HT-9-M and 24 % for HT-9-F when compared to the bulk unirradiated hardness. The region around Bragg peak shows a hardness increase of approximately 25 - 30 %. For irradiation at 300 $°C$, figure 2.25(b), the hardness increase in the flat damage region (damage $\sim$ 1 dpa) was 7 % and 17 % for HT-9-M and HT-9-F respectively. This is contrary to what one might expect, as traditionally radiation hardening is expected to be a maximum at around 300 $°C$. The full width half maximum of the hardness peak

is larger for the 300 $°C$ irradiation temperature than that for the room temperature irradiation, suggesting a greater defect mobility.

Performing nanoindentation in the cross-section of the irradiated layer allows a measurement of hardness with an increased irradiation depth spatial resolution, compared to indents into the irradiated surface. This is because indents into the irradiated surface will only provide a measurement of hardness from the irradiated layer in an average sense, since the plastic zone of a large indent will incorporate a more widely varying damage profile. In addition, cross-sectional indention allows specific measurement of the deep proton Bragg peak, which is much harder to incorporate and depict in the hardness data for more conventional irradiated surface indents.

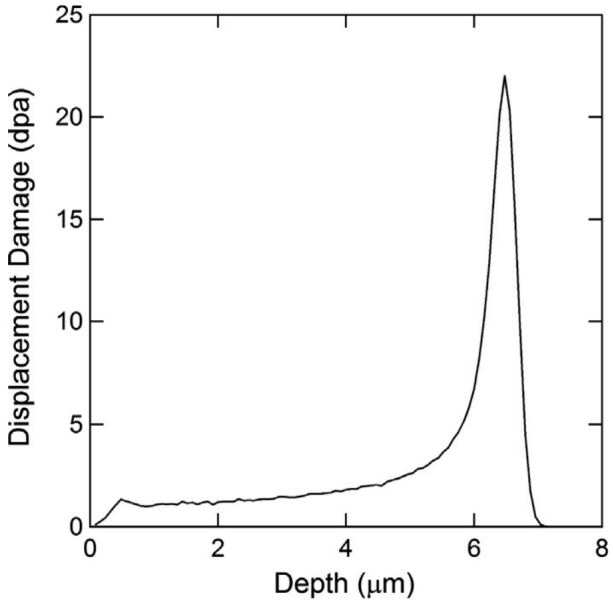


Figure 2.26: SRIM calculation of the damage profile for 1 MeV proton irradiation. Figure from [164].

Yabuuchi et al. (2014) [164] used the more conventional method of placing indents into the irradiated surface to investigate the hardening of SUS316L austenitic stainless steel. Irradiation was carried out with 1 MeV protons at 300 $°C$ in the Dynamitron accelerator at Tohoku University, Japan. The fluence was varied for different samples, and a nominal displacement damage of the flat region of the damage profile (between

1 μm - 4 μm) was calculated using SRIM to be 0.1, 0.3 and 1 dpa. An example of the damage profile for 1 MeV proton irradiation in iron is given in figure 2.26. Arrays of Berkovich indents were placed into the irradiated surface to a depth of 2000 nm. Indentation hardness with respect to indentation depth for each sample is given in figure 2.27.

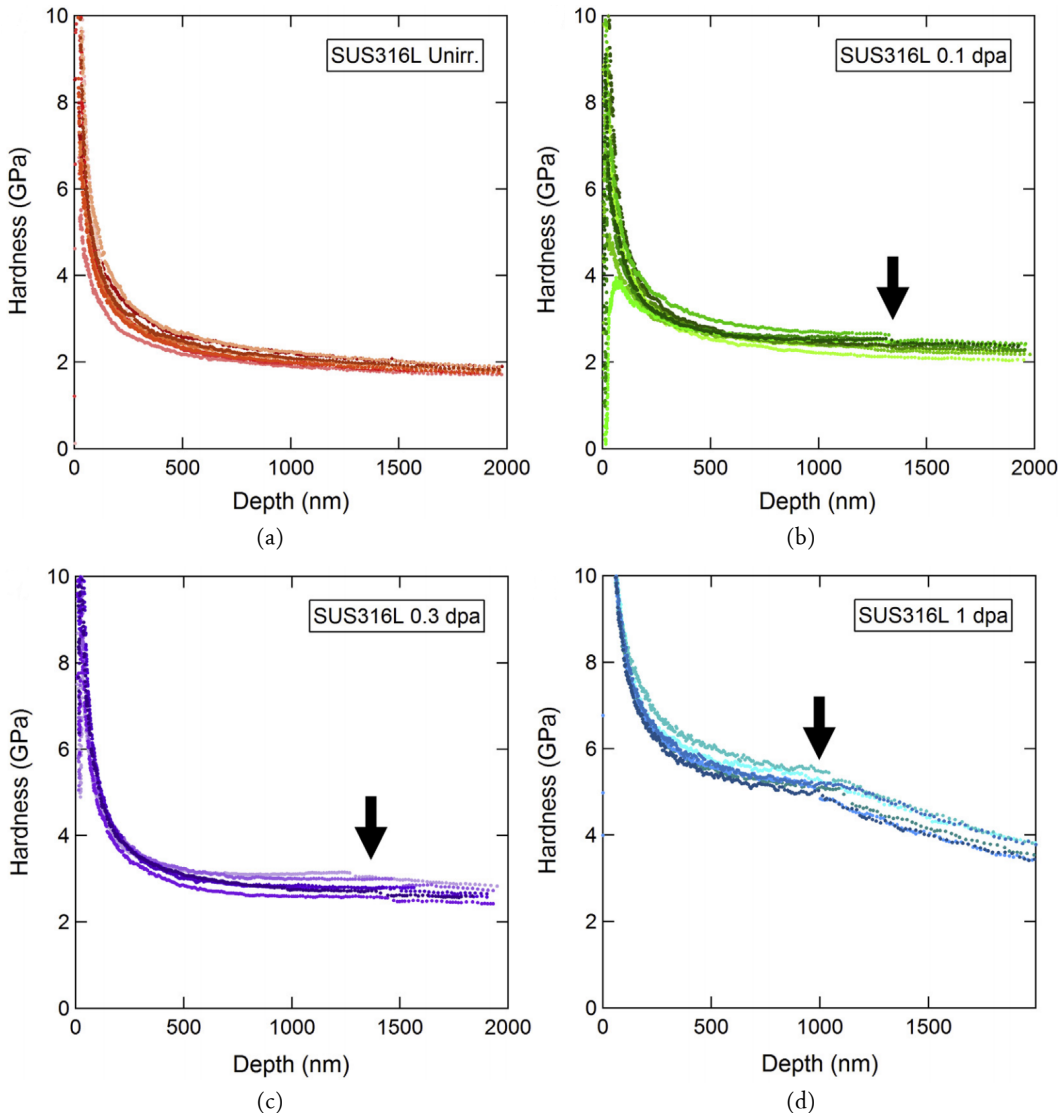


Figure 2.27: 2000 nm indents into proton irradiated surface of SUS316L austenitic steel. (a) Unirradiated. (b) Irradiated to 0.1 dpa. (c) Irradiated to 0.3 dpa. (d) Irradiated to 1 dpa. Figures from [164].

The indentation hardness with respect to indentation depth in the austenitic steel SUS316L before irradiation is shown in figure 2.27(a), figures 2.27(b), (c) and (d) show the measured hardness for samples irradiated at 0.1, 0.3 and 1 dpa respectively. Both (b) and (c) show a similar increase in hardness of approximately 1 GPa when compared to the unirradiated specimen in (a). The hardness increase measured in (d) was much larger at approximately 3.5 GPa. A marked drop in hardness is observed in the irradiated specimens between 1000 - 1500 nm indentation depth, and is highlighted by a bold arrow in figures 2.27(b), (c) and (d). The authors explain this by suggesting that at this point, the plastic zone reaches the irradiated-unirradiated boundary. However, the authors fail to explain why this boundary appears to be shifted closer to the irradiated surface in the 1 dpa specimen, shown in figure 2.27(d).

2.6.4 Summary of nanoindentation

Nanoindentation provides a rapid, non destructive way of examining the mechanical response of precise surface regions. Properties that can be studied include; indentation modulus and hardness, grain boundary slip, and time dependent creep. However, the shape, size and magnitude of the elastic and plastic zone around the indent is not well understood, and is affected by both the local crystallography and indenter shape. The lack of knowledge of the elastic and plastic zones underneath the indenter tip could mean that unintended substrates layers within the bulk volume are examined. Similarly, strain fields in a shallow irradiated layer could also be interacting with the unirradiated bulk, leading to falsely determined mechanical properties.

It is also difficult to extract engineering relevant properties, such as yield stress, from the load displacement curve. The well known Tabor approximation is that hardness is three times the yield stress [165], however many questions remain over the accuracy of this approximation since it assumes an average effective strain, yet it is unclear which regions under the indent are experiencing the strain [166]. In reality, the strain

distribution under an indent is complex, and also dependent on the shape of the indenter.

Attempts have been made to model the complex stress state by utilising crystal plasticity finite element modelling (CPFEM), thus extracting properties such as yield stress, Young's modulus, and critical resolved shear stress (CRSS) [167, 168, 169, 170]. Although this area of research is progressing, advanced CP models require a large number of assumptions which can affect the accuracy of results provided by the finite element analysis.

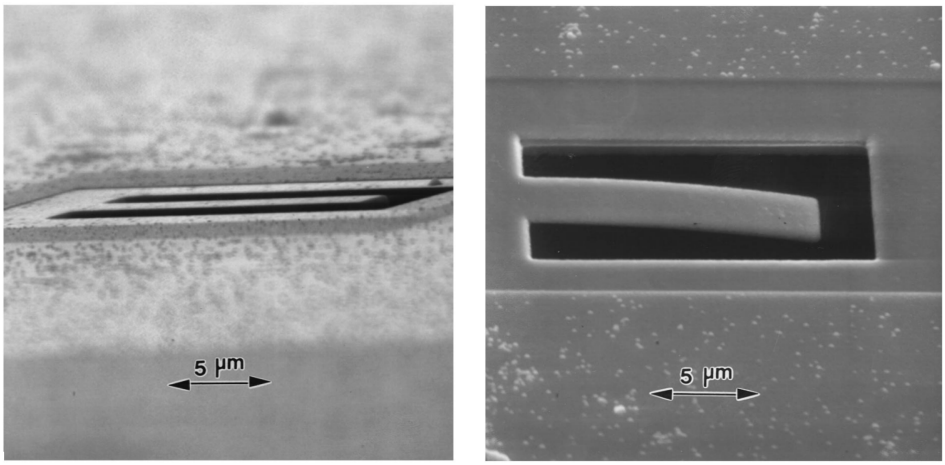
Novel experimental techniques have been developed in an effort to overcome some of the limitations of extracting engineering relevant mechanical properties from small test volumes. The majority of these use the load-displacement resolution of nanoindenters to test FIB prepared specimens with well defined geometries and stress states.

2.6.5 FIB prepared microcantilever test specimens

The first example of a microcantilever test that utilised the load-displacement resolution of a nanoindentation system was from Weihs et al. (1988) [171]. The authors produced microcantilever beams in single crystal silicon using lithographic techniques, deflecting the end of the microcantilever using a diamond indenter tip and recording the continuous load-displacement data. However, this fabrication technique limits the range of materials that can be studied, and of these materials, the properties of the deposited material may not be comparable to that of the bulk.

The continued development of focused ion beam (FIB) systems since the late 1970's have allowed microscale specimens with well-defined geometries to be fabricated from essentially any material [172, 173]. The first example the use of a FIB to mill microcantilever beams was in the work carried out by McCarthy et al. (2000) [174]. The authors investigated the residual stress in an aluminium thin-film deposited on a silicon substrate by measuring the post-deposition deflection of cubic cross-sectioned microcantilevers. To fabricate the microcantilevers a 3 mm x 3 mm x 0.5 mm piece of single

crystal silicon was uniformly polished to a thickness of 10 μm. Using a VCR dimpler, a tool commonly using in the preliminary stages of TEM sample preparation, a 1 mm diameter area was thinned to 5 μm. The specimen was then placed into a FIB workstation and a beam with a large 2800 Å spot size was rastered over a 15 mm x 20 mm area to further reduce the sample thickness to 0.5 - 1.0 μm. The probe size was reduced to 1100 Å and microcantilever beams were milled with lengths of 16 - 20 μm and widths 3 - 6 μm.

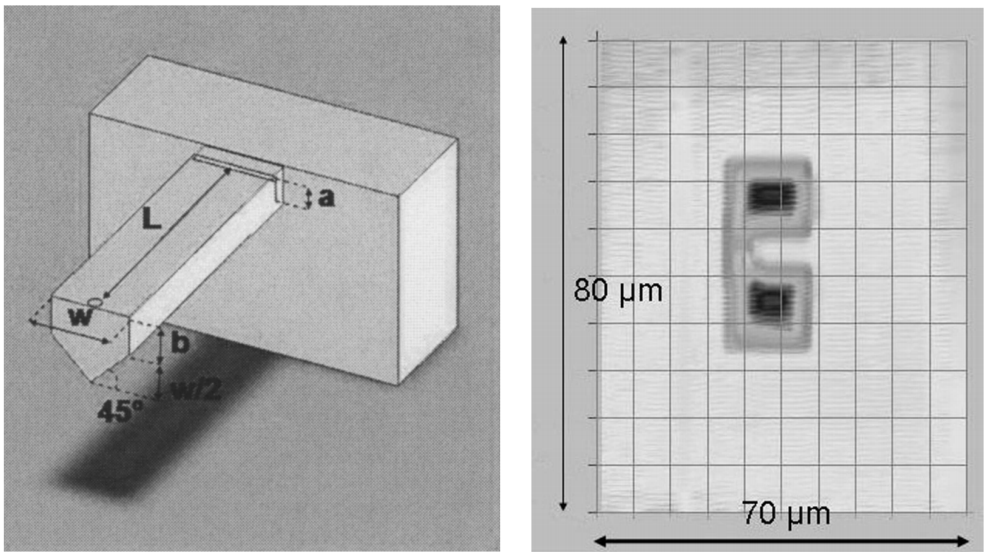


(a) (b)

Figure 2.28: SEM micrographs of silicon microcantilevers. (a) Microcantilever prior to Al deposition showing no deflection, viewed at 80° tilt. (b) Microcantilever post Al deposition showing deflection, viewed at 45° tilt. Figures from [174].

A layer of aluminium was deposited on the microcantilevers to a thickness of 0.8 - 1.2 μm using a turbo-molecular pumped evaporator. The specimens were then placed back into the FIB to remove the aluminium that had laterally deposited on the sides of the beams rather than the top surface. An SEM micrograph at 80° tilt was recorded for every microcantilever prior to Al deposition, this was to determine whether any residual stresses induced by FIB machining could be observed. No residual stresses could be observed for the microcantilever sizes used in the experiment, as demonstrated by a representative microcantilever in figure 2.28(a). The authors reported that after

Al deposition all beams produced deflections, measured by SEM imaging at 45° tilt to be between 0.15 μm and 1.58 μm at 15 μm from the fixed end, an example is shown in figure 2.28(b). The authors also reported that an initial deflection of the beam occurred prior to Al deposition if the thickness was < 0.3 μm. Two contributing sources for this residual stress were proposed; one may be intrinsic stresses born from p-doping the silicon wafer, the other from stress induced by FIB damage to the top layer. The latter could conceivably produce the small residual stresses observed since Rubanov and Munroe (2004) [175] found that a 30 keV rastered gallium ion beam produces a 30 nm amorphous damage film, which would form approximately 10 % total thickness in a 0.3 μm beam. It has been shown that a reduction of the accelerating voltage to 6 - 10 keV can reduce the depth of this damage layer by a factor of two [175, 176], which should help mitigate the effects of residual stress in gallium exposed silicon seen by McCathy et al.



(a) (b)

Figure 2.29: (a) Schematic diagram of pentagonal fracture test microcantilever. (b) Topographical surface scan of microcantilever using the nanoindenter tip. Figures from [146].

Although the method developed by McCathy et al. had its obvious success when measuring the residual stress of thin films, it didn't allow the easy determination of material properties from load-displacement data. Di Maio and Roberts (2005) [146] developed a novel fabrication and deflection technique to determine the fracture toughness of tungsten carbide (WC) coatings. Contrary to the McCathy method, microcantilever beams were FIB milled directly from the upper surface without the need for prior sample thinning. However, this method forces the beam cross-section to be non-rectangular due to the specimen position on the surface. The pentagonal cross-section fabricated by the authors is demonstrated in the schematic diagram in figure 2.29(a), also shown is the FIB machined notch to initiate crack propagation. Beams were displaced using a commercial nanoindenter system from MTS systems corporation (Oak Ridge, TN). An accurate placement of the tip was achieved by using the nanoindenter in scanning contact mode, where the tip was engaged onto the surface and a piezoelectric stage was used to systematically scan the tip across the surface to build a topographical map. An example of a topographical surface scan is shown in figure 2.29(b). The nanoindenter tip could then be positioned over the free end of the microcantilever, and load-displacement data record during deflection. The critical load at fracture could then be used to determine fracture toughness.

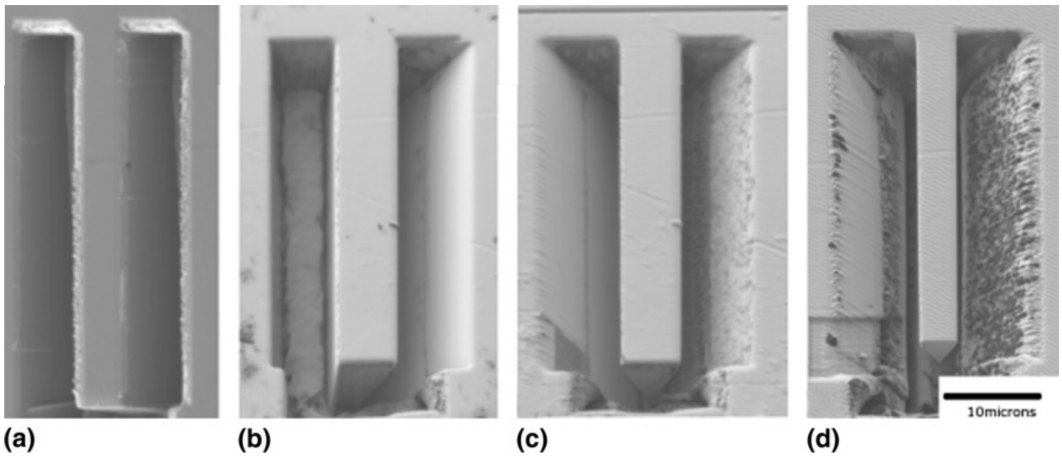


Figure 2.30: Secondary electron micrographs describing each stage of microcantilever fabrication. (a) A U-shaped trench is milled at a high beam current. (b) and (c) Initial undercuts from both sides at a stage tilt of 30°, aligning the microcantilever with the FIB x-axis at each rotation. (d) Undercuts are re-milled and free end trimmed using a finer beam current. Figure from [147].

A similar method was used by Armstrong et al. (2009) [147] to measure the elastic anisotropy of copper. FIB machining was carried out on a FEI FIB200 (Hillsboro, OR) using 30 keV Ga^+ ions, figure 2.30 details the fabrication process. A U-shaped trench with dimensions of 5 x 30 μm was initially milled using a large beam current of approximately 5000 pA to a depth of 10 μm, shown in figure 2.30(a). The sample was then tilted to 30° and aligned so that the microcantilever central arm was parallel to the microscope x-axis. A beam current of 3000 pA was used to undercut the microcantilever, the sample was then rotated 180° around the surface normal and re-aligned, the same beam current was used to undercut the central arm from the opposite side [figure 2.30(b) and (c)]. This produced a microcantilever that was free of the underlying material and attached only to the bulk at the 'fixed' end. A low beam current of 1000 pA was then used to remove any redeposited material on the lateral sides of the cantilever, producing a well-defined clean geometry [figure 2.30(d)]. The final step was to remove 1 μm from the 'free' end (tip) of the microcantilever with a fine beam current, this was to improve the accuracy of microcantilever depth measurements.

From simple beam theory it can be shown that the compliance, S, of a triangular prismatic cantilever rigidly fixed at one end is,

$$S = \frac{\delta}{P} = \frac{L^3}{3EI} \tag{2.17}$$

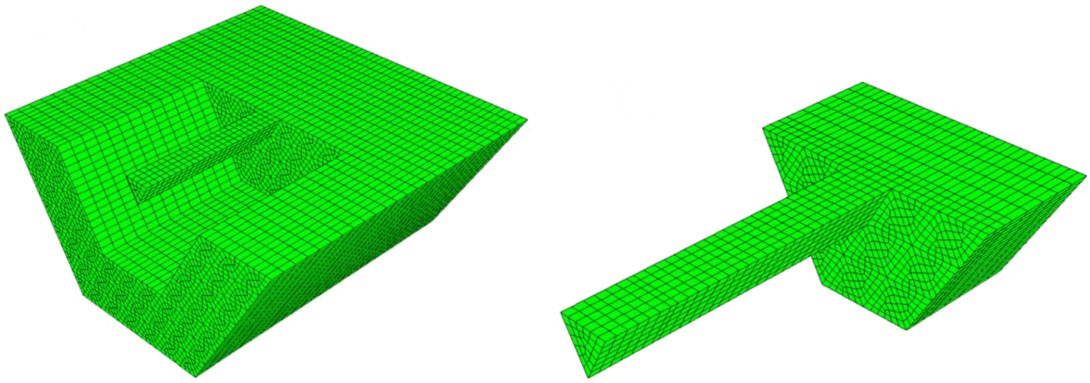
Where δ is the displacement of cantilever, P is the applied load, L is the distance between the loading point and fixed end, E is the elastic modulus and I is the second moment of area, given by the equation,

$$I = \frac{ah^3}{36} \tag{2.18}$$

where a is the cantilever width and h is the cantilever thickness. By loading each microcantilever at increasingly smaller values of L, a linear plot of δ/P against L^3 could be obtained, and the elastic modulus calculated from the gradient, $12/Eah^3$. However, it was observed that the gradient became non-linear as L was decreased. This was explained by flexure of the bulk 'base' material at the fixed-end that is unaccounted for in simple beam theory. An updated equation for the beam compliance is approximated as,

$$S = \frac{1}{3EI}L^3 + \theta_{m0}L^2 \tag{2.19}$$

where θ_{m0} is the slope of the fixed end due to unit bending moment. As L is increased the flexure of base, thus slope of fixed-end, has a decreasing influence on the overall beam compliance due to the increasing dominance of the L^3 term. The authors found that the gradient of the δ/P vs. L^3 plot was approximately linear, thus L^3 dominance, for aspect ratios $(L : a) \geq 6$. For aspect ratios < 4 the L^2 term was seen to dominate, leading to the failure of the simple beam approximation.



(a) (b)

Figure 2.31: Finite element model of a microcantilever. (a) Encapsulating bulk material included. (b) Bulk material reduced. Figure from [177].

Gong and Wilkinson (2009) and (2010) [177, 148] built upon previous work by utilising finite-element (FE) modelling to account for the flexure of the base material. The model included all of the cantilever beam and some of the encapsulating bulk material. The outer surfaces of the bulk material were fully 'encastre' (movement restricted in all axes) except the upper surface and the surface attached to the fixed end that were free to flex. The responses of several models incorporating various amounts of bulk material were compared. The authors found that the model containing the largest amount of bulk material, shown in figure 2.31(a), was only 1 % more stiff than the model shown in figure 2.31(b), so the more simplistic model was seen as good compromise between computational expense and realistic representation.

A finite element approximation may also be used to extract material properties such as elastic modulus and yield stress by fitting the load-displacement curves to the experimental data. Gong and Wilkinson (2009) [177] used a manual method of reverse fitting to calculate the critical resolved shear stress (CRSS) on the three slip systems of single-crystal α-titanium. The models were implemented in the commercially available ABAQUS FE software and simulated the bending behaviour of single-crystal beams in all tested crystal orientations. To achieve this, the constitutive equation from Dunne's [178] physically based crystal plasticity (CP) model was written in a user defined ma-

terial (UMAT) subroutine. By making the plastic velocity gradient, $\boldsymbol{L}^p$, dependent on a simple yield criterion (derived and discussed in section 4.2.2) and by defining the interaction volume, ΔV, as $26b^3$, the CRSS could be determined for various single crystal microcantilever beams.

2.6.6 Microcantilever summary

Although literature involving microcantilevers is very limited, the technique shows a lot of promise in allowing the examination of a wide range of properties including elasticity, plasticity, and fracture on a size scale comparable to ion irradiation damage levels. Their advantage over other micromechanical specimen geometries, such as micropillars are numerous, these include; ability to examine a large range of crystallographic orientations; the relative ease to achieve higher accuracy during fabrication; and the ability to test microstructural features such as grain boundaries. However, size effects do pose a large problem when comparing to bulk tested values, but these are shown to be reduced for microcantilevers with widths greater than approximately 5 μm. This is discussed further in the following section.

2.6.7 Micromechanical size effects

The strength of crystals may be increased if their size is made sufficiently small. This strength dependence on specimen size is known as the 'micromechanical size effect', and was first noted in the work by Taylor (1924) [179] regarding the preparation of metallic wires with micron sized diameters. A similar hardening effect was later observed in iron, copper and silver wire by Brenner (1956) [180]. By performing tensile tests on wire specimens with diameters ranging from 1.2 μm to 15 μm, the strength at fracture could be measured (figure 2.32).

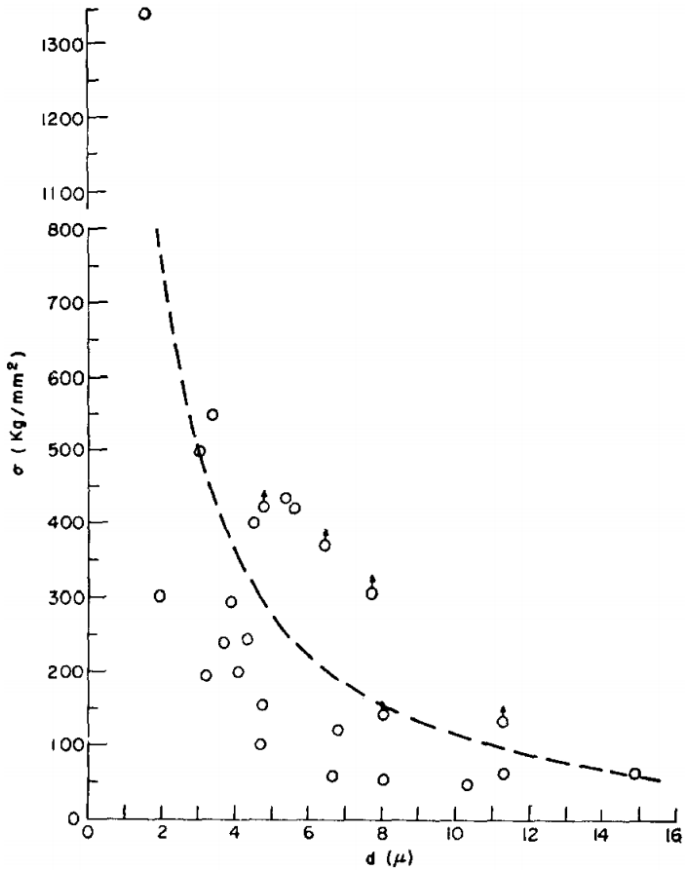


Figure 2.32: The effect of specimen varying diameter on the strength of iron wire. Figure from [180].

The author noticed that the surface condition of the wire greatly influenced their strengths. Wires containing pits, corrosion and grain boundaries were seen to have greatly reduced strengths. The author also notes a very large scatter in the wire strength which increases as a function of decreasing size. This is representative of a statistical distribution of defects. The macroscopic tensile strength of pure iron is $\backsim$ 200 MPa [181] which equates to $\backsim$ 20 $^{kg}/_{mm^2}$. Figure 2.32 shows that size effects are still present in the specimens with diameters $>$ 10 μm, with average strengths approximately two to five times the macroscopic value, although it can be seen that below a diameter of 10 μm the wire strength dramatically increases. The large increase in strength below a critical size is typical of the micromechanical size effect and can also be seen in nanoindentation.

Indentation size effects

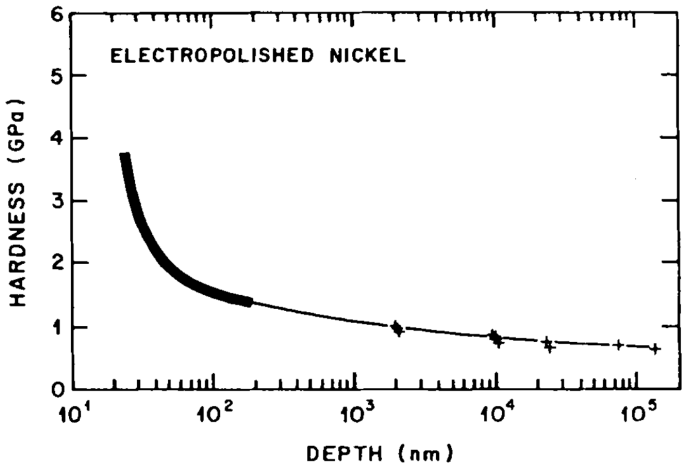


Figure 2.33: Increase in hardness with penetration depth for electropolished nickel. Figure from [154].

Similarly to Taylor's wire whisker specimens, nanoindentation is also subject to a micromechanical size effect. This is known as the indentation size effect, which is an observed increase in hardness as the indent size decreases. This phenomenon was first observed in indentation by Gane (1970) [182] who showed that for indents of diameter 1 μm or less, the hardness was several times that of a macroscale test. Questions remained over the validity of Gane's results due to the presence of a 5 nm thick oxide or carbonaceous layer contributing to the hardness increase. Although subsequent investigation by Pethica and Tabor (1979) [183] showed that even for atomically clean surfaces the hardness on the 100 nm scale was up to four times the macroscale value. Pethica et al. (1983) [154] investigated this further still by measuring the hardness nickel, gold and silicon using a Berkovich indenter tip with penetration depths as low as 20 nm. Figure 2.33 shows the variation of hardness with penetration depth for electropolished nickel from the nanoscale all the way up to the near-macroscale. Indentation size effects have in part been attributed to the formation of geometrically necessary dislocations (GNDs) that act to cause local hardening via dislocation pinning [184].

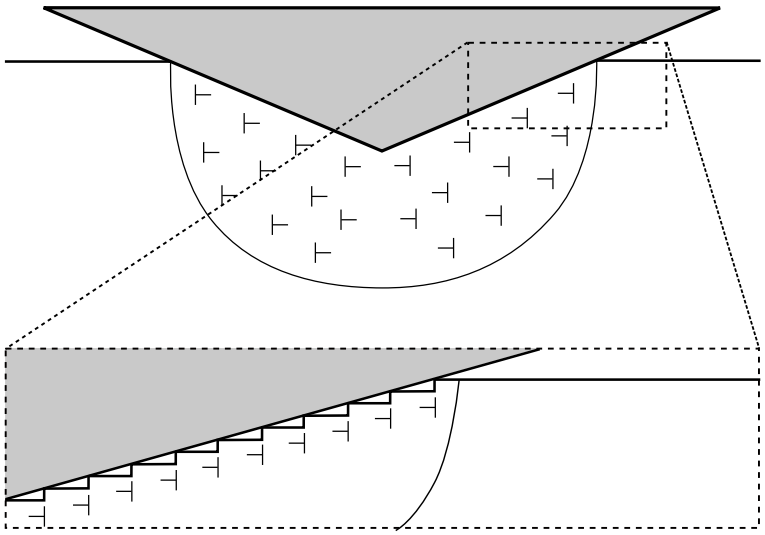


Figure 2.34: Geometrically necessary dislocations as created by a ridged indentation. The dislocation structure is idealised by circular dislocation loops. Figure redrawn from [185].

In the work by Ashby (1970) [186], a distinction is made between dislocations that accumulate in a crystal lattice in the presence of homogeneous strain fields, known as statistically stored dislocations (SSDs), and those that accommodate strain gradients in the case of inhomogeneous strain fields, known as GNDs. For simplicity, it is assumed that the strain gradients around the indent is accommodated by circular loops with Burgers vectors normal to the plane of the surface, shown by the planer schematic diagram in figure 2.34. It should be noted that SSDs will also be present and thus contribute to the deformation resistance, but as indention size is decreased the larger strain gradients present will mean that the contribution GNDs have to the hardening will increase, thus increasing their significance [185]. Nix and Gao (1998) [185] developed a model to account for the indentation size effect of the form, They predicted that the measured hardness, H, will vary with the inverse square root of the indent depth, h, such that,

$$\frac{H}{H_0} = \left(1 + \frac{h_*}{h}\right)^{\frac{1}{2}} \tag{2.20}$$

Where H is the measured hardness, h is the indent depth, H_0 is the hardness that would arise from the SSD alone, in the absence of any GNDs, e.g. for indents of infinite depth. h_* is a length that characterises the depth dependence of hardness and is dependent on the indenter geometry and H_0. This law can then be used to calculate the effective strain gradient, and subsequently the GND density.

Nix and Gao (1998) [185] showed that it was possible to account for the observed indentation size effects wholly from the formation of GNDs in the presence of plastic strain gradients. However, strain gradient plasticity theories do not consider changes in the fundamental deformation mechanisms associated with limiting the physical specimen size. For example, the previous work in tension tested fine metallic wires [180] demonstrated that hardening via the formation of GNDs cannot alone provide a satisfactory explanation to all micromechanical size effects.

Micromechanical size effects in FIB prepared specimens

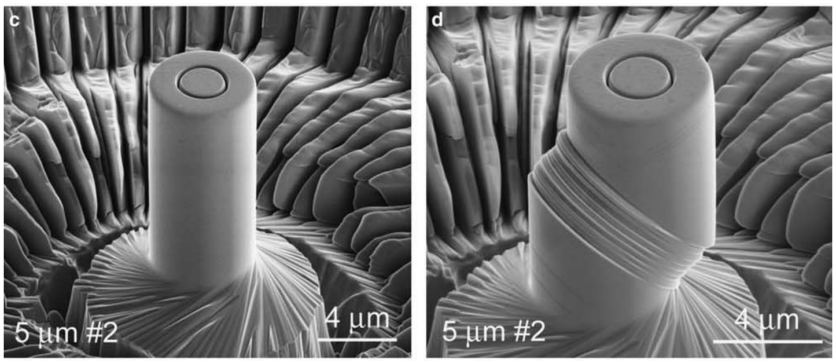


Figure 2.35: SEM micrograph of pure nickel micropillar with 5 μm diameter, before and after deformation. Figure from [187].

As the demand for ever smaller devices grew, so too did the importance of having a full understanding of how deformation mechanisms themselves are affected by the size of the deforming volume. Further development of FIB systems allowed Uchic et al. (2004) and Dimiduk et al. (2005) [150, 187] to fabricate micropillar compression specimens that minimised strain gradients, allowing the exploration of micromechanical size effects in

specimens with limited GND density. Annular milling was used to machine a roughly cut pillar specimen with highly tapered side profile. A 'lath-like' milling technique was then used to reduce the taper to form the final specimen (figure 2.35). Specimens were then deformed using a nanoindenter with a flat diamond punch tip. Various sizes of pure nickel micropillars were deformed, results are shown in figure 2.36. The micropillar specimens showed an increase in average yield stress with decreasing test volume.

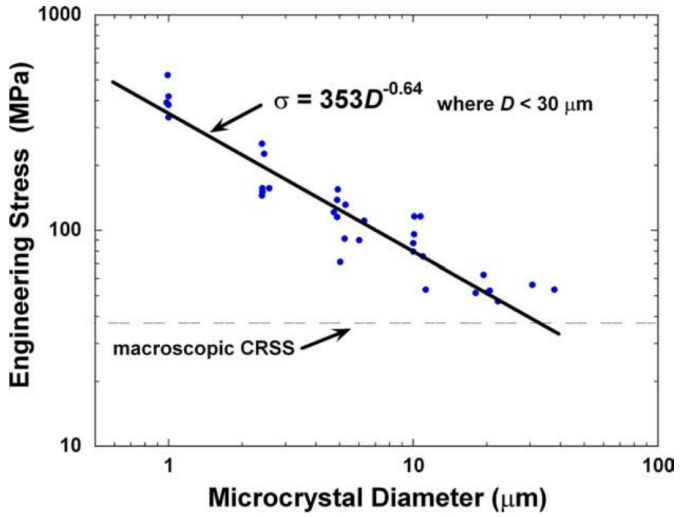


Figure 2.36: Mechanical size effect behaviour in FIB machined pure nickel micropillar specimens. Figure from [187].

Several comprehensive reviews of the micropillar size effect literature have been published [188, 189, 190]. The micropillar size effect has been attributed to four distinct mechanisms:

1. Source truncation. For small volume specimens with low Frank-Read source density, the dislocation loops emitted by the sources expand and intersect free surfaces, causing the dislocation line shorten into two segments. This prevents further plasticity until enough stress can operate one of the shortened dislocations [188].

2. Dislocation starvation. As test volume decreases, dislocations are more likely to leave the pillar via the free surface before dislocation multiplication and interaction

occurs. New dislocations have to be nucleated which requires high stresses [191].

3. Source limitation. For materials with a homogeneous source distribution, smaller sample volumes contain fewer dislocation sources [192].

4. Exhaustion hardening. The limited number of mobile dislocation sources in smaller volumes can lead to the activation of stronger dislocation sources or sources on low Schmid factor slip systems. Also, dislocation pinning from forest hardening and back stresses from dislocation pile-ups act to increase the activation stress of weaker active sources, leading to exhaustion hardening [193].

Micropillar size effects have been shown to be suppressed in certain ODS alloys. Girault et al. (2010) [194] investigated the dependency of CRSS on micropillar diameter in single crystal nickel-based ODS superalloy, Inconel MA6000. TEM investigation revealed the oxide population had diameters of between 20-30 nm with an average spacing of < 100 nm. Micropillars were fabricated with diameters of 200 nm up to 4000 nm and deformed using a flat diamond punch in a similar manner to Uchic. CRSS was measured to be close to the expected bulk value and independent of pillar diameter. Although, pillars of diameter < 2000 nm stress-strain data became stochastic, showing large strain bursts. The authors suggest that size-dependent mechanisms such as dislocation starvation or source exhaustion are either not operative or dominated by hardening mechanisms caused by the dislocation interaction with the high density of internal obstacles.

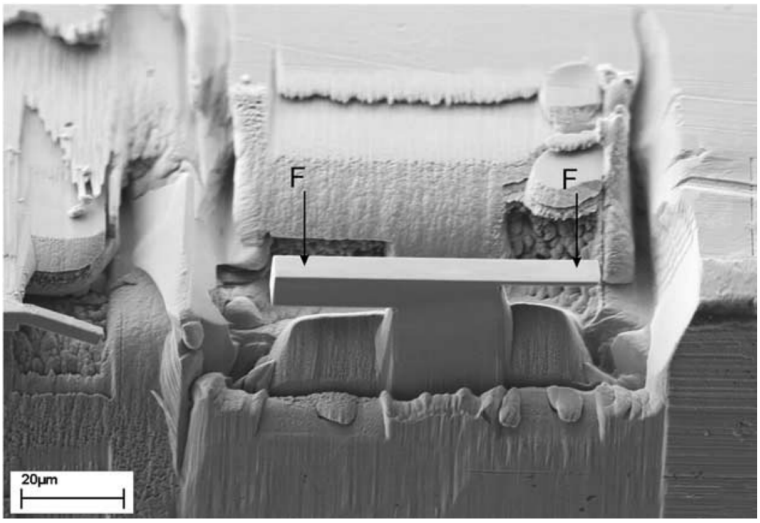


Figure 2.37: Microcantilever beams with square cross-section, produced by Motz et al (2005) [195].

Motz et al. (2005) [195] were the first to investigate micromechanical size effects in nanoindenter displaced microcantilever beams. Similar to the method employed by Di Maio and Roberts [146] (section 2.6.5), single crystal copper microcantilevers of depths 1 to 7.5 μm were FIB milled from the bulk, however the authors situated microcantilevers on the sample edge which, with appropriate sample orientation, allowed the fabrication cuboid specimens, shown in figure 2.37. Load-displacement data was recorded using a nanoindenter and modeled using ABAQUS FE software to extract the flow stress for each beam, results are shown in figure 2.38.

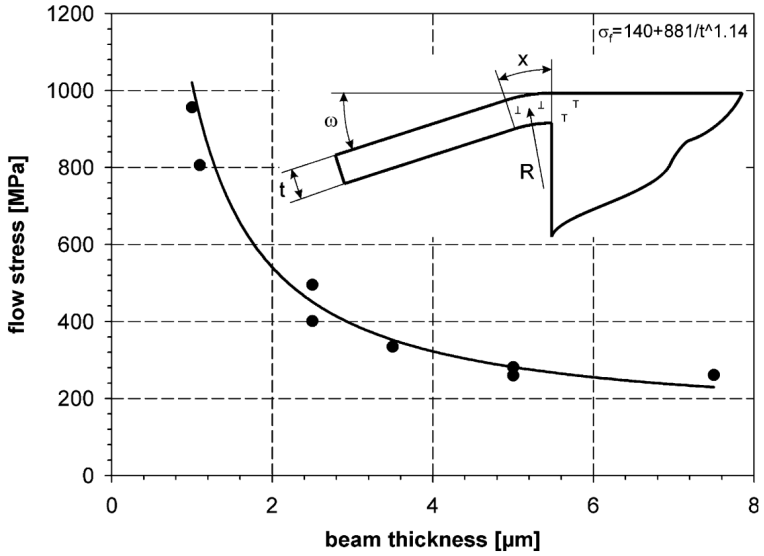


Figure 2.38: Flow stress dependence on microcantilever depth. Figure from [195].

The flow stress was seen to increase as microcantilever depth was reduced, with a pronounced increase in flow stress for depths < 4 μm. The previously discussed work by Ashby [186] states that strain gradients, as found in beam bending, must be accommodated by a density of GNDs. According to Taylor's rule, this increased dislocation density would lead to an increase in flow stress, σ_f, and can be described by the relation,

$$\sigma_f = \frac{\alpha \mu b}{\sqrt{\rho_{GND} + \rho_{SSD}}} \tag{2.21}$$

where α is a dimensionless constant, μ is the shear modulus, b the modulus (norm) of the Burgers vector, ρ_{GND} and ρ_{SSD} are the GND and SDD density respectively [195]. However, the authors found that the strong increase in flow stress could not be fully explained with a strain gradient plasticity model alone. This is because the strain gradient plasticity model assumes an array of dislocations each of which contributed a Burgers vector amount of bending. The authors suggests in realistic beams the size effect will strongly depend on the dislocation source density.

Experimental data [177] and 3D discrete dislocation plasticity analysis [196] of micro-

cantilever tests considered a source dependent size effect by requiring that dislocations originate from the lowest strength sources in regions of locally high stress. Once emitted from the source, the dislocation would then glide to a location of zero resolved shear stress (RSS) to provide the required plastic strain gradient. This interpretation implies that the microcantilever size effect has a strong source dependency not accounted for in conventional strain gradient plasticity models. Additionally, it was found that continued nucleation from the same source gave rise to 'soft pile-ups' of dislocations in the locations of zero RSS. Back-stress from the soft pile-ups acted on the source from which the dislocation originated, increasing the activation stress for further dislocation nucleation. It was suggested that these two mechanisms combine to give rise to the observed microcantilever size effect.

Tarleton et al. (2015) [197] used a planer discrete dislocation plasticity model to simulate end-loaded microcantilevers in order to interpret size effect behaviour observed experimentally. The authors first noted that soft pile-up locations occur along a line of zero RSS whose medial position depends on the slip plane angle. This is due to presence of a shear stress with respect to the neutral axis in cantilever bending. Unlike the pure bending case, the zero RSS isoline will likely not be at the beam neutral axis. To illustrate this, zero RSS isolines are drawn in figure 2.39 for slip plane angles oriented by an anti-clockwise angle, θ, relative to the beam axis.

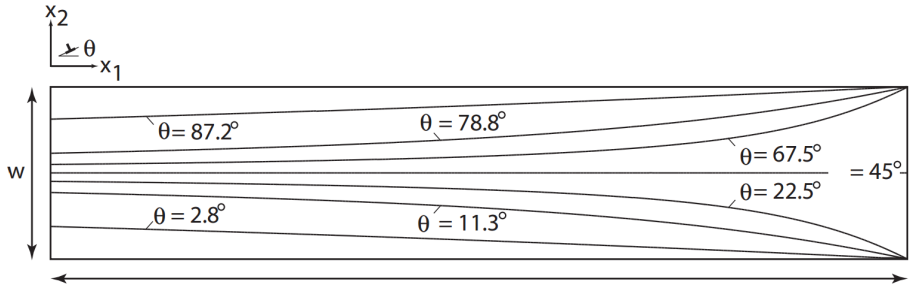


Figure 2.39: Zero RSS isolines for different slip plane angles. Figure from [197].

This means that the length of the soft pile-up, which affects both the hardening and flow stress, is dependent on the slip plane angle. As the slip plane angle, θ, approaches

0° or 90°, the zero RSS isoline approaches the lower or upper free surfaces. Although the RSS on such a plane is low, if the slip plane was to become active, the pile-up length could break the free surface creating a channel of easy slip through continuous source activation.

The authors also explored the physical interpretation of requiring GNDs to nucleate from a restricted density of sources. It was suggested that a source limited strengthening regime should exist when the beam size is sufficiently small that the slip band spacing is on the order of $1/\sqrt{\rho_s}$, where ρ_s is the source density; it is implied that slip band spacing decreases linearly with beam size. To demonstrate this, six source densities, each with twenty one different source structures (determined using statistical variation) were modelled for three different beam sizes. The primary, secondary and tertiary slip systems were at θ angles of 45°, 105°, 165°respectively.

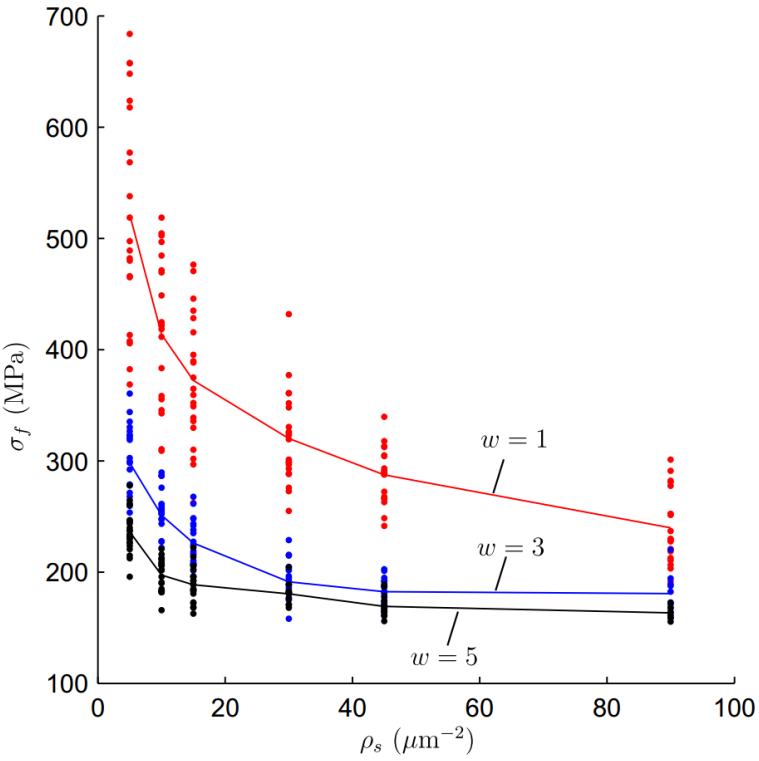


Figure 2.40: The flow stress dependency on source density for microcantilever beam widths of 5 μm, 3 μm and 1 μm. Figure from [197].

The smallest beam size, 1 μm, is source limited throughout the range of source densities simulated. Whereas the 3 μm and 5 μm became source limited for source density values below approximately 25 μm^{-2} and 15 μm^{-2} respectively. Figure 2.40 demonstrates that the source density dominates the size effect in small beams and for beams of low source density. The authors state that there was linear scaling of slip band spacing with beam size, particularly for larger source densities. This demonstrates that GNDs dominate the size effect in microcantilever beams for the beams that are not source limited, i.e. primarily in larger beams.

The authors conclude:

- Highly localised stresses found in microcantilever bending greatly enhance the effect statistical variations in the source population (strength and position) has on the yield and plastic flow.
- Soft pile-ups occur at isolines of zero RSS, whose position is dictated by the slip plane orientation and could differ greatly from the beam neutral axis position.
- GNDs and source limitation combine to produce the observed size effect, the contribution of the latter significantly increases as beam size is reduced.

2.6.8 Size effects in irradiated micromechanical test specimens

The flow stress of a material, and the resultant characteristic lengthscale, is dependent on a superposition of contributions from multiple features, such as dispersed obstacles of various types and lengths, dislocation size and number density, grain boundaries and dislocation source density. The affect irradiation damage has on micromechanical size effect is not yet well documented in the literature, the most applicable to this project is the work carried out by Kiener et al (2011) [198] and Hardie et al. (2016) [199].

Kiener et al (2011) [198] investigated the effect 1.1 MeV proton irradiation at 80 °C had on mechanical properties of [1 0 0] single crystal copper nano-compression specimens of diameters varying from 80 nm to 1500 nm. Each specimen was FIB fabricated so that

the pillar was situated in the flat portion of the proton damage profile to a dose of 0.8 dpa. Figure 2.41 shows the size-dependent yield stress for the range of pillar diameters tested.

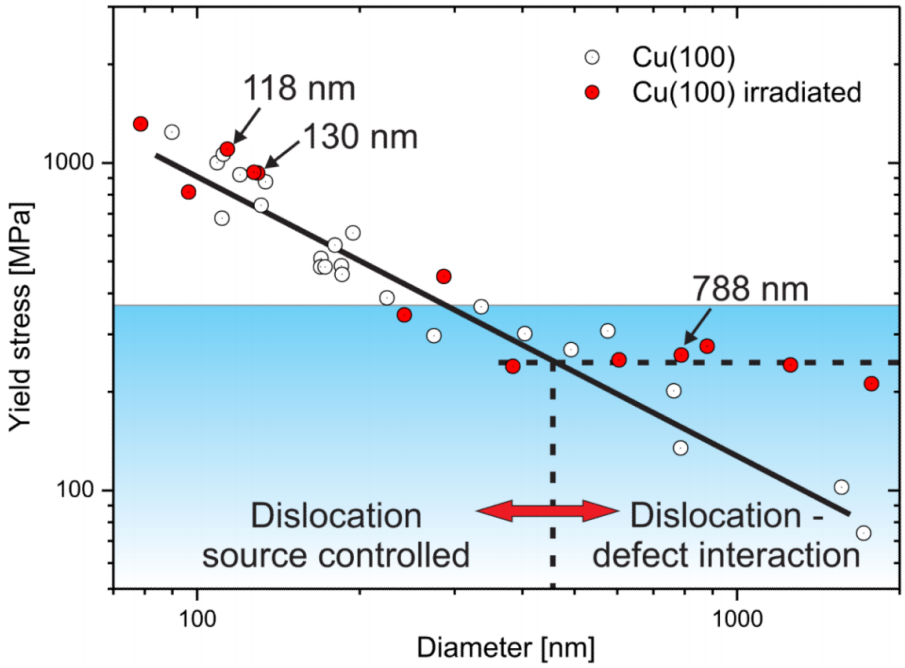


Figure 2.41: Unirradiated material (open circles) exhibits size-dependent yield over the range of pillar diameters tested. The irradiated material (red circles) transitions to size dependent behaviour for pillar diameters smaller than ∼ 400 nm. Figure from [198].

The non-irradiated pillars display size-dependent behaviour throughout the entire range of pillar diameters tested, whereas the irradiated pillars only displayed size dependent behaviour for pillar diameters below ∼ 400 nm. Above this size, the author notes that the measured yield stresses were within the scatter typically observed (220 - 280 MPa) for the sample dimensions and conditions examined, i.e. seemingly independent of size. The author explains that in the large pillars, larger dislocation sources are operated by lower stresses in the absence of defects. However, if defects are introduced, their obstacle strength and spacing control the onset of plasticity. As pillar size is decreased, the stress needed to activate fewer and smaller dislocation sources will eventually become higher than the obstacle strength, thus pillars become relatively unaffected by the

presence of defects.

Hardie et al. (2016) [199] investigated the mechanical behaviour of Fe6%Cr under both heavy ion and neutron irradiation. Both irradiation cycles were performed at an irradiation temperature of 288 °C to the same dose (1.7 dpa). However, due to the nature of the two irradiation methods, the damage rate for heavy ion was much larger than that for neutron irradiation. Neutron irradiation was carried out in capsule 6A in the ATR1 materials test reactor in INL, USA. Iron ion irradiation was carried out at the 3 MV-Tandetron accelerator at HZDR, Germany, producing irradiation depths of ∼ 2.4 μm, allowing relatively large triangular cross-sectioned microcantilevers to be FIB fabricated from the irradiated surface. Figure 2.42 displays the microcantilever data obtained from both irradiated samples in comparison to the unirradiated control.

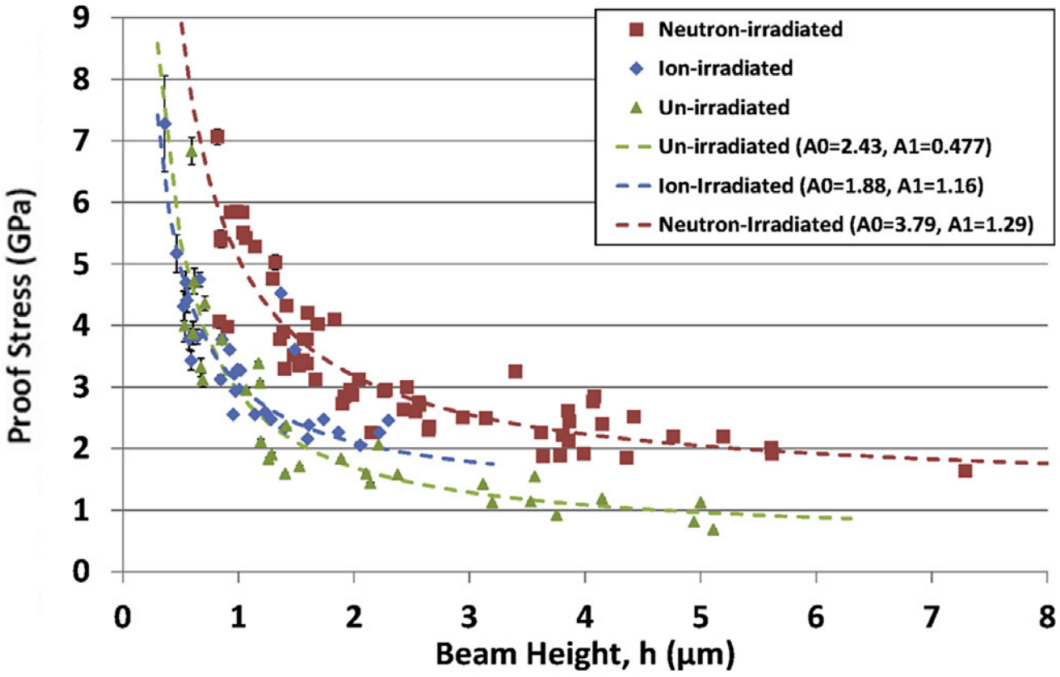


Figure 2.42: The dependency of proof stress on microcantilever height for unirradiated, heavy ion irradiated and neutron irradiated Fe6%Cr. Figure from [199].

When comparing ion irradiated to unirradiated microcantilevers, there appeared to be no difference to the measured proof stress below 1 μm beam depth. This suggests

that at this size range, the size effect mechanisms, such as source limitation, dominate over hardening from irradiation induced defects. A critical beam size is reached (~ 1 μm beam depth) when the yield stress increase due to size effect mechanisms is much lower than that caused by irradiation hardening mechanisms. At this point the mechanical response of the irradiated beams appeared to diverge from the unirradiated, although this is ambiguous due to the large scatter in the irradiated yield stress.

Radiation hardening in the neutron irradiated beams was discernible and consistent across the range of beam sizes measured, however only beam depths of > 1 μm were tested. From these results it appears that the nature of defects produced by neutron irradiation and their interaction with gissile dislocations is different to those produced by ion irradiation. The authors suggested that the neutron irradiated material was likely to have exhibited Cr enrichment associated with radiation induced dislocation loops which, unlike the dislocation loops, cannot be annihilated via interaction with a glissile dislocations, and therefore will continue to contribute to the stress required to onset plasticity.

FIB introduction of defects

FIB milling of micromechanical test specimens may introduce defects within the test volume that have the potential to affect their mechanical response. Shim et al. (2009) [200] undertook a study in Mo-alloy micropillars in an attempt to quantify these effects. Directionally solidified pillars were FIB milled and tested in compression, these were compared to pillars that were not subjected to FIB milling. Two different specimens were FIB prepared, one was left in the as-polished state and the other was etched prior to FIB milling, labeled $P - FIB$ and $PE - FIB$ respectively. Stress-strain curves for the three types of pillar tested are shown in figure 2.43.

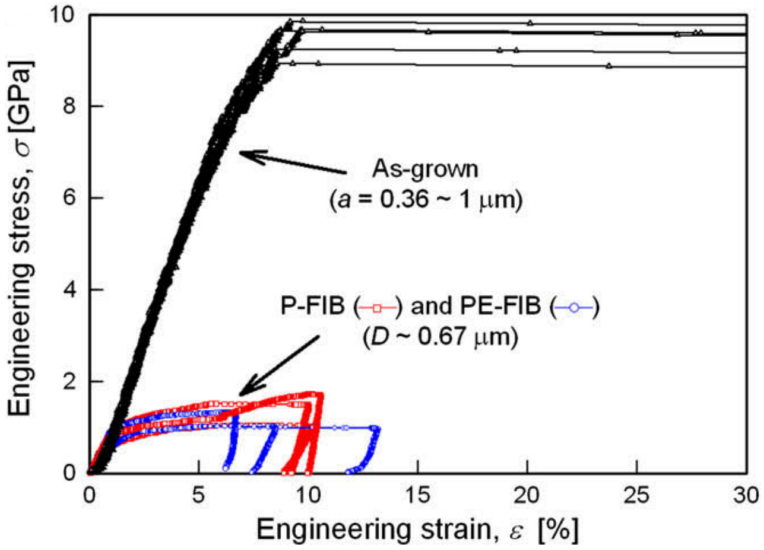


Figure 2.43: A comparison of the stress-strain curves for the as-grown and FIB milled pillar specimens. Note that a is the edge length of the square cross-section and d is the diameter of the circular cross-section. Figure from [200].

The directionally solidified Mo-alloy pillars tested in the as-grown condition displayed a yield stress that was very close to the theoretical strength ($\sim G/25$, where G is the shear modulus). Indicating that these pillars contained little to no defects prior to testing. In comparison, there was a marked difference in the yield and plastic flow behaviour between the FIB prepared pillars and those tested in the as-grown condition. The yield stresses of the FIB prepared specimens were approximately an magnitude lower than the as-grown pillars. Additionally, a certain amount of stable work hardening behaviour in the FIB prepared specimens indicated the presence of FIB induced defects, compared to the catastrophic strain jump after yield of the as-grown pillars, indicating a 'clean' microstructure.

FIB induced defects are unlikely to produce such a significant change in the mechanical response of micromechanical test specimens examined in this project due to the complex microstructure of the HIP consolidated materials. As discussed in section 2.5.2, mechanical alloying introduces large number of defects, dislocations and residual stress, not all of which can be completely removed during consolidation. This will help

to mitigate any changes to the mechanical response from FIB induced defects.

2.6.9 Micromechanical size effect summary

Micromechanical size effects have been observed in almost all test specimen geometries approaching the nanometre scale, regardless of material composition. Although, certain materials have shown a suppression of size effect in micropillar specimens, such as the ODS nickel superalloy investigated by Girault et al. [194]. The author suggests that the size-dependent mechanisms normally present in micropillars, such as dislocation starvation or source exhaustion, are dominated by hardening mechanisms caused by the dislocation interaction with the high density of internal obstacles. As specimen size is decreased below a critical size, shown to be ~ 1 μm microcantilever depth by Hardie et al. [199], the yield stress increase due to size effect mechanisms start to dominate over obstacle/defect controlled mechanisms.

Tarleton et al. [197] used a planer discrete dislocation plasticity model to simulate end-loaded microcantilevers. They confirmed that the contribution of source limitation becomes increasingly significant as beam size decreases, and suggested that GNDs and source limitation combined to produce the observed size effect. A source limited regime was found in sufficiently small beam geometries where the slip band spacing was limited by the source density, ρ_s. Thus the regime can be defined by,

$$w \leq \frac{1}{\sqrt{\rho_s}} \tag{2.22}$$

where the beam geometry is defined by the beam width, w, if the beam aspect ratio is 6 . Additionally, soft pile-ups were seen to occur at isolines of zero RSS, and also contributed to the size effect by increasing the activation of stress of the source that produced the pile-up, via back-stresses.

2.6.10 Microcantilevers in self-ion irradiated Fe-Cr alloys

While the field of FIB machined micromechanical test geometries is growing, there is still very little literature currently published regarding the use of microcantilevers to extract mechanical properties from shallow ion irradiated layers. At the time of writing (December 2016), work reported within the literature only covers microcantilevers fabricated in heavy ion and neutron irradiated materials, i.e. no work on proton irradiated materials. Although there is large body of literature regarding FIB milled micropillars in irradiated layers, the FIB machined micromechanical work in this thesis focuses entirely on microcantilevers, for which the geometry and stress distributions are very different. Therefore, this section will only discuss work regarding microcantilevers fabricated in heavy ion irradiated iron-based alloys.

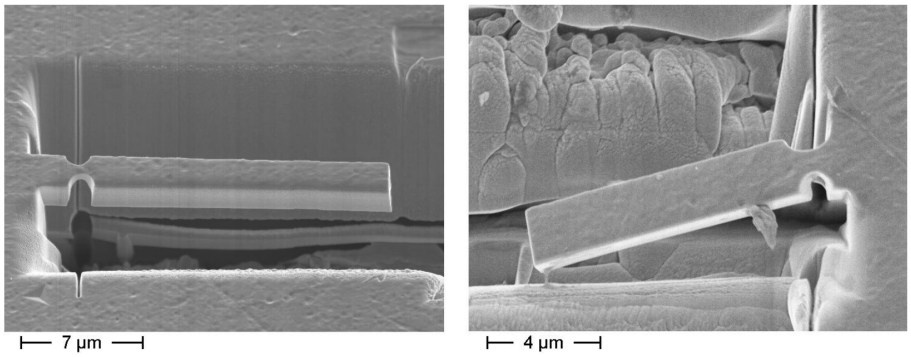


Figure 2.44: SEM micrograph of microcantilever, machined with a 1 μm waist. Figure from [201].

Heavy ion irradiation in iron-based alloys produces very shallow damage layers, approximately 1 μm deep for 2 MeV Fe^+ ions. As such, test geometries in the irradiated layer must be fabricated to this size limit. Using a similar method to that used by Armstrong et al. (2009) [147], described in section 2.6.5 (p69), Halliday et al. (2009) [201] FIB machined microcantilevers with a 1 μm thin waist, as shown in figure 2.44. Two irradiation doses were used, a lower dose that gave an average displacement damage of 0.35 dpa, and a higher dose, that gave an average displacement damage of 5.33

dpa. Simple beam theory was used to calculate the stress-strain curves from the load-displacement data, results for beams fabricated in pure iron are given in figure 2.45.

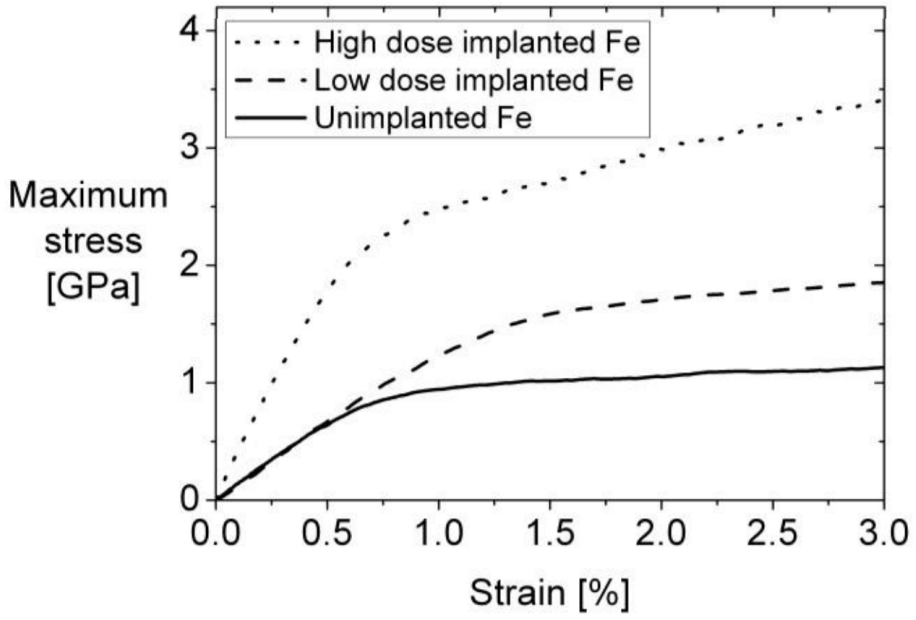


Figure 2.45: Stress-strain curves calculated using simple beam theory for waisted beams produced by Halliday et al. (2009) [201] in pure iron. Figure from [201].

Damage from self-ion irradiation produced a clear hardening response in waisted microcantilevers in pure iron, as shown in figure 2.45. A significant yield stress increase was observed in both irradiated specimens when compared to the unirradiated. The rate of work hardening increased in both irradiated specimens, with a much more significant rate increase measured for the higher dose. However, a large elastic modulus of 374 GPa was measured in the high dose specimen, much larger than the theoretical value of 139 GPa expected for this crystal orientation. This was likely caused by poor measurement, or a defected microcantilever unnoticed by the author. A greater number of specimens are needed to increase the accuracy of the results.

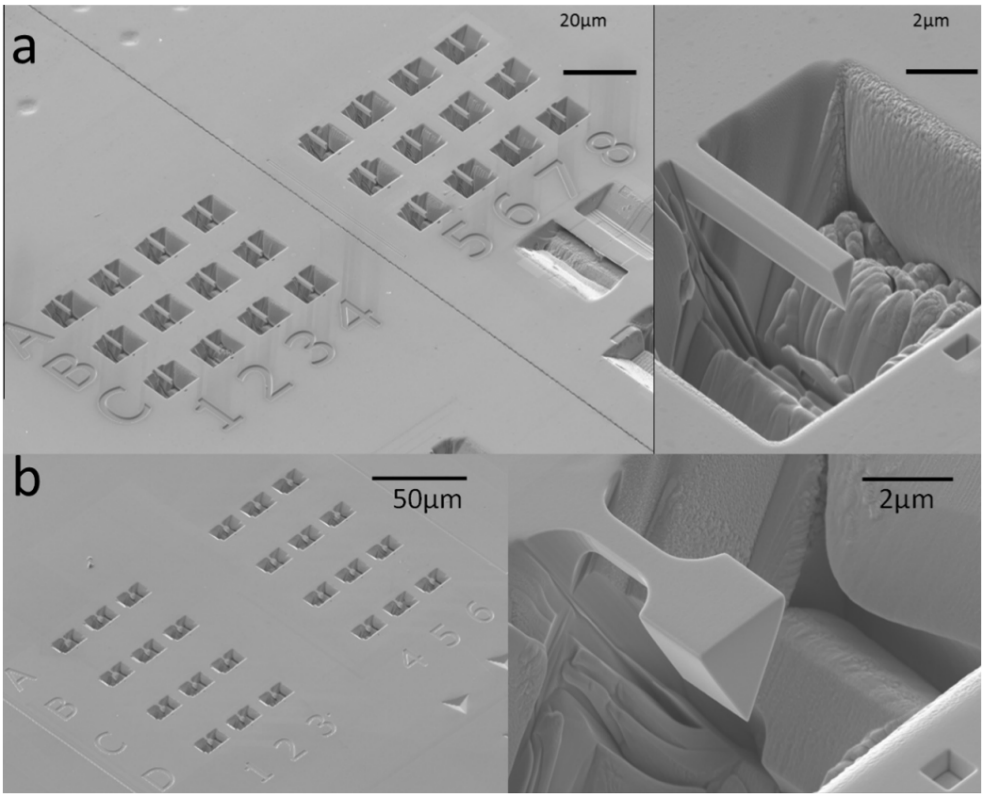


Figure 2.46: SEM micrograph of irradiated and unirradiated arrays of microcantilevers, boundary described by a visible FIB milled line. Also shown in typical microcantilevers, (a) triangular, uniform cross-section and (b) waisted beam. Figure from [202].

Hardie (2013) [203] used two different beam geometries to examine Fe^{+} irradiated layers in Fe-Cr binary alloys. Similar to Halliday et al. (2009), the author FIB milled waisted microcantilevers with a gauge section at the base, allowing greater control over the distribution of the plastic zone. These were compared to more simplistic microcantilevers with a triangular, uniform cross-section. Both microcantilever geometries are shown in figure 2.46(b) and (a) respectively.

For both microcantilever geometries, FE modelling was used to extract mechanical properties such as yield stress and elastic modulus, via a progressive convergent approximation to match simulated load-displacement data to the experimental data. This method, developed by C.D. Hardie and T.B. Britton (both formerly at the University of Oxford) is described in greater detail in section 3.4.4. Typical stress-strain data

produced by FE fitting for waisted microcantilevers is shown in figure 2.47. Results for the average mechanical property measurements recorded for both microcantilevers geometries, in irradiated and unirradiated regions of the sample, are given in table 2.4.

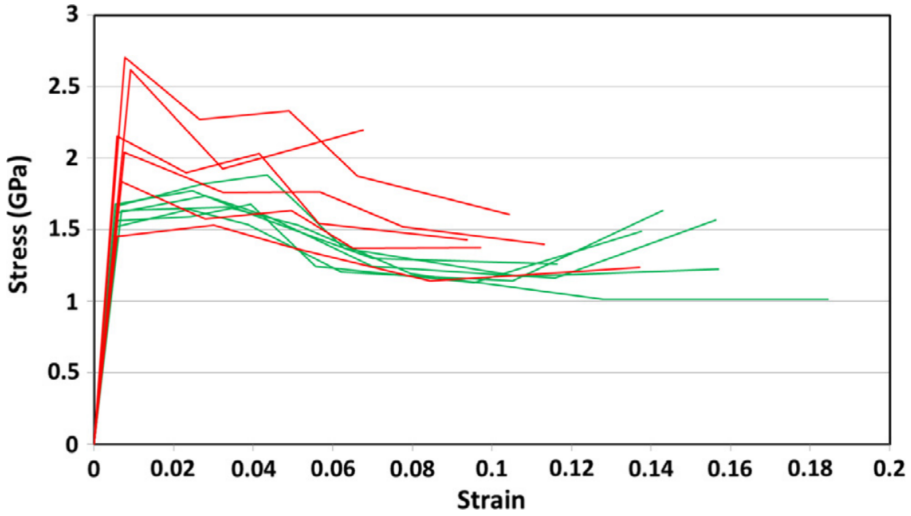


Figure 2.47: Stress-strain curves for FEA matched models of load-displacement data produced by waisted beams in Fe-12Cr. Unirradiated microcantilevers in shown in green and irradiated in red. The first deviation from elasticity denotes the yield stress. Figure from [202].

	Unirradiated			Irradiated		
		SD	%		SD	%
Uniform cross-section						
Elastic modulus (GPa)	205	14	6.7	195	30	15.4
Yield stress (GPa)	1.8	0.3	17.6	1.7	0.2	9.6
Waisted beam						
Elastic modulus (GPa)	277	26	9.5	299	50	16.9
Yield stress (GPa)	1.6	0.1	3.8	2.1	0.4	22.2

Table 2.4: Average mechanical property measurements produced by FEA analysis for both microcantilever geometries in unirradiated and irradiated Fe-12Cr. Table from [202].

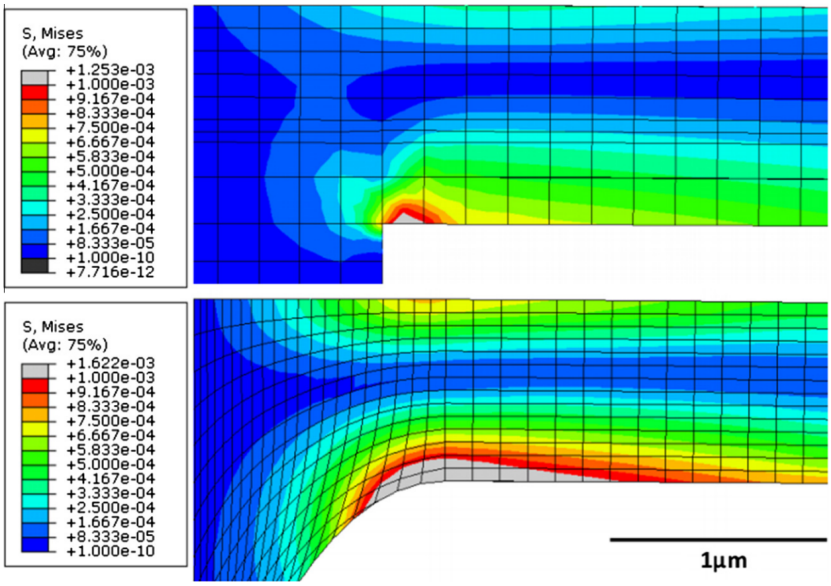


Figure 2.48: Vertical cross-section along the central beam axis of two FE models, showing von Mises stress distribution in microcantilevers of different geometries. Beam with triangular, uniform cross-section (top), waisted beam with non-uniform cross-section (bottom). Figure from [202].

There was no significant change in the yield stress measured for the irradiated triangular, uniform cross-section beams compared with the unirradiated; the measured yield stress was 1.7 GPa (standard deviation 0.2 GPa) and 1.8 GPa (standard deviation 0.3 GPa) respectively. In contrast, the waisted, non-uniform cross section beams showed a significant increase in the yield stress measured for irradiated specimens compared with those in the unirradiated condition, 2.1 GPa (standard deviation 0.4 GPa) and 1.6 GPa (standard deviation 0.1 GPa) respectively. There was a notable increase in elastic modulus in the waisted beams compared to the triangular cross-section beams, this was most likely due to the difficultly in accurately measuring the fillet radius of the waisted beams.

As the average yield stress measured for both unirradiated microcantilevers was greater than 1.5 GPa (compared to 300 MPa for macroscale tensile tests in the same material), it was clear that they were subject to the microcantilever size effect. As discussed in section 2.6.7, the microcantilever size effect is highly source density depen-

dent, particularly for the beam sizes used by Hardie (2013). Armstrong et al. (2015) [202] suggests that the lower yield stress in the waisted beams, compared to those with a triangular cross-section, was due to the presence of a smaller stress gradient along the cantilever in the waisted beams, demonstrated in figure 2.48. With a small stress gradient, there is an increased chance of it containing a dislocation source, resulting in a lower yield stress. This agrees with the results in table 2.4. Due to the much larger stress gradient in the triangular cross-section beams (figure 2.48), the deformation tended to be far more stochastic. Armstrong et al. go on to suggest that even for irradiated triangular cross-section beams, the yield stress was still controlled by the activation of single sources, hence the lack of hardening between irradiated and unirradiated beams in table 2.4.

This thesis aimed to build upon these results by developing a method for examining the mechanical properties of irradiated materials that was not as heavily influenced by microcantilever size effects. This used data gathered from a size effect study to fabricate microcantilever geometries in irradiated specimens that closely approximated to the macroscale mechanical properties measured from four-point flexure tests. It was not possible to achieve the large geometries needed with heavy ion irradiation, hence the use of proton irradiation in the work presented in this thesis.

Chapter 3

3 Characterisation of materials

This chapter characterises the microstructure and the mechanical behaviour of materials used in this thesis. After providing the material compositions, as supplied by manufacturers, electron backscattered diffraction (EBSD) was used to determine material grain size and morphology. The room temperature macromechanical yield stress and elastic modulus of each material was then determined from a four-point flexure test that uses digital image correlation (DIC) as a strain gauge. Lastly, micromechanical size effect was characterised for the materials used in this thesis. Microcantilevers of varying size were fabricated, and the dependency of yield stress on beam depth was measured. This was used to identify the microcantilever size needed to approximate to macroscale mechanical properties in chapter 5.

3.1 Research materials

Several alloys have been studied during the course of this research, the nominal compositions of which are given in table 3.1 and 3.2.

EUROFER 97 and ODS EUROFER

EUROFER and its ODS counterpart ODS EUROFER have been widely studied in the literature and hence are useful as reference materials for comparison to the in-house produced alloys. Both alloys were provided by Dr. Rainer Lindau of Karlsruhe Institute of Technology (KIT), Germany. Due to the large amount of literature available, these were ideal to use as reference alloys when investigating in-house produced steels.

An industrial batch of EUROFER was produced by BOHLER EDELSTAHL GmbH in Austria (commissioned by KIT). A rolled plate of 14 mm thickness was normalised at a temperature of 980 $^{\circ}C$ for 30 min and tempered at a temperature of 760 $^{\circ}C$ for 90

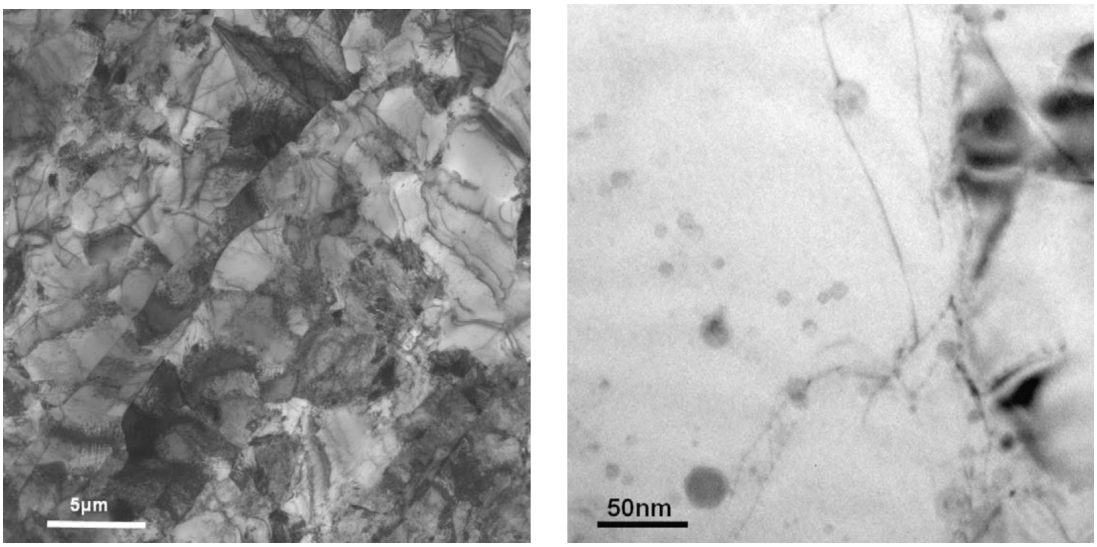
min followed by air cooling [204, 7].

ODS EUROFER was produced by Plansee Ltd using the mechanical alloying method developed by INCO, discussed in more detail in section 2.5.2. The alloy composition was gas-atomised to produce a fine powder and then mechanically alloyed in an inert atmosphere with 0.3 wt% Y_2O_3 powder in a attritor mill. The powder was then degassed and consolidated in a hot isostatic press (HIP) at 1150 $°C$, then subjected to hot rolling with intermediate heat treatments and post-rolling heat treatments. Unfortunately, the exact conditions of temperature, time and pressure have been withheld by the manufactures [205]. Both EUROFER and ODS EUROFER were used in the as-received condition.

Material	Fe	Cr	W	Mn	V	Ta	Si	C	N	Y_2O_3
EUROFER	Bal.	8.82 to 8.96	1.07 to 1.15	0.38 to 0.49	0.18 to 0.20	0.13 to 0.15	0.04 to 0.07	0.11 to 0.12	0.009 to 0.017	-
ODS EUROFER	Bal.	8.90	1.10	0.45	0.20	0.08	0.10	0.14	0.11	0.30

Table 3.1: Nominal compositions of EUROFER 97 and ODS EUROFER in wt%.

Transmission electron microscopy TEM of ODS EUROFER, performed by Klimiankou et al. (2003) [206], revealed that the distribution of oxide particles varied intergranularly, as well as locally within each grain. The author noted that the particle diameter varied between 3 - 45 nm, with a statistical average of 12 nm. Williams et al. (2010) [207] found that some grains showed a particle density of 4 x10^{23} m^{-3}, however the author notes that due to particle-free regions, the overall average particle density would be much lower.



(a) (b)

Figure 3.1: Bright field TEM micrographs of ODS EUROFER. (a) Complex grain structure. (b) Oxide particles of varying sizes. Figure from [207]

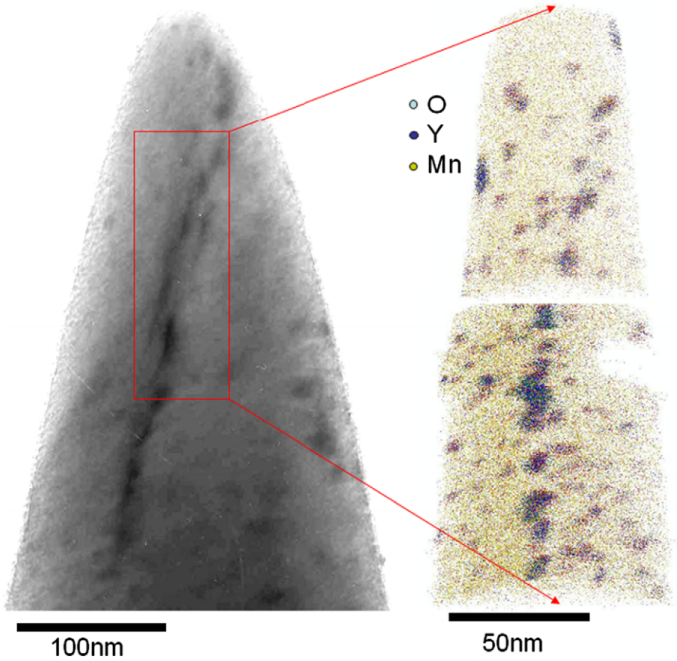


Figure 3.2: (Left) Bright field TEM micrograph of an APT specimen prior to analysis, showing a grain boundary within the analysis volume. (Right) Corresponding APT reconstruction of specimen, showing oxide particles present both along the grain boundary and in the material bulk. Figure from [207]

14WT and 14YWT

As part of a collaborative study between Chris Burrows and Mike Gorley (both at University of Oxford) [208, 209], two separate ODS alloys were fabricated to investigate the effect of HIPing temperature on the size and number density of nanoscale precipitates. The two ODS steels and their non ODS counterparts were manufactured by mechanically alloying gas-atomised Fe-14Cr-3W-0.2Ti, with the addition of $0.25Y_2O_3$ powder in the case of ODS. Mechanical alloying was performed using a planetary ball mill at 250 rpm in an argon atmosphere for 60 h. The mechanically alloyed powders were then degassed, placed in a mild steel can and HIPed at a pressure of 150 MPa and a temperature of either 950 $°C$ or 1150 $°C$ for 4 h to produce alloys designated 14YWT 950 and 14YWT 1150 respectively. The non-ODS counterparts are designated 14WT 950 and 14WT 1150.

The composition of the alloys were independently measured pre and post consolidation by the London & Scandinavian Metals Analytical Services using X-ray fluorescence and inert gas fusion techniques. Table summarises the compositional data for a 14WT and 14YWT reference alloy.

Material	Fe	Cr	W	Mn	Ti	Al	Si	C	N	Y_2O_3
14WT	Bal.	13.06	2.65	0.35	0.21	0.17	0.15	0.11	0.03	-
14YWT	Bal.	13.34	2.66	0.33	0.21	0.11	0.18	0.09	0.20	0.30

Table 3.2: Measured compositions of 14WT and 14YWT in wt%.

Both alloys also showed minimal nickel, molybdenum and cobalt, however aluminium, which was also undesired, was present in significant quantities. Milling components, such as balls and pot, can introduce impurities into the powder. To reduce this, the steel AISI 52 - 100 was chosen for the fabrication of all milling components, due to its low nickel content (< 0.3 wt%) but retained high hardness. However, contamination from milling components does not explain the introduction of aluminium into the

powders. Burrows (2015) [208] reports that likely sources for the aluminium contamination could not be identified in the production or analysis processes and suggested that contamination must occur during gas atomisation.

Using HRTEM and atom probe tomography (APT), Burrows (2015) [208] characterised the oxide particles found in 14YWT alloy at the two HIPing temperatures, results are shown in figures 3.3 and 3.4. The alloy consolidated at 950 $^{\circ}C$ was found to have an particle number density of 7 x10^{23} m^{-3} with an average diameter of 2.4 nm. The particles were seen to modestly coarsen for the 1150 $^{\circ}C$ consolidation temperature and were found to have a particle number density of 2 x10^{23} m^{-3}, with an average diameter of 3.2 nm.

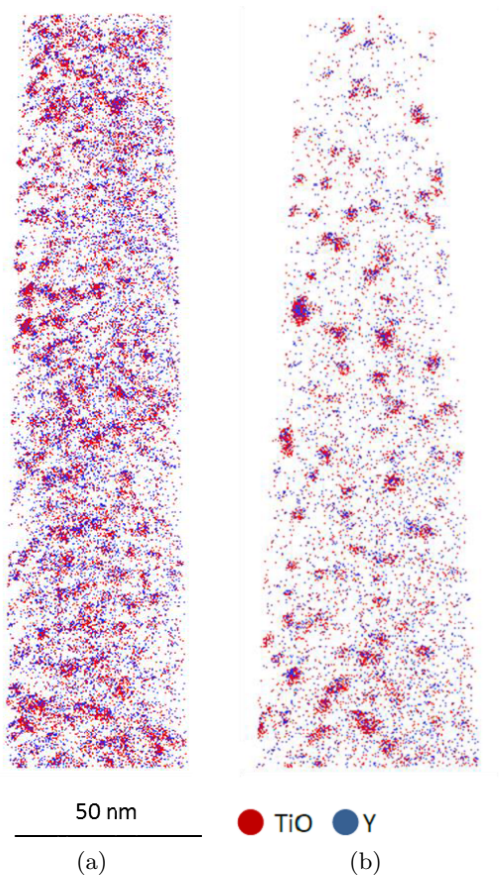
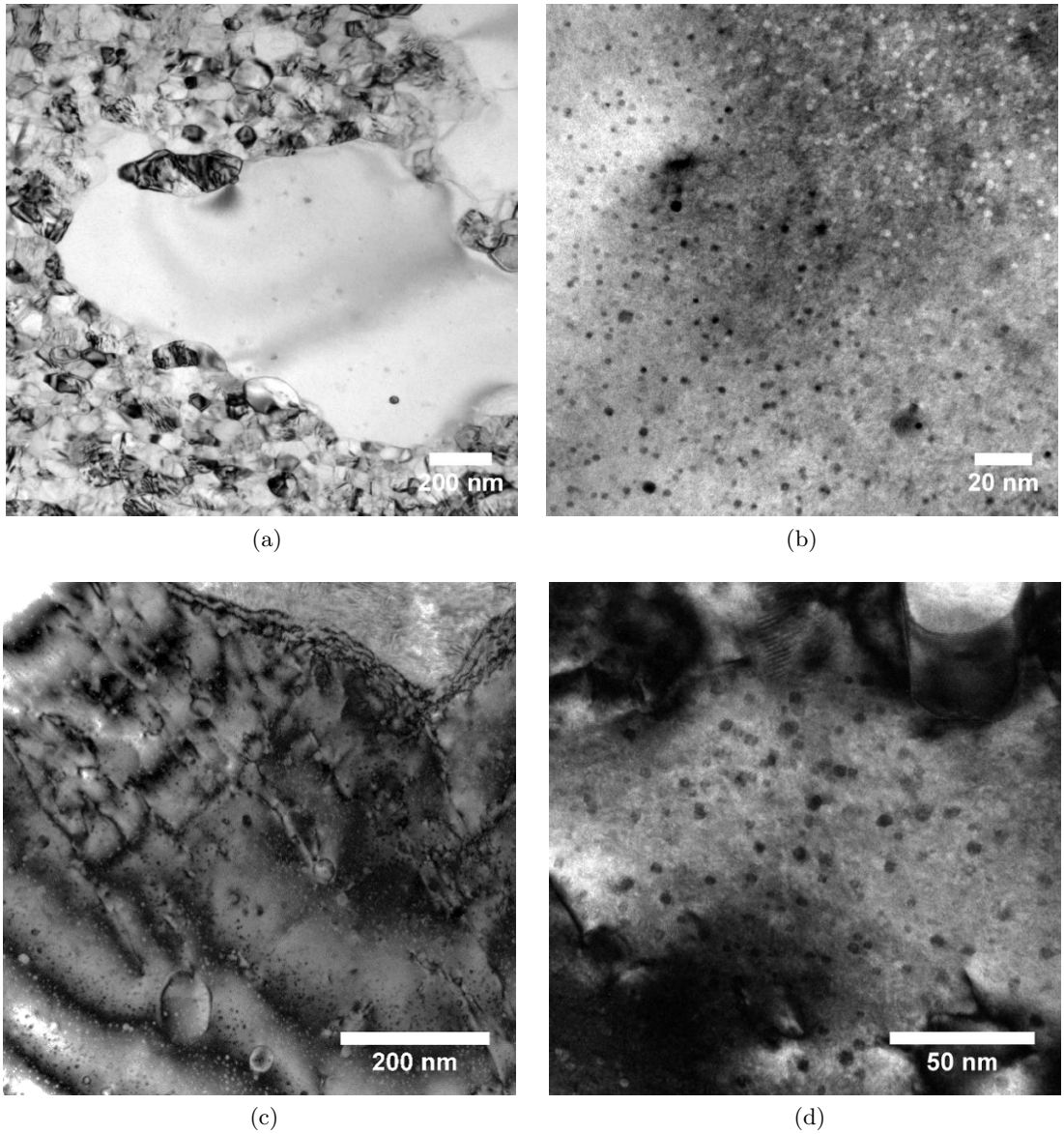


Figure 3.3: APT reconstruction shown using atom maps of titanium oxide and yttrium particle-forming ions in samples consolidated at (a) 14YWT 950. (b) 14YWT 1150. Figure from [208].



(a) (b)

(c) (d)

Figure 3.4: Bright field TEM micrographs of in-house produced ODS alloys. (a) 14YWT 950. Heterogeneous microstructure, showing areas of very fine grains. (b) 14YWT 950. Dense particle dispersion taken from the coarse grain shown in (a). (c) 14YWT 1150. Dense particle dispersion in coarser grained area. (d) 14YWT 1150. Dense particle dispersion in single 100 nm grain. Figure from [208].

3.2 EBSD crystallography characterisation

3.2.1 Scanning electron microscopy

Electron backscattered diffraction (EBSD) was used to characterise the grain size and morphology of the materials described in section 3.1. EBSD is a scanning electron microscopy (SEM) technique that allows crystallographic orientation, grain boundary misorientation, texture measurement and phase morphology to be characterised and quantified at a macro to sub-micron lengthscale. EBSD analysis was carried for each material listed in section 3.1, except for 14YWT 950, which could not be indexed. A detailed description of the EBSD technique is beyond the scope of this thesis, the work by Engler and Randle (2009) [210] or Schwartz et al. (2009) [211] provide a good introduction to the relevant theory.

Other SEM techniques, such as secondary electron (SE) imaging and energy dispersive X-ray spectroscopy (EDX), were also used in this project. SE imaging, in particular, was used extensively, including the examination of surfaces prior to FIB milling, imaging of microcantilevers at all stages of fabrication, and measurement of nanoindent placement with respect to the irradiated surface. EDX was used to determine the local chemistry around nanoindents in 14YWT 1150 in chapter 5.

The SEM microscopes used in this project were a JEOL 6500F, a Zeiss Auriga dual column SEM-FIB and a Zeiss Merlin. Each system uses a field emission source to provide high spacial resolution, with resolutions at 15 keV of 3 nm (6500F), 1 nm (Auriga) and 0.8 nm (Merlin). The JEOL 6500F, fitted with an OIM EBSD detector (EDAX, Mahwah, NJ, USA), was used for EBSD characterisation; the Zeiss Auriga was used for microcantilever fabrication and measurement, and the Zeiss Merlin was used for EDX mapping.

3.2.2 Sample preparation

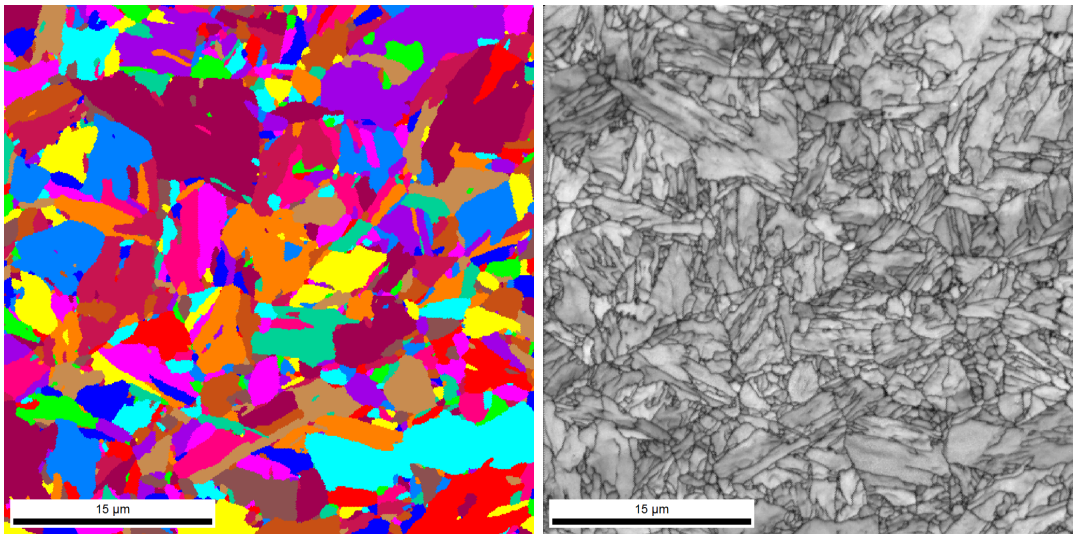
High quality sample preparation was necessary for all experimental techniques used throughout this project. First, the specimens were subjected to mechanical grinding using an increasing grade of silicon carbide paper to remove the initial deformation layer created during sectioning, with 4000 grit used as a final grade. The damage layer produced from grinding was then removed using a suspension of 1 μm diamond polishing compound. A final mechanical polish was applied using a suspension of colloidal silica, with a particle diameter of $\sim$ 40 nm, for 4 - 8 minutes (depending on material hardness) to remove the damage produced by the diamond stage. Polishing time was kept to a minimum to achieve the desired finish without causing excess relief.

The quality of the EBSD pattern was highly sensitive to the surface preparation, since the diffraction signal comes from a layer only a few nanometres thick. Therefore, the specimen surface is required to be free from damage and oxidation, and due to the a high tilt angle of 70°, the surface topology must be kept to a minimum. Thus, to gain the highest possible EBSD pattern quality, specimens required a further polishing stage applied after the final mechanical polish. Specimens were placed into a PECS II low-angle argon ion milling system (Gatan, Pleasanton CA, USA). The surface was exposed to 5 keV argon ions for 30 minutes, with the beam positioned at a grazing angle of 3° to remove the small damage layer produced by final mechanical polishing.

3.2.3 EBSD mapping of research materials

The grain structures of the EUROFER and 14WT based alloys, and their ODS counterparts were investigated. The grain structure and distribution was imaged using EBSD and carried out on the JOEL 6500F. For ease of comparison, all EBSD grain maps were produced in a 40 x 40 μm area, at 17.3 mm working distance using a 100 nm step size. For all EBSD maps, a grain is defined as being encircled by a grain boundary of misorientation angle $\geq 15°$. An EBSD grain map for 14YWT 950 could not be produced, since Kikuchi patterns of consistent enough quality could not be obtained. Instead, a FIB micrograph of the grain structure was produced using the in-lens secondary electron detector of the Zeiss Auriga.

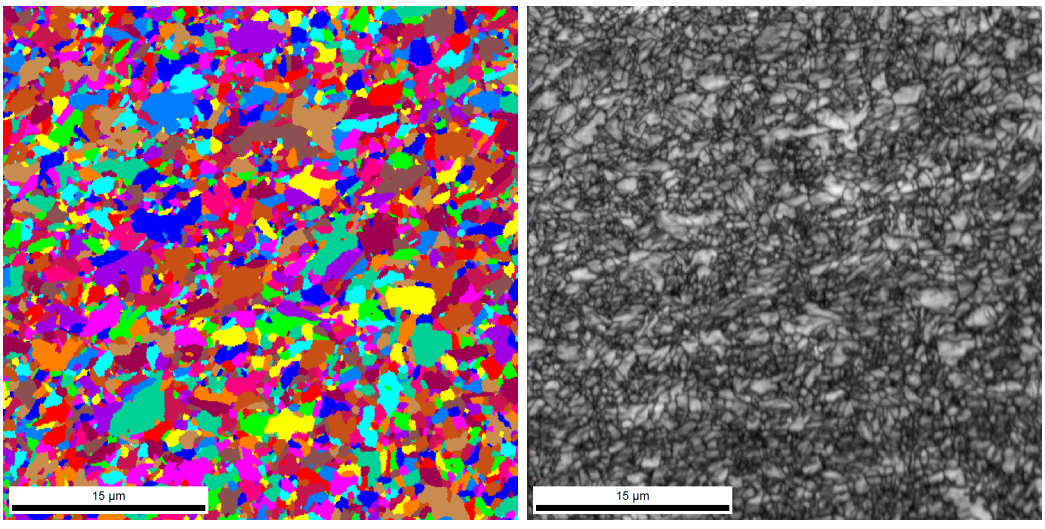
EUROFER



(a) (b)

Figure 3.5: EBSD images of EUROFER showing, (a) unique grain map, (b) image quality map. Map area of 1600 μm^2, with 0.1 μm step size.

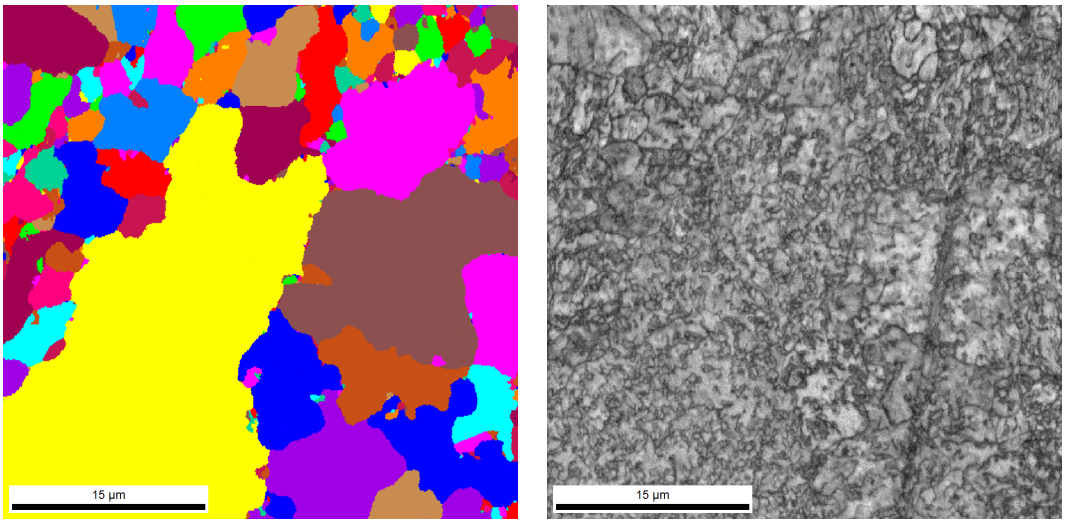
ODS EUROFER



(a) (b)

Figure 3.6: EBSD images of ODS EUROFER showing, (a) unique grain map, (b) image quality map. Map area of 1600 μm^2, with 0.1 μm step size.

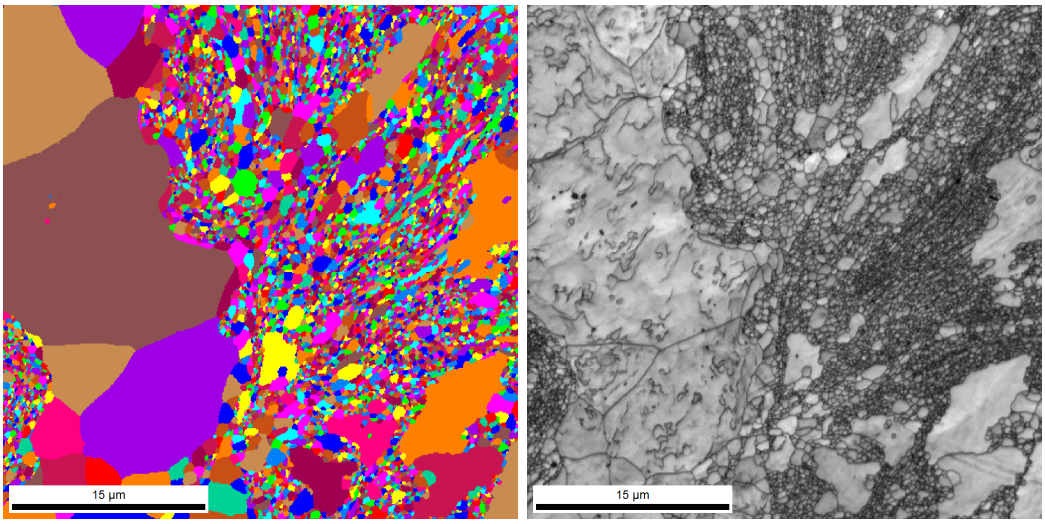
14WT 1150



(a) (b)

Figure 3.7: EBSD images of 14WT 1150 showing, (a) unique grain map, (b) image quality map. Map area of 1600 μm^2, with 0.1 μm step size.

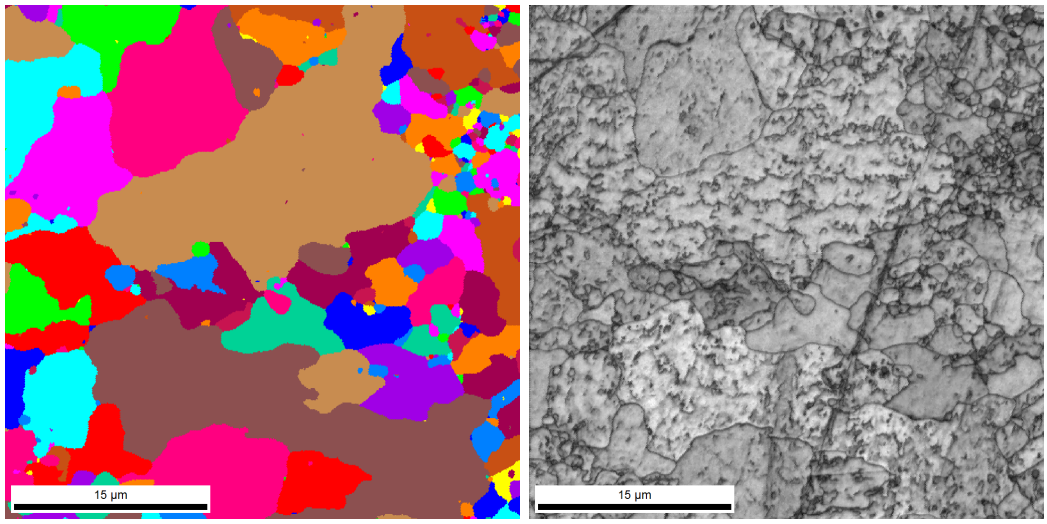
14YWT 1150



(a) (b)

Figure 3.8: EBSD images of 14YWT 1150 showing, (a) unique grain map, (b) image quality map. Map area of 1600 μm^2, with 0.1 μm step size.

14WT 950



(a) (b)

Figure 3.9: EBSD images of 14WT 950 showing, (a) unique grain map, (b) image quality map. Map area of 1600 μm^2, with 0.1 μm step size.

14YWT 950

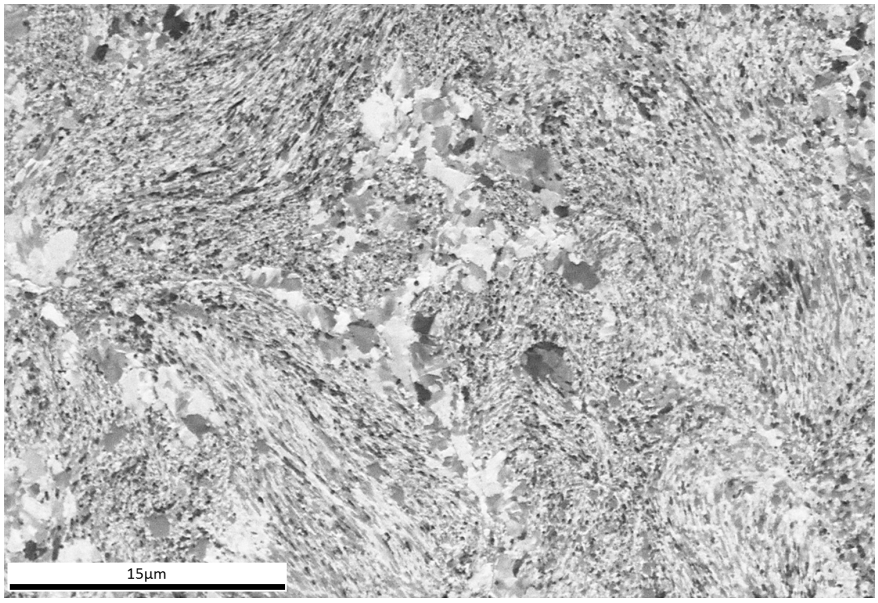


Figure 3.10: FIB micrograph of 14YWT 950 surface using the in-lens detector. Map area of approximately 1550 μm^2.

Figure 3.5 and 3.6 show a representative unique grain colour and image quality map for EUROFER and ODS EUROFER respectively. Figure 3.5(a) indicated that EUROFER has a wide distribution of grain sizes, with grain diameters between 0.6 μm and 7 μm. The modal grain diameter was 3.8 μm with a standard deviation of 1.0 μm. Comparatively, figure 3.6(a) indicated that ODS EUROFER had a more homogeneous distribution of grain sizes than EUROFER, with grain diameters between 0.3 μm and 3 μm. The modal grain diameter was 1.2 μm with a standard deviation of 0.4 μm.

Figure 3.7 and 3.8 show a representative unique grain colour and image quality map for 14WT 1150 and 14YWT 1150 respectively. Figure 3.7(a) indicated that 14WT 1150 had a distribution of grain diameters between 1 μm and 14 μm, with an modal grain diameter of 8.9 μm and a standard deviation of 3.2 μm. Although 14WT 1150 showed a heterogeneous grain morphology, comparatively 14YWT 1150 displayed a much more heterogeneous distribution of grain sizes. From figure 3.8(a), it can be seen that the grain size distribution may be separated into three groups (tri-modal). The smallest group had grain diameters < 2 μm and had an modal diameter of 0.5 μm with standard deviation of 0.4 μm. The middle sized group had grain diameters ranging from 3 μm to 8 μm, with an modal value of 5.4 μm and a standard deviation of 1.8 μm . The largest group had sizes > 8 μm, a much larger map is needed for an accurate modal grain diameter for this group.

Figure 3.9 shows a representative unique grain colour and image quality map for 14WT 950. Figure 3.9(a) indicated that 14WT 950 has a distribution of grain diameters between 1 μm and 11 μm, with an modal diameter of 6.2 μm and a standard deviation of 2.1 μm. Figure 3.9(a) also shows a reasonably heterogeneous bimodal distribution, large grains with diameters > 6 μm were interspersed with pockets of finer grained material. This is in contrast to the FIB micrograph of 14YWT 950, shown in figure 3.10, where the majority of the material in the micrograph appears highly fine grained but interspersed with pockets of slightly coarser grained material. The TEM micrograph

of the same material, performed by Burrows (2015) [208] and shown in figure 3.4(a), showed that the fine grained areas had grain sizes between 10 - 100 nm. Grain sizes in this size range were not possible to resolve using EBSD, since the interaction volume for backscattered electrons at 20 keV and 70° would incorporate multiple grains and grain boundaries [212].

Material	Grain size range /μm	Modal value /μm	Standard deviation /μm
EUROFER	0.6 - 7	3.8	1.0
ODS EUROFER	0.3 - 3	1.2	0.4
14WT 950	1 - 11	6.2	2.1
14WT 1150	1 - 14	6.7	1.6
14YWT 1150 (tri-modal)	< 2 3 - 8 > 8	0.5 5.4 -	0.4 1.8 -

Table 3.3: Summary of grain size distributions as determined by EBSD analysis for material array (excluding 14YWT 950).

3.2.4 Discussion of microstructure characterisation

A number of studies have reported heterogeneous bimodal microstructures in mechanically alloyed ODS steels [213, 214, 215]. However, EBSD of 14WT 950 (figure 3.9) suggests that heterogeneous microstructures may also be observed in non ODS steels. An explanation of this is summarised from Boulnat et al. (2014) [216] and Hilger et al. (2016) [217] as follows:

1. High energy attrition of the mechanically alloyed powder can cause a heterogeneous spatial distribution of stored energy, as well as local variations of solute composition. This heterogeneity of the initial microstructure stimulates the nucleation of recrystallised grains, giving rise to a fine-grained microstructure that

forms in expense to the initial deformed grains [218].

2. Once the stored energy is lowered, the dense dispersion of nano-sized oxide particles in ODS alloys provides a strong grain boundary pinning effect, which is particularly efficient in ultrafine grains.

The first point explains why a heterogeneous microstructure was observed for each in-house produced alloy, regardless of oxide content (apart from ODS EUROFER). Although ODS EUROFER was mechanically alloyed, it displayed a uni-modal microstructure. This suggests that either the mechanically alloying process performed by Plansee Ltd produced a cleaner more homogeneous powder, or the post-processing treatments (which the in-house produced alloys were not subjected to) helped to removed any microstructural heterogeneity. The second point provides an explanation to the resistance of the fine grained areas of 14YWT 950 and 1150 to coarsening during consolidation, in comparison to their non ODS counterparts.

Unlike the in-house material, EUROFER did not display pockets of fine grains; this was most likely due to being melt processed instead of mechanically alloyed. However, there was a grain morphology difference between regions of the EBSD micrograph. Certain grains showed a lath-like structure, normally associated with martensite, others showed a more equiaxed structure, normally associated with ferrite. However, the lath-like grains are unlikely to be martensite, since martensitic laths tend to be much finer, and the EUROFER used in this project is shown to have a yield stress much smaller than that expected for a ferritic/martensitic steel (section 3.3.3). The EUROFER was likely to have been duel-phase (austenitic and ferritic) during normalisation at 980 $^{\circ}C$, but tempered at a temperature too high (760$^{\circ}C$) to retain a martensitic structure, leading to growth of the laths.

3.2.5 Summary of EBSD characterisation

A heterogeneous grain size distribution was seen in all mechanically alloyed steels except ODS EUROFER, most likely due to its post processing heat treatments. The addition of nanoscale oxides stabilised the fine recrystallised grains produced during consolidation. This resulted in an accentuated heterogeneous microstructure in the ODS alloys compared to their non ODS counterparts, so much so that 14YWT 1150 showed a very pronounced size difference between the smallest and largest grains. From the FIB micrograph in figure 3.10, it was clear that a large area fraction of the imaged 14YWT 950 surface showed a highly refined grain structure which was not possible to resolve using EBSD. The TEM micrograph of the same material, performed by Burrows (2015) [208], showed the grain size of the fine grained area was between 10 - 100 nm. It was argued that EUROFER was completely ferritic but retained the morphology of a martensitic lath-like structure in certain grains.

3.3 Determination of macroscale mechanical properties

The work reported in this section uses a four point flexural test to measure macromechanical properties of the research materials described in section 3.1. Digital image correlation (DIC) was used to measure strain directly from the bend specimens. Stress was calculated from simple beam theory, using load data recorded from a load cell attached to the load-frame cross-head. The macromechanical properties were characterised by the elastic modulus and yield stress, derived from the stress-strain data for each specimen. These results were then used as bulk comparisons for micromechanical bend tests in later sections (3.4.5) and (5.4.3).

3.3.1 Strain measurements using digital image correlation

Since its initial conception and development in the early 1980's by a research group at the University of South Carolina [219, 220, 221], DIC has become a widely accepted

and commonly used tool for measuring surface deformation in the field of experimental solid mechanics. Full field displacements and strains may be directly obtained by comparing an image of the specimen surface in the reference (undeformed) state with images recorded in current (deformed) state.

This project uses a single fixed camera to record planar images of the flexural specimen side profile prior to and during deformation to create a 2D displacement map. The 2D DIC method is comprised of three consecutive steps: (1) specimen and experimental preparation, (2) recording of images and (3) processing the acquired images using dedicated software to obtain desired displacement and strain information. This section briefly describes the procedure used at each of these steps.

Experimental set-up for four point flexural test

The four-point flexure tests were performed in custom-built molybdenum windowed bend jig and loaded using an Instron 3366 testing rig. Images of the specimen surface in the reference and current state were recorded with a Qimaging Retiga 4000R digital camera using a Questar QM-100 long distance microscope lens system. The lens was capable of producing a 2 mm x 2 mm field of view with 2048 x 2048 pixels at $\backsim$ 200 mm working distance. Due to the combination of high magnification and long working distance, a high level of illumination was needed. This was provided by an in-lens illumination system and an additional ringed illumination system attached to the front of the lens. The experimental set-up is shown in figure 3.11.

To perform four-point flexure tests, matchstick specimens with dimensions of approximately 1 mm x 1 mm x 12 mm were prepared by sectioning with a cubic boron nitride blade on an Isomet 4000 saw. The matchsticks were then mechanically polished to a 0.25 μm diamond finish on all four 1 mm x 12 mm faces.

Figure 3.11: The experimental set-up for four point flexural tests with DIC measured strain. Shown is the custom-built windowed bend jig and the optical system used for image capture.



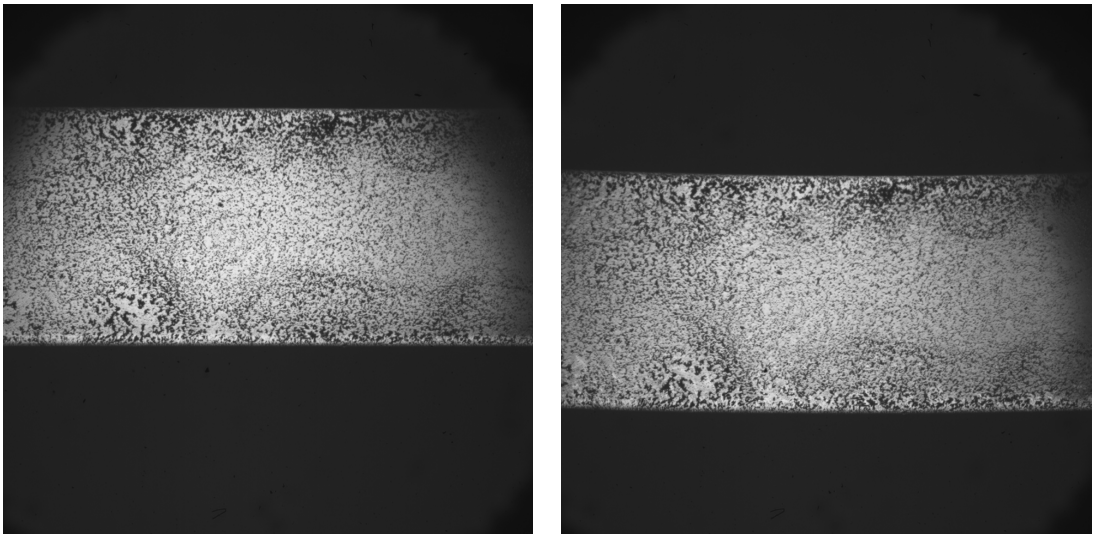
Figure 3.12: Custom-built molybdenum windowed bend jig with a deformed matchstick sample loaded into place.

The molybdenum four-point bend jig, shown in figure 3.12, was custom designed and fabricated in-house, machined with a window to allow full viewing of the specimen under load. The matchstick specimens sit on the two lower molybdenum rollers, separated by 10 mm, and are deformed by loading the two upper rollers, separated by 5 mm, to form a four point bend (illustrated in figure 3.12). Upon initial loading, a systematic amount of 'settling in' was anticipated, due to components being forced into contact with each other. This settling-in period, together with system compliance that occurred throughout the test, was manifested as rigid body movement during DIC. This rigid body movement is accounted for in DIC as strain was taken directly from the specimen surface.

Surface speckle preparation

DIC requires that the specimen surface have a random grey intensity distribution, i.e. speckle pattern, which deforms together with the specimen surface, acting as a carrier of deformation information [222]. This pattern can be either the natural texture of the surface or introduced artificially, usually performed by spraying black paint through a nebuliser. However, due to the small scale of the flexure tests in this project, paint gave an inadequately large spatial distribution of speckle. Instead, a speckle pattern was produced using graphite powder.

Finely divided graphite powder was obtained from Graphit '33' dry lubricant spray (CRC industries, Horsham, PA, USA). One short spray (0.5s burst) was applied to a 1:3 mixture of ethanol and acetone (approx 40 - 50 ml total volume) and atomised in an ultrasonic bath for 1 minute. Immediately after, the polished matchstick specimens were briefly immersed in the atomised mixture and air dried in a horizontal position (surface of interest facing up), ensuring an even evaporation of the volatile mixture. After the drying, a fine dispersion of graphite remained, forming a speckle pattern, demonstrated in figure 3.13.

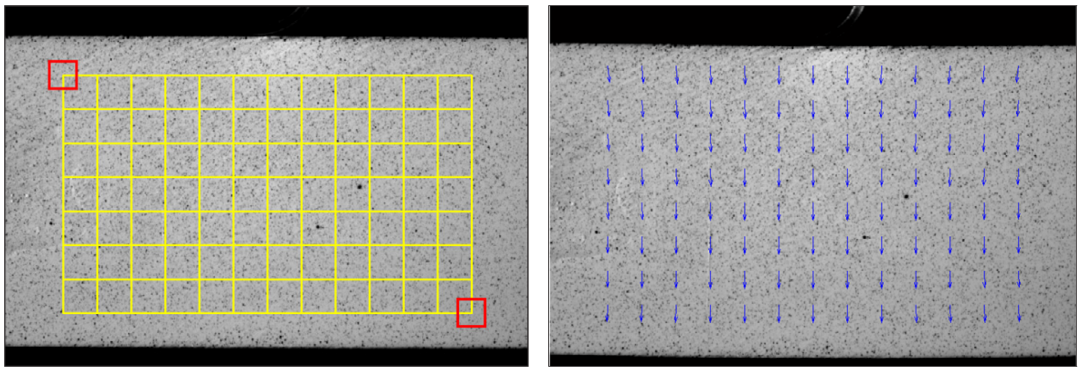


(a) (b)

Figure 3.13: Raw image of 14WT 950 bend test specimen prepared with graphite speckles for digital image correlation. (a) Reference state. (b) During deformation. Specimen depth was 1.11 mm.

DIC and strain measurement

After recording digital images of the specimen surface before and during loading, DaVis 7.2 DIC software package produced by LaVision GmbH was used to extract deformation information from the image set. A full description of the DIC method is beyond the scope of this thesis: for a more detailed explanation see Pan et al. (2009) [222] and Sutton et al. (2009) [223]. However, in order to give a general understanding of how strain data was obtained from flexural tests, the following will provide a brief overview of the basic principle of DIC.



(a) (b)

Figure 3.14: (a) Reference image with two imposed square subsets, shown in red, used for tracking the motion of its centre point. The intersection points of the yellow grid demonstrates the position of subset centre points within the region of interest. (b) Displacement vectors calculated at the subset centre points in the deformed (current) image. Figure from Pan et al. (2009) [222].

The primary aim of DIC is to calculate displacement and strain fields for a material undergoing deformation. First, it was necessary to define a region of interest by applying a mask in the reference image, which was then further divided into evenly spaced sub-sections, known as subsets. Displacement of the subset is computed by tracking pixels within a given reference subset to corresponding pixels in a current (deformed) image. The reason why a defined group of pixels (subset) is preferred over an individual pixel for tracking displacement between images, is that a subset of pixels contains a much larger spatial variation of intensity, helping to distinguish itself from other subsets [223].

To evaluate the degree of similarity between intensity signals of the reference subset and deformed subset, either a cross-correlation or sum-squared difference criterion may be used; this project uses the former. Cross-correlation is most often carried out in the Fourier domain, since the fast Fourier transform (FFT) may be implemented with high computational speed. The reference and deformed subset are matched by finding the position of the peak in the correlation coefficient distribution, allowing the position of the deformed subset to be determined. The change in position of the deformed subset with respect to the reference subset allows the displacement vector to be calculated,

and is evaluated at the subset centre, shown in figure 3.14(b) [222].

It is expected that the shape of the subset will change between the reference image and the deformed image. This is accounted for using a shape function, which maps the displacement evaluated at the subset centre to points throughout the subset using the assumption of deformation continuity [222]. However, such a shape function may describe points between pixels, i.e. sub-pixel locations. Therefore, before evaluating a correlation criterion, sub-pixel intensities must be provided using a sub-pixel interpolation scheme. DaVis 7.2 uses a B-spline algorithm to fit a high order polynomial to interpolate between pixel intensities.

After obtaining full-field displacements to sub-pixel resolution, full-field strains may be calculated. Strains are more difficult to resolve than the displacement fields since their calculation requires numerical differentiation, which is sensitive to noise. This means that any noise in the displacement field will be amplified in the strain field, thus averaging is required to smooth the data. The noise present in the strain field is graphically represented in the initial DIC image, shown in figure 3.16. In this case, the error in strain is approximately ± 0.0023 % (which was representative of all samples tested). The noise in displacement field, thus strain field, is primarily caused by pixel intensity variations produced by CCD detector noise. The main contributions to CCD noise is 'shot noise' and thermally generated noise [224]. In this project, strain is smoothed by averaging strain across a linear strain gauge for each frame.

For a given distance from the centre of the neutral axis (isosurface of zero stress and strain), the stress and strain between the inner supports is uniform along the length of the beam and varies linearly from top to bottom of beam. For this work, the maximum tensile and compressive values are found at the lower and upper surfaces respectively. The neutral axis may be observed in the deformed image in figure 3.16 as a band of white, i.e. zero strain, separating two regions of tensile and compressive strain represented by a chromatic scale of red and blue respectively. Engineering strain was measured along

a virtual horizontal linear strain gauge, extracting the tensile strain from the full-field strain previously calculated. The virtual strain gauge was positioned as close as possible to the lower surface, i.e. surface of maximum strain, so as to be compared to maximum stress using simple beam theory.

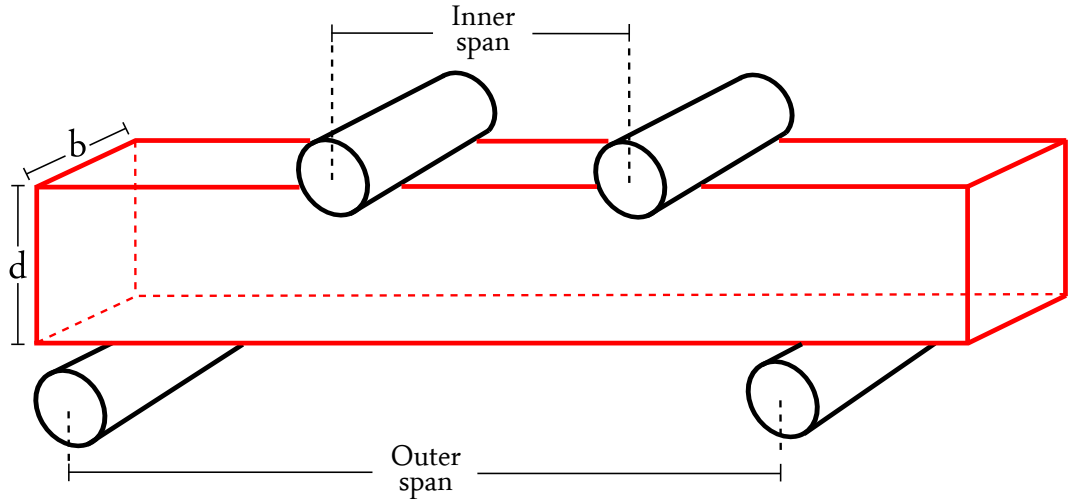


Figure 3.15: A schematic diagram of the four point flexure test arrangement.

For a four point flexure of a rectangular prismatic beam with a separation of the inner support (5 mm) half of the separation of outer supports (10 mm), the maximum stress, σ_{max}, is given by [225],

$$\sigma_{max} = \frac{3Pl_1}{bd^2} \tag{3.1}$$

Where P is the applied load, l_1 is the distance between the inner and outer supports, b and d are the beam width and depth respectively, as shown in the schematic diagram in figure 3.15. Using simple beam theory to provide maximum stress has several limitations. Most importantly, simple beam theory is only valid for Hookean behaviour, i.e. elastic deformation. In the analysis in section 3.3.3, the stress data calculated from simple beam theory was used to provide the Young's modulus and the stress at which the deformation becomes non-Hookean (yield stress); flow stress calculated from simple

beam theory is ignored (although shown on stress-strain graphs). Other limitations arise from the assumptions made to simplify the equations. Namely, that the material is homogeneous and isotropic (on the macroscale); the Young's modulus is constant in compression and tension; bending is only in one plane; the radius of curvature is large in comparison to cross-sectional dimensions, and each layer of the beam is free to expand or contract [226].

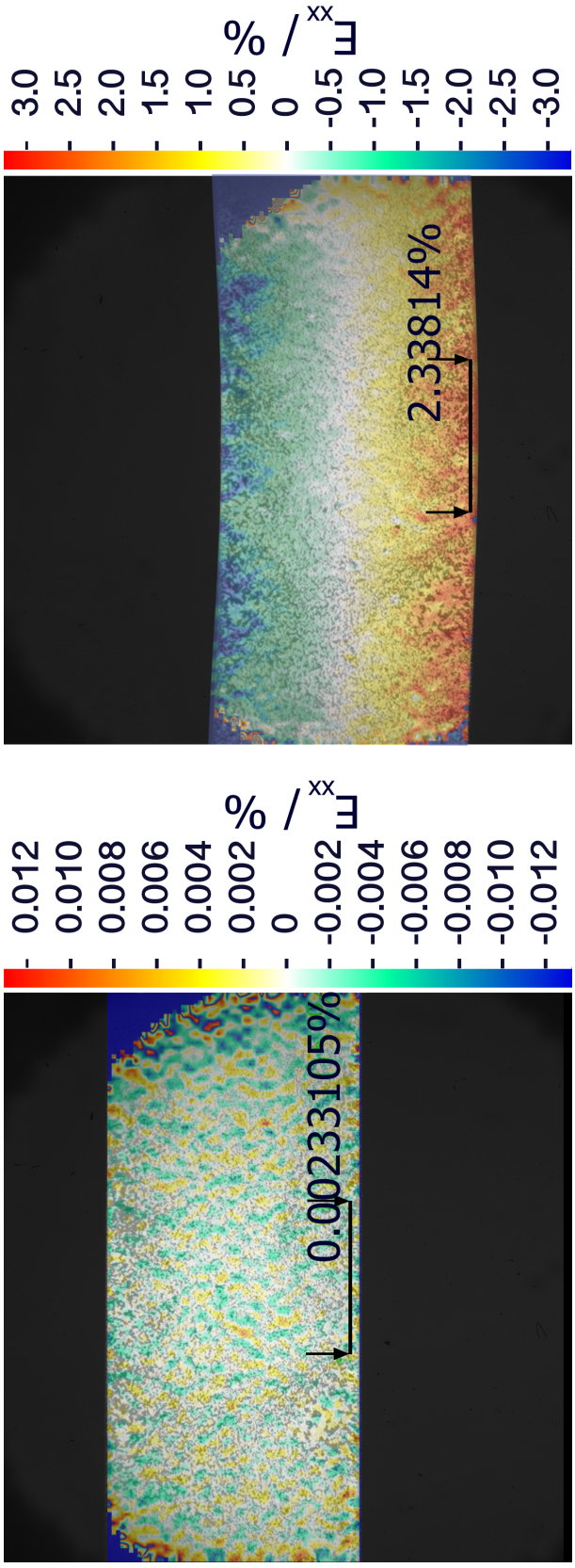
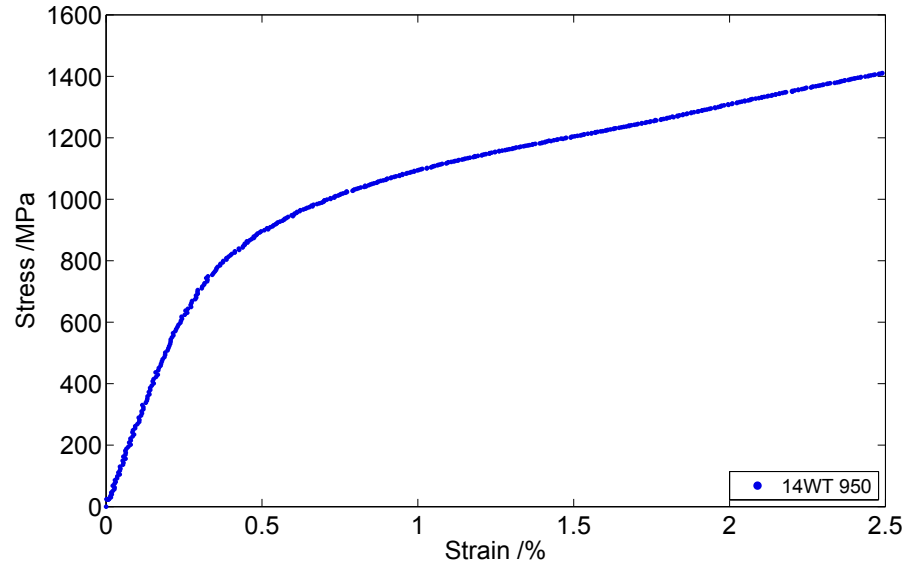


Figure 3.16: Pictured is a 14WT 950 four-point flexure specimen. On the left is the first image after the reference image, and on the right is a representative image during deformation. The virtual horizontal linear strain gauge is placed along the bottom of the specimen, where an E_{xx} strain map is also shown (x direction is along the beam axis). The strain map clearly shows the neutral axis as region of white, indicating zero strain, separating two regions of tensile and compressive strain represented by a chromatic scale of red and blue respectively. The strain map produced independently by the software has been imposed on the corresponding deformed image.

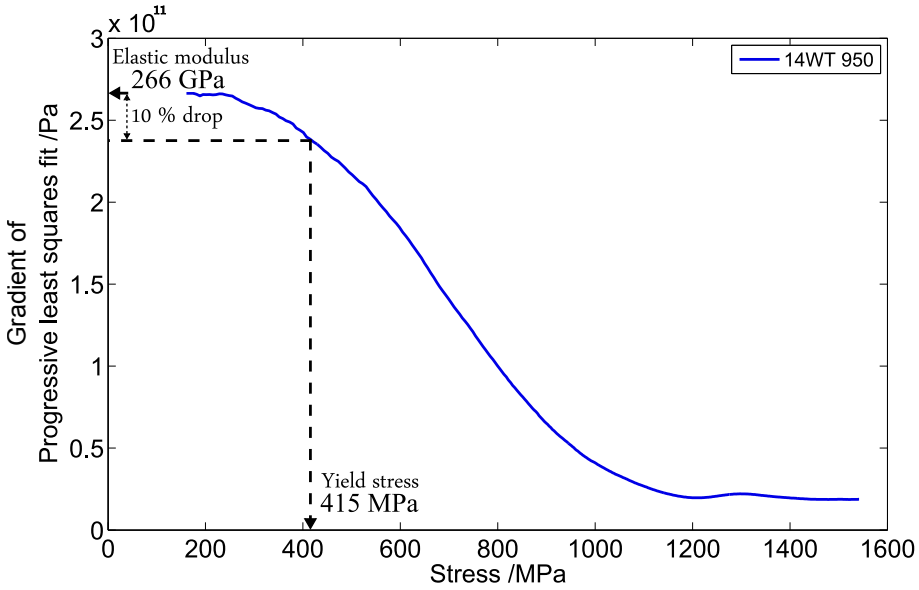
3.3.2 Determining elastic modulus and yield stress from stress-strain curves

To determine the elastic modulus and yield stress of the materials tested in four-point flexure, a progressive linear least squares fit was employed. The linear regression was found for a data set of a constant size, which was then progressively moved through the stress-strain data at single data point increments. At each iteration, the gradient of the linear regression was recorded, along with the corresponding stress and strain value (taken at the mid-point of the fit). The data set size for the linear least squares regression was chosen to be small enough to be clearly within the elastic region for the first iteration, but large enough to smooth the data.

The yield stress was defined by a 10 % drop in the fitted gradient. Yield stress was found to be independent of the size of the data set chosen (within the maximum and minimum defined). Elastic modulus was defined as the gradient of the least squares regression at the initial iteration. Figure 3.17 demonstrates the determination of elastic modulus and yield stress for the 14WT 950 four-point flexure specimen, shown in figure 3.13 and 3.16, by plotting the gradient of the progressive least squares regression with the corresponding stress data.



(a)



(b)

Figure 3.17: (a) Stress-strain data for a 14WT 950 four-point flexure specimen. (b) Gradient of progressive least squares fit against corresponding stress data, demonstrating the determination of elastic modulus and yield stress.

3.3.3 Four-point flexural test results

EUROFER and ODS EUROFER

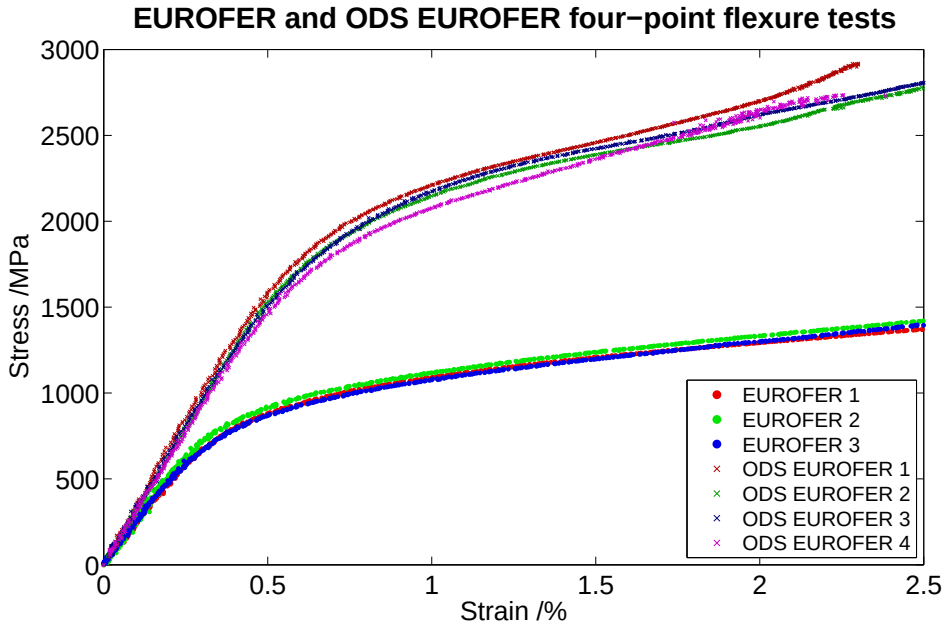


Figure 3.18: Stress-strain data for the four-point flexure of EUROFER and ODS EUROFER, showing three and four repeats respectively. Stress was calculated using simple beam theory, and strain measured using DIC.

Flexure test	Elastic modulus /GPa	Yield stress /MPa
EUROFER 1	244 ± 3	$425\ ^{+17}_{-22}$
EUROFER 2	262 ± 5	$444\ ^{+23}_{-18}$
EUROFER 3	250 ± 3	$393\ ^{+15}_{-10}$
ODS EUROFER 1	340 ± 5	$1062\ ^{+49}_{-80}$
ODS EUROFER 2	305 ± 4	$1306\ ^{+19}_{-19}$
ODS EUROFER 3	315 ± 5	$1119\ ^{+30}_{-51}$
ODS EUROFER 4	302 ± 4	$1174\ ^{+26}_{-34}$

Table 3.4: Elastic modulus and yield stress for four-point flexure test of EUROFER and ODS EUROFER. Elastic modulus and yield stress measured using the method described in section 3.3.2.

14WT 950 and 14YWT 1150

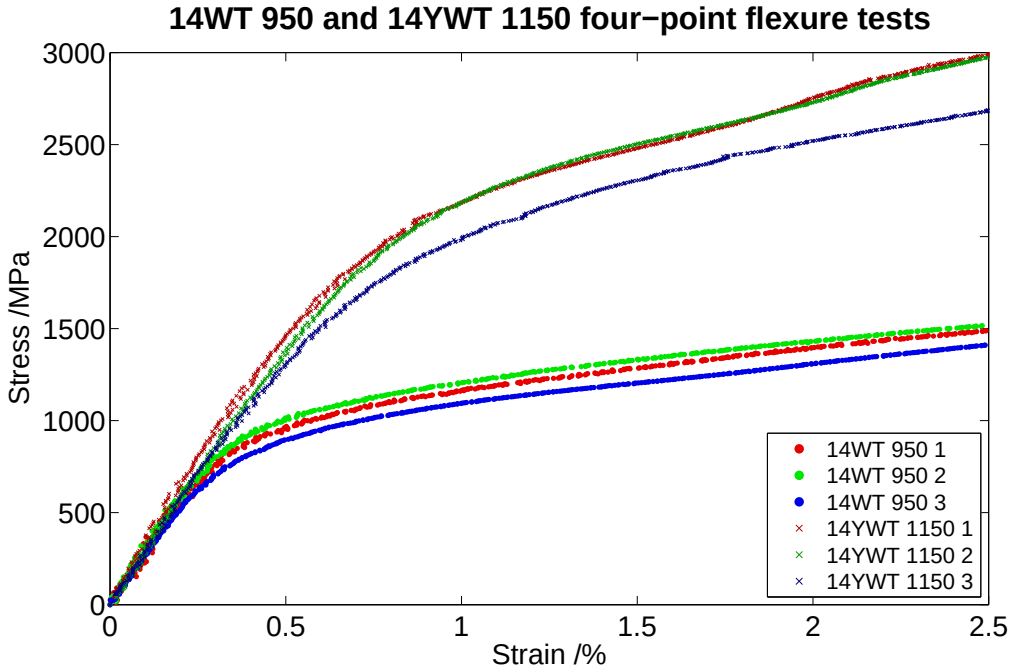


Figure 3.19: Stress-strain data for the four-point flexure of 14WT 950 and 14YWT 1150, showing three repeats each. Stress was calculated using simple beam theory, and strain measured using DIC.

Flexure test	Elastic modulus /GPa	Yield stress /MPa
14WT 950 1	282 ± 8	$434\ ^{+38}_{-44}$
14WT 950 2	294 ± 6	$416\ ^{+60}_{-37}$
14WT 950 3	266 ± 3	$415\ ^{+7}_{-14}$
14YWT 1150 1	321 ± 8	$810\ ^{+61}_{-36}$
14YWT 1150 2	297 ± 5	$878\ ^{+86}_{-70}$
14YWT 1150 3	280 ± 5	$839\ ^{+42}_{-34}$

Table 3.5: Elastic modulus and yield stress for four-point flexure test of 14WT 950 and 14YWT 1150. Elastic modulus and yield stress measured using the method described in section 3.3.2.

14YWT 950

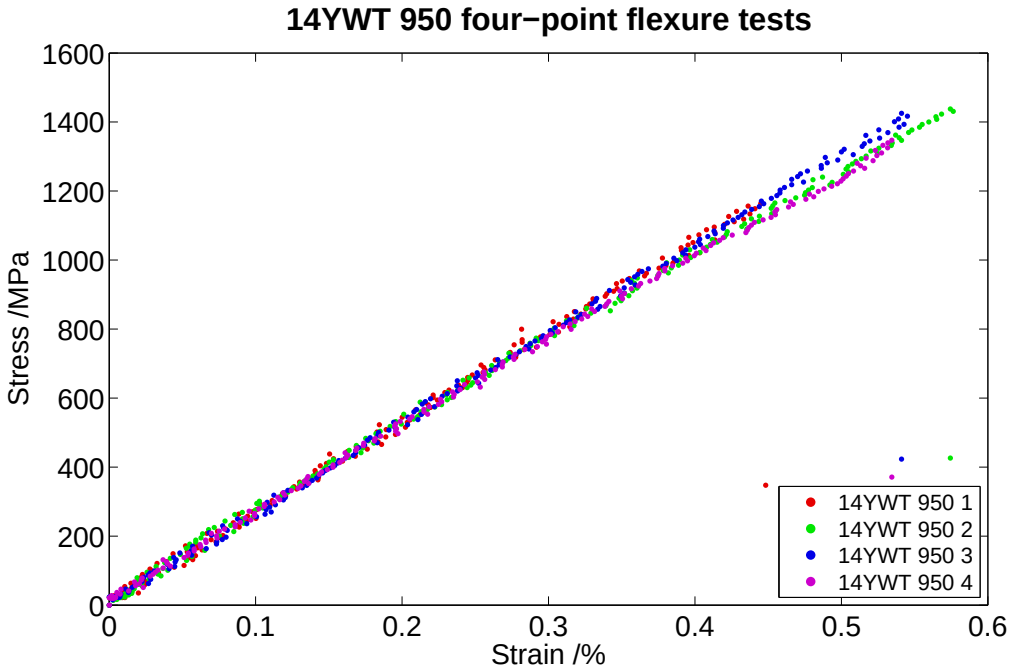


Figure 3.20: Stress-strain data for the four-point flexure of 14YWT 950, showing four repeats. Stress was calculated using simple beam theory, and strain measured using DIC.

Flexure test	Elastic modulus /GPa	Fracture stress /MPa
14YWT 950 1	252 ± 4	1164
14YWT 950 2	264 ± 5	1438
14YWT 950 3	255 ± 3	1425
14YWT 950 3	253 ± 2	1347

Table 3.6: Elastic modulus and fracture stress for four-point flexure test of 14YWT 950. Elastic modulus measured using the method described in section 3.3.2, fracture stress measured as the last recorded stress before fracture.

Summary of four-point flexural test results

Material	Average elastic modulus /GPa	Average yield stress /MPa	Average specimen depth /mm
EUROFER	252 ± 4	421 $^{+18}_{-17}$	1.28
ODS EUROFER	316 ± 5	1165 $^{+31}_{-46}$	0.68
14WT 950	281 ± 6	421 $^{+35}_{-32}$	1.10
14YWT 950	255 ± 4	1344 (Fracture stress)	1.14
14YWT 1150	299 ± 6	842 $^{+63}_{-47}$	0.71

Table 3.7: Average elastic modulus and yield stress for four-point flexure test of material array.

3.3.4 Discussion of four-point flexural test results

Figures 3.18, 3.19 and 3.20 show the four point flexural test stress-strain data for the material array described in section 3.1. 14WT 1150 could not be tested since the material geometry and quantity did not allow flexural test specimens to be fabricated, instead figure 3.19 plots the 14WT 950 data with 14YWT 1150. The error bounds of the elastic modulus were given by the standard error of the linear least squares regression within a 95 % confidence interval, the subsequent error in yield stress was found from propagating the standard error in elastic modulus.

The mechanical response to four-point flexure was very similar for both EUROFER and 14WT 950, with an average elastic modulus of 252 ± 4 GPa and 281 ± 6 GPa respectively, and an average yield stress of 421 $^{+18}_{-17}$ MPa and 421 $^{+35}_{-32}$ MPa respectively. Comparatively, ODS EUROFER and 14YWT 1150 had an average elastic modulus of 316 ± 5 GPa and 299 ± 6 GPa respectively, and an average yield stress of 1165 $^{+31}_{-46}$ MPa and 842 $^{+63}_{-47}$ MPa respectively. Although the yield stress of ODS EUROFER was measured to be significantly higher than that of 14YWT 1150, the stress-strain profile

of the two ODS steels were very similar, with very little plastic strain occurring between the yield stress and 1500 MPa in both materials.

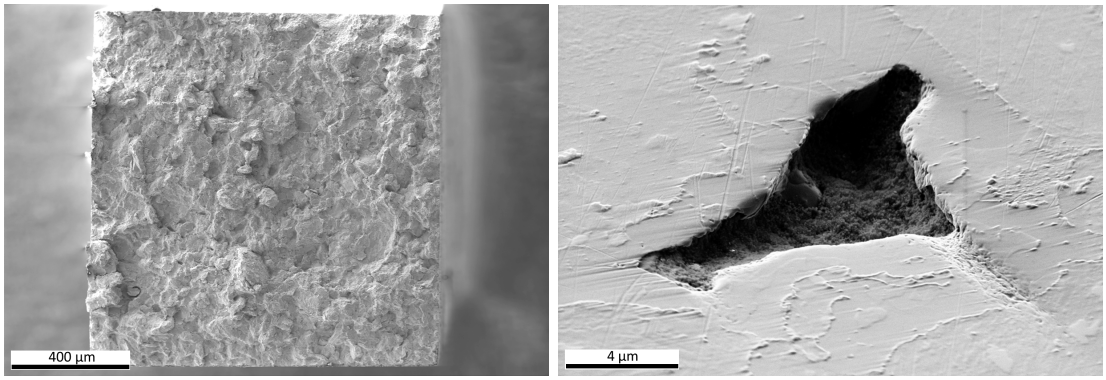
Literature values for the yield stress for EUROFER are between 500 - 600 MPa [227, 228, 138, 229, 204] and 950 - 1150 MPa for ODS EUROFER [138, 227, 230, 231]. The flexure results in this project gave an average yield stress for EUROFER that was approximately 80 MPa below the lower range of literature values, and an average yield stress for ODS EUROFER that was 15 MPa above the upper range of literature values. At the time of writing, no literature containing yield stress values determined by four-point flexure tests for these materials has been published. Instead, the literature values for yield stress were determined by tensile tests.

Due to test geometry, tensile tests give a more defined yield stress, whereas for flexure tests the onset of plastic deformation is more gradual and more difficult to determine. A different stress-strain profile and the subsequent definition of yield stress as a 10 % drop in tangential modulus could be the source of the discrepancy between yield stress calculated in this project, compared to those from tensile tests in literature.

Elastic moduli recorded in this project were found to be between 252 GPa and 316 GPa; this was higher than the expected value of 190 - 220 GPa for an iron-chromium based alloy [232]. The most likely reason for this discrepancy was a lack of spatial resolution from the lens; high resolution was needed to record small changes in strain during elastic deformation. This was further supported by a correlation between specimen depth and elastic modulus; the measured elastic modulus increased with deceasing specimen depth (shown in table 3.7). However, the lens used is currently the best commercially available. The only way to increase the resolution in strain would be to increase the specimen size, which was limited by the quantity of material available. The lack of spacial resolution in stain did not effect the yield stress measured, since the simple beam stress, given by equation 3.1, was only dependent on load.

In all tests, specimens of 14YWT 950 alloy failed to yield; instead they each under-

went brittle fracture at an average fracture stress of 1344 MPa. Figure 3.21(a) shows an example of a brittle fracture surface for a 14YWT 950 flexure specimen. Closer inspection of the polished surface showed widely spaced ($\sim$ 200 μm apart) voids where the powder had poorly consolidated. Each were approximately 4 μm - 16 μm wide. An example void is shown in figure 3.21(b). The maximum stress in a four-point flexure test occurs on the outer surfaces between the inner rollers (5 mm apart), this region would have contained many of these voids, giving rise to numerous areas of possible crack nucleation.



(a) (b)

Figure 3.21: 14YWT 950 four-point flexure specimen. (a) SEM micrograph of flexure test fracture surface. (b) SEM micrograph of polished surface, showing poorly consolidated material.

3.3.5 Summary of macroscale mechanical behaviour

Four-point flexure tests were carried out for the material array, with the exclusion of 14WT 1150, as the material geometry and quantity did not allow specimen manufacture.

- EUROFER had an average elastic modulus and yield stress of 252 ± 4 GPa and 421 $^{+18}_{-17}$ MPa respectively.
- 14WT 950 had an average elastic modulus and yield stress of 281 ± 6 GPa and 421 $^{+35}_{-32}$ MPa respectively.
- ODS EUROFER had an average elastic modulus and yield stress of 316 ± 5 GPa and 1165 $^{+31}_{-46}$ MPa respectively.
- 14YWT 1150 had an average elastic modulus and yield stress of 299 ± 6 GPa and 842 $^{+63}_{-47}$ MPa respectively. Although, the stress-strain profile of ODS EUROFER and 14YWT 1150 were very similar.
- 14YWT 950 was subject to brittle fracture for every test, with an average fracture stress of 1344 MPa. This was determined to be due to the presence of voids caused by poorly consolidated material, giving rise to many possible sites of crack nucleation.

The elastic moduli were higher than the values expected from literature. It was determined that a lack to spatial resolution caused discrepancy in elastic modulus. This was supported by a negative correlation between specimen size and and elastic modulus. This didn't effect measurement of yield, since stress was only dependent on load.

3.4 Characterisation of the microcantilever size effect in ODS steels

As discussed on page 78, Girault et al. (2010) [194] determined that the presence of nanoscale oxides in the nickel superalloy, MA6000, caused the operative mechanisms governing size effects in micropillars to be dominated by dislocation-oxide hardening mechanisms. The work reported in this section aimed to determine the significance of the microcantilever size effect in ODS steels, and to characterise the dependency of yield stress on specimen size for use in later work regarding irradiation hardening in the in-house produced alloys (chapter 5).

A focused ion beam (FIB) microscope was used to mill microcantilever specimens in the material surface. These specimens were then imaged and measured using an SEM and tested by loading in a G200 nanoindenter (Agilent technologies, Santa Clara, CA, USA). The following subsections provides a brief description of the method used at each stage in the process. A specific explanation of microcantilever fabrication in an irradiated layer will be provided in chapter 5, section 5.4.

3.4.1 Focused ion beam (FIB)

The FIB microscopes used for the milling of microcantilevers in this project were a dual beam Zeiss Auriga FIB/SEM and an FEI FIB200-TEM single beam system (Hillsboro, OR, USA). The setup of a FIB system resembles that of an SEM. However, while an SEM uses a focused beam of electrons to image a surface, a FIB uses a focused beam of heavy ions that can be rastered across the surface. Both microscopes used a gallium ion source operated at 30 kV with an emission current of approximately 2 μA. The beam current was then reduced through a selected aperture, which allowed a maximum operating current of 20 nA and a minimum of 1 pA. The resolution of the of the two systems at the smallest beam current were 2.5 nm (Auriga) and 7 nm (FIB200).

As the primary beam reaches the sample, a small amount of material is sputtered, which exits the surface as either secondary ions or neutral atoms. As the beam rasters

across the surface, the signal from the sputtered material, usually secondary electrons, is collected to form an image. At low beam currents, the spot size is small and very little material is sputtered. As the beam current is increased, larger amounts of material may be removed by sputtering, allowing the precision milling of test geometries down to the sub-micron scale. A 30 kV gallium beam in iron, leads to an interaction volume $\sim$ 20 nm deep [233].

3.4.2 Microcantilever manufacture

Microcantilevers were FIB milled using methods developed by Di Maio and Roberts (2005) [146] and Armstrong et al. (2009) [147], described on page 69. Calculation of the material properties from the microcantilever mechanical response, either by simple beam equations or finite element analysis, required the assumption of perfectly sharp edges and corners. Due to the Gaussian beam profile, FIB fabrication of microcantilevers will produce filleted corners and rounded edges. Errors were minimised by using low beam currents during the final milling stage. The geometry of the microcantilever specimens was measured using SEM imaging in the Zeiss Auriga.

3.4.3 Microcantilever testing

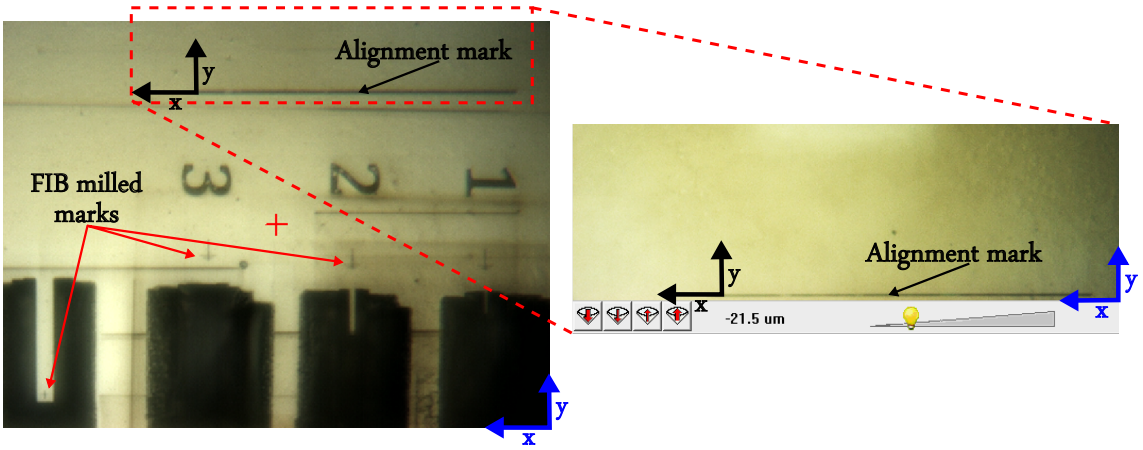
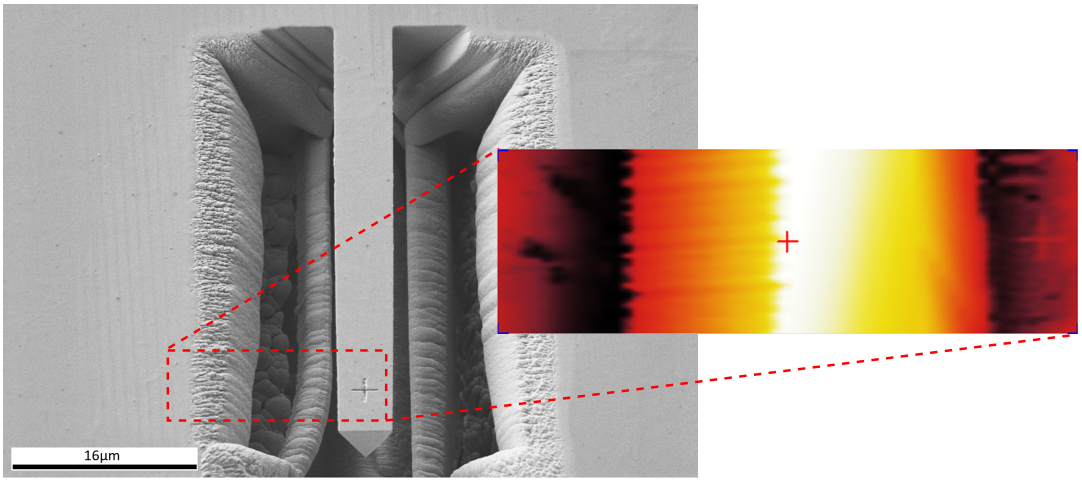


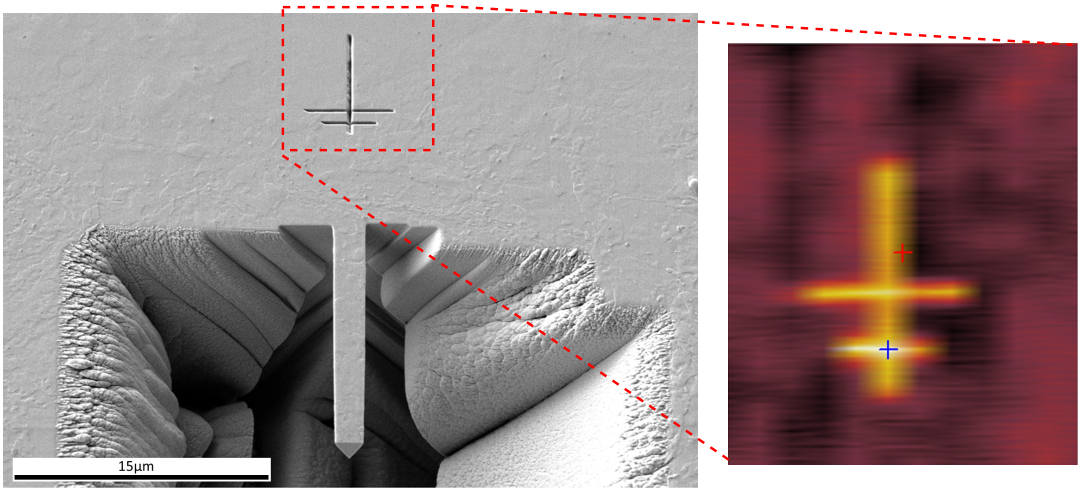
Figure 3.22: Alignment of material axis with nanoindenter axis using the G200's in-built optical microscope with 40x objective. The alignment mark was 80 μm long.

The G200 nanoindenter is fitted with two indentation heads, XP and DCM, and an optical objective, which can be selected to be either 10x or 40x. For microcantilever deflection, the DCM indentation head was used. The DCM head allowed a greater resolution in displacement and load, with maximum resolutions of 0.2 pm and 2 nN respectively [234]. Before testing, the microcantilever beams were aligned with the indenter y-axis, using an alignment mark that was pre-milled in the FIB. The specimen was manually rotated until the alignment mark was aligned with the indenter x-axis, as demonstrated in figure 3.22. The mark was then scanned by utilising the in-built NanoVision scanning facility to confirm alignment; using a piezoelectric stage, the tip was rastered across the surface to build up a topographic map, which was displayed in a pseudo-colour plot. In turn, each microcantilever specimen was then located with respect to the nanoindenter position using the scanning facility and displaced.

To ensure that the smaller, more delicate test specimens were not damaged during scanning, each beam was located by scanning a FIB milled mark made at a known distance from the microcantilever. The tip was then offset from the mark in the y-axis to the required position on the beam. For larger beams, it was necessary to place the mark on the beam itself, due to a 20 μm offset limit imposed by the software which could not be altered. The tip was first engaged on the bulk material, close to the FIB milled mark, and a small scan load of 0.5 μN was applied. The low scan load ensured that any beam displacement during scanning was well within the elastic region. Two examples of a scanned mark for a large and a small microcantilever is given in figure 3.23(a) and (b) respectively, shown alongside is the corresponding SEM micrographs with the scan placements highlighted in red.



(a)



(b)

Figure 3.23: SEM micrographs of microcantilevers with corresponding nanoindenter surface scans of FIB milled marks. (a) Microcantilever beam in 14YWT 1150 with a depth of 4.83 μm. (b) Microcantilever beam in 14YWT 1150 with a depth of 1.85 μm.

All beams were tested using a displacement controlled method with a displacement rate that varied with beam depth, to ensure a constant strain rate between differing beam sizes. A beam with depth and length of 1 μm and 6 μm respectively was displaced at a rate of 4 nms^{-1}, giving rise to a maximum (simple beam) strain rate of $\sim$ 0.02 %s^{-1}. Load-displacement data was recorded during both loading and unloading stages. Before beam testing, the system was allowed to thermally stabilise to reduce thermal drift; drift was kept between 0 and 0.05 nms^{-1}

3.4.4 Microcantilever analysis

The microcantilever beams reported in this thesis were analysed using simple beam theory and finite element modelling. In each case, the load-displacement data recorded during testing was used to extract elastic modulus and yield stress.

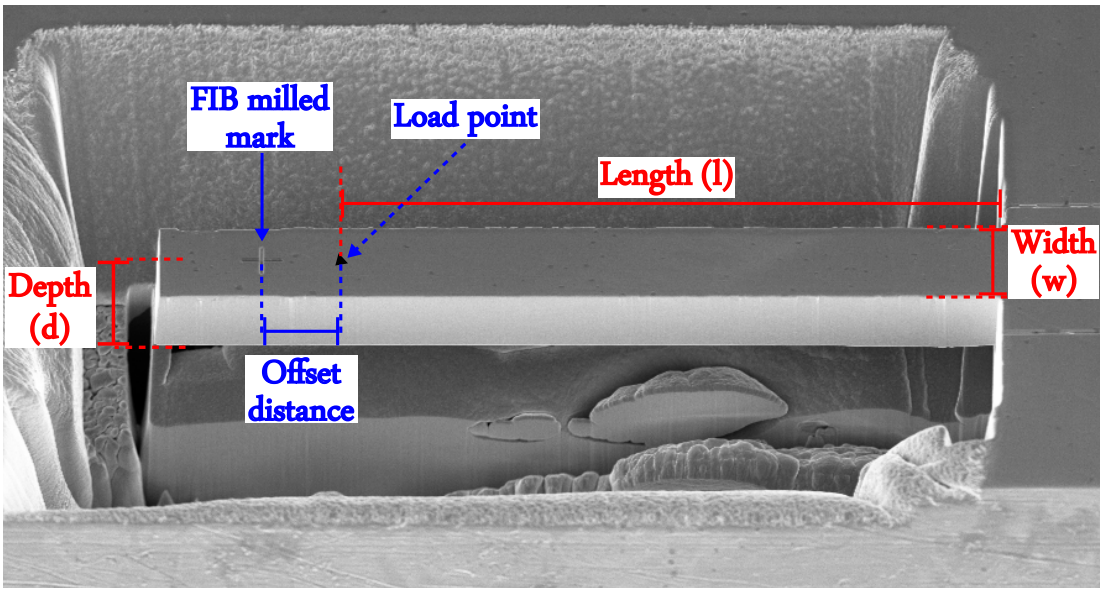


Figure 3.24: SEM micrograph showing a side view of an example untested microcantilever. The approximate position of the load point and the dimensions used for analysis are lablled.

Simple beam theory

Simple beam theory was used to calculate the stress and strain from the load-displacement data. The maximum stress, σ_{max}, and maximum strain, ε_{max}, for a triangular prismatic beam under load is located at the bottom edge at the fixed-end, and was calculated arithmetically using the following relations:

$$\sigma_{max} = \frac{24Pl}{wd^2} \tag{3.2}$$

$$\varepsilon_{max} = \frac{2d\delta}{l^2} \tag{3.3}$$

where P is the applied load and δ is the displacement of the beam at the load point. The beam width, length and depth are given by w, l and d respectively and are defined in figure 3.24. Certain assumptions are made when using simple beam theory [226]:

1. The beam is symmetric about the plane normal to the surface, parallel to the beam axis and central with respect to the beam.
2. Deflection of the beam is in this plane.
3. The beam has a constant cross-section.

The beam theory equations also assume that the bulk material at the fixed-end of the microcantilever is perfectly rigid. Realistically however, flexure of the base will occur during loading; this is discussed in more detail in section 2.6.5. Armstrong et al. (2009) [147] found that as the aspect ratio (l/w) decreases the flexure of the fixed end becomes more significant. The authors suggest that an aspect ratio ≥ 6 is needed to minimise the error introduced from the fixed-end flexure. As such, all beams tested in this thesis had an aspect ratio of 6.

Finite element modelling

Simple beam theory assumes that the cantilever fixed-end is completely rigid, and does not account for stress and deformation within the bulk material around the fixed-end. This stress and deformation can be accounted for using a FE model with appropriate geometry. Simulated load-displacement data from the FE models were fitted to the experimental data via a progressive convergent approximation. This was carried out by adjusting the elastic and plastic material properties in a standard elastic-plastic model with isotropic hardening. The commercially available FE software, ABAQUS 6.14-2, was used to generate a mesh of finite elements that was representative of the specific geometry of each microcantilever. The following section details the FE model before briefly describing the fitting process. Following from the work by Gong and Wilkinson (2009) [177], as discussed in section 2.6.5 on page 71, a small volume of material, 'base', was modelled at the fixed-end of the beam to represent the attachment to the bulk. An example model is shown in figure 3.25.

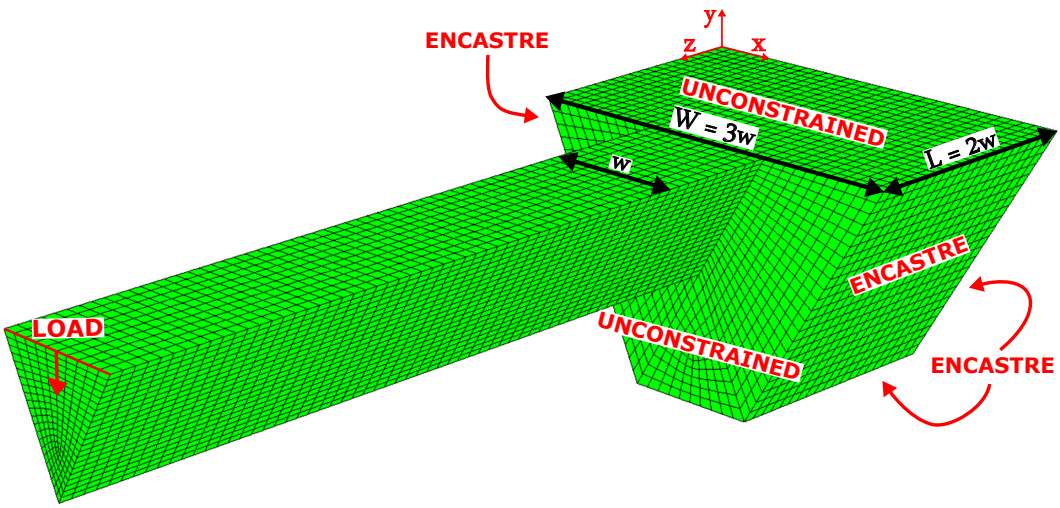


Figure 3.25: FE model showing a cantilever attached to a small volume of bulk material, and the boundary conditions applied.

The size of the base was varied with beam size, such that the width and length of the base were 3x and 2x the beam width respectively, and geometry was chosen such

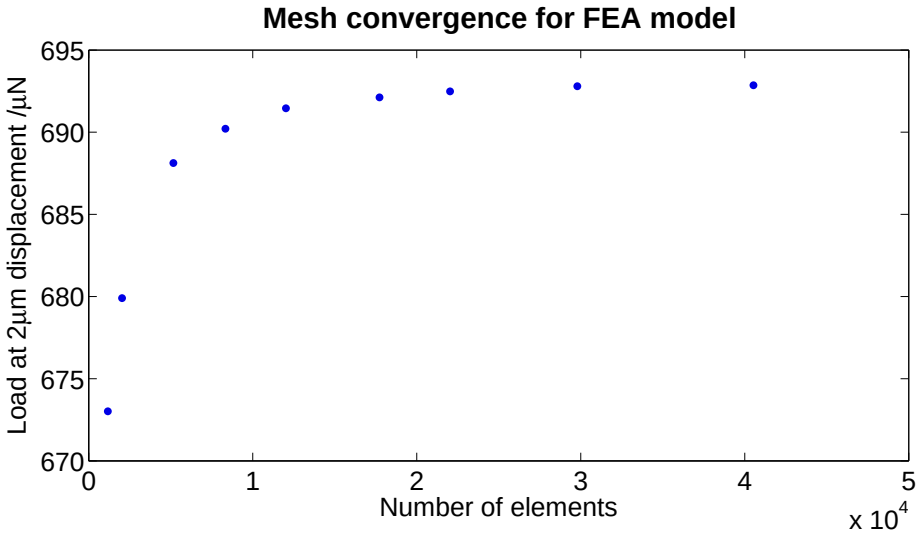


Figure 3.26: Mesh convergence study for an elastic 5 x 5 x 30 μm microcantilever.

that the depth of the base was 2x the beam depth. An encastre boundary condition was applied to all faces of the base with the exception of the upper and inner faces, as shown in figure 3.25. This was to allow the realistic flexure of the fixed end. To avoid complicated deformation of nodes at the load point, the load was applied along a line across the surface of the beam. Experimentally, a small amount of surface deformation will occur during loading. However, from post-test observation in the SEM, this was seen to be small enough to be negligible, even for the larger beam sizes, and was not considered in the analysis.

An ABAQUS standard twenty noded hexahedral element with reduced integration (C3D20R) was used for all simulations (a schematic diagram of the element can be found in figure 4.1 on page 151). To reduce computational time but maintain the accuracy of the simulation, a mesh convergence study was carried out to optimise the number of elements in the model. Elastic tests of varying mesh densities for a 5 x 5 x 30 μm cantilever were simulated, and the load at a maximum tip displacement of 2 μm was recorded (analogous to stiffness). Figure 3.26 shows that there was a convergence of the simulation at $\sim$ 3 x10^4 elements. However, increasing the number of elements from

2.2 x10^4 to 3 x10^4 increased the computational time by 30 % for only a 0.05 % change in simulation output, therefore the number of elements was kept at $\sim$ 2.2 10^4 for all experimental simulations.

Automation of the fitting process

A series of analysis tools were written in MATLAB by C.D. Hardie and T.B. Britton (both formerly at the University of Oxford) for the automation of experimental data interpretation and FEA progressive convergence fitting. A brief description of the analysis tools is given below; for a more detailed explanation, see Hardie (2013) [203].

Before the tests were analysed, the raw load-displacement data was corrected for the spring stiffness and surface find via a manual point selecting program. The corrected data was then used for the simple beam calculation of the stress-strain data. Similarly to section 3.3.2, the simple beam yield was defined by a 10 % drop in elastic modulus by fitting a progressively moving gradient to the stress-strain data.

After simple beam calculations, the FE model was fitted to the corresponding corrected raw data. Firstly, the elastic region was simulated by specifying initial estimates of elastic mechanical properties, the value of the elastic modulus was then amended until experimental and simulation load-displacement gradients were within 0.2 % of each other. A fourth degree polynomial then was fitted to the plastic region of the load-displacement data to smooth the stochastic fluctuations characteristic of micro-cantilever work hardening; the plastic displacement part of the polynomial was then split into a pre-specified number of matching points, shown in figure 3.27(d).

An isotropic hardening model was used to simulate the plastic behaviour in the FE analysis. This uses the von Mises yield criterion to define the onset of plasticity [235]. The plastic stress (or flow stress) is defined as the values of stress required to plastically deform the model to a given plastic strain. Using an initial estimate of the yield stress, the plastic stress is adjusted in order to change the applied load at each matched point.

The simulated load was then fitted to the experimental load via a progressive convergent approximation, demonstrated in figure 3.27(a) and (b). After the simulation was fitted to the matching point, the maximum plastic strain was used to define the initial plastic strain for the next matching point. Yield stress was defined as the stress at zero plastic strain.

The experimental and FE simulated load-displacement curves for a typical microcantilever test are shown in figure 3.27(a) to (e). The FE calculated flow stress at each matched point may then be plotted against the respective strain data to show the stress-strain response of the microcantilever. An example is shown in figure 3.27(f). In the FE fitting example, shown in figure 3.27, the progressive convergence fit deviated from the experimental load-displacement data after the fifth increment and was therefore excluded from the stress-strain plot in figure 3.27(f). The automated progressive convergence fitting process often failed to fit the FE model to the experimental data at large plastic strains, but since the work in this project was predominately interested the elastic behaviour and yield stress, this was not considered a problem. All yield data used in this project were extracted from models that had a good fit for at least the first two matched points.

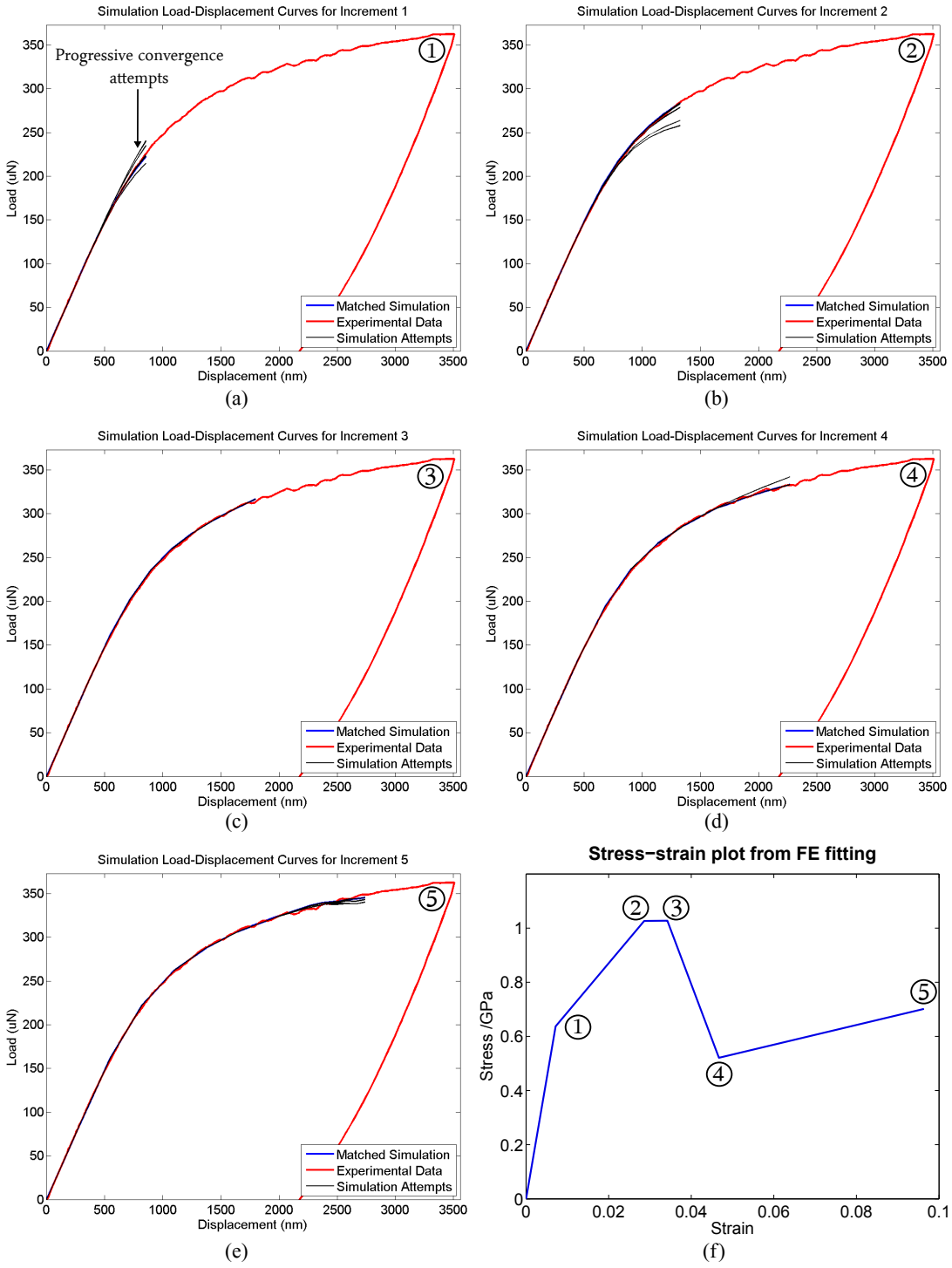


Figure 3.27: Automated FE progressive convergence fitting of a 14WT 1150 micro-cantilever with a specimen depth of 4.86 μm. (a) to (e) Fitting of the first to fifth matched point respectively, with a yield stress of 0.64 GPa at the first matched point. (f) Corresponding FE-calculated stress-strain plot for the first five matched points.

3.4.5 Microcantilever size effect results

Microcantilever specimens with depths of 0.78 μm to 6.82 μm were fabricated in the reference alloys, EUROFER and ODS EUROFER, and in-house produced alloys, 14WT 1150 and 14YWT 1150. The dependency of elastic modulus and yield stress on specimen size was investigated using the method for FE model fitting described in the previous section. The results are presented in figure 3.28 and 3.29. The dependency of yield stress on specimen size from this project are then compared to results from previous Materials for Fusion and Fission Power (MFFP) projects.

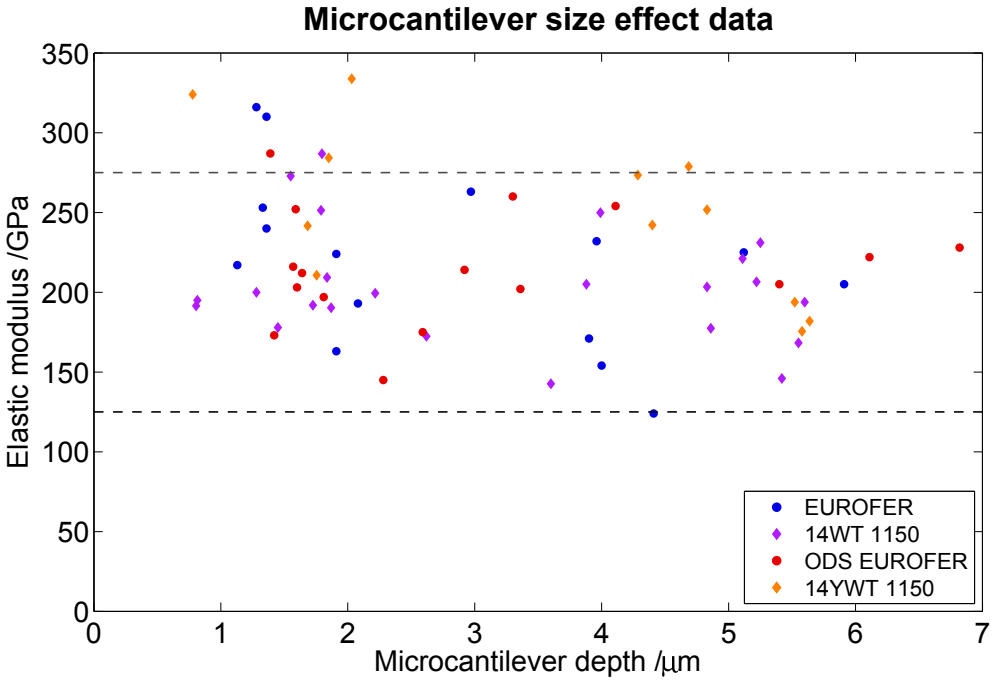


Figure 3.28: Elastic modulus dependence on microcantilever depth. Dashed lines show the minimum and maximum elastic modulus for single crystal iron.

Figure 3.28 shows the FE measured elastic modulus for each microcantilever tested. A large scatter is observed for all beam sizes, which may be attributed to presence of specific crystallographic orientations in the beams, particularly around the fixed end. Ferritic steels are elastically anisotropic: $\alpha-$iron has an elastic modulus of 276 GPa along the <111> direction and 129 GPa along the <100> direction [236]; these values

are represented on figure 3.28 as dotted lines.

Specimens of depth > 2 μm showed elastic moduli in good agreement with the range expected for single crystal $\alpha-$iron. As the specimen size increased, it was expected that the elastic moduli would tend to macroscale values, approximately 190 - 220 GPa for an iron-chromium based alloy [232]. The scatter of ODS EUROFER followed this expected behaviour, which could be due a fine homogeneous grain structure, as observed in figure 3.6. The other materials, with more heterogeneous grain morphology, showed showed a large scatter for range of specimen sizes measured.

For beam depths < 2.5 μm the mean modulus measured was 230 GPa with a standard deviation of 49 GPa. As the specimen size increased the mean modulus and standard deviation decreased to 207 GPa and 39 GPa respectively. The decrease in modulus and scatter with increasing specimen size may be due to an increased number of grains tested and an increase in accuracy of measurement. A combination of increasing scatter and increasing measurement error, with decreasing specimen size, is the most likely reason why certain microcantilevers with depths < 2 μm were measured to have elastic moduli greater than the maximum single crystal value.

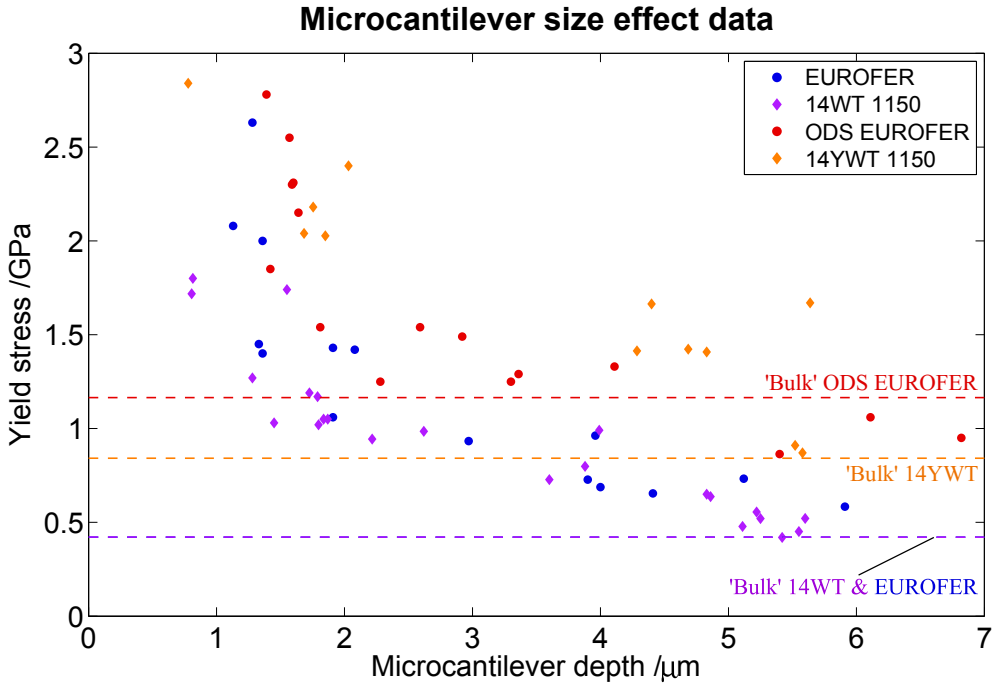


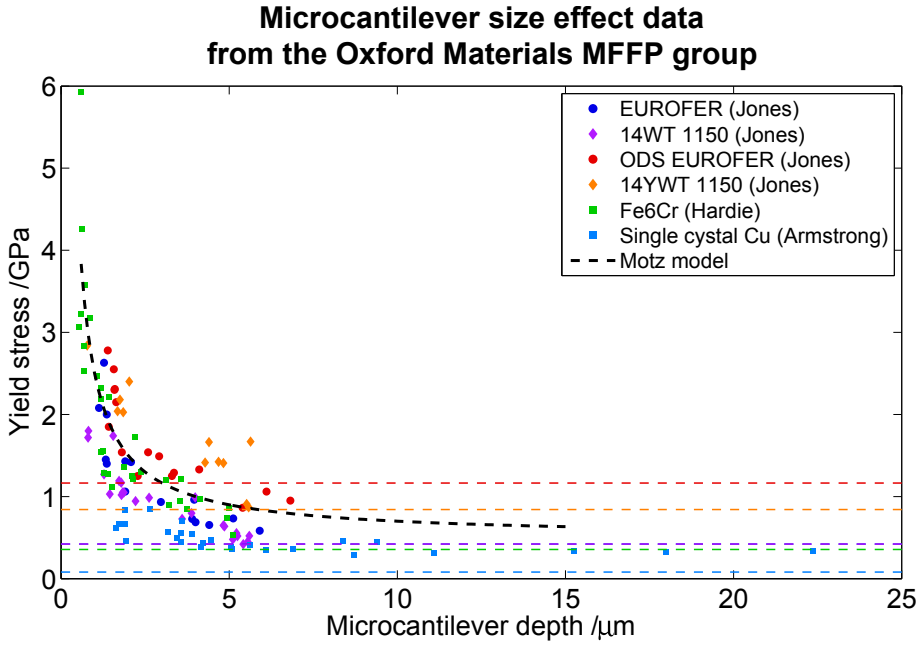
Figure 3.29: Yield stress dependence on microcantilever depth. Dashed lines show corresponding macroscale yield stress as measured by four-point flexure tests in section 3.3.3. Microscale yield stress for 14WT 1150 is compared with the macroscale yield stress for 14WT 950, due to insufficient material quantity in 14WT 1150 for macroscale tests. Yield stresses were calculated by FE model fitting using the method described in section 3.4.4.

The yield stress dependency on specimen size is plotted in figure 3.29 for reference alloys, EUROFER and ODS EUROFER, and in-house produced alloys 14WT 1150 and 14YWT 1150. There was a clear increase in yield stress with decreasing specimen size, with a rapid increase in yield stress as beam depth was decreased below ~ 3 μm. This was in good agreement with the literature for micromechanical test geometries, discussed in section 2.6.7, that observes an almost universally consistent increase in apparent strength as specimen size approaches the sub-micron scale.

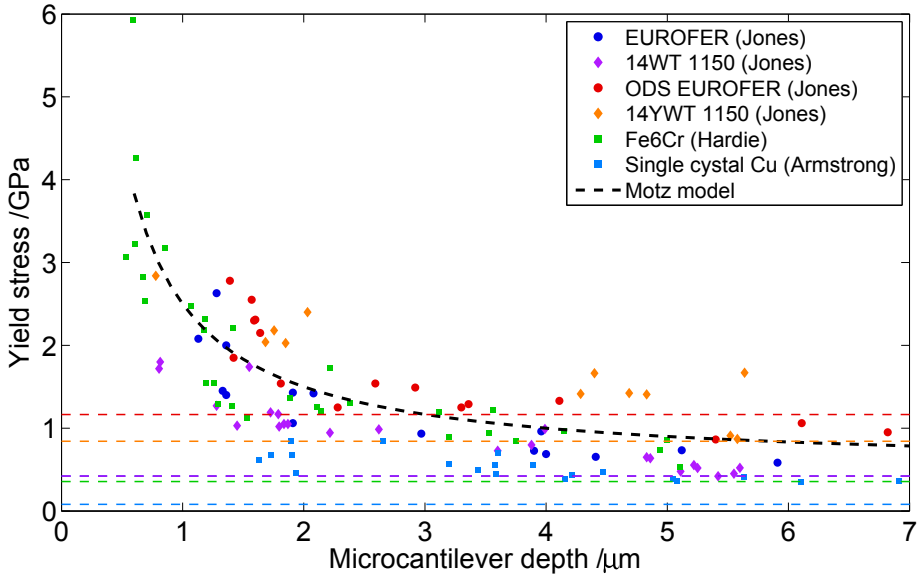
Macroscale yield stresses for each material are also displayed in figure 3.29. These values were provided by the four-point flexure tests performed in section 3.3.3, and are shown by dotted lines with colours corresponding to that of the relevant microscale data. Due to insufficient material quantities, macroscale yield values for 14WT 950 were used

as a comparison for 14WT 1150 microcantilever yield stress. This is seen as an adequate comparison, since the two materials possess similar microstructure (section 3.2.3), with equivalent compositions. It is further justified by the two materials, 14WT 950 and 14WT 1150, possessing a similar hardness response to nanoindentation (section 5.2). At specimen depths ≥ 5 μm, the microcantilever yield stresses tended to macroscale values for all materials except 14YWT 1150, which showed a much greater scatter in yield stress in these larger beams. This scatter in yield stress was most likely due to the extreme microstructural heterogeneity observed in EBSD characterisation of this material (figure 3.8 on page 106), and further investigated using EBSD and EDX in section 5.3.4. The lower extreme of the scatter approximates closely to macroscale yield values, which could suggest that regions of lower strength in 14YWT dominate the macromechanical response.

Unlike the micropillar specimens of Girault et al. (2010) [194] (discussed in section 2.6.7 on page 78), the introduction of a fine dispersion of oxides appeared to have no apparent effect on the observed size effect when compared to their non-ODS counterparts. All materials exhibited a large scatter in yield stress as specimen size decreased, and EUROFER, in particular, displayed a similar mechanical response to ODS EUROFER for beam depths < 2.5 μm. This suggests that dislocation source limitation is the dominant mechanism governing the mechanical response of the materials at these length scales, rather than dislocation blocking effects of the oxide particles. As specimen size increased, yield stresses tended to bulk values, suggesting that these microcantilevers were no longer source limited.



(a)



(b)

Figure 3.30: Yield stress dependence on microcantilever depth. Dashed lines show corresponding macroscale yield stress. Data from this project, alongside tests carried out by Hardie (2016) [199] and Armstrong (2009) [237] on Fe6Cr and single crystal copper respectively. Data from Hardie and Armstrong are calculated from simple beam theory, with the former using 0.2 % proof stress offset. Model data from Motz et al. (2005) [195], parameters from Tarleton et al. (2015) [197], as described in the text. (a) 0 to 25 μm beam depth. (b) 0 to 7 μm beam depth of same graph.

Figure 3.30 plots microcantilever size effect data from this project with those of previous projects within Oxford Materials' MFFP group. The data from Hardie (2016) [199] was in Fe6Cr, analysed using simple beam theory with yield stress determined by a 0.2% strain offset. The data from Armstrong (2009) [237] was also analysed with simple beam theory using a 10% tangential modulus drop to determine yield stress in single crystal copper. Data from this project shows a good agreement with data using the same beam geometry in previous projects, and demonstrates that the microcantilever size effect is largely material independent. However, there exists a small variance in where yield starts to significantly diverge from macroscale values.

As discussed in section 2.6.7 on page 81, a density of geometrically necessary dislocations (GNDs) is needed to accommodate the plastic strain gradients found in cantilever bending. Instead of a continuum of GNDs, Tarleton et al. (2015) [197] explored the nucleation of GNDs at restricted number of dislocation sources to accommodate the necessary strain gradients, and found that GND density and source limitation combine to produce the observed size effect. Source limitation becomes increasingly significant as slip band spacing (which deceases linearly with specimen size) approaches the average separation distance of dislocation sources (source limited regime). A increase in scatter as specimen size is decreased may be attributed to a natural statistical variation in source strength. Smaller beams have fewer sources in the concentration of stress at the fixed-end, thus the strength of these sources have a greater influence on the measured plastic properties.

The onset of the source limitation regime may be observed as a rapid increase in apparent strength and divergence away from macroscale/near-macroscale values. For the materials tested in this thesis, this occurred at a beam depth of between 2 μm and 4 μm. Due to this, when attempting to evaluate macroscale mechanical properties for ion irradiated materials in chapter 5, microcantilevers were fabricated with depths $\geq$ 4.5 μm.

A study of copper microcantilevers by Motz et al. (2005) [195] found that the strong size dependency of flow stress at beam depths approaching the sub-micro scale can be approximately fitted with a power law of the form,

$$\sigma_f(d) = Ad^{-n} \tag{3.4}$$

Where A is a proportionality constant, dependent on beam geometry and material, and d is a characteristic sample dimension (in this case beam depth). Tarleton et al. (2015) [197] report that literature values for n range from $0.2 < n < 1$ and is generally dependent on the material and loading conditions. The authors also suggest that the literature values of n are generally underestimated due to fitting a power law, such as (3.4), to experimental data that predicts that $\sigma_f(d) \to 0$ for increasing beam size. Realistically, $\sigma_f(d) \to \sigma_0$ for large beams, where σ_0 is the material's macroscopic yield stress. The authors update (3.4), and account for the $\sigma_f(d)$ dependence on source density by using a power law of the form,

$$\sigma_f(d) = A(d/w_s)^{-n} + \sigma_0 \tag{3.5}$$

Where w_s is the average dislocation source spacing. The power law given in (3.5) was fitted to the experimental data by the MFFP group (C. A. Jones, C. D. Hardie and D. E. J. Armstrong), and is represented by a black dotted line in figure 3.30. The fitted power law used $A = 2$, $n = 1$, $w_s = 1$ and $\sigma_0 = 0.5$. This was in good agreement with the literature as summarised by Tarleton et al. (2015) [197].

3.4.6 Summary of microcantilever size effects

Microcantilevers with beam depths varying from 0.78 μm to 6.82 μm were fabricated in EUROFER, ODS EUROFER, 14WT 1150 and 14YWT 1150. By fitting an appropriately sized FE model to experimental load-displacement data, elastic modulus and yield stress were measured. A large scatter in elastic moduli was found, and attributed to

microstructural heterogeneity. Beam depths > 2 μm showed individual elastic moduli in good agreement with the range expected for single crystal $\alpha-$iron, and an average modulus of 207 GPa with a standard deviation of 39 GPa. The modulus expected for polycrystalline ferritic steel was between 190 to 220 GPa. For beam depths < 2.5 μm the average modulus was found to be 230 GPa with a standard deviation of 49 GPa. The larger scatter was attributed to an increase in measurement error and a greater probability of examining fewer crystallographic orientations.

The onset of the source limitation regime was observed to be at beam depths between 2 μm and 4 μm. Due to this, when approximating macroscale mechanical properties for ion irradiated materials in chapter 5, microcantilever with depths ≥ 4.5 μm were fabricated.

As beam depth is increased, source limitation becomes less dominant and the size effect produced by mobile dislocation pinning from a density of GNDs becomes more significant. This is further explored in chapter 4, where GNDs are modelled as a continuum using a lengthscale dependent crystal plasticity model, implemented within ABAQUS 6.14-2.

Chapter 4

4 Computational plasticity study of the microcantilever size effect

The work reported in this chapter uses a lengthscale-dependent crystal plasticity model to simulate the microcantilever size effect. The simulations were performed using a user defined material (UMAT), developed by Dunne et al. [178, 238], implemented within ABAQUS 6.14-2 commercially available finite element software. The UMAT produces a lengthscale dependent response by making the plastic strain dependent on the geometrically necessary dislocation (GND) density. The simulation of the GND density evolution with plastic strain, allowed the contribution GNDs had to the microcantilever size effect to be determined, and demonstrated that other mechanisms must be included if simulations were to match experimentally found results. Before the results are presented, the field of computational plasticity is briefly introduced, then the relevant theory needed to understand how the UMAT obtains a solution is described and lastly, the process used to develop the model and check the code is discussed.

4.1 Introduction to computational plasticity

When creating a new structural material, one of the primary engineering objectives is to understand its performance under expected working conditions. To achieve this, an engineer will need to consider the linear and nonlinear mechanical behaviour associated with the material's response to the working conditions. Currently, this analysis is most likely to involve computer simulation of the system utilising commercially available finite element software. Since the late 1960s computers have been used to model elasto-plastic behaviour in materials [239, 240]. The exponential growth of computer performance since has allowed for a similar increase in model complexity; this performance increase along with cost reduction has made the field of computational plasticity more feasible

for an increasing number of research groups.

Often problems necessitate the assumption of linearity only, however it is evident that many situations also demand the consideration of nonlinear behaviour, such as in the case of modeling the elastic and plastic behaviour of microcantilevers. Modeling linear and nonlinear continuum mechanics both involve satisfying the requirements of equilibrium, compatibility, constitutive equations, and boundary conditions [241]. However, in the linear case an assumption is made that the deformation of the solid is small and the effect of changes in the material's geometry can be ignored, whereas in nonlinear cases, the magnitude of the deformation is unrestricted [242].

The description of a material's mechanical behaviour and physical quantities with continuous mathematical functions is known as continuum mechanics. The material behaviour of a solid is usually governed by 3 laws; conservation of mass, conservation of energy, and conservation of momentum. The conservation laws are not on their own sufficient to fully understand the behaviour of the material; we need to know the constitutive equations that describe the relation between different physical quantities that are specific to the material in question. Unfortunately, there are few problems for which solutions can be found analytically. This is usually because of irregular and/or complicated boundary conditions [242, 243].

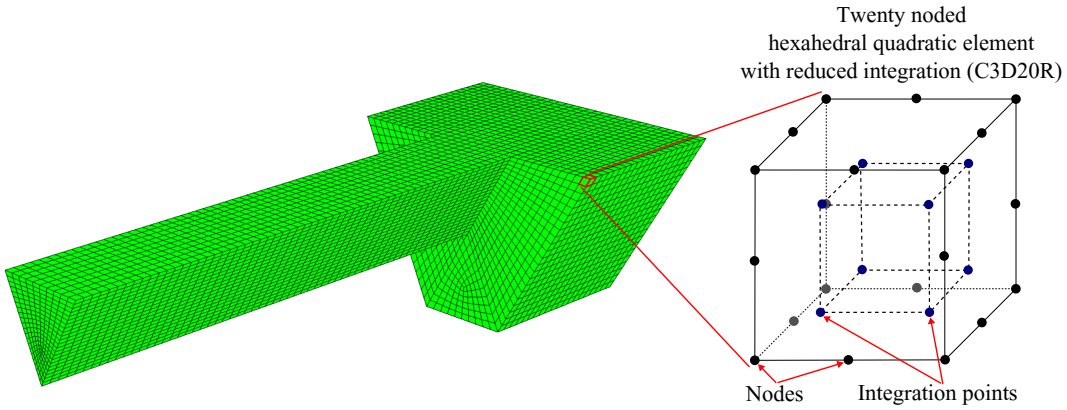


Figure 4.1: Model of microcantilever discretised into finite elements. Shown alongside is a schematic diagram of the twenty noded hexahedral quadratic element (C3D20R) used in this study.

A common way to approximate a solution is by employing the finite element method (FEM), where the space continuum is discretised into a finite number of elements, such as lines (1D), triangles and squares (2D), tetrahedra and hexahedra (3D). Each element is described by a set of points, called nodes, upon which both the geometry and primary variables in the governing equations are approximated; shape functions are used to interpolate solutions throughout each element, a schematic diagram of the element used in this study is shown in figure 4.1. The response of each element within the body is expressed in terms of a finite number of degrees of freedom given to each nodal point. For example, in the stress analysis of a solid, the finite element could be described by a hexahedron defined by twenty nodes (as is the case in this thesis), and the primary variables could be the displacement in Cartesian directions. The implication is that when using FEM, the requirement for equilibrium cannot be satisfied at every point in the continuum (strong integral form), instead the equilibrium condition only has to be met in an average sense (weak integral form) [244]. A weak integral form of the governing equations can be obtained by using the principle of virtual work, principle of stationary total potential energy, or Hamilton's principle [242, 241]. The finite element approximations are then introduced to discretise these integral equations, which produces a finite set of algebraic equations in the primary variable. This can then be solved using an iterative integration process such as the central difference method, tangential stiffness method, or Newton-Raphson method. The integration of the constitutive equations is evaluated at integration points within the element, and shape functions are used to determine how the discrete solutions for field variables, such as stress and strain, are represented throughout the element.

4.2 Computational plasticity theory

4.2.1 Introduction

The crystal plasticity model used in this chapter is implemented within the commercial FE software, ABAQUS 6.14.2, via a subroutine called a UMAT (user defined material model). ABAQUS has an interface that allows a user to implement general constitutive equations into an FE model produced within the software. The crystal plasticity UMAT model, written in FORTRAN, describes the deformation of a each crystal orientation assuming crystallographic slip via dislocation glide as the primary deformation mode. Crystal orientation will rotate during deformation, at the same time threshold stress of each slip system will increase due to the hardening mechanisms built into the model; the mechanical response and the texture will change accordingly.

The UMAT used in this project implicitly integrates the constitutive equations using the Newton-Raphson iterative method. For each time increment, Δt, ABAQUS calls the UMAT at each integration point and provides the UMAT with the stress, $\boldsymbol{\sigma}_t$, and state variables, $SDVs$, at the start of time increment, t; the deformation gradient at the start, $\boldsymbol{F}_t$, and end of the time increment, $\boldsymbol{F}_{(t+\Delta t)}$; time increment size, Δt; temperature, T; material constants and element number. In turn, the UMAT provides ABAQUS with the updated stresses for the end of the time increment, $\boldsymbol{\sigma}_{(t+\Delta t)}$, the material Jacobian (tangential stiffness matrix), $\frac{\partial \Delta \boldsymbol{\sigma}}{\partial \Delta \boldsymbol{\varepsilon}}$, and the SDVs at the end of the increment.

Under the guidance of Dr E. Tarleton (University of Oxford), this section comprehensively covers the operation of the crystal plasticity UMAT of Dunne et al. [178, 238]; The thesis by Kiwanuka (2013) [245] also provides a good grounding in the mathematics involved in the UMAT. First, the deformation gradient is introduced in subsection 4.2.2 and lays out the necessary theory in order to understand the origin of the UMAT's constitutive lengthscale-dependent equation. Subsection 4.2.3 then describes the implicit integration of the constitutive equations. Lastly, subsection 4.2.5 provides a step by step summary of the implicit integration implementation for ease of reference.

4.2.2 The deformation gradient

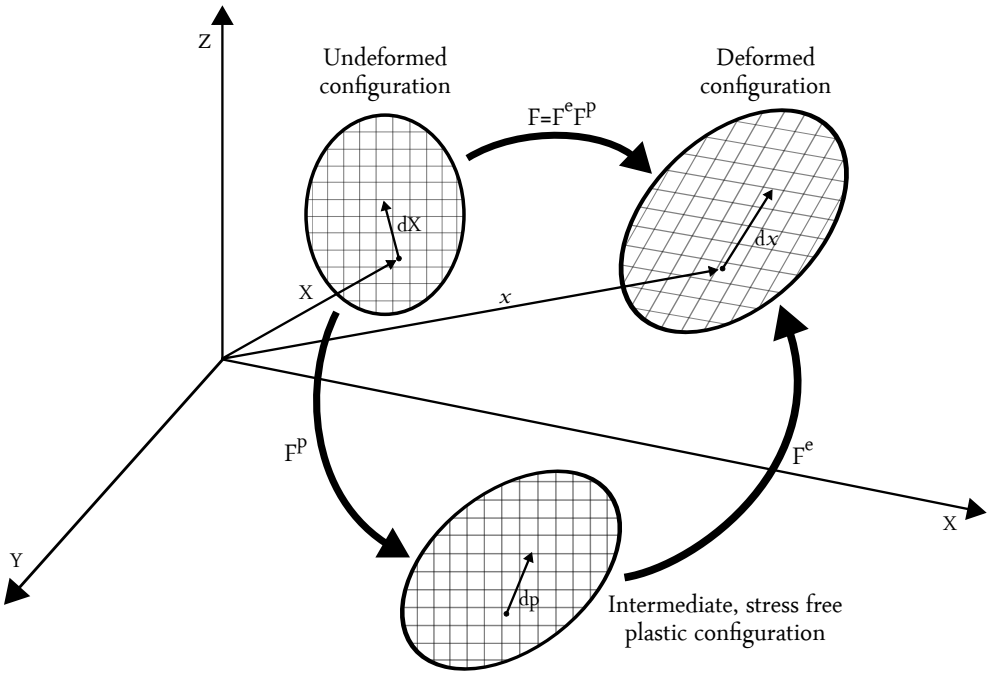


Figure 4.2: A schematic diagram of the a representative piece of material in the three configurations and the corresponding multiplicative decomposition of the deformation gradient.

Many engineering stress-strain problems can be modeled using a kinematic infinitesimal strain theory. This assumes that any deformation and the rigid-body rotations that accompany them are small enough to be negligible. However, when modeling systems in excess of elastic strains the deformation becomes so large that is can no longer be neglected, and the continuum mechanical model must involve a finite strain theory. Generally, deformation consists of two components: a shape change or stretch, and a rigid-body rotation. To describe deformation, let us consider an imaginary material in an undeformed configuration prior to loading, shown in figure 4.2. Here, quantities are measured relative to the global co-ordinate system, XYZ, often referred to as the *material co-ordinate system*. We then apply a load so that the material undergoes a deformation to change its state to the deformed configuration. A change in configuration

of a continuum body can be described by a displacement field, which is a vector field composed of all displacement vectors relating each particle in the undeformed body to its counterpart in the deformed body. The deformation gradient tensor is a second order tensor which maps the vectors in the undeformed configuration to those in the deformed configuration.

$$d\mathbf{x} = \boldsymbol{F} d\mathbf{X} \tag{4.1}$$

The infinitesimal undeformed vector, $d\mathbf{X}$, is transformed to its deformed counterpart, $d\mathbf{x}$, by the deformation gradient, $\boldsymbol{F}$. rearranging gives,

$$\boldsymbol{F} = \frac{\partial \mathbf{x}}{\partial \mathbf{X}} \tag{4.2}$$

The deformation gradient describes the complete displacement field; this includes both stretch and rigid-body displacement. Before solving a continuum mechanics problem it is necessary to separate out the rigid body rotations from the stretch since only stretch contributes to the internal stress. When modeling large deformations, the strain will usually go beyond the material's elastic limit, thus plastic deformation must be considered. From figure 4.2, we see that in order for vector $d\mathbf{X}$ to transform to the deformed vector $d\mathbf{x}$ it has to undergo elastic and plastic deformation. We can separate out the elastic from the plastic deformation by introducing an intermediate stress-free configuration; this is a virtual state in which $d\mathbf{X}$ is transformed to $d\mathbf{p}$ via a purely plastic deformation. Thus this transformation can be mapped by a purely plastic deformation gradient,

$$d\mathbf{p} = \boldsymbol{F}^p d\mathbf{X} \tag{4.3}$$

Rearranging to define the plastic deformation gradient,

$$\boldsymbol{F}^p = \frac{\partial \mathbf{p}}{\partial \mathbf{X}} \tag{4.4}$$

The vector $d\mathbf{x}$, in the deformed configuration can then then be mapped from vector, $d\mathbf{p}$, via a purely elastic deformation gradient, $\boldsymbol{F}^e$, given by

$$d\mathbf{x} = \boldsymbol{F}^e d\mathbf{p} \tag{4.5}$$

From this the elastic deformation gradient can be defined as,

$$\boldsymbol{F}^e = \frac{\partial \mathbf{x}}{\partial \mathbf{p}} \tag{4.6}$$

Subsituting (4.4) into (4.6) gives,

$$d\mathbf{x} = \boldsymbol{F}^e \boldsymbol{F}^p d\mathbf{X} \tag{4.7}$$

By looking at equivalent terms in (4.2), we see that the deformation gradient is given by

$$\boldsymbol{F} = \boldsymbol{F}^e \boldsymbol{F}^p \tag{4.8}$$

This is known as the multiplicative decomposition of the deformation gradient. The crystal plasticity UMAT includes all rigid body rotation within $\boldsymbol{F}^e$, so that $\boldsymbol{F}^p$ only maps a purely plastic deformation.

Since the finite element method is an incremental process it is often more convenient to consider plasticity in terms of plastic strain rate. In a similar manner to formulating the deformation gradient, consider a vector field composed of all the velocity vectors relating each particle's velocity in the undeformed body to its counterpart in the deformed body. An incremental velocity vector related to an incremental change in position in the deformed configuration may be given by the relation,

$$d\mathbf{v} = \frac{\partial \mathbf{v}}{\partial \mathbf{x}} d\mathbf{x} \tag{4.9}$$

We call the spatial rate of change of velocity, the velocity gradient, $\boldsymbol{L}$,

$$\boldsymbol{L} = \frac{\partial \mathbf{v}}{\partial \mathbf{x}} \tag{4.10}$$

It is also important to consider the deformation gradient in rate form,

$$\dot{\boldsymbol{F}} = \frac{\partial}{\partial t}\left(\frac{\partial \mathbf{x}}{\partial \mathbf{X}}\right) = \frac{\partial \mathbf{v}}{\partial \mathbf{X}} = \frac{\partial \mathbf{v}}{\partial \mathbf{x}}\frac{\partial \mathbf{x}}{\partial \mathbf{X}} = \boldsymbol{L}\boldsymbol{F} \tag{4.11}$$

In terms of $\boldsymbol{L}$,

$$\boldsymbol{L} = \dot{\boldsymbol{F}}\boldsymbol{F}^{-1} \tag{4.12}$$

All square matrices may be separated out into their symmetric and asymmetric parts, so the decomposition of the velocity gradient takes the form,

$$\boldsymbol{L} = sym(\boldsymbol{L}) + asym(\boldsymbol{L}) = \frac{1}{2}(\boldsymbol{L} + \boldsymbol{L}^T) + \frac{1}{2}(\boldsymbol{L} - \boldsymbol{L}^T) \tag{4.13}$$

The decomposition of $\boldsymbol{L}$ allows us to calculate the rates of strain, otherwise known as rate of deformation, $\boldsymbol{\Phi}$, and the rate of continuum spin, $\boldsymbol{\omega}$, independently [241]. The rate of deformation and continuum spin are given by the symmetric and asymmetric parts of the velocity gradient respectively, so that,

$$\boldsymbol{L} = \boldsymbol{\Phi} + \boldsymbol{\omega} \tag{4.14}$$

where,

$$\boldsymbol{\Phi} = \frac{1}{2}(\boldsymbol{L} + \boldsymbol{L}^T) \tag{4.15}$$

The rate of continuum spin is written by,

$$\boldsymbol{\omega} = \frac{1}{2}(\boldsymbol{L} - \boldsymbol{L}^T) \tag{4.16}$$

In a similar fashion to the multiplicative decomposition of the deformation gradient, the velocity gradient can also be decomposed into its elastic and plastic parts, $\boldsymbol{L}^e$ and $\boldsymbol{L}^p$. The multiplicative decomposition of the velocity gradient is given by the equation,

$$\boldsymbol{L} = \boldsymbol{L}^e\boldsymbol{L}^p \tag{4.17}$$

ABAQUS provides the UMAT with the deformation gradient at the beginning of the time increment, $\boldsymbol{F}_t$, and at the end of the time increment, $\boldsymbol{F}_{t+\Delta t}$. Since the time increment is known, this allows us to calculate the total velocity gradient, $\boldsymbol{L}$, using the relation provided in (4.12). By using the decomposition of the velocity gradient in

(4.17), we are able to find $\boldsymbol{L}^e$, as $\boldsymbol{L}^p$ is calculated in the UMAT using a constitutive equation.

Lengthscale dependent constitutive equation for the plastic velocity gradient

Busso (2000) [246] suggests an expression for the plastic velocity gradient, $\boldsymbol{L}^p$ as,

$$\boldsymbol{L}^p = \sum_{\kappa} \dot{\gamma}^{\kappa} \mathbf{s}^{\kappa} \otimes \mathbf{n}^{\kappa} \tag{4.18}$$

where $\dot{\gamma}^{\kappa}$ is the shear strain rate on the κ^{th} slip system, and $\mathbf{s}^{\kappa}$and $\mathbf{n}^{\kappa}$ are the slip direction and normal to the κ^{th} slip system respectively. Equation (4.18) is summed over all slip systems. Cottrell (1953) [247] provides an expression for the shear strain rate, $\dot{\gamma}$, produced by the glide of a density, ρ_m, of mobile dislocations with and average glide velocity, $\bar{v}$, and a Burgers vector magnitude, b, as

$$\dot{\gamma}^{\kappa} = \rho_m b \bar{v} \tag{4.19}$$

Dislocation glide is almost always obstacle limited; it is their interaction with sessile dislocations, solutes or precipitates, grain boundaries, or the periodic friction of the lattice that ultimately controls the plastic flow and yield stress in a crystalline structure. It is assumed that the time taken for a dislocation to unpin from an obstacle is much greater than the time taken to glide between pinning points. Therefore it can be seen from (4.19), that the average dislocation velocity, and thus shear strain rate, must be dominated by the waiting time between unpinning events. Seeger (1955) [248] first suggested the idea that the dislocation glide velocity is determined by the rate at which dislocation segments are unpinned by local thermal activation to overcome the energy barrier of an individual obstacle. Gibbs (1969) [249] gives an expression for the rate of successful thermal activation events, in terms of the Gibbs free energy, as

$$\Gamma = \frac{\nu b}{2l} exp\left(-\frac{\Delta G}{kT}\right) \tag{4.20}$$

where ν is the escape attempt frequency, l is the pinning distance, ΔG is the Gibbs free energy, k and T are the Boltzman constant and temperature respectively. The average

glide velocity, $\bar{v}$, is given by the product of the jump length of the thermal activation event, d, and the rate of successful attempts to surmount the energy barrier, Γ, to give

$$\bar{v} = \frac{d\nu b}{2l} exp\left(-\frac{\Delta G}{kT}\right) \tag{4.21}$$

By combining (4.21) and the expression for the Gibbs free energy under a stress field [250],

$$\Delta G = \Delta F - \tau \Delta V \tag{4.22}$$

Where ΔF is the Helmholtz free energy, τ is the resolved shear stress acting on the slip plane and ΔV is the activation volume, we get an equation for the average glide velocity as,

$$\bar{v} = \frac{d\nu b}{2l} \exp\left(-\frac{\Delta F}{kT}\right) \exp\left(\frac{\tau \Delta V}{kT}\right) \tag{4.23}$$

The activation volume is defined by $\Delta V = lbd$, i.e. a volume bounded by the distance between pinning points, l , Burgers vector magnitude, b, and the thermal activation jump length needed to surmount the barrier, d. By using the definition,

$$\sinh(x) = \frac{e^x - e^{-x}}{2} \tag{4.24}$$

and substituting (4.23) into (4.19), considering both forward and reverse thermal activation events, we get an updated expression for the shear strain rate [178],

$$\dot{\gamma}^\kappa = \rho_m \nu b^2 \exp\left(-\frac{\Delta F}{kT}\right) \sinh\left(\frac{\tau^\kappa \Delta V}{kT}\right) \tag{4.25}$$

with a further approximation, suggested by Dunne et al. (2007) [178], that $d \approx l$. Busso (2000) [246] and later Dunne et al. (2007) and (2012) [178, 238] argue that the predominant pinning mechanism is dislocation forest interactions caused by the development of GNDs, and statistically stored dislocations (SSDs) at low strain gradients. Therefore, the rate of slip is dominated by the mean free path length between sessile GNDs and sessile SSDs. We can introduce a lengthscale dependent mechanical response by making the distance between pinning points, l, dependent on the dislocation density within the activation volume. Strain rate, and subsequent plastic deformation, will decrease as

GND density increases. The definitions of GNDs and SSDs are given in the work by Ashby (1970) [186], discussed on page 75, both are assumed sessile in this work.

Due to the previous assumption that the majority of pinning points are produced by other dislocations, Dunne et al. (2007) [178] assumes that the length of a thermal activation jump event, d, may approximate to the Burgers vector, b. From this, the activation volume, $\Delta V = lbd$, then becomes

$$\Delta V = lb^2. \tag{4.26}$$

where the distance between pinning points is equal to the mean free path between dislocations,

$$l = \frac{1}{\sqrt{\psi(\rho_{GND} + \rho_{SSD})}} \tag{4.27}$$

A coefficient, ψ, is needed to represent the probability of pinning, since not all GNDs or SSDs act as pinning points.

GNDs are required to accommodate lattice curvature whenever there is non-uniform plastic deformation. They were first investigated in detail by Nye (1953) [251], who related the GND density to the net Burgers vector of an array of dislocations penetrating an infinitesimal surface within a closed Burgers circuit. [251, 246, 252, 238, 253]. A closure failure of this Burger's circuit can be described by the change in length of a closed line around the dislocation. Acharya and Bassani (2000) [252] defined the cumulative Burgers vector, $\boldsymbol{b}_c$, of all dislocations lines that belong to the interior of a loop formed by the closed curve, c, with respect to the deformed configuration (refer to figure 4.2 for configuration definitions) as

$$\boldsymbol{b}_c = \oint_c \boldsymbol{F}^{e-1} d\boldsymbol{x} \tag{4.28}$$

where, $d\boldsymbol{x}$, is an infinitesimal vector along the curve in the deformed configuration. Applying Stoke's theorem,

$$\boldsymbol{b}_c = \oint_c \boldsymbol{F}^{e-1} d\boldsymbol{x} = \iint_s (\mathrm{curl}\boldsymbol{F}^{e-1})^T \boldsymbol{n} ds = \iint_s \boldsymbol{G}_D^{eT} \boldsymbol{n} ds \tag{4.29}$$

where $\boldsymbol{n}$ is normal to the surface, s, whose boundary curve is, c. The 'curl' implies a cross product with the gradient operator, $\boldsymbol{\nabla}$, performed with respect to the deformed configuration, and 'Curl' is used for the undeformed configuration. The presence of GNDs is defined by the existence of at least one closed curve in C for which the cumulative Burgers vector is non-vanishing. $\boldsymbol{G}_D^{eT}$ represents the geometric dislocation tensor in the deformed configuration as a function of $\boldsymbol{F}^e$.

We can also describe the cumulative Burgers vector, $\boldsymbol{B}_C$, of all the dislocation lines within a closed curve with respect to the undeformed configuration, such that,

$$\boldsymbol{B}_C = \oint_C \boldsymbol{F}^p d\boldsymbol{X} = \iint_S (\mathrm{Curl}\boldsymbol{F}^p)^T \boldsymbol{N} dS = \iint_S \boldsymbol{G}_U^{pT} \boldsymbol{N} dS \tag{4.30}$$

where $\boldsymbol{X}$ is an infinitesimal vector along the curve in the undeformed configuration. $\boldsymbol{G}_U^{pT}$ represents the geometric dislocation tensor in the undeformed configuration as a function of $\boldsymbol{F}^p$. From the definition of Nye's tensor [251],

$$\boldsymbol{G}_D^{eT} = \sum_{\kappa} (\boldsymbol{\rho}_{GND}^{\kappa} \otimes \mathbf{b}^{\kappa}) = \mathrm{curl}\boldsymbol{F}^{e^{-1}} \tag{4.31}$$

and we may also say (from 4.30),

$$\boldsymbol{G}_U^{pT} = \sum_{\kappa} (\boldsymbol{\rho}_{GND}^{\kappa} \otimes \mathbf{b}^{\kappa}) = \mathrm{Curl}\boldsymbol{F}^p \tag{4.32}$$

Where $\mathbf{b}^{\kappa}$ is the Burger's vector on the κ^{th} slip system , $\boldsymbol{\rho}_{GND}^{\kappa}$ is the GND density on the κ^{th} slip system, and the summation is over all slip systems. Equation (4.32) is formulated in detail by Busso (2000) [246]. From this equation, we see that the GND density is related to the $\mathrm{Curl}\boldsymbol{F}^p$, meaning that GND densities are only non-zero in the presence of strain gradients. This is investigated further in section 4.3.5.

The UMAT used in this work calculates the GND density from the Curl$\boldsymbol{F}^p$, e.g. from (4.32), but other codes may use the curl$\boldsymbol{F}^{e^{-1}}$. We can prove $\boldsymbol{G}_U^{pT} = \boldsymbol{G}_D^{eT} = \boldsymbol{G}^T$ by introducing the identity tensor, $\boldsymbol{I}$, into the relation found within the contour integral in (4.30),

$$\boldsymbol{F}^p d\boldsymbol{X} = \boldsymbol{F}^p \boldsymbol{I} d\boldsymbol{X} = \boldsymbol{F}^p \boldsymbol{F}^{-1} \boldsymbol{F} d\boldsymbol{X} \tag{4.33}$$

By using the definition, $d\mathbf{x} = \boldsymbol{F} d\mathbf{X}$ (4.1) and rearranging (4.33) we get,

$$\boldsymbol{F}^p d\boldsymbol{X} = \boldsymbol{F}^p \boldsymbol{F}^{-1} d\boldsymbol{x} \tag{4.34}$$

The multiplicative decomposition of the deformation gradient in (4.8) gives $\boldsymbol{F}^{-1} = (\boldsymbol{F}^e \boldsymbol{F}^p)^{-1}$, so substituting simplifies (4.34) to,

$$\boldsymbol{F}^p d\boldsymbol{X} = \boldsymbol{F}^{e^{-1}} d\boldsymbol{x} \tag{4.35}$$

Therefore,

$$\boldsymbol{G}_U^{pT} = \boldsymbol{G}_D^{eT} = \boldsymbol{G}^T \tag{4.36}$$

From this, it is clear that $\boldsymbol{b}_c$ and $\boldsymbol{B}_C$ describe the same closure failure, with the difference between them being the reference frame in which Nye's Tensor, $\boldsymbol{G}$, is calculated.

The velocity gradient used within the UMAT was developed by Dunne et al. (2007) [178] improved by Dunne et al. (2012) [238]. It is derived by combining (4.18), (4.25), (4.26) and (4.27), where GND density, ρ_{GND}, is given by (4.32) and gives the expression,

$$\boldsymbol{L}^p = sym \left\{ \sum_{\kappa} \rho_m \nu b^2 \exp\left(-\frac{\Delta F}{kT}\right) \sinh\left(\frac{(\tau_r^\kappa - \tau_c^\kappa)\gamma_0 b^2}{kT(\psi(\rho_{GND} + \rho_{SSD}))^{\frac{1}{2}}}\right) \mathbf{s}^\kappa \otimes \mathbf{n}^\kappa \right\} \tag{4.37}$$

Where the SSD density, ρ_{SSD}, and mobile dislocation density, ρ_m, are given by predetermined constants.

For simplicity, $\boldsymbol{L}^p$ becomes,

$$\boldsymbol{L}^p = sym\left\{\sum_{\kappa}\alpha \sinh \beta(\tau_r^{\kappa} - \tau_c^{\kappa})\mathbf{s}^{\kappa} \otimes \mathbf{n}^{\kappa}\right\} \tag{4.38}$$

Where τ_r^{κ} and τ_c^{κ} are the resolved shear stress and critical resolved shear stress on the κ^{th} slip system respectively. γ_0 is the shear strain that is work conjugate to the resolved shear stress [238, 254]. α and β are constants used to simplify (4.37) to (4.38). Where,

$$\alpha = \rho_m \nu b^2 \exp\left(-\frac{\Delta F}{kT}\right) \tag{4.39}$$

$$\beta = \frac{\gamma_0 b^2}{kT(\psi(\rho_{GND} + \rho_{SSD}))^{\frac{1}{2}}} \tag{4.40}$$

4.2.3 Implicit integration implementation

Given a deformation gradient at the beginning and end of the time increment, $\boldsymbol{F}_t$ and $\boldsymbol{F}_{t+\Delta t}$, and internal state variables at the beginning of the time increment, t, the UMAT's purpose is to update these values for the end of the time increment, $t + \Delta t$, and find the stress, $\boldsymbol{\sigma}_{t+\Delta t}$, and material Jacobian, $\frac{\partial \boldsymbol{\Delta\sigma}}{\partial \Delta\boldsymbol{\varepsilon}}$ at $t + \Delta t$. The UMAT used in this project, provided by Dunne et al., solves these equations implicitly, meaning all quantities are written at the end of the time increment and stress is forced to converge back onto the yield surface within a specified tolerance using a plastic corrector term. In the UMAT the reduction of this stress residual to a tolerance of $\leq 10^{-12}\, MPa$ is carried out via the Newton-Raphson iterative method. We introduce this method by stating the stress at the end of the time increment, $\boldsymbol{\sigma}_{t+\Delta t}$, written in terms of an elastic trial stress, $\boldsymbol{\sigma}^{tr}$, and the plastic corrector term.

$$\boldsymbol{\sigma}_{t+\Delta t} = \boldsymbol{D}(\boldsymbol{\varepsilon}_t^e + \Delta\boldsymbol{\varepsilon}^e) = \boldsymbol{D}(\boldsymbol{\varepsilon}_t^e + \Delta\boldsymbol{\varepsilon} - \Delta\boldsymbol{\varepsilon}^p) = \boldsymbol{\sigma}^{tr} - \boldsymbol{D}\Delta\boldsymbol{\varepsilon}^p \tag{4.41}$$

Total strain increment, $\Delta\boldsymbol{\varepsilon}$, is found using the decomposition of strain, i.e. $\Delta\boldsymbol{\varepsilon} = \Delta\boldsymbol{\varepsilon}^e + \Delta\boldsymbol{\varepsilon}^p$. $\boldsymbol{D}\Delta\boldsymbol{\varepsilon}^p$ is the plastic corrector term, where $\boldsymbol{D}$ is the global elastic constitutive

matrix, $\boldsymbol{D}$ can be found from the local stiffness matrix, $\boldsymbol{C}$, using appropriate rotation matrices, $\boldsymbol{T}$, and is given by,

$$\boldsymbol{D} = \boldsymbol{T}_\sigma \boldsymbol{C} \boldsymbol{T}_\sigma^T \tag{4.42}$$

the rotation matrices, $\boldsymbol{T}_\sigma^{-1}$and $\boldsymbol{T}_\varepsilon$, are updated at each time increment due to crystal rotation.

The trial stress is,

$$\boldsymbol{\sigma}^{tr} = \boldsymbol{\sigma}_t + \boldsymbol{D}\Delta\boldsymbol{\varepsilon} + (\boldsymbol{\omega}\boldsymbol{\sigma}_t - \boldsymbol{\sigma}_t\boldsymbol{\omega})\Delta t \tag{4.43}$$

The strain increment, $\Delta\boldsymbol{\varepsilon}$, can be found by recalling the equation for rate of deformation in (4.15),

$$\Delta\boldsymbol{\varepsilon} = \boldsymbol{\Phi}\Delta t \tag{4.44}$$

given in terms of the symmetric part of the velocity gradient, $\boldsymbol{L}$, is

$$\Delta\boldsymbol{\varepsilon} = \frac{1}{2}\left(\boldsymbol{L} + \boldsymbol{L}^T\right)\Delta t \tag{4.45}$$

The Velocity gradient, $\boldsymbol{L}$, can be found from the deformation gradient, $\boldsymbol{F}$, using the relation given in (4.12), and the rate of continuum spin, $\boldsymbol{\omega}$, is calculated using (4.16). The stress at the end of the time increment, $t+\Delta t$, is initially assumed to be the elastic trial stress, $\boldsymbol{\sigma}_{t+\Delta t} = \boldsymbol{\sigma}^{tr}$. This stress is then used to calculate the resolved shear stress (RSS) on each slip system. The RSS, τ_r^κ, on the κ^{th} slip system in Voigt notation is,

$$\tau_r^\kappa = (\boldsymbol{n}^\kappa \otimes \boldsymbol{s}^\kappa) \colon \boldsymbol{\sigma}_{t+\Delta t} \tag{4.46}$$

Where $\boldsymbol{n}^\kappa$ and $\boldsymbol{s}^\kappa$ are the slip plane normal and slip direction on the κ^{th} slip system respectively. Yield occurs if

$$\frac{\tau_r^\kappa}{\tau_c} > 1 \tag{4.47}$$

where τ_c is the CRSS.

Note that the initial trial stress used will not be the final solution, but used as an initial guess to iterate via the Newton-Raphson loop to a more accurate solution. A

slip system is active if the RSS exceeds the critical value. If the slip system is active then $\Delta\boldsymbol{\varepsilon}^p$ is > 0, and the plastic corrector term will need to be included. The stress is then updated iteratively within the time increment to find a solution. The plastic strain increment, $\Delta\boldsymbol{\varepsilon}^p$, given in terms of the symmetric part of the plastic velocity gradient, $\boldsymbol{L}^p$, given by

$$\Delta\boldsymbol{\varepsilon}^p = \frac{1}{2}\left(\boldsymbol{L}^p + \boldsymbol{L}^{pT}\right)\Delta t \tag{4.48}$$

or simplified to,

$$\Delta\boldsymbol{\varepsilon}^p = \mathrm{sym}\left(\boldsymbol{L}^p\right)\Delta t \tag{4.49}$$

The consistency condition states that the stress state should remain on the yield surface, thus the stress residual within the increment needs to be reduced to achieve an accurate solution. This comes with computational cost, hence the stress residual is only reduced to a specified tolerance. The stress residual is given by,

$$\boldsymbol{\psi} = \boldsymbol{\sigma}_{t+\Delta t} - \boldsymbol{\sigma}^{tr} + \boldsymbol{D}\Delta\boldsymbol{\varepsilon}^p \tag{4.50}$$

applying the differential operator to give,

$$\delta\boldsymbol{\psi} = \delta\boldsymbol{\sigma} - \delta\boldsymbol{\sigma}^{tr} + \boldsymbol{D}\delta\Delta\boldsymbol{\varepsilon}^p \tag{4.51}$$

The differential operator applied to the equation for $\Delta\boldsymbol{\varepsilon}^p$, given in (4.49) and combining with the constitutive equation for $\boldsymbol{L}^p$ in (4.38) gives,

$$\delta\Delta\boldsymbol{\varepsilon}^p = \delta\mathrm{sym}\left\{\sum_\kappa \alpha \sinh\beta(\tau_r^\kappa - \tau_c^\kappa)\Delta t\mathbf{s}^\kappa \otimes \mathbf{n}^\kappa\right\} \tag{4.52}$$

differentiating to give

$$\delta\Delta\boldsymbol{\varepsilon}^p = \mathrm{sym}\left\{\sum_\kappa \alpha\beta \cosh\beta(\tau_r^\kappa - \tau_c^\kappa)\Delta t\mathbf{s}^\kappa \otimes \mathbf{n}^\kappa\delta\tau_r^\kappa\right\} \tag{4.53}$$

By using the relation, $\delta\tau_r^\kappa = (\boldsymbol{n}^\kappa \otimes \boldsymbol{s}^\kappa)\colon \delta\boldsymbol{\sigma}$ [178], substituting into (4.53), for ease of notation, we replace the tensor quantity previously differentiated with $\boldsymbol{P}$ [178]. Therefore we get,

$$\delta\Delta\boldsymbol{\varepsilon}^p = \boldsymbol{P}\delta\boldsymbol{\sigma} \tag{4.54}$$

where

$$\boldsymbol{P} = \sum_{\kappa} \alpha\beta \cosh \beta(\tau_r^{\kappa} - \tau_c^{\kappa}) \Delta t \boldsymbol{A}^{\kappa} \otimes \boldsymbol{A}^{\kappa} \tag{4.55}$$

and

$$\boldsymbol{A}^{\kappa} = \boldsymbol{n}^{\kappa} \otimes \boldsymbol{s}^{\kappa} \tag{4.56}$$

Substituting (4.54) into (4.51) to get an expression for the stress residual in terms of the stress increment,

$$\delta\boldsymbol{\psi} = \delta\boldsymbol{\sigma} - \delta\boldsymbol{\sigma}^{tr} + \boldsymbol{D}\boldsymbol{P}\delta\boldsymbol{\sigma} \tag{4.57}$$

rearranging to get,

$$\delta\boldsymbol{\psi} = [\boldsymbol{I} + \boldsymbol{D}\boldsymbol{P}]\, \delta\boldsymbol{\sigma} - \delta\boldsymbol{\sigma}^{tr} \tag{4.58}$$

A first order approximation of $\boldsymbol{\psi}(\boldsymbol{\sigma})$ using a Taylor expansion gives,

$$\boldsymbol{\psi}(\boldsymbol{\sigma}) = \boldsymbol{\psi} + \frac{\partial \boldsymbol{\psi}}{\partial \boldsymbol{\sigma}} \delta\boldsymbol{\sigma} = \boldsymbol{\sigma}_{t+\Delta t} - \boldsymbol{\sigma}^{tr} + \boldsymbol{D}\Delta\boldsymbol{\varepsilon}^{p} + [\boldsymbol{I} + \boldsymbol{D}\boldsymbol{P}]\, \delta\boldsymbol{\sigma} = 0 \tag{4.59}$$

This can then be rearranged to give the stress increment,

$$\delta\boldsymbol{\sigma} = [\boldsymbol{I} + \boldsymbol{D}\boldsymbol{P}]^{-1} \left\{ \boldsymbol{\sigma}^{tr} - \boldsymbol{\sigma}_{t+\Delta t} - \boldsymbol{D}\mathrm{sym} \left(\sum_{\kappa} \alpha \sinh \beta(\tau_r^{\kappa} - \tau_c^{\kappa}) \Delta t \mathbf{s}^{\kappa} \otimes \mathbf{n}^{\kappa} \right) \right\} \tag{4.60}$$

The stress is then updated iteratively within the Newton loop with,

$$\boldsymbol{\sigma}^{(n+1)} = \boldsymbol{\sigma}^{(n)} + \delta\boldsymbol{\sigma} \tag{4.61}$$

where,

$$\boldsymbol{\sigma}^{(0)} = \boldsymbol{\sigma}^{tr}$$

This stress is then inputted back into (4.46), and the loop continues until a suitably low stress residual is achieved,

$$|\boldsymbol{\psi}| \leqslant 10^{-12} MPa$$

at which point,

$$\boldsymbol{\sigma}_{t+\Delta t} = \boldsymbol{\sigma}^{(n)}$$

If a limit of fifty iterations is exceeded, $n > 50$, then the stress is deemed to have failed

to converge, and the simulation is terminated.

Finally, we need to provide ABAQUS with the consistent tangent stiffness matrix, or Jacobian, $\boldsymbol{J}$. From (4.58) with $\psi \approx 0$ and by using the relation $\delta\boldsymbol{\sigma}^{tr} \equiv \boldsymbol{D}\delta\boldsymbol{\varepsilon}$ [178], we can rearrange to find an expression for the stress in differential form as,

$$\delta\boldsymbol{\sigma} = [\boldsymbol{I} + \boldsymbol{DP}]^{-1}\boldsymbol{D}\delta\boldsymbol{\varepsilon} \tag{4.62}$$

This allows calculation of the material Jacobian,

$$\boldsymbol{J} = \frac{\partial\Delta\boldsymbol{\sigma}}{\partial\Delta\boldsymbol{\varepsilon}} = [\boldsymbol{I} + \boldsymbol{DP}]^{-1}\boldsymbol{D} \tag{4.63}$$

4.2.4 UMAT implementation of the GND density calculation

Nye's tensor, from (4.32), can be given in terms of the summation of dislocation dyadics, $\boldsymbol{d}_\kappa$, such that,

$$\boldsymbol{G}_U^{pT} = \mathrm{Curl}\boldsymbol{F}^p = \sum_{\kappa=1}^{n} \rho_\kappa \boldsymbol{d}_\kappa \tag{4.64}$$

Where $\boldsymbol{d}_\kappa$ is given by the dyadict product of the unit line vector, $\mathbf{l}_\kappa$, and the unit Burgers vector, $\boldsymbol{b}_\kappa$, for the κ^{th} slip system:

$$\boldsymbol{d}_\kappa = \mathbf{l}_\kappa \otimes \boldsymbol{b}_\kappa \tag{4.65}$$

The Curl$\boldsymbol{F}^p$ (a 3 x 3 square matrix), from the equation for Nye's tensor (4.64), can be rewritten as a [9 x 1] column vector represented by $\boldsymbol{\Lambda}$. The relationship between Nye's tensor and the dislocation density vector, $\boldsymbol{\rho}_{GND}$, can then be given as,

$$\boldsymbol{A}\boldsymbol{\rho}_{GND} = \boldsymbol{\Lambda} \tag{4.66}$$

Where $\boldsymbol{A}$ represents a matrix of dislocation dyadics; for each slip system there is a dyadic vector, $\boldsymbol{d}_\kappa$, rearranged as a [9 x 1] vector, these then form matrix $\boldsymbol{A}$,

$$\boldsymbol{A} = [\boldsymbol{d}_1\boldsymbol{d}_2...\boldsymbol{d}_n] \tag{4.67}$$

$\boldsymbol{A}$ is therefore a [9 x n] matrix, with n being the total number of slip systems. In this project, the total number of slip systems is 28 (24 edge slip systems, and 4 screw systems). From (4.66) we see that the inverse of $\boldsymbol{A}$ must be taken to calculate the GND densities on each slip system. Since there are more columns than rows, the UMAT takes the right inverse, $\boldsymbol{A}^{-R}$, given by

$$\boldsymbol{A}^{-R} = \boldsymbol{A}^T(\boldsymbol{A}^T\boldsymbol{A})^{-1} \tag{4.68}$$

The GND densities on each slip system can then be calculated from,

$$\boldsymbol{\rho}_{GND} = \boldsymbol{A}^{-R}\boldsymbol{\Lambda} \tag{4.69}$$

This results in a [28 x 1] vector for $\boldsymbol{\rho}_{GND}$, with each component representing the GND density on the 28 respective slip systems.

4.2.5 Crystal plasticity UMAT implementation summary

For ease of reference, a summary is provided below of how the UMAT calculates the stresses and material Jacobian at time $t + \Delta t$, from the knowledge of the stresses at time, t, and deformation gradient at time, t and $t + \Delta t$ (provided by ABAQUS).

1. ABAQUS gives the UMAT the deformation gradient at the start and end of the increment, $\boldsymbol{F}_t$ and $\boldsymbol{F}_{t+\Delta t}$. With knowledge of the time increment, Δt, also given by ABAQUS, the velocity gradient, L, can then be found using the relation,

$$\boldsymbol{L} = \dot{\boldsymbol{F}}\boldsymbol{F}^{-1}$$

Where the time increment, Δt, is a fraction of 1, and subsequently dimensionless; at the beginning of the simulation $t = 0$, and at the end of the simulation $t = 1$.

2. Determine the rates of deformation and continuum spin using the symmetric and asymmetric parts of $\boldsymbol{L}$,

$$\boldsymbol{\Phi} = \frac{1}{2}(\boldsymbol{L} + \boldsymbol{L}^T)$$

$$\boldsymbol{\omega} = \frac{1}{2}(\boldsymbol{L} - \boldsymbol{L}^T)$$

3. Stress at the end of the time increment, $\boldsymbol{\sigma}_{t+\Delta t}$ is given in terms of an elastic trial stress and plastic corrector term

$$\boldsymbol{\sigma}_{t+\Delta t} = \boldsymbol{\sigma}^{tr} - \boldsymbol{D}\Delta\boldsymbol{\varepsilon}^p$$

4. Initially stress is assumed to be purely elastic, e.g. the elastic trial stress, $\boldsymbol{\sigma}^{tr}$. This elastic trial stress is used to calculate the RSS, τ^κ, on the κ^{th} slip system,

$$\tau^\kappa = (\boldsymbol{n}^\kappa \otimes \boldsymbol{s}^\kappa) \colon \boldsymbol{\sigma}_{t+\Delta t}$$

5. Determine active slip systems using,

$$\frac{\tau_r^\kappa}{\tau_c} > 1$$

where τ_c is the CRSS.

6. If yield condition is met then the plastic corrector term, $\boldsymbol{D}\Delta\boldsymbol{\varepsilon}^p$, is > 0. The plastic strain increment, $\Delta\boldsymbol{\varepsilon}^p$, is given by

$$\Delta\boldsymbol{\varepsilon}^p = \mathrm{sym}\left(\boldsymbol{L}^p\right)\Delta t$$

If $\Delta\boldsymbol{\varepsilon}^p > 0$ then a Newton-Raphson iterative loop within the overall time increment is needed to determine the stress and Jacobian at the end of the time increment, $\boldsymbol{\sigma}_{t+\Delta t}$ and $\frac{\partial\boldsymbol{\sigma}}{\partial\boldsymbol{\varepsilon}}$.

7. For the Newton-Raphson loop we need to determine stress residual, $\boldsymbol{\psi}$,

$$\boldsymbol{\psi} = \boldsymbol{\sigma}_{t+\Delta t} - \boldsymbol{\sigma}^{tr} + \boldsymbol{D}\Delta\boldsymbol{\varepsilon}^p = 0$$

8. The plastic strain increment, $\Delta\boldsymbol{\varepsilon}^p$, is given in terms of the constitutive equation for $\boldsymbol{L}^p$ by

$$\Delta\boldsymbol{\varepsilon}^p = \delta\mathrm{sym}\left\{\sum_{\kappa}\alpha\sinh\beta(\tau_r^{\kappa} - \tau_c^{\kappa})\Delta t\mathbf{s}^{\kappa}\otimes\mathbf{n}^{\kappa}\right\}$$

9. Determine the stress increment

$$\delta\boldsymbol{\sigma} = [\boldsymbol{I} + \boldsymbol{DP}]^{-1}\left(\boldsymbol{\sigma}^{tr} - \boldsymbol{\sigma}_{t+\Delta t} - \boldsymbol{D}\Delta\boldsymbol{\varepsilon}^p\right)$$

10. Update the stress at the end of the time increment, by adding the new stress increment to the previous increment.

$$\boldsymbol{\sigma}^{(n+1)} = \boldsymbol{\sigma}^{(n)} + \delta\boldsymbol{\sigma}$$

Each time around the loop the RSS is updated using the new stress $\boldsymbol{\sigma}_{n+1}$, the new stress residual can then be determined.

11. The Newton-Raphson loop is iterated within the time increment until the stress residual, $\boldsymbol{\psi}$, is reduced to a specified tolerance,

$$|\boldsymbol{\psi}| \leqslant 10^{-12} MPa$$

If $|\boldsymbol{\psi}| \geq 10^{-12}$ then a new increment is found and the stress updated. After the stress residual has been reduced to the specified tolerance, the stress at the end of the time increment can be found from the stress used in the last Newton-Raphson loop, $\boldsymbol{\sigma}_{t+\Delta t} = \boldsymbol{\sigma}^{(n)}$. If a limit of fifty iterations is exceeded, the stress is deemed to have failed to converge, and the simulation is terminated.

12. Determine the Jacobian for the end of the time increment.

$$\boldsymbol{J} = \frac{\partial \Delta \boldsymbol{\sigma}}{\partial \Delta \boldsymbol{\varepsilon}} = [\boldsymbol{I} + \boldsymbol{D}\boldsymbol{P}]^{-1} \boldsymbol{D}$$

4.3 UMAT code check and model optimisation

4.3.1 Introduction

The UMAT, developed by Dunne et al. (2012) [238], was used to investigate the contribution GNDs have to the microcantilever size effect. For this investigation the UMAT was implemented within the commercially available ABAQUS 6.14-2 finite element (FE) software. The UMAT required the use of a twenty-noded quadratic hexahedral element with reduced integration (C3D20R), as shown in figure 4.1. Before beginning these investigations, the validity of the model had to be checked and the code optimised for the material used in the experimental part of the project. First, approximate values for the constants used within the UMAT were determined.

4.3.2 Identification of UMAT constants

Approximations for certain constants could be found or derived from literature; others had to be found by matching single crystal cantilever simulations to load-displacement data of an experimental 5 x 5 x 30 μm 14WT 1150 microcantilever through a manual trail and error process. Table 4.1 displays the values obtained for each UMAT constant, and whether the value was obtained from literature or from manual fitting. The purpose of the fitting was to obtain realistic approximations to the values of the constants used within the UMAT. Clearly, the values derived from this method are only approximations, since lattice orientation and grain size of the experimental microcantilever were not taken into account. The parameters used within the UMAT for the remainder of the investigation are given in table 4.1, unless otherwise stated.

Material property	Value	Reference
Elastic modulus, $E_{<100>}$	170 GPa	Fitted to data
Shear modulus, G	80 GPa	[255]
Poisson's ratio, v	0.3	[255]
Burger's vector, b	2.5 x 10^{-10} m	[256]
Helmholtz free energy, ΔH	2.6 x 10^{-20} J	[256]
Boltzman constant, k.	1.381 x 10^{-23} JK^{-1}	[256]
Temperature, T	293 K	
Attempt frequency, ν.	1.0 x 10^{11} s^{-1}	[256]
Density of Statistically stored dislocations, ρ_{SSD}	1 x 10^{10} m^{-2}	[256]
CRSS, τ_c	90 MPa	Fitted to data
Density of mobile dislocations, ρ_m	6 x 10^9 m^{-2}	Fitted to data
Reference strain, γ_0	8 x 10^{-6}	Fitted to data
Probability of pinning, ψ	4 x 10^{-5}	Fitted to data

Table 4.1: Material properties are for ferrite iron from literature and the rest, from experimental matching with a 5 x 30 μm 14WT 1150 microcantilever.

4.3.3 Mesh convergence

The accuracy of a FE model greatly depends on the mesh density. For most cases, the finer the mesh, the more accurate the solution. If the mesh is progressively refined, then the solution will asymptotically tend to a stable result, given enough iterations. If an analytical solution exists, then the model solution will converge an exact result. A valid solution is obtained by allowing the values of interest to converge to a stable result, and ensuring that specific values extracted from the solution are not derived from areas on or near a singularity. As the mesh is refined the computational time needed to reach a solution increases, so there is a compromise between solution stability and

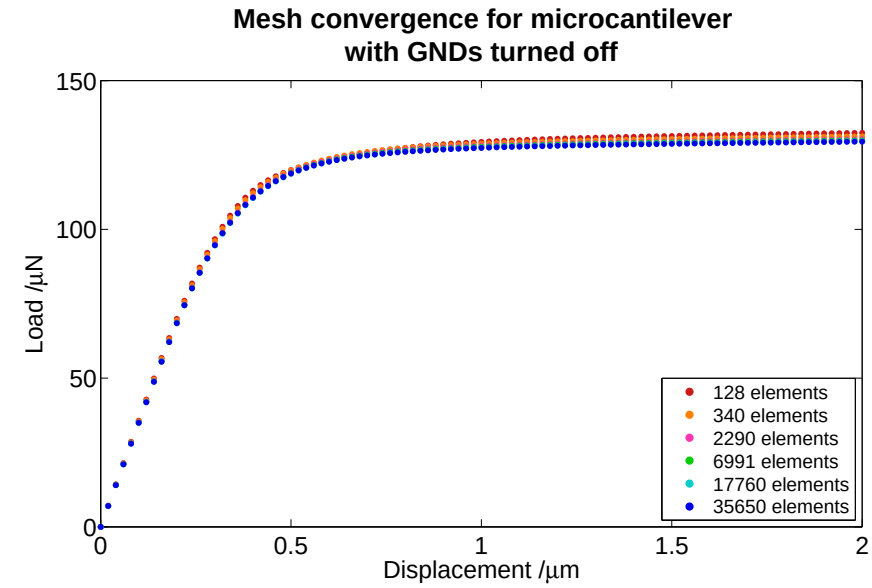
computational cost. However, the maximum computational time for a simulation was on the order of 1 - 2 hours, so the mesh convergence study focused on solution stability.

The mesh convergence study for this project looked at a typical sized microcantilever using constants suggested by literature and approximate single crystal matching of an experimental microcantilever (given in table 4.1). The total number of elements was varied from $\sim$ 100 to $\sim$ 40,000 and plotted against load at a tip displacement of 2 μm, results are presented in figure 4.3(b). Values of load at 2 μm displacement were chosen for the mesh convergence as this was where the variance between the FE solutions was greatest. Special consideration should be given to the stress concentrations, particularly singularities, i.e. at the lower vertex at the fixed end of the cantilever model.

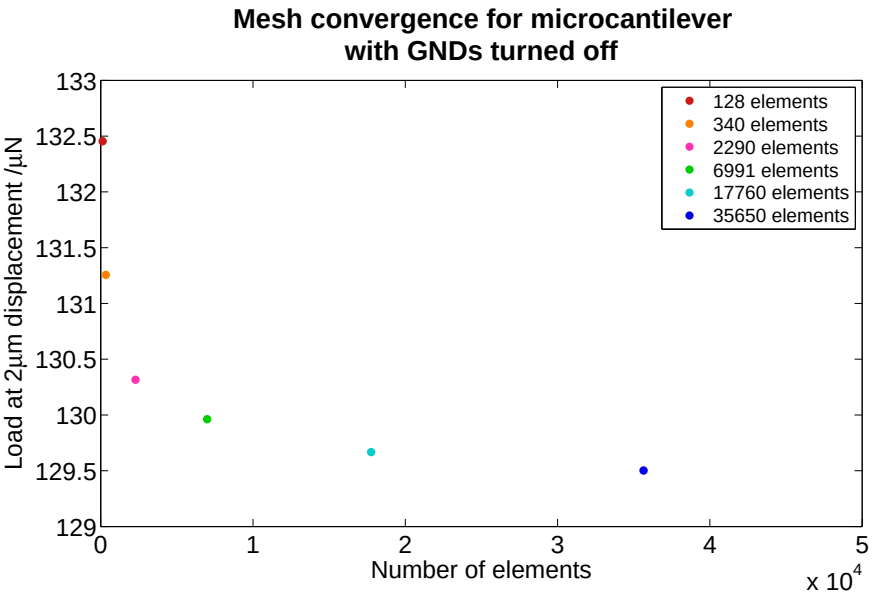
FE modelling allows for a perfectly sharp corners, resulting in singularities at these points. The stress at a singularity does not converge towards a specific value: as the mesh is refined further the stress in the five elements that make up the vertex will tend towards infinity. St. Venant's principle allows us to ignore singularities as long as the stress is taken at a suitable distance away from this point. The introduction of plasticity also allows the model to negate a singularity, although the stress concentration at the lower vertex still remains an important consideration when analysing a solution. It is at this point that the material will first yield; in a realistic cantilever this vertex will be a fillet and not a singularity, generally providing a larger area of stress concentration, but of a lower maximum stress. This may lead to slight differences in yield behaviour, since yield in the model will occur at any integration point with a stress greater than the CRSS on the κ^{th} slip system. Whereas realistically, yield is dependent on the distribution and activation stress of dislocation sources.

The UMAT provides an option for excluding the part of the code that describes the evolution of GNDs during plastic flow. If this portion of the code is excluded then no hardening will occur, since the code assumes the all work hardening to be product of Taylor hardening provided by a density of GNDs. For simplicity, the mesh convergence

was initially carried out with GND evolution excluded, i.e. perfect plasticity. The results from the mesh convergence study, displayed in figure 4.3 and 4.4, were carried out on a 5 x 30 μm microcantilever meshed using an unbiased structured meshing algorithm (discussed further in section 4.3.5).

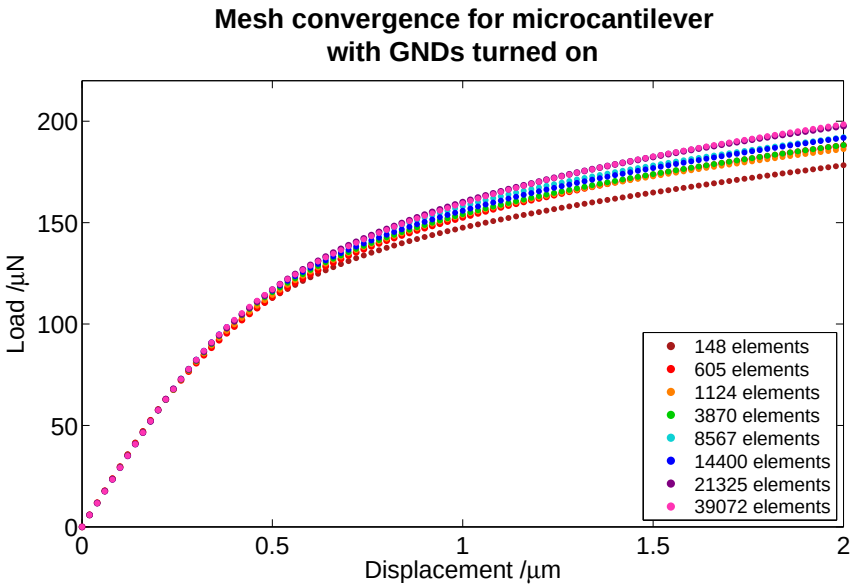


(a)

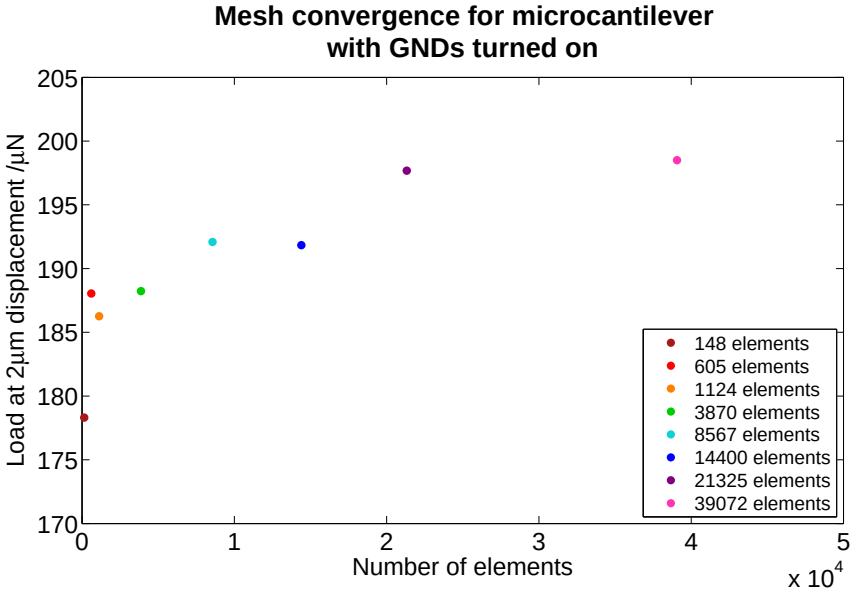


(b)

Figure 4.3: Mesh convergence study without GNDs, e.g. no work hardening. (a) The load against displacement for six microcantilevers with varying element number. (b) A plot of the load value at 2 μm displacement against element number, as element density increases, the FE solution converges to a specific value.



(a)



(b)

Figure 4.4: Mesh convergence study with GNDs included. (a) The load against displacement for eight microcantilevers with varying element number. (b) A plot of the load value at 2 μm displacement against element number, as element density increases, the FE solution converges to a specific value.

Figure 4.3(a) and (b) shows the FE model tending towards a specific solution as the mesh is refined. Figure 4.3(b) plots the load at 2 μm displacement with an increasing mesh density. Doubling the number of elements from $\sim 1.8\,\text{x}10^4$ to $\sim 3.6\,\text{x}10^4$ did not significantly alter the solution. The mesh convergence study was then carried out on the same microcantilever with GND work hardening included with in the slip rule.

Similar to the case with GNDs excluded from the UMAT (figure 4.3), figure 4.4 also shows the FE model tending towards a specific solution. Both models reach an acceptably stable solution when the number of elements reaches $\sim\ 2\,\text{x}10^4$. However, unlike for case where GNDs are excluded, refining the mesh with GNDs included increases the work hardening observed.

4.3.4 GND check

The UMAT describes the slip on the first twenty four slip systems for BCC crystal structures. It neglects the $\{321\}\langle 111\rangle$ slip systems to simplify the calculations, since the majority of the slip occurs on on the systems with lower stacking fault energy, i.e. $\{110\}\langle 1\bar{1}1\rangle$ and $\{211\}\langle \bar{1}11\rangle$ [257]. To check whether the distribution of GNDs calculated within the model were realistic, it was necessary to check whether the GND density found on the κ^{th} slip system follows the corresponding Schmid factor. For the GND check, a 5 x 30 μm microcantilever with a uniform structured mesh was used. Figure 4.5 shows a graphical representation of the GND density in both the undeformed (a) and deformed (b) microcantilever, with a representative element highlighted in red. This element was used to plot GND density against displacement for all twenty four slip systems, shown in figure 4.6. Each slip system is represented by a solution dependent variable (SDV), from SDV57 through to SDV80.

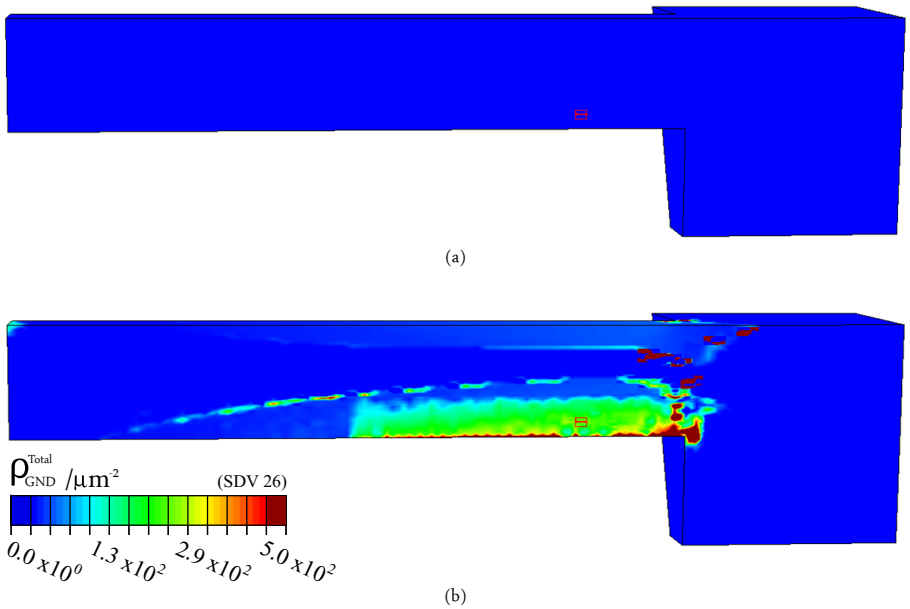


Figure 4.5: Element chosen for GND check outlined in red. (a) Undeformed 5x30 μm single crystal microcantilever with unity rotation matrix, cut along the central axis. (b) Deformed version, with deformation scale factor equal to zero, showing the total GND density (SDV 26).

SDV	Slip system	Schmid factor	GND density at 2μm displacment $/\mu\text{m}^{-2}$
71	$(1\ \bar{1}\ 2)[\bar{1}\ 1\ 1]$	0.471	10.4
72	$(1\ 1\ \bar{2})[1\ 1\ 1]$	0.471	9.8
70	$(\bar{1}\ 1\ 2)[1\ \bar{1}\ 1]$	0.471	8.4
69	$(1\ 1\ 2)[1\ 1\ \bar{1}]$	0.471	7.4
64	$(0\ 1\ \bar{1})[\bar{1}\ 1\ 1]$	0.408	9.4
63	$(0\ 1\ \bar{1})[1\ 1\ 1]$	0.408	9.2
67	$(1\ 0\ 1)[\bar{1}\ 1\ 1]$	0.408	9.0
65	$(0\ 1\ 1)[1\ \bar{1}\ 1]$	0.408	8.3
59	$(\bar{1}\ 0\ 1)[1\ 1\ 1]$	0.408	8.2
66	$(0\ 1\ 1)[1\ 1\ \bar{1}]$	0.408	7.8
60	$(\bar{1}\ 0\ 1)[1\ \bar{1}\ 1]$	0.408	7.5
68	$(1\ 0\ 1)[1\ 1\ \bar{1}]$	0.408	5.3
75	$(1\ \bar{2}\ 1)[1\ 1\ 1]$	0.236	6.4
76	$(1\ 2\ \bar{1})[\bar{1}\ 1\ 1]$	0.236	6.4
73	$(1\ 2\ 1)[1\ \bar{1}\ 1]$	0.236	6.3
74	$(\bar{1}\ 2\ 1)[1\ 1\ \bar{1}]$	0.236	6.1
77	$(2\ 1\ 1)[\bar{1}\ 1\ 1]$	0.236	5.6
78	$(\bar{2}\ 1\ 1)[1\ 1\ 1]$	0.236	5.2
80	$(2\ 1\ \bar{1})[1\ \bar{1}\ 1]$	0.236	5.2
79	$(2\ \bar{1}\ 1)[1\ 1\ \bar{1}]$	0.236	4.3
57	$(1\ 1\ 0)[\bar{1}\ 1\ 1]$	0.000	0
58	$(1\ 1\ 0)[1\ \bar{1}\ 1]$	0.000	0
61	$(\bar{1}\ 1\ 0)[1\ 1\ 1]$	0.000	0
62	$(\bar{1}\ 1\ 0)[1\ 1\ \bar{1}]$	0.000	0

Table 4.2: The Schmid factor and corresponding GND density for the twenty four BCC slip systems coded in the UMAT.

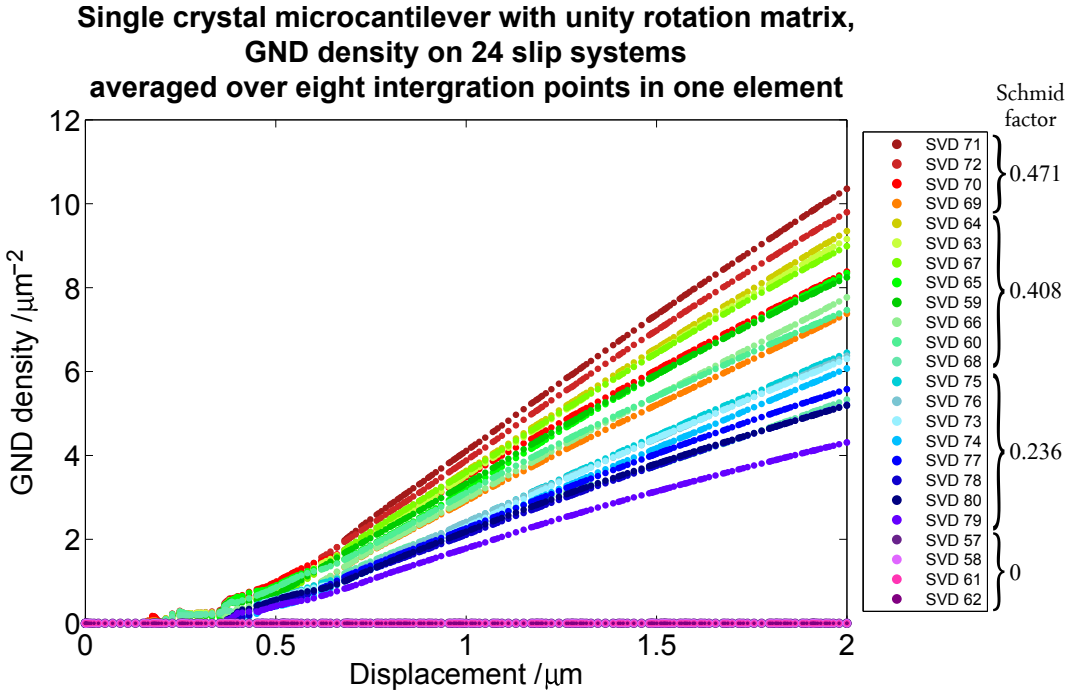


Figure 4.6: The GND density on all twenty four BCC slip systems written in the UMAT, averaged over eight integration points in the element highlighted in figure 4.5(b). The SDVs coloured in red, green, blue and purple, represent Schmid factors 0.471, 0.408, 0.236 and 0 respectively.

Table 4.2 shows the Schmid factor on each of the twenty four slip systems included in the UMAT. For the crystal orientation chosen, there are four different Schmid factors, 0.471, 0.408, 0.236 and 0; these are colour coded in figure 4.6 with a variance of red, green, blue and purple respectively. The GND density was expected to be highest on the slip systems with the highest Schmid factor, and zero on the slip systems with a Schmid factor of zero. However, it can be seen that some slip systems with larger Schmid factors, contained lower GND densities than slip systems with smaller Schmid factors, e.g. $(1\ 1\ 2)[1\ 1\ \bar{1}]$ (SDV 69) with a Schmid factor of 0.471 contained a lower GND density than all but one of the slip systems with a Schmid factor of 0.408.

There are two likely reasons for this. Firstly, the Schmid factors were calculated for the crystal orientation in the beam prior to load, with [0 0 1] direction aligned with the beam axis, the [1 0 0] with the beam width and [0 1 0] with the beam depth. With each

time increment, there will be a slight rotation of the crystal lattice as the cantilever is displaced, leading to a change in the Schmid factor not accounted for in table 4.2, particularly as the GND densities shown are those calculated at 2 μm displacement.

Secondly, the GND density is calculated from Nye's tensor, or the curl$\boldsymbol{F}^p$ (equation 4.32), which results in a second order tensor (9 components). The code extrapolates this onto 24 edge slip systems and 4 screw dislocation systems, using the method detailed in section 4.2.4. The version of the code used in this project was found to contain a source of error in the calculated GND density. Slip systems (and corresponding components of the $\boldsymbol{A}$ matrix) that were determined to have a RSS lower than the CRSS would be excluded from the $\boldsymbol{A}$ matrix. If the dimensions of $\boldsymbol{A}$ were not [9 x n] then it was possible that a solution to $\boldsymbol{A}^{-R}$ was non-existent, leading to leading to very large values for GND density at specific integration points. However, this error was unlikely to have had much effect, since the representative element chosen did not contain any noticeable spikes in the GND density. Also, the plot in in figure 4.6 demonstrates that the calculated GND densities generally correlate well with the respective Schmid factor of that slip system.

Next, the lengthscale dependency of the plastic strain, $\boldsymbol{\varepsilon}^p$, needed to be examined to check whether the CP model matched the experimentally observed size effect. This test was initially performed on a 5 x 30 μm microcantilever comprised of nodal points that were seeded using a swept mesh with a size bias focused towards the fixed end, as shown in figure 4.7. A bias was used as it was seen as a good compromise between having a sufficient mesh density, particularly surrounding the fixed end, and computational expense. The mesh was created using the swept meshing technique using the medial axis meshing algorithm. Using this method allowed the mesh to have a more regular geometry when used in combination with a bias. To test the size dependence of the CP model, microcantilevers of two different sizes, 5 x 30 μm and 1 x 6 μm, were modelled. Both microcantilevers had the same mesh density, and the displacement of the free end was adjusted to give the same strain throughout the simulation. The microcantilever

models were run with GNDs excluded from the UMAT, figure 4.8(a), and then again with GNDs included, figure 4.8(b).

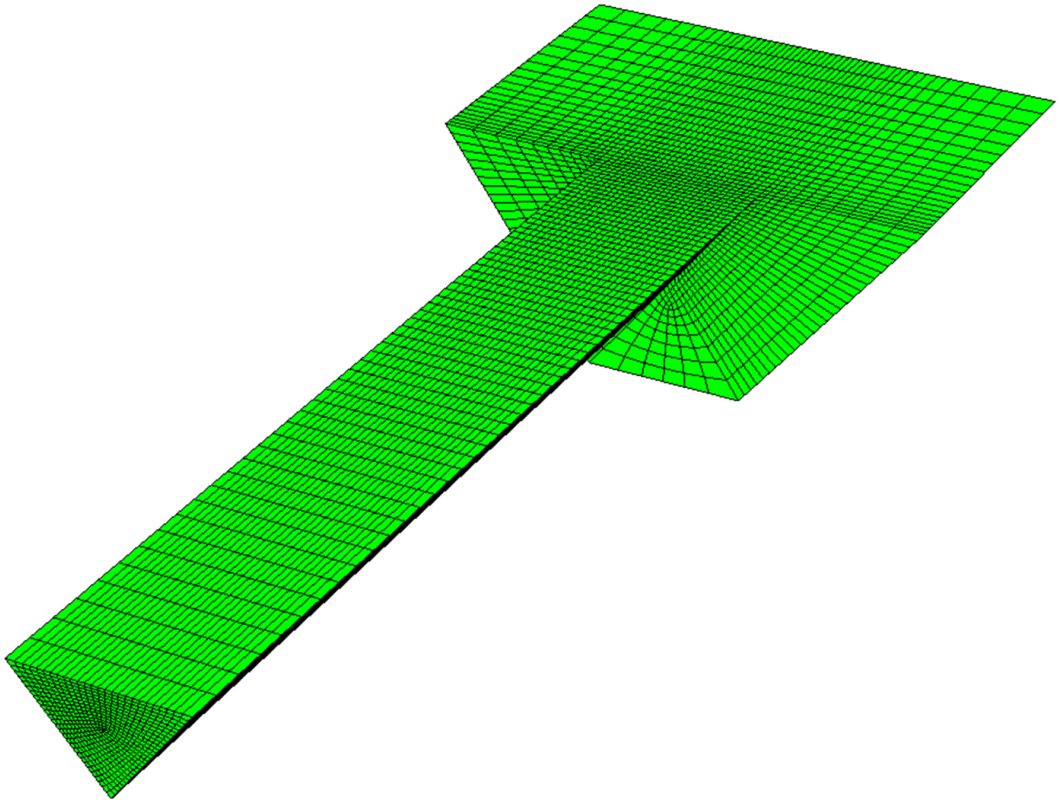
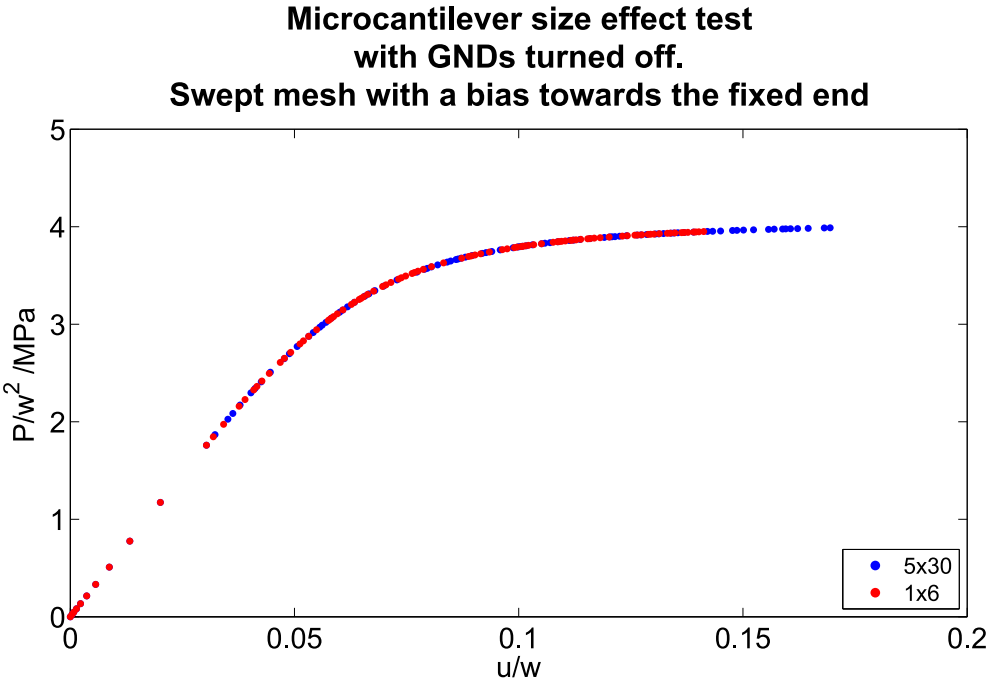
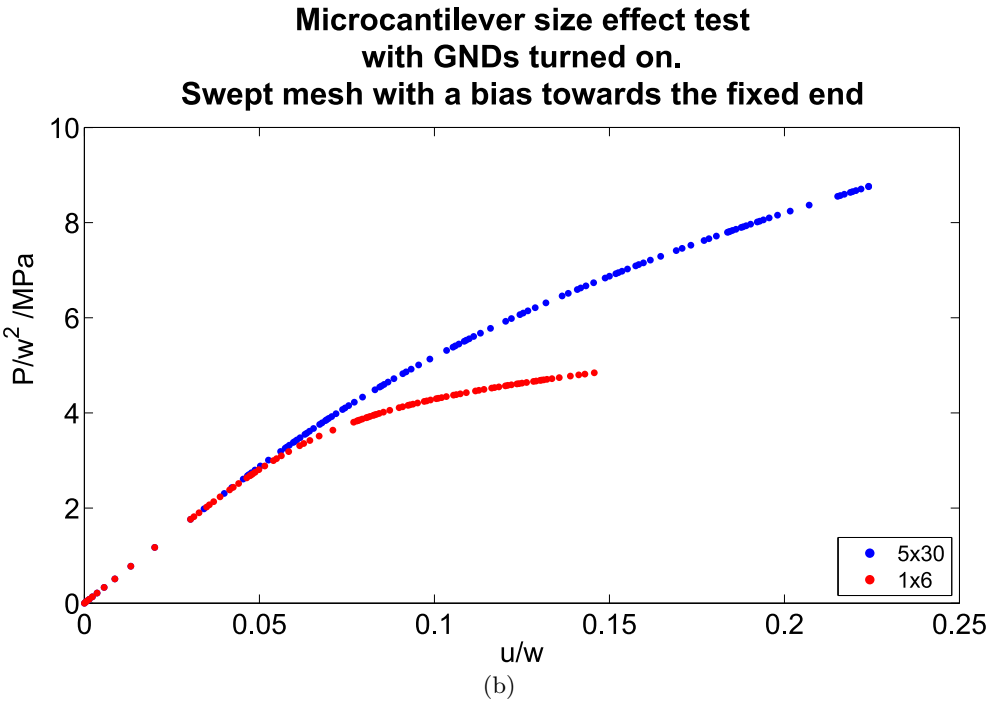


Figure 4.7: 5x30 μm microcantilever with a Swept mesh, biased towards the fixed end.



(a)



(b)

Figure 4.8: Microcantilever of two sizes, 5x30 μm and 1x6 μm, meshed with a swept algorithm with a bias towards the fixed end. Both plots use a load, P, and displacement, u, normalised with cantilever width, w. (a) The two microcantilevers with the GNDs turned off, showing no work hardening behaviour. (b) The two microcantilevers with the GNDs turned on. Here size dependent behaviour is the reverse of what was expected.

To compare load-displacement data from microcantilevers of different sizes figure 4.8(a) and (b) plots load, P, against displacement, u, is normalised with microcantilever width, w. This is analogous to a stress-strain plot. To prove this, recall that the simple beam equation for maximum stress (equation 3.2, p136) is,

$$\sigma_{max} = \frac{24Pl}{wd^2}$$

where P is the applied load on the beam at the load-point. The beam width, length and depth are given by w, l and d respectively. Simple beam stress can also be written as,

$$\sigma_{max} = \frac{P}{w^2}\beta \tag{4.70}$$

where,

$$\beta = \frac{24lw}{d^2} \tag{4.71}$$

For the microcantilevers in this work $\beta = \sim 144$. Recalling the simple beam equation for maximum strain (equation 3.3 p136), with u as displacement of the beam at the load point gives,

$$\varepsilon_{max} = \frac{2du}{l^2}$$

For the microcantilevers in this work, $w = d = \frac{l}{6}$ so that,

$$\varepsilon_{max} = \frac{u}{w}\gamma \tag{4.72}$$

where,

$$\gamma = \frac{1}{18} \tag{4.73}$$

We see from figure 4.8(a) that no work hardening or size dependent behaviour is present, this was as expected since, in this case, GNDs were excluded from the UMAT. The UMAT used in this project assumes all work hardening to be a result of dislocation pinning, or forest hardening, from a density of GNDs and SSDs. The size dependent behaviour in the UMAT results from the need to accommodate the plastic deformation

gradient, $\boldsymbol{F}^p$, within a smaller volume. In the case of microcantilevers, since the strain is inhomogeneous, this leads to large strain gradients. From (4.32), we see that GND density, ρ_{GND}, is proportional to the curl$\boldsymbol{F}^p$; leading to an increase in GND density for smaller microcantilevers, which in turn leads to less plastic strain, $\boldsymbol{\varepsilon}^p$, manifesting in an increase in work hardening, for a given increment in stress.

Figure 4.8(b) (with GND included) demonstrates a reversal of the expected size dependent behaviour. The larger 5 x 30μm microcantilever is more resistant to plastic flow than its smaller 1x6μm counterpart. If the model was functioning correctly the smaller microcantilever should have a higher GND density, thus causing a decrease in plastic strain, simulating an increase in dislocation pinning sites. Possible reasons for the failure of the model were thought to be:

- The meshing technique used.
- The complexity of the model with the addition of a base section.

These two points were investigated in the following section, after verifying the length-scale dependent hardening of UMAT using simple cubic models under uniaxial tensile and shear stress.

4.3.5 Meshing techniques

The UMAT requires the use of a twenty-noded quadratic hexahedral element with eight integration points, known within ABAQUS as C3D20R, shown in figure 4.1. ABAQUS provides two native top-down meshing techniques when using a hexahedral element, structured and swept. The structured meshing technique generates a mesh by fitting a predefined mesh topology, such as a cube or equilateral prism, onto the geometry of the region of interest. Swept meshing is most commonly used when structured technique either can not be used or fails to provide an adequate mesh. The swept meshing technique first creates a two dimensional mesh on one side of the region of interest, known

as the source side. The nodes of the source side are then copied one element layer at a time along a sweep path, until the final side, known as the target side, is meshed.

The element size created by the various meshing techniques was found to have a profound affect on the solution obtained. After the failure of the lengthscale dependent FE model to simulate the kind of size dependence that is observed experimentally, the effect that the two main meshing techniques, namely the structured and swept technique, had on the solution obtained was investigated.

Initially, A simple cubic model was used to examine the size effect in both shear and tensile stress fields. Once the size dependent behaviour was verified for the simple cubic case, the model complexity was then increased to a simplistic prismatic microcantilever that excluded the base. The aim was to discover the meshing technique that caused the reversal in the expected size effect, and to refine a technique to be used in a more realistic simulation of a microcantilever.

Simple cubic models

Cubic FE models were used to verify that the UMAT gave geometric size dependent solutions. The cubic models of size, 5 x 5 μm and 1 x 1 μm, were meshed using the structured technique, and subjected to shear and tensile stress fields. Figure 4.9(a) and (b) show the undeformed and deformed sheared cube, respectively. The cube was subjected to a shear stress applied to the upper surface, while the lower surface was constrained. Figure 4.9(b) displays a graphical representation of the total GND density, which is stored within the UMAT as SDV26.

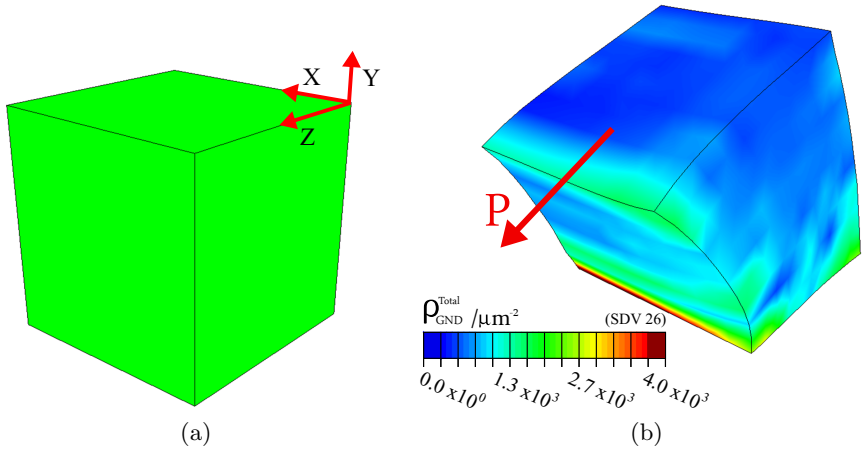


Figure 4.9: Size effect test on a simple cube undergoing a shear stress. (a) Undeformed cube. (b) Deformed cube.

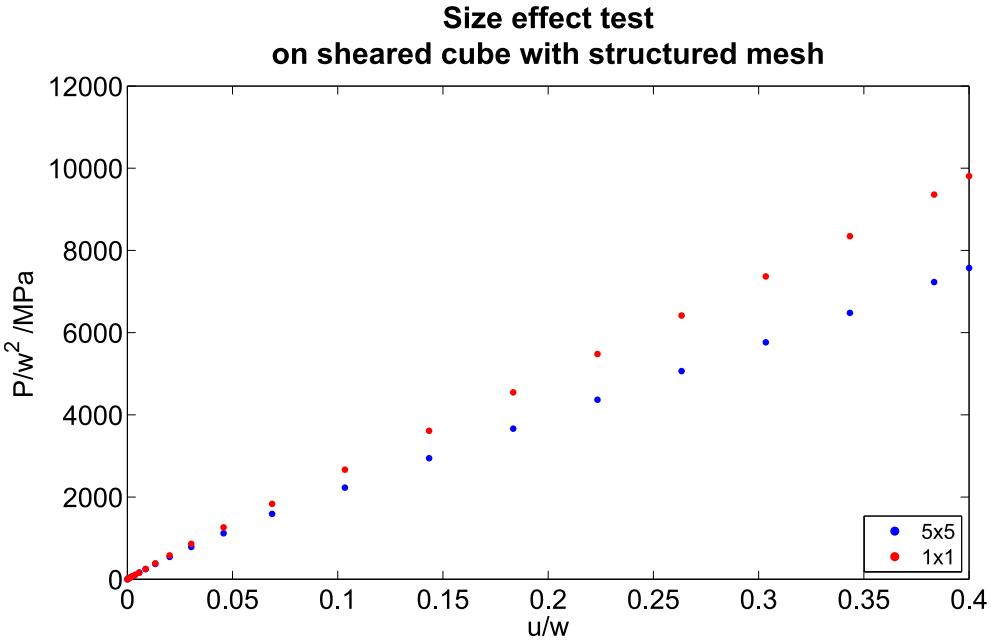


Figure 4.10: Size dependent behaviour of sheared cube.

Figure 4.10, plots normalised load (shear stress) against normalised displacement (shear strain) for the 5 x 5 μm and 1 x 1 μm shear deformed cubes. As the volume of the cube is decreased from 125 μm^3 to 1 μm^3 , the cube's apparent strength increases. This size effect is similar to that observed in experimental mechanical tests, of this approximate size range. This simple test demonstrated that is was possible to recreate micromechanical size dependency using the UMAT in its current form.

In a similar manner to the pure shear example, Figure 4.11(a) and (b) show the undeformed and deformed tensile cube, respectively. The tensile stress was applied to the front surface, and the back surface was constrained in such a way as to allow no movement of the nodes accept contraction.

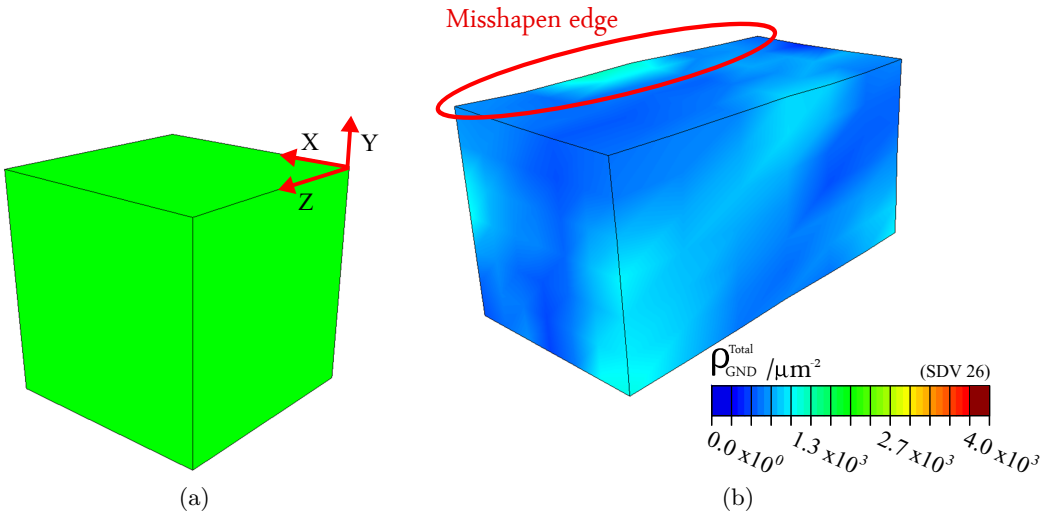


Figure 4.11: Size effect test on a simple cube undergoing a tensile stress. (a) Undeformed cube. (b) Deformed cube. Presence of shear deformation evidenced by misshapen edge, highlighted in red.

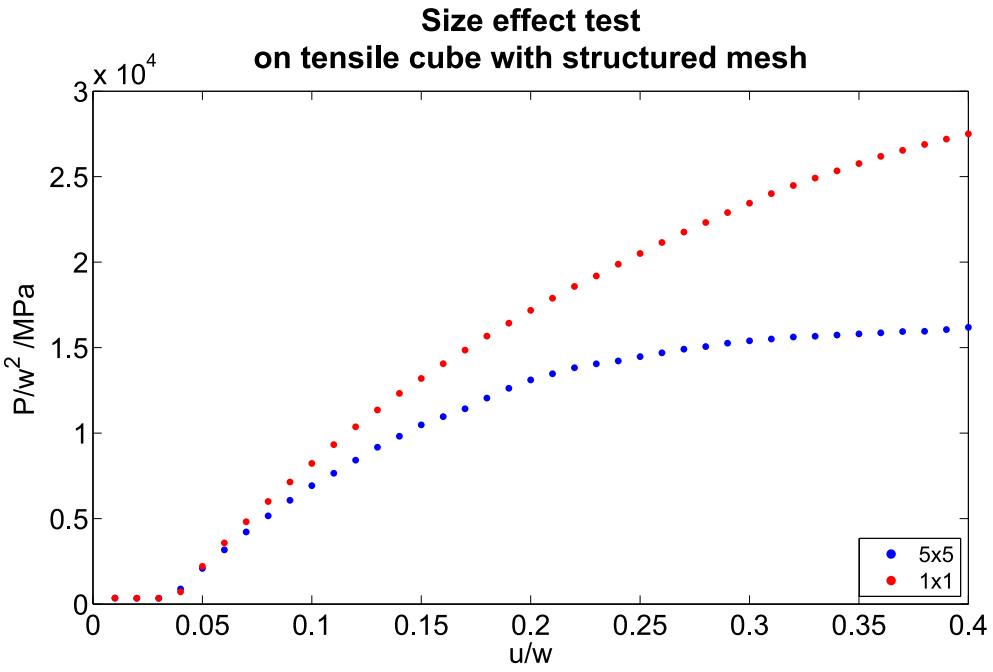


Figure 4.12: Size dependent behaviour of tensile cube.

Figure 4.12, plots normalised load (stress) against normalised displacement (strain) for the 5 x 5 μm and 1 x 1 μm tensile cubes. Both the sheared cube and the tensile cube displayed size dependent behaviour. It was expected that size effects would be present in the shear cube, however the size effects observed in the tensile cube were unexpected. This was because the size dependent hardening behaviour in the UMAT is derived solely from the evolution of the GND density. Since this was a pure tensile test, the GND density was expected to be zero, as GNDs by definition accommodate strain gradients [186, 258]. Thus, no size dependent behaviour should be displayed.

It was necessary to investigate why a significant GND density, $\sim$ 1 x10^3 μm^{-2} , was observed in a seemingly homogeneous strain field. In a realistic pure tensile specimen, only the SSD density will evolve with increasing homogeneous strain [186]. Within the UMAT the SSD density is kept constant and $\boldsymbol{\rho}_{SSD} \ll \boldsymbol{\rho}_{GND}$, this is to prevent the plastic velocity gradient, $\boldsymbol{L}^P$, from becoming undefined at small strains or slip systems with zero Schmid factor, e.g. for when the GND density is zero.

As previously shown (equation 4.32), the UMAT calculates GND density from curl of the plastic deformation gradient , $\boldsymbol{F}^p$,

$$\sum_{\kappa}(\boldsymbol{\rho}_{GND}^{\kappa} \otimes \mathbf{b}^{\kappa}) = \text{Curl}\boldsymbol{F}^p$$

One of the advantages with simulating a trivial case such as a cube under pure tensile deformation is that it allows the easy calculation of the deformation gradient, and subsequently the curl$\boldsymbol{F}^p$ by hand. These manually calculated tensors can then be used to check whether the relevant SDVs provided by the UMAT are correct.

For a simple cube under large uniaxial plastic deformation in the $\hat{\boldsymbol{z}}$ direction, such as the case in figure 4.11, the stretch ratio, λ, in each axial direction is,

$$\lambda_x = \frac{w}{w_0} \quad \lambda_y = \frac{d}{d_0} \quad \lambda_z = \frac{l}{l_0} \tag{4.74}$$

Where w, d, and l, are width, depth, and length respectively. All metals obey the incompressibility condition which enforces deformation without volume change, and is given by the boundary condition,

$$\lambda_x \lambda_y \lambda_z = 1 \tag{4.75}$$

The deformation imposed is uniaxial in the $\hat{\boldsymbol{z}}$ direction, thus

$$\lambda_x = \lambda_y = \frac{1}{\sqrt{\lambda_z}} \tag{4.76}$$

By considering that the deformation is along the Z-axis, any point, Z, in the undeformed cube becomes the point $z = \lambda_z Z$ in the deformed cube. By using this definition of the deformation and by using the relation for the deformation gradient in (4.2), result in the following relations:

$$\frac{\partial x}{\partial X} = \lambda_x \quad \frac{\partial y}{\partial Y} = \lambda_y \quad \frac{\partial z}{\partial Z} = \lambda_z \tag{4.77}$$

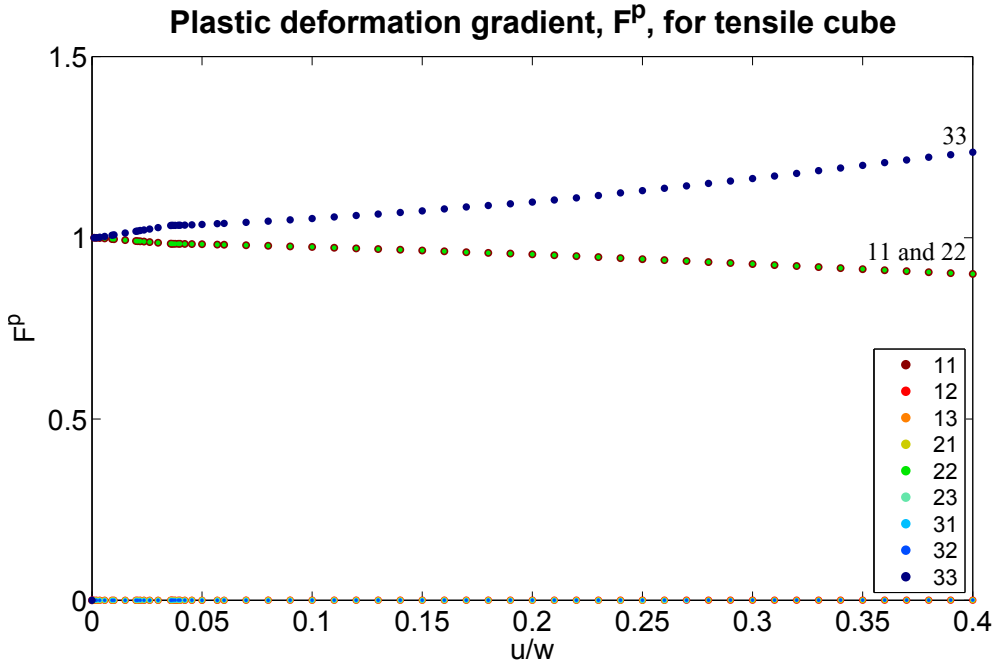
For a large strain case, the elastic strains can be ignored and all deformation assumed to be plastic, such that,

$$\boldsymbol{F}^p = \frac{\partial \boldsymbol{x}}{\partial \boldsymbol{X}} = \begin{pmatrix} \frac{\partial x}{\partial X} & \frac{\partial x}{\partial Y} & \frac{\partial x}{\partial Z} \\ \frac{\partial y}{\partial X} & \frac{\partial y}{\partial Y} & \frac{\partial y}{\partial Z} \\ \frac{\partial z}{\partial X} & \frac{\partial z}{\partial Y} & \frac{\partial z}{\partial Z} \end{pmatrix} = \begin{pmatrix} \frac{1}{\sqrt{\lambda_z}} & 0 & 0 \\ 0 & \frac{1}{\sqrt{\lambda_z}} & 0 \\ 0 & 0 & \lambda_z \end{pmatrix} \tag{4.78}$$

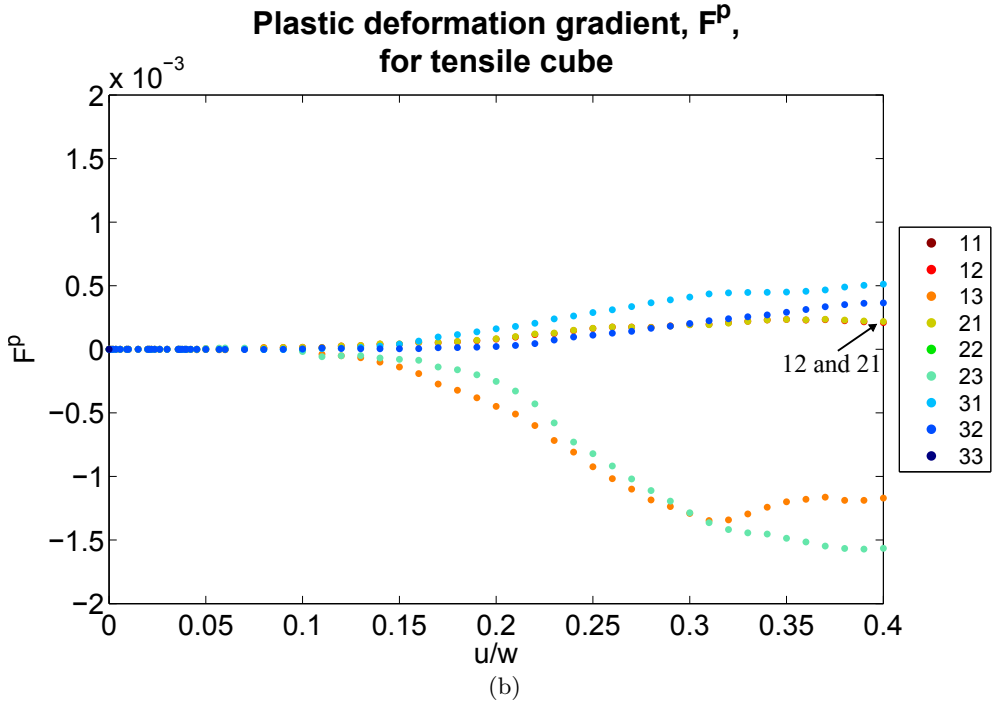
Mathmatically, the curl$\boldsymbol{F}^p$ is the cross product with the gradient operator, $\boldsymbol{\nabla}$, which can be represented by the following matrix operator if the tensor [259],

$$\boldsymbol{\nabla} \mathrm{x} \boldsymbol{F}^p = \begin{pmatrix} 0 & -\frac{\partial}{\partial z} & \frac{\partial}{\partial y} \\ \frac{\partial}{\partial z} & 0 & -\frac{\partial}{\partial x} \\ -\frac{\partial}{\partial y} & \frac{\partial}{\partial x} & 0 \end{pmatrix} \boldsymbol{F}^{pT} = \begin{pmatrix} 0 & 0 & 0 \\ 0 & 0 & 0 \\ 0 & 0 & 0 \end{pmatrix} \tag{4.79}$$

Thus, the curl$\boldsymbol{F}^p$ and the subsequent GND densities calculated should be zero in a uniaxial tensile test. The manually derived tensor components could then be checked against the ones calculated by the UMAT, given in figures 4.13 and 4.14(a). The deformation gradient was averaged over every nodal point in the cube and plotted against normalised displacement.



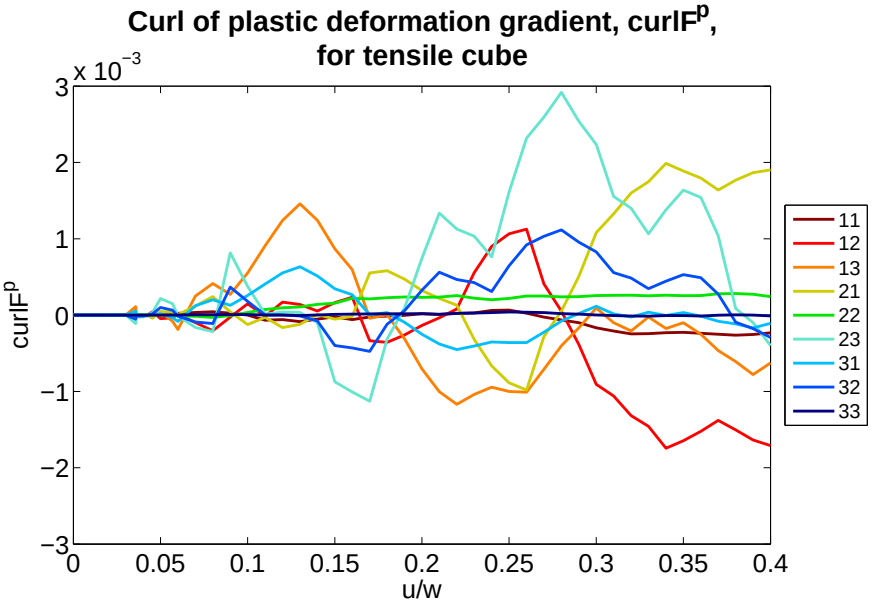
(a)



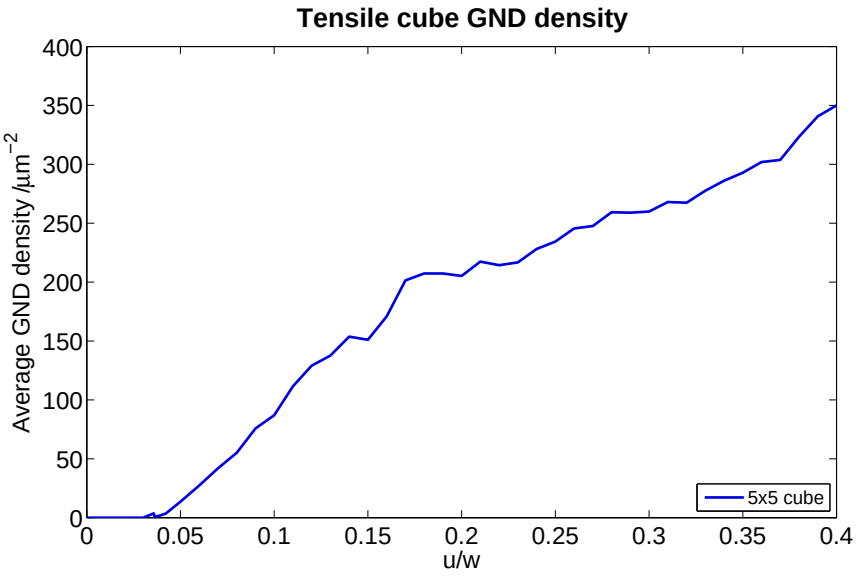
(b)

Figure 4.13: (a) The deformation gradient for a 5x5 μm uniaxial tensile cube plotted against normalised displacement. (b) The same graph but the vertical axis plotted on a smaller scale.

Figure 4.13(a) shows that the component of the deformation gradient, $\boldsymbol{F}_{33}$, was > 1, showing extension of the cube in the z-axis, $\boldsymbol{F}_{11}$ and $\boldsymbol{F}_{22}$ were < 1, demonstrating contraction in the x and y-axis. This was expected as the incompressibility condition demands a constant volume. The components $\boldsymbol{F}_{11}$ and $\boldsymbol{F}_{22}$ are equal to $\frac{1}{\sqrt{\lambda_z}}$, as predicted in (4.78). With closer inspection, using figure 4.13(b), the other components of the deformation gradient diverge away from zero after an approximate normalised displacement of 0.1. This is also demonstrated by a non-zero Curl$\boldsymbol{F}^p$, plotted in figure 4.14(a). A non-zero Curl$\boldsymbol{F}^p$ is not predicted theoretically in (4.79), and explains the non-zero GND density observed in figure 4.14(b) and 4.11(b), this also explains the size effect plotted in figure 4.12.



(a)



(b)

Figure 4.14: (a) The curl of the deformation gradient, curl$\boldsymbol{F}^p$, for a 5x5 μm uniaxial tensile cube plotted against normalised displacement. (b) The subsequent GND density calculated from (a), averaged over every integration point.

These cubic models were used to de-bug the code, so a small number of elements had to be used. To accommodate the large displacements imposed on a relatively coarse mesh, certain nodes were displaced in such a way that some of the shear strain components became non-zero. This is demonstrated by the slightly misshapen edges of the deformed cube in figure 4.11(b), highlighted in red and a closer inspection in figure 4.15. As the shear components became non-zero, the curl$\boldsymbol{F}^p$ became non zero and subsequently the GND density also became non-zero, introducing size dependent behaviour observed in figure 4.12.

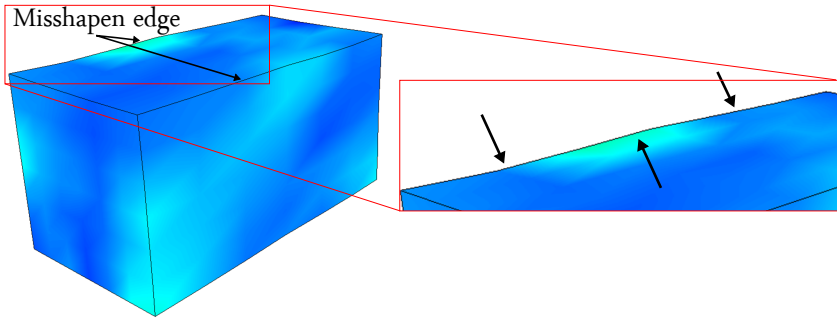


Figure 4.15: Uniaxial tensile cube, showing the presence of shear deformation due misshapen edge.

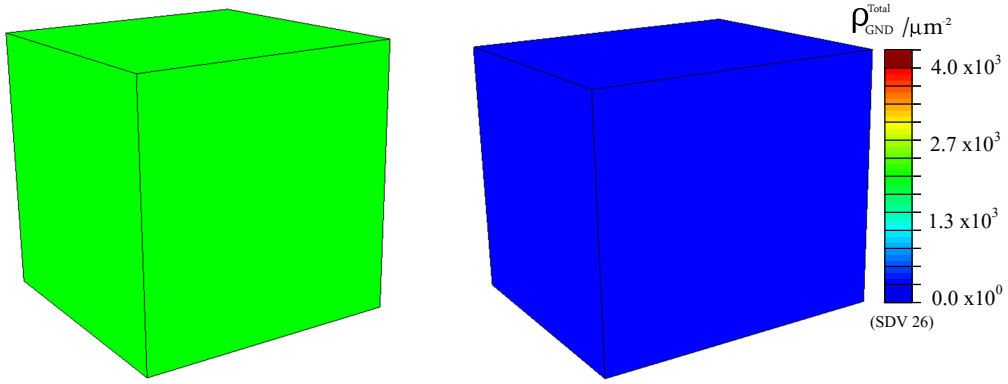
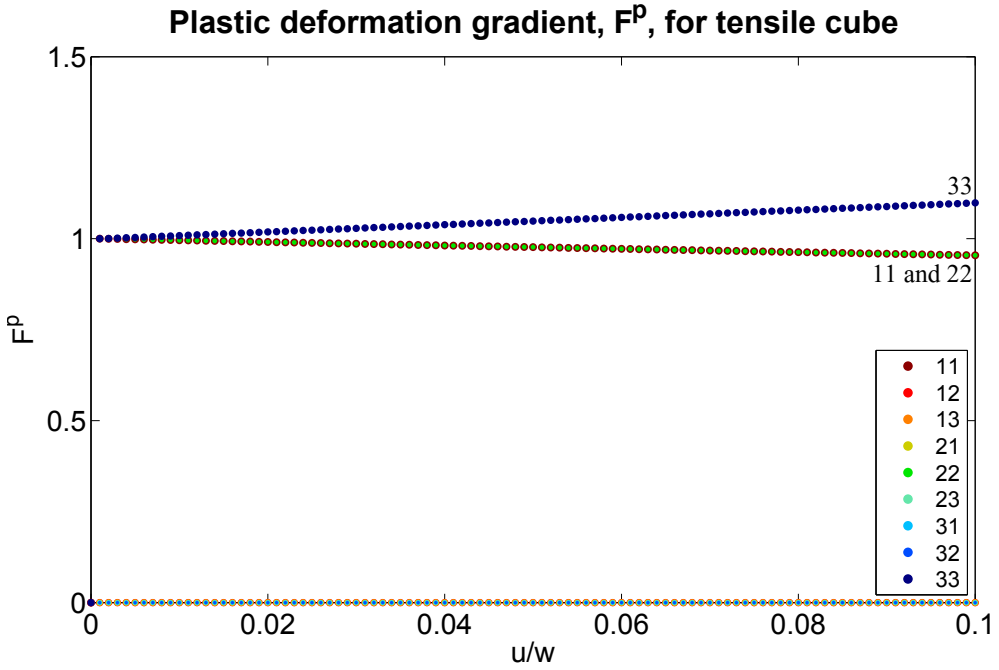
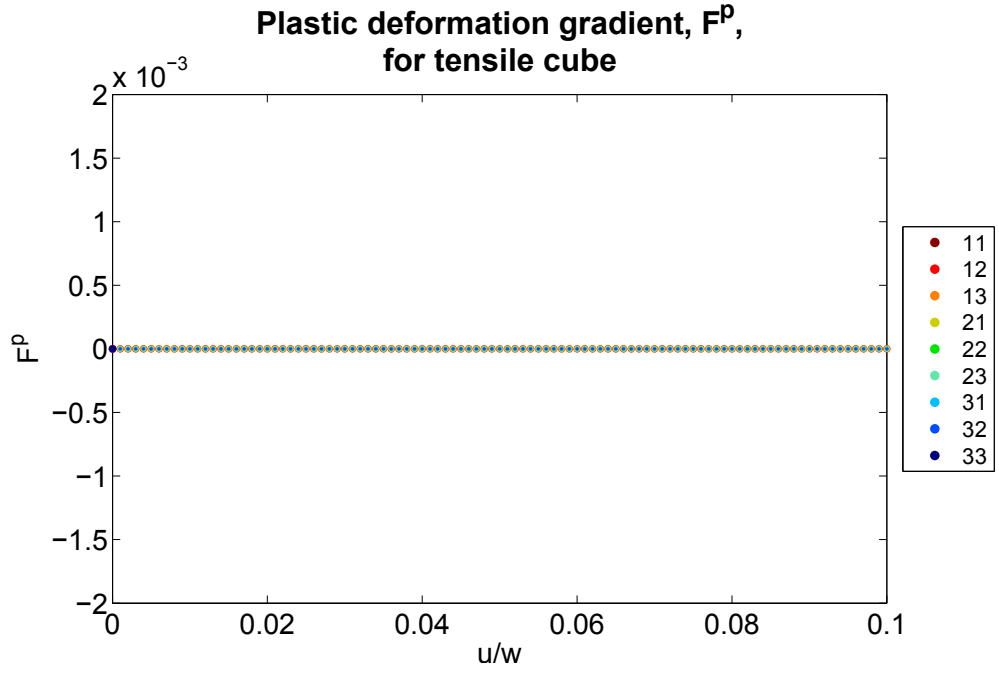


Figure 4.16: Size effect test on a simple cube undergoing a tensile stress. (a) Undeformed cube. (b) Deformed cube. The mesh is refined and the displacement reduced in comparison to the tensile cube shown in figure 4.11.

To prevent this from happening, the mesh was refined by doubling the number of elements and the displacement was reduced by a factor of four. The two updated cubes, before and after deformation are shown in figure 4.16(a) and (b) respectively. The same check is repeated in the new tensile cube to ensure the UMAT gave solutions that matched the theoretically derived values given in (4.78) and (4.79).

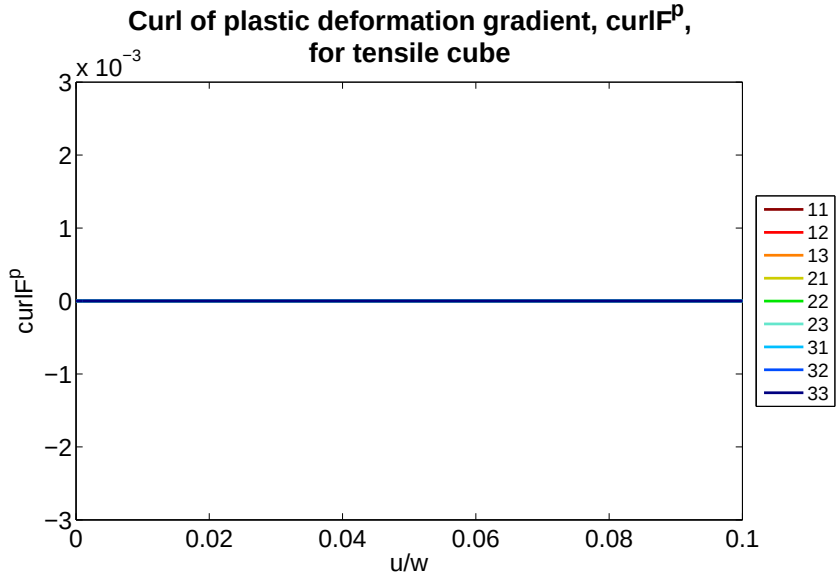


(a)

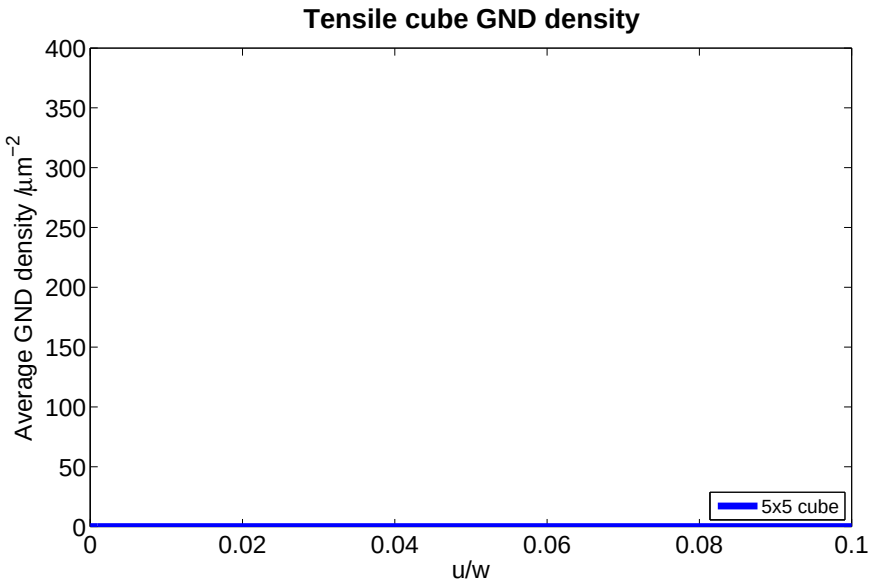


(b)

Figure 4.17: (a) The deformation gradient for a 5x5 μm uniaxial tensile cube (small strain) plotted against normalised displacement. (b) Same graph but on a smaller scale.



(a)



(b)

Figure 4.18: (a) The curl of the deformation gradient, curl$\boldsymbol{F}^p$, for a 5x5 μm uniaxial tensile cube plotted against normalised displacement. (b) The subsequent GND density calculated from (a), averaged over every integration point.

Again, the component of the deformation gradient, $\boldsymbol{F}_{33}$, was > 1, showing extension of the cube in the z-axis, $\boldsymbol{F}_{11}$ and $\boldsymbol{F}_{22}$ were < 1, demonstrating contraction in the x and y-axis, shown in figure 4.17. However this time, all other components were zero, as predicted theoretically. The curl$\boldsymbol{F}^p$ is plotted in figure 4.18(a)

Figure 4.18(a) plots the curl$\boldsymbol{F}^p$ and figure 4.18(b) gives the subsequent plot of the GND density, averaged over all integration points. Figure 4.18(a) shows all components of the curl$\boldsymbol{F}^p$ are zero, as predicted. It then follows that the GND density remains zero for the entire simulation. The simulation was then run for a 1x1 μm cube and the normalised load was plotted against normalised displacement, for both sized cubes.

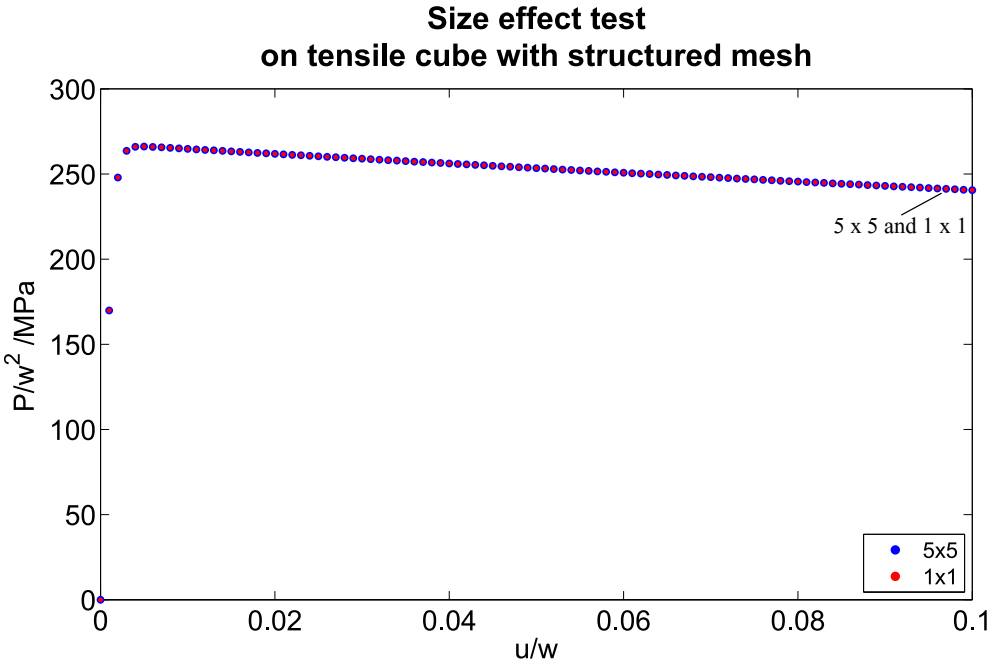
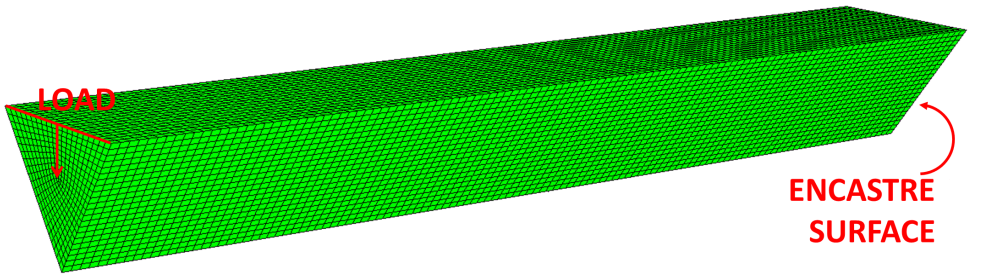


Figure 4.19: Normalised load plotted against normalised displacement for a 5x5 μm and 1x1 μm uniaxial tensile cube.

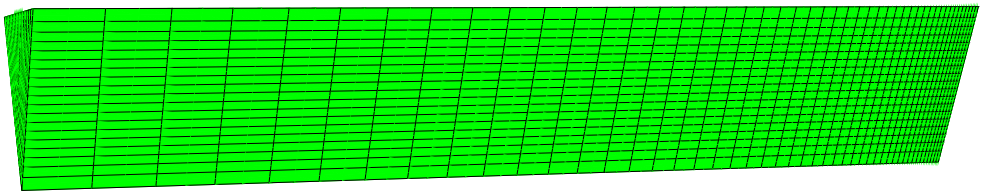
Simple microcantilevers with no base

The plot of normalised load against normalised displacement in figure 4.19, shows that no size dependent behaviour is present for uniaxial stress within the UMAT in its current form. This was expected, as UMAT introduces the size dependent behaviour through the pinning effect of GNDs; since no GNDs are present in a uniaxial test there will be no size effect.

Since the cubic shear and tensile simulations gave size dependent behaviour in accordance to the expected behaviour, the most likely cause of the for the reversal of the expected size effect in the microcantilever shown in figure 4.8(b) was thought to be caused by either an ABAQUS complexity problem, e.g. the addition of a base, or an elemental problem, caused by the particular meshing technique used.



(a)



(b)

Figure 4.20: Microcantilevers with base section excluded to examine how the meshing algorithm affects size dependent behaviour. (a) Structured mesh, no bias. (b) Swept mesh with bias towards the encastre end.

To help exclude a geometric complexity cause for the size effect reversal, two different sized simple prismatic microcantilevers were modelled, i.e. without a base section. In a similar manner to microcantilevers modelled in section 4.3.4, the two beam sizes were 5 x 30 μm and 1 x 6 μm.The rear surface was set to an encastre boundary condition, while the load was applied along the top edge of the free end. The first set of microcantilevers, shown in figure 4.20(a), used the same meshing technique used to mesh the cubic models, e.g. structured and unbiased, and the second, shown in figure 4.20(b), used the same meshing combination as the microcantilever in figure 4.7, e.g. Swept with a size bias towards the fixed end. The results for the two sets of microcantilevers are presented in figure 4.21 and figure 4.22.

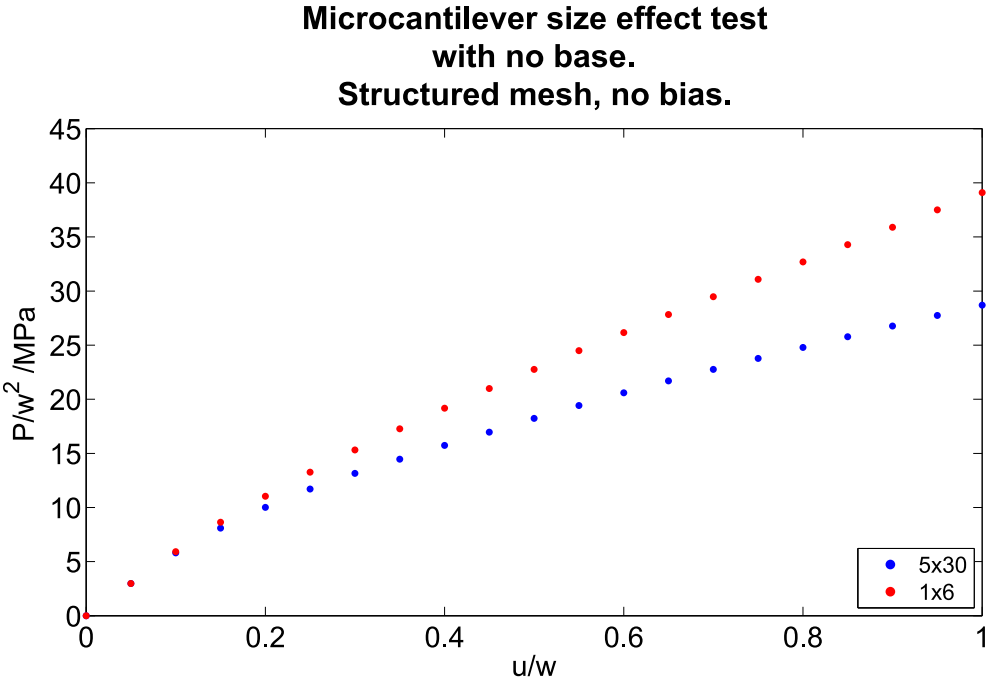


Figure 4.21: Structured mesh without a bias, showing a decrease in the size effect as the mesh is refined.

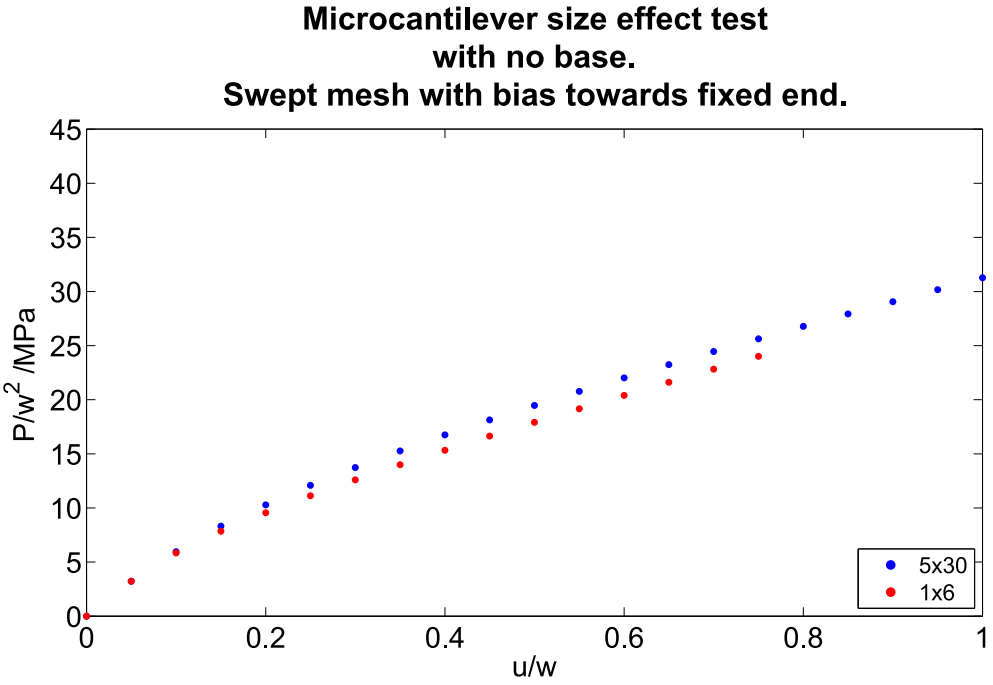
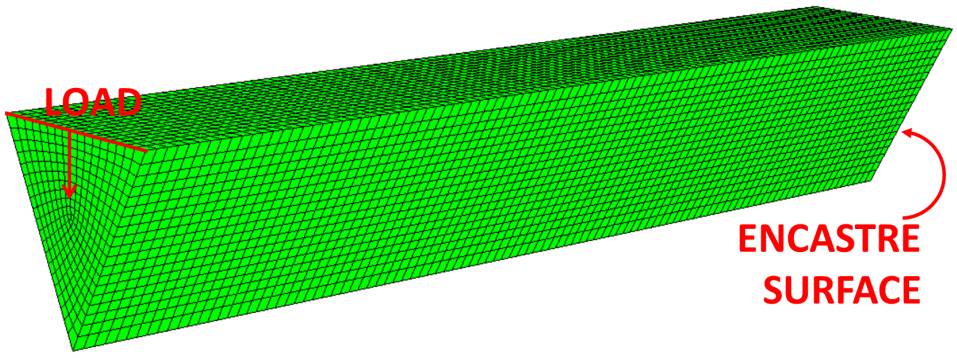
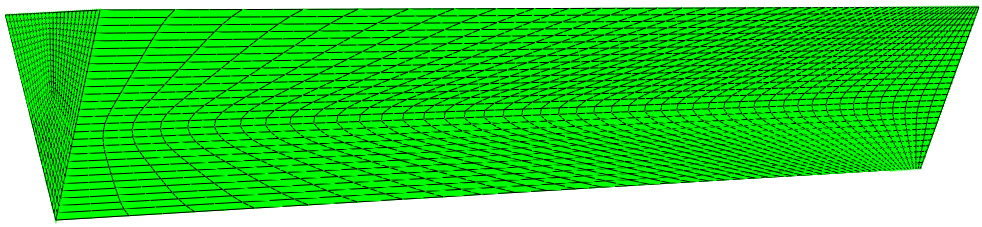


Figure 4.22: Swept mesh with bias towards the encastre end, showing a reversal of the size dependent behaviour expected.

The set of microcantilevers that were meshed using an unbiased structured meshing technique displayed the 'smaller is stronger' size effect which is more consistent with that of literature and the work previously carried in the characterisation of microcantilever size effects (section 3.4.5). However, the set of microcantilevers that used a combination of a swept meshing technique with an element size bias focused towards the fixed end, show a reversal of the size dependent behaviour expected. Figure 4.22 appears to show that the apparent strength of the microcantilever decreases as the geometry size decreases, i.e. smaller is weaker.



(a)



(b)

Figure 4.23: Microcantilevers with base section excluded to examine how the meshing algorithm affects size dependent behaviour. (a) Swept mesh, no bias. (b) Structured mesh with bias towards encastre end.

Two more sets of simple microcantilevers were modelled: those in the first set were meshed using a homogeneous swept mesh, i.e. no bias, and the second set were meshed using a combination of a structured meshing technique and a bias to finer meshing focused towards the fixed end. These microcantilevers are shown in figure 4.23(a) and (b) respectively. The results for the two sets of microcantilevers are presented in figure 4.25 and figure 4.24.

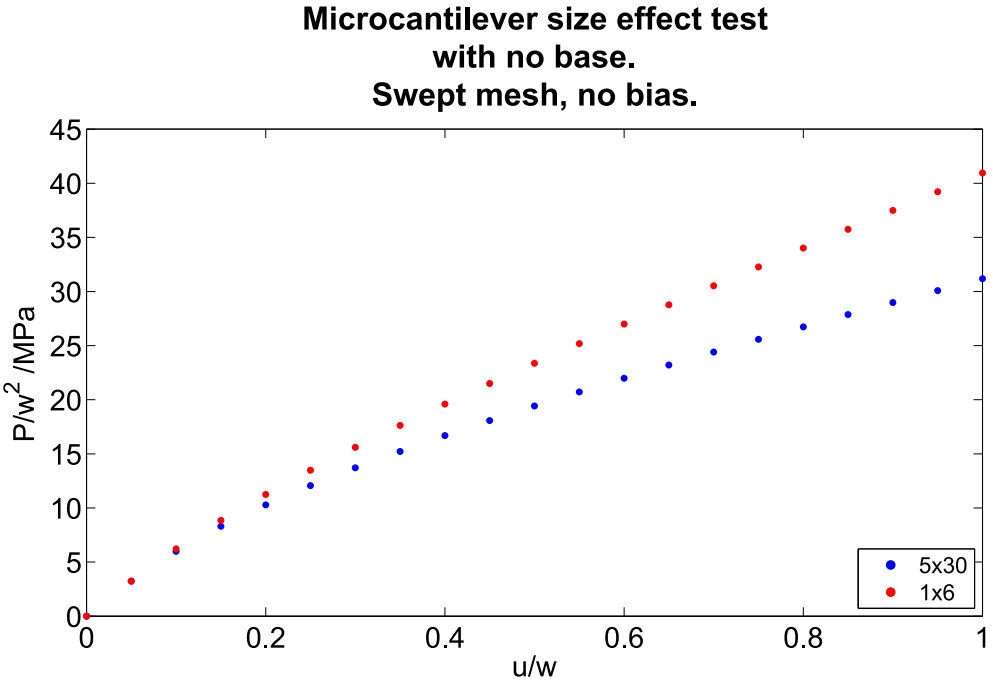


Figure 4.24: Swept mesh without a bias, showing size dependent behaviour.

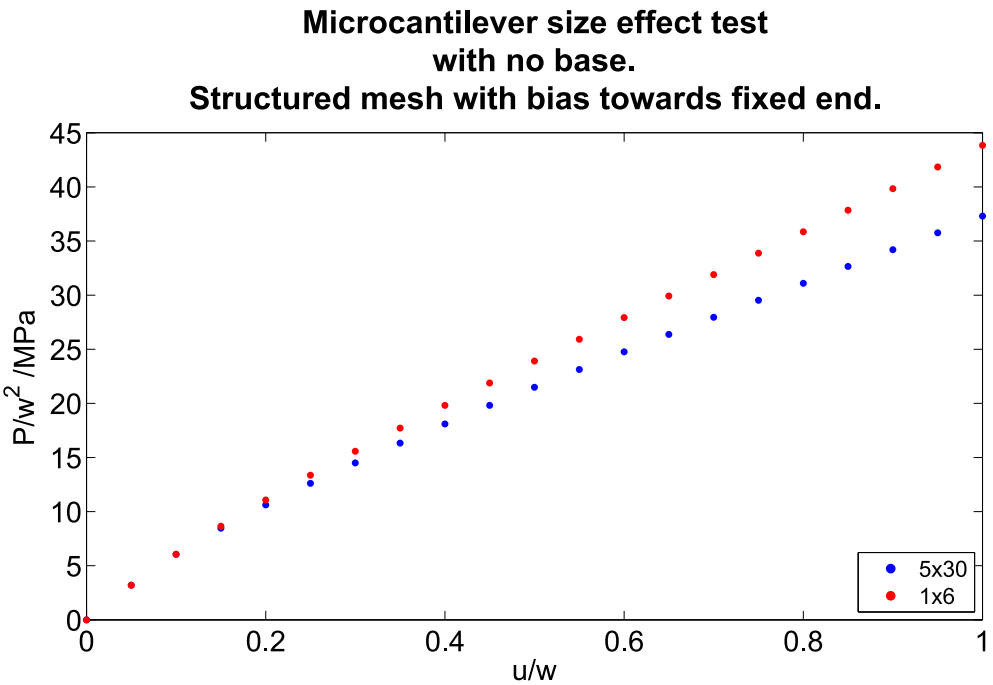
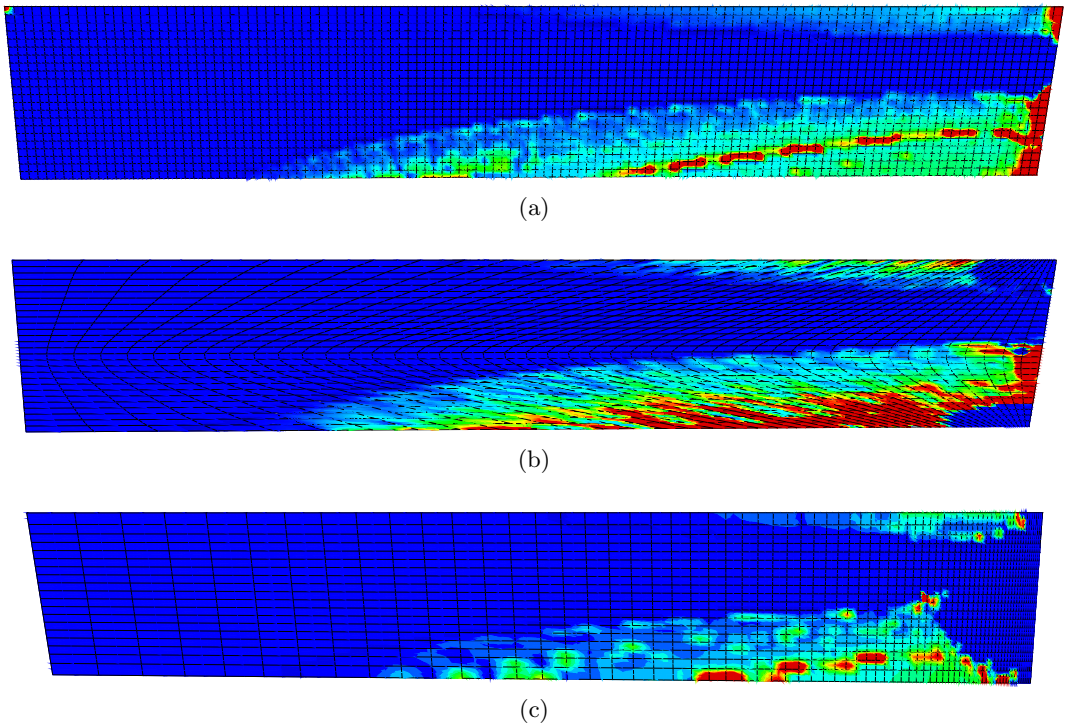


Figure 4.25: Structured mesh with a bias towards the encastre end, showing size dependent behaviour.

Both sets of microcantilevers shown in figures 4.24 and 4.25 display an apparent strength increase with a decrease in model size. This behaviour was more consistent with experimental evidence. Since both meshing algorithms returned conventional size effects, the cause of the size effect reversal was inferred to be the meshing bias, more specifically, due to the reduction of the physical size of the element. This is evident when viewing the GND density for each beam, as shown in figure 4.26.



(a)

(b)

(c)

Figure 4.26: Representation of the total GND density across all slip systems in three simple 1x6 μm prismatic microcantilever beams, each modelled to the same strain with a deformation scale factor of zero. Free-end left hand side, fixed end (encastre) right hand side. (a) Fine unbiased structured mesh. (b) Structured mesh with a size bias towards the fixed end. (c) Swept mesh with size bias towards the fixed end. All figures were set to the same scale, however the colour scale was not included as figures are used for qualitative purposes to demonstrate the critical element size.

Figure 4.26(a) shows the total GND density across all slip systems for a simple microcantilever meshed using an unbiased structured mesh. The neutral axis that runs the length of the beam can clearly be seen; it lies a third of the distance from the top to the bottom edge and is a line of zero stress and strain, thus this region has a GND density of zero. As expected, the GND density in this beam matches the stress concentration at the top and bottom of the microcantilever. Figure 4.26(b) shows a similar representation of the total GND density for a simple microcantilever using a structured mesh with an element size bias focused towards the fixed end. This particular meshing technique forces the elements to become very small at both the top and bottom corner at the fixed end. As the elements decrease in size, it is evident that the GND density abruptly falls to zero. This effect is further magnified in the microcantilever shown in figure 4.26(c), which is meshed using a swept mesh with an element size bias focused towards the fixed end. Using this meshing combination forced the elements to uniformly decrease in size across the width of the microcantilever. As the elements decreased in size they became increasingly more likely to return a GND density of zero, until just before the fixed end where the GND density, again, abruptly stops. This sudden drop in the GND density is investigated further in figure 4.27.

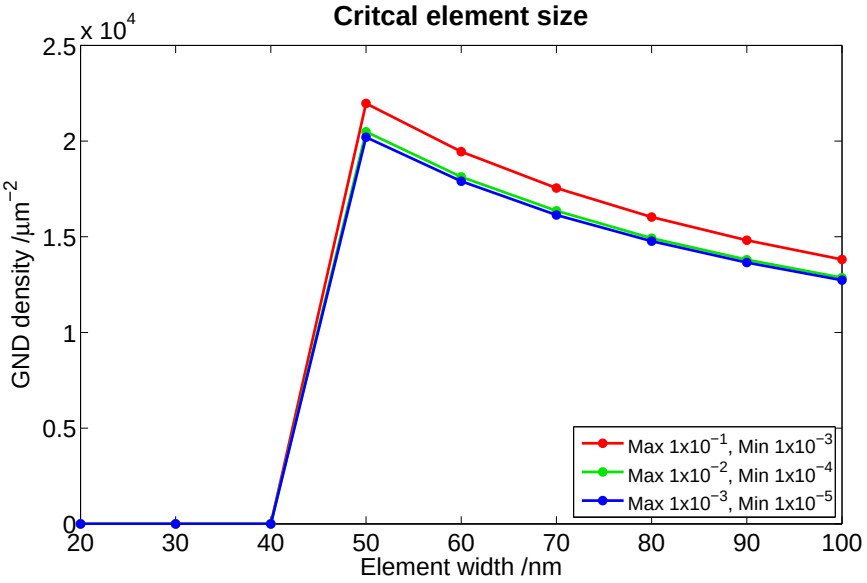


Figure 4.27: Investigation to find the critical element size needed to observe an abrupt drop in the GND density. A single cubic C3D20R element under pure shear was used, and the GND density averaged over eight integration points was taken at a displacement normalised with width, u/w, value of 0.4. The effect the time increment had on the critical element size was also examined, three sets of maximum and minimum time increments were used, with the initial value set as the median value between the maximum and minimum. Note that the time increment is a fraction of 1, so is dimensionless.

To investigate the variance of GND density with element size, a single cubic C3D20R element was displaced using a pure shear load and the element width was decreased from 100nm to 20nm. The GND density was taken at a maximum displacement normalised with width u/w, value of 0.4 and averaged over all eight integration points. The effect the variance of the time increment had on the GND density and critical element size was also investigated. Results are plotted in figure 4.27.

As the element size is decreased the GND density increases until a critical cubic element width of 50 nm is reached; GND density abruptly drops to zero if the element size is decreased past this critical value. Although decreasing the time increment from a max/min value of $1\text{x}10^{-1}/1\text{x}\ 10^{-3}$ to $1\text{x}10^{-2}/1\text{x}\ 10^{-4}$ (dimensionless) led to a small decrease in the GND density. This effect quickly saturated as the min/max time incre-

ment was decreased by another order of magnitude to 1x10^{-3}/1x 10^{-5}, and this also approximately tripled the computational time.

The explanation as to why a decrease in element size increases the GND density, and why a critical element size is observed is not currently known. This will need further investigation and possibly an amendment to the finite element code. However, modelling at the nanoscale is much more suited to atomistic models than continuum plasticity.

The failure of the model to calculate GND densities below an element width of 50 nm explains the size effect reversal observed in figure 4.8(b) and 4.22. Both microcantilevers used a swept mesh with an element size bias towards the fixed end. As the element width in the 1x6 μm microcantilever decreased past the critical value of 50nm, the GND density fell to zero and the element exhibited perfect plasticity, e.g. no work hardening. Since such a large number of elements in the stress concentration were affected, the impact they had on the work hardening response of the beam was enough to give the appearance of a significant size effect reversal. The microcantilevers meshed using a structured mesh with a size bias were also affected; their load/displacement data is shown in figure 4.25 and GND density representation is in figure 4.26(b). However, fewer elements were affected, thus decreasing the magnitude of the size effect but not completely reversing it.

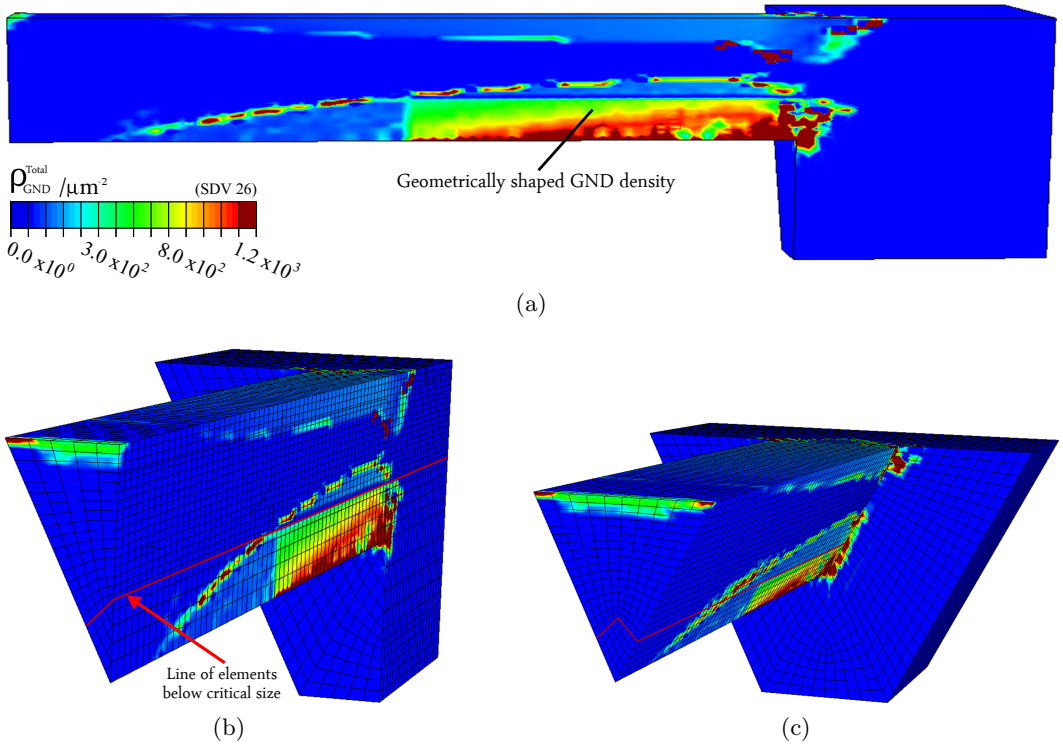


Figure 4.28: 1x6 μm microcantilever showing a geometrically shaped GND density. (a) Side view of microcantilever, with cut along cental axis. (b) Front view of microcantilever, with cut along central axis. Highlighted is element boundary line that lies on the GND distribution boundary. (c) Front view of microcantilever. Highlighted is element boundary line that lies on the GND distribution boundary.

Whilst running simulations it was noticed that the distribution of GNDs in the 1x6 μm microcantilever had a well defined geometric shape, shown in figure 4.28. The GND density has a particularly abrupt stop along a horizontal elemental boundary, where the stress and GND density fell to zero. This was clearly an artifact of the model and can be explained by the critical element size error as previously discussed. The line of elements that showed an abrupt drop in the GND density, were the smallest in the model, as shown in figure 4.28(b) and (c). This reduction of element geometry to below the critical size caused these particular elements in the model return a GND density of zero. This affected very few elements and did not significantly reduce the validity of the model.

4.3.6 UMAT check and model optimisation summary

- The solutions calculated for microcantilevers containing $\backsim$ 2x10^4 elements was deemed acceptably stable.

- GND density correlated well increasing Schmid factor as expected, however some possible inaccuracies in calculation the GND densities on specific slip systems were found. This could be due to the how the UMAT extrapolates a second-order tensor (curl$\boldsymbol{F}^p$) on twenty four individual slip systems.

- Size effects were observed in a simple cube under a pure shear load, but not for a cube under pure a pure tensile load. This was to be expected since the lengthscale dependency of the crystal plasticity model is achieved by making $\Delta\dot{\boldsymbol{\varepsilon}}^p$ $\propto (\rho_{GND})^{-\frac{1}{2}}$.

- A critical cubic element width of 50 nm was found, where if the element size was decreased below this limit then the GND density for that element fell to zero. This was the cause of the size effect reversal observed in initial microcantilever simulations.

- An optimised meshing algorithm was chosen to be an unbiased structured mesh with as few elements below a width of 50 nm as possible.

- The effect varying the time increment had on the GND density was examined, and a max/min increment of 1x10^{-2}/1x10^{-5} was seen appropriate compromise between a stable solution and computational time. This also allowed a large reduction of the time increment if needed.

4.4 Modelling of the GND contribution to microcantilever size effects

4.4.1 Introduction

As discussed in chapter 2 section 2.6.7 and demonstrated in chapter 3 section 3.4.5, a strength dependence on size is observed in micromechanical testing, particularly in geometries approaching the sub-micron scale. This phenomenon has long been attributed to the formation of statistically stored dislocations (SSDs) in the case of homogeneous deformation [186], and geometrically necessary dislocations (GNDs), in the case of non-homogeneous deformation [184]. It has also been demonstrated that source limitation and dislocation pile-up significantly contribute to the size effects observed experimentally [195, 196]. However, GNDs still remain an important consideration when examining microcantilever size effects. The exact contribution GNDs have to the size dependent mechanical response of microcantilevers is still not fully understood. It is the this contribution, separated from the other contributing mechanisms, that this section investigates.

4.4.2 Simulation details

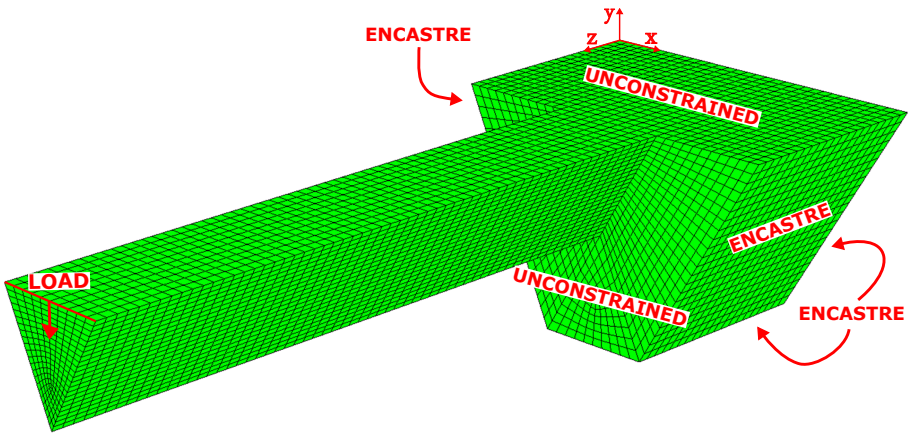


Figure 4.29: 5x30 μm microcantilever model with an unbiased structured mesh.

Three equilateral triangular prismatic microcantilever models of beam widths, 5 μm, 3 μm, and 1 μm, with a 1:6 width:length aspect ratio and beam depth equal to width, were modelled in ABAQUS 6.14-2 using a crystal plasticity UMAT provided by Dunne et al. [178, 238]. The crystal orientation matrix, or G-matix, was set to the identity matrix throughout each microcantilever, meaning the [100], [010] and [001] direction was orientated along the x, y and z-axis respectively. The UMAT describes the slip on the first twenty four BCC slip systems, e.g. $\{110\}\langle 111\rangle$ and $\{211\}\langle 111\rangle$. The density of GNDs calculated by the UMAT was geometry size dependent, this resulted in a lengthscale dependent slip rule as GNDs are assumed here to be the dominant pinning mechanism for mobile dislocations. The load was applied along a line at the tip of the free end, see figure 4.29, and the displacement was adjusted to give an equivalent strain for each microcantilever. Each surface of the base was given encastre boundary conditions, except top surface and the surface at the microcantilever's fixed end, this was to allow a realistic flexure of the base. The mesh was constructed using the unbiased structured meshing technique previously described in section 4.3.6 on page 211. The total number of elements for each sized microcantilever was kept constant at $2.698\,\text{x}10^4$ elements and a max/min increment of $1\text{x}10^{-2}/1\text{x}10^{-5}$ time increment was chosen, as

discussed in 4.3.6. All chosen values for the UMAT constants are given in table 4.1.

4.4.3 Results and discussion

In a similar manner to section 4.3.4 and 4.3.5, load, P, and displacement, w, normalised with microcantilever width, P/w^2 and u/w, was plotted for each simulation. The normalised load-displacement curves for three different sized microcantilevers, 5x30 μm, 3x18 μm, and 1x6 μm, are shown in figure 4.31. Figure 4.31 uses simple beam theory to plot maximum stress against maximum strain from the load and displacement values given by ABAQUS.

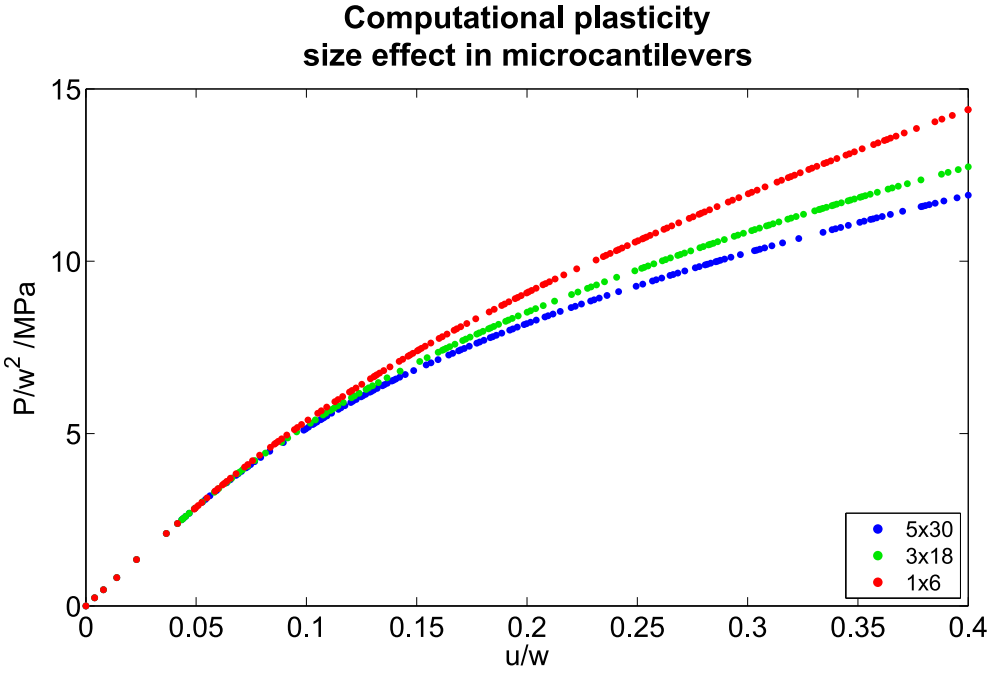


Figure 4.30: Microcantilever size effect resulting from the lengthscale-dependent slip rule given by Dunne (2007) and (2012) [178, 238]. Normalised stress plotted against normalised strain.

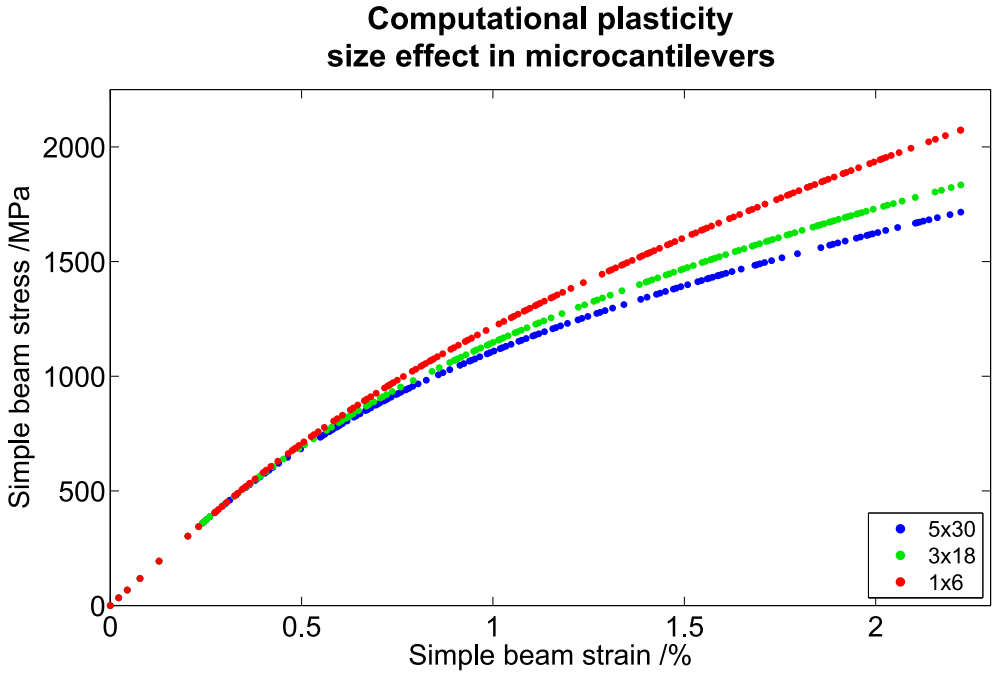


Figure 4.31: Simple beam stress plotted against simple beam strain.

Figure 4.31 and 4.31 demonstrates the lengthscale dependency of the constitutive equation describing plastic strain within the crystal plasticity UMAT for three different sized microcantilever specimens. As the microcantilever width is decreased from 5 μm to 1 μm the apparent strength increases. This increase in simulated work hardening is caused by a decrease in the increment in plastic strain rate, $\Delta\dot{\varepsilon}^p$, with decreasing geometry size. If tested to the same strain, smaller microcantilever geometries will have higher GND densities, since the strain gradients required to produce the required deformation are larger. Such that,

$$\Delta\dot{\varepsilon}^p \propto \frac{1}{\sqrt{\rho_{GND}}} \tag{4.80}$$

where ρ_{GND} is the total density calculated by summing the GND densities in each slip system, recalling equation (4.32),

$$\sum_{\kappa}(\boldsymbol{\rho}_{GND}^{\kappa} \otimes \mathbf{b}^{\kappa}) = \text{curl}\boldsymbol{F}^{p}.$$

From this definition we see that with increasing strain gradient, or more specifically the 'curl' of the plastic deformation gradient, curl$\boldsymbol{F}^p$, the GND density increases, which decreases the increment in plastic strain rate. Since the decrease in strain rate is dependent on the curl of the deformation gradient, the hardening introduced will become increasingly larger with plastic strain. This means that the size dependency introduced by the UMAT will be much less significant during the onset of plasticity in the simulated load-displacement data, since the total GND is low.

To investigate this, the values of stress and strain from figure 4.31 were used to find the yield stress for each beam. The yield stress was found by defining yield as a 10 % drop in tangential stiffness, which was calculated from the gradient of an iterative linear regression in a similar manner to section 3.3.2. A plot of the tangential stiffness against simple beam maximum stress is given in figure 4.32.

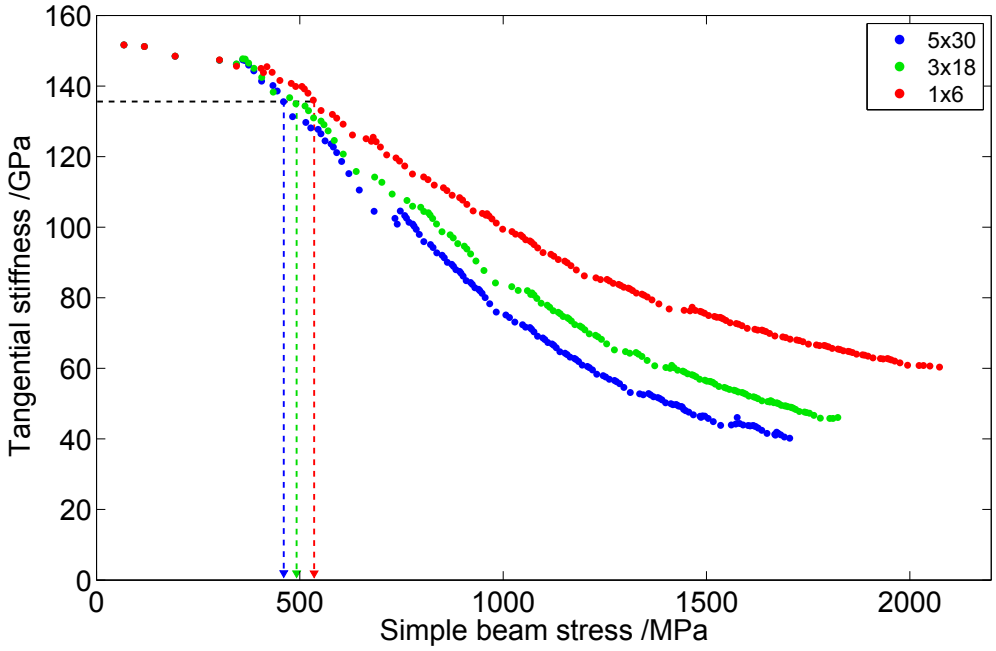


Figure 4.32: Simple beam tangential stiffness, plotted against simple beam stress. Yield was defined to be a 10% drop in stiffness.

The elastic modulus was found to be 152 GPa, therefore a 10 % drop in tangential stiffness equates to approximately 137 GPa. This is represented by a black dotted line in figure 4.32. There was a discrepancy between the tangential stiffness measured elastic modulus and that given in the material properties (170 GPa) in table 4.1. Since the tensile and compressive stress in this work was primarily in the [0 0 1] direction, and the elastic modulus in the UMAT was set to 170 GPa for <1 0 0> directions, it was expected that measured elastic modulus in figure 4.32 would be very close to that given in the material properties. The reason for the discrepancy of $\sim$ 18 GPa could be due to using simple beam theory to calculate the elastic modulus.

Since no data points in figure 4.32 were exactly at 137 GPa, the data points closest were used to define yield. The corresponding yield stress for each sized beam is given by a dotted line in their respective colours. The yield was determined to occur at a simple beam strain of 0.31 %, 0.34 % and 0.37 %, which corresponds to a displacement normalised with width,u/w, of 0.056, 0.060 and 0.066 for the 5x30 μm, 3x18 μm and 1x6 μm microcantilever respectively. These values are given in table 4.3. The error bounds were found from the tangential stiffness data point above and below the point closest to 137 GPa.

Microcantilever depth /μm	Yield stress /MPa	Yield strain /%	Yield normalised displacement
5	460 ± 15	0.31 ± 0.13	0.056 ± 0.002
3	475 ± 13	0.34 ± 0.14	0.060± 0.002
1	533 ± 12	0.37 ± 0.11	0.066 ± 0.002
Bulk value from 4pt flexure test	$\backsim$ 420	-	-

Table 4.3: Corresponding yield stresses from the simple beam stress-strain plot, and a comparison with the bulk yield value for 14WT 1150 given in section 3.7.

The values for yield stress for each size microcantilever beam are plotted in figure 4.33, alongside the microcantilever size effect data presented in section 3.4.5 and data presented by Hardie (2013) [203] for Fe-6Cr binary alloy.

Figure 4.33, shows that the CP simulated microcantilever size effect is significantly weaker than that measured experimentally. Recalling from table 4.1 that the UMAT was calibrated using a 14WT 1150 $\sim$ 5 x 30 μm experimental microcantilever, the 5 x 30 μm model simulated a yield within the range expected for a non-ODS microcantilever beam, and showed good agreement with the 14WT 1150 experimental beams with $>$ 5 μm beam depth. However, as the the microcantilever geometry is reduced in size, the CP model fails to account for the magnitude of the size effect observed experimentally.

There are several explanations for the failure of the model to simulate the magnitude of the yield stress increase at microcantilever depths/widths lower than 5μm. Firstly, there are other contributing factors to the microcantilever size effect that can not explicitly be modelled within a continuum model, such as source limitation and the suppression of sources caused by the back-stresses from the build up of soft pile-ups [197]. Secondly, the model utilises a density of GNDs, dependent on the strain gradient,

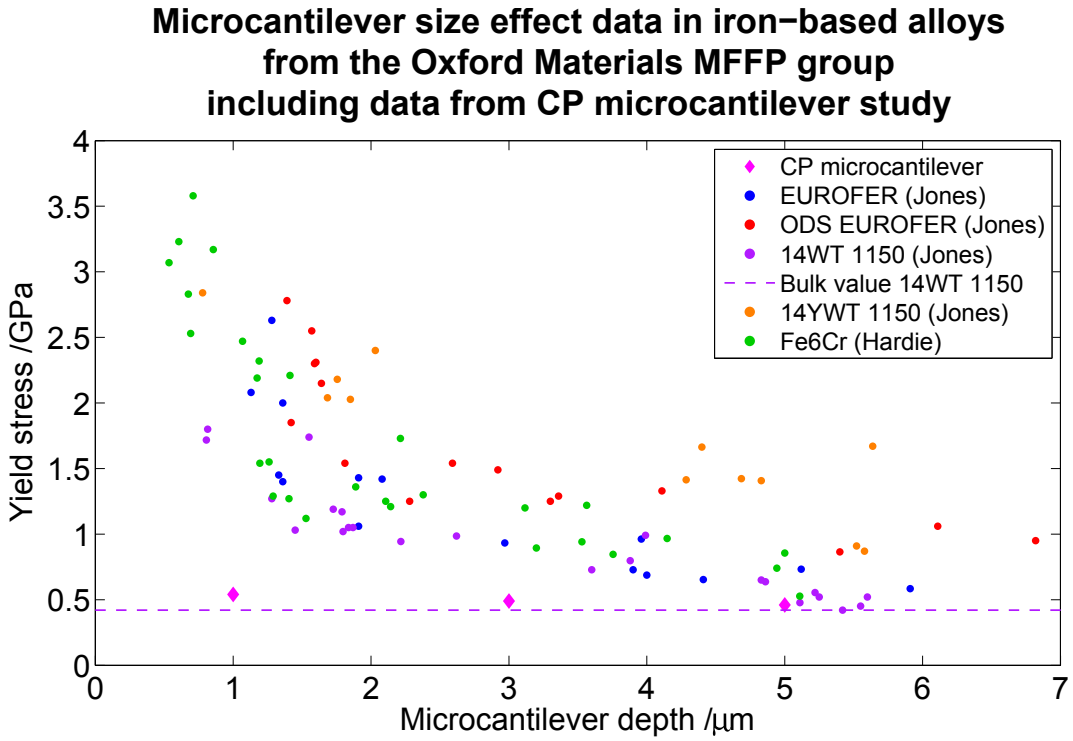


Figure 4.33: Microcantilever size effect data in iron-base alloys from the MFFP group, together with the CP size effect data from this study. The data from Hardie (2016) [199] was in an iron-chromium binary alloy, defining yield as an 0.2 % prrof stress.

to act as a hardening mechanism. However, during the onset of plasticity the plastic deformation gradient, $\boldsymbol{F}^p$, by its nature, is very small; thus at this point, the GNDs and their contribution to the size effect is also very small. To demonstrate this, two plots were created. The first averaged the total GND density on all slip systems, SDV 26, across eight integration points for a single element. The second plot looked at the GND density on the primary slip system, $(1\ \bar{1}\ 2)[\bar{1}\ 1\ 1]$ (SDV71), averaged over 3248 integration points for 406 elements.

GND study

A graphical representation of the total GND density in the three microcantilever beams is presented in figure 4.34. SDV26 represents the total GND density across all 24 slip systems and is shown as a smoothed contour map between the limits of 0 and $1.2\,\text{x}10^{3}$ μm^{-2}. The element used as the representative element is outlined in red. The placement for the representative element was chosen to be far enough from the fixed end and edges as to avoid GND density spikes that often occur here due to stress concentrations and singularities. Only one element was chosen due to the computational expense of storing data for over 100,000 integration points at every time step. Results are shown in figure 4.35, and summarised in table 4.4.

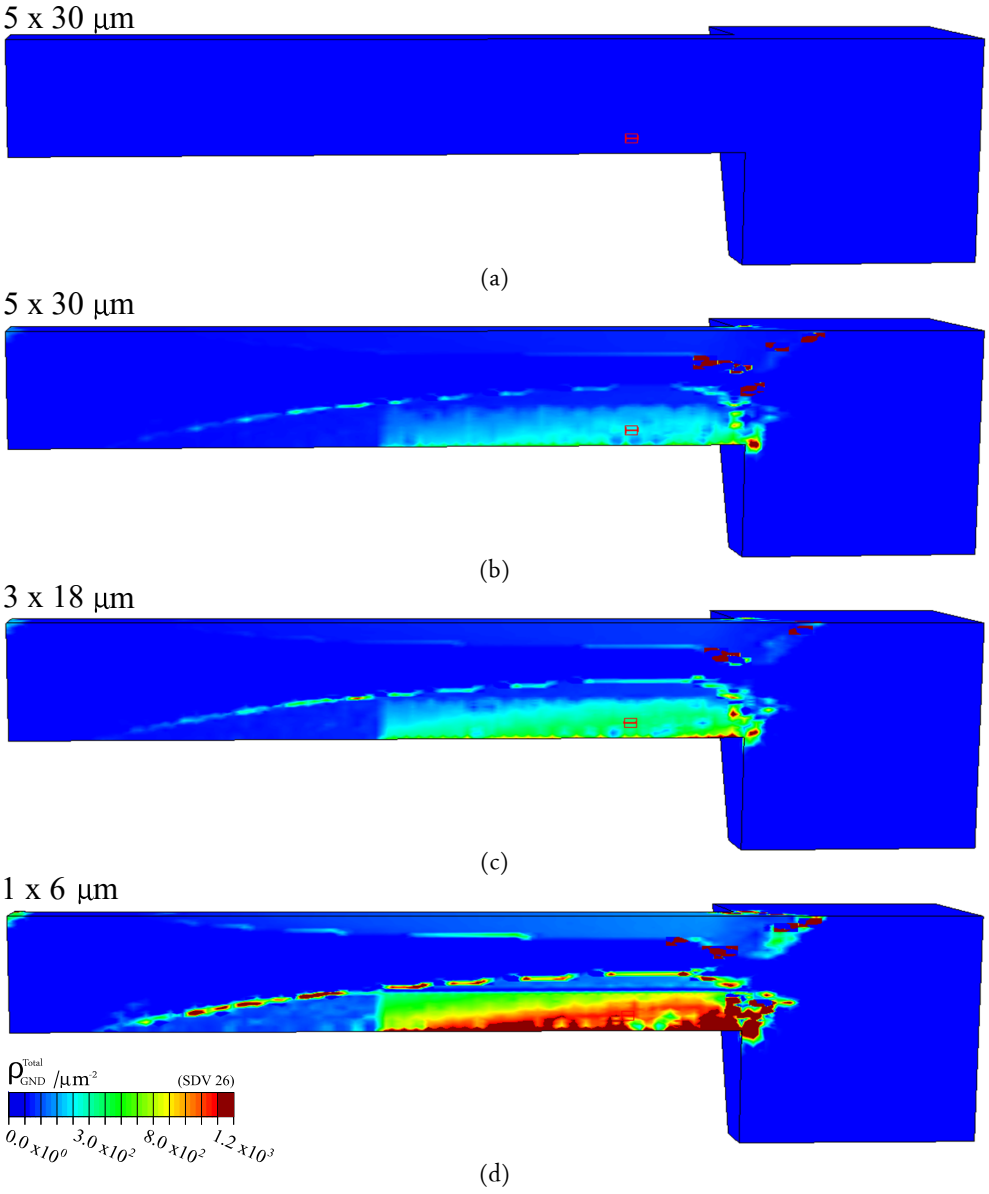


Figure 4.34: A plot of GND density in units of μm^{-2} for microcantilevers of three different sizes and one undeformed. Each microcantilever has been subjected to the same strain, and the deformation scale factor has been reduced to zero for easy comparison. The representative element used in figure 4.35 is highlighted in red. (a) Undeformed 5x30 μm microcantilever. (b) Deformed 5x30 μm microcantilever (c) Deformed 3x18 μm microcantilever (d) Deformed 1x6 μm microcantilever.

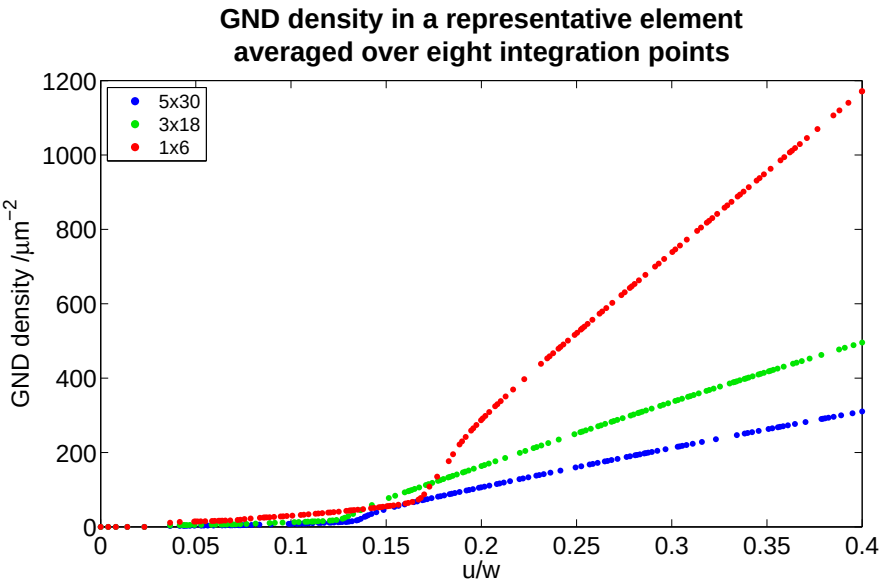


Figure 4.35: GND density in three different sizes of microcantilever averaged over eight integration points for a representative element, highlighted in figure

Beam depth /μm	Total GND density in representative element at maximum displacement /μm^{-2}	Dislocation spacing /nm
5	3.1 x10^2	56
3	5.0 x10^2	44
1	1.2 x10^3	29

Table 4.4: Summary of results from figure 4.35. GND density values taken at 2 μm beam displacement, corresponding to 0.4 u/w and $\sim$ 2.2 % simple beam strain.

Figure 4.34 shows a graphical representation of the total GND density summed over the 24 slip systems included in the UMAT. Each microcantilever shown is deformed to the same strain, and the GND density contour map is to the same scale. We can see that

the GND density approximately follows the stress concentration, such that the average GND density is highest along the bottom edge and lower vertex at the fixed end. The volume of bulk material contains an increasingly greater density of GNDs as the sample size is decreased. This suggests that the bulk material, particularly near the fixed end has a greater influence on the mechanical properties in smaller microcantilevers. The geometric shape of the GND density distribution in the 1 x 6 μm beam is discussed in section 4.3.5 (p210).

From figure 4.35, the total GND density in the representative element increases slowly after a brief period of elastic behaviour until a period of more rapid build up of GNDs takes place, initiating at around 0.15 u/w. The GND density increases with decreasing beam size, as was expected. However, in this element, the GND densities of each sized microcantilever do not drastically diverge until approximately 0.17 u/w ($\sim$ 1 % simple beam strain), which is significantly past the yield strain of $\sim$ 0.3 % given in table 4.3. While figure 4.35 serves as a good representation of the behaviour of the GND density in elements where $\tau_r^\kappa > \tau_c^\kappa$, it does not however fully describe the behaviour of elements where plasticity is first initiated, e.g. the lower vertex at the fixed end.

The total GND density could not be stored at every increment for every element as this would be too computationally expensive, hence why a representative element was used. However, any SDVs, such as the GND density on the primary slip system, could be extracted for any number of elements, although with much lower resolution in strain than for the representative element. SDV 71, the GND density of the primary slip system, was averaged over 3248 integration points for 406 elements. The elements chosen are shown in figure 4.36, highlighted by the black dotted line. The GND density on the primary slip system plotted against normalised displacement is given in figure 4.37 and summarised in table 4.5.

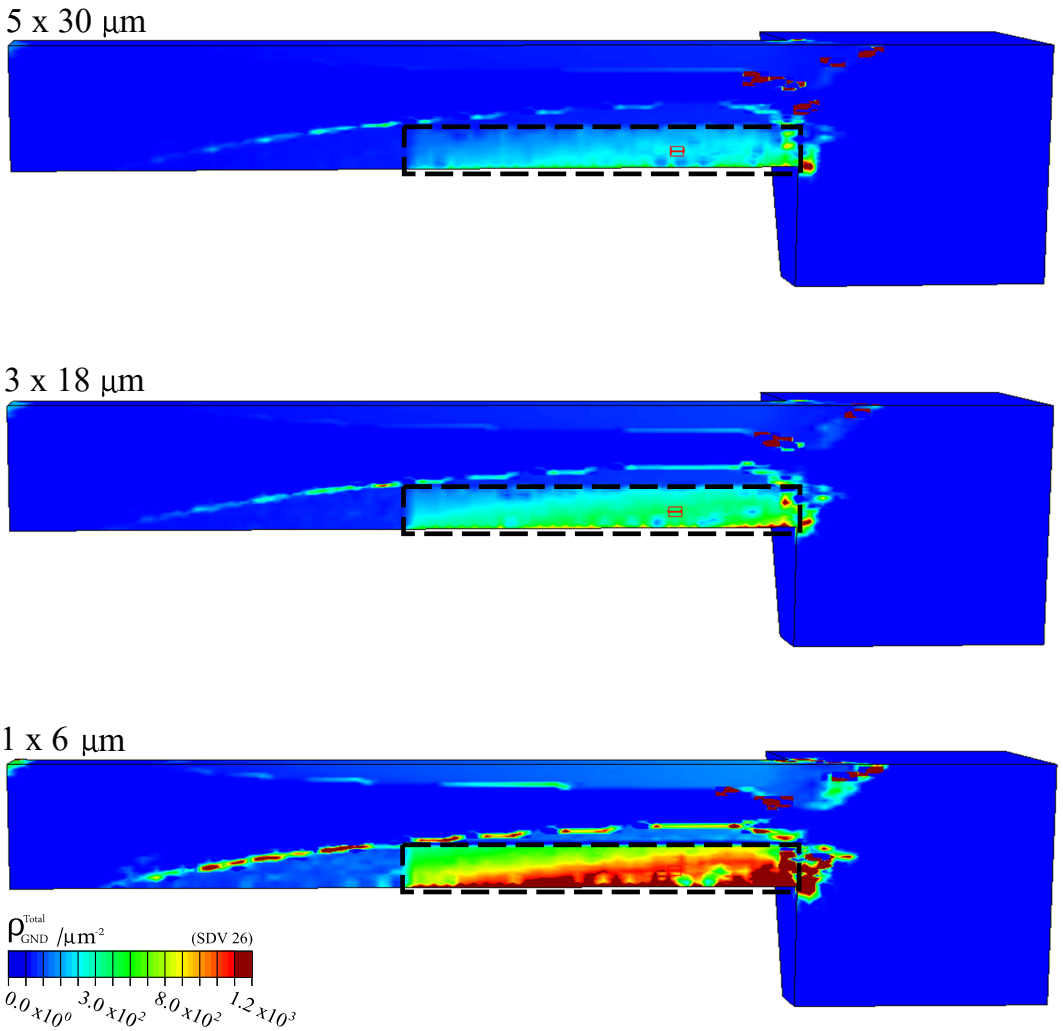


Figure 4.36: 5x30 μm, 3x18 μm and 1x6 μm microcantilevers, the 406 elements encompassed by the black dotted line were used to average the GND density on the primary slip system.

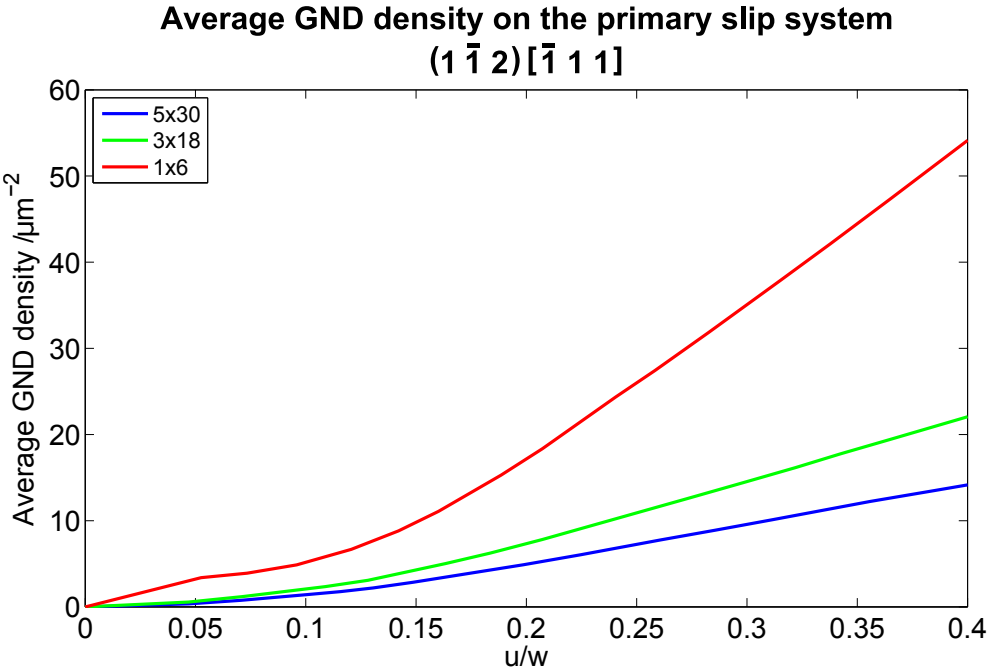


Figure 4.37: GND density for the primary slip system, (1 $\bar{1}$ 2)[$\bar{1}$ 1 1] (SDV71), averaged over 3248 integration points for 406 elements.

Beam depth /μm	Average GND density on primary slip system at yield /μm^{-2}	Average GND density on primary slip system at maximum displacement /μm^{-2}
5	0.3	14.0
3	0.6	22.0
1	3.4	54.0

Table 4.5: Summary of results from figure 4.37. GND density values on the primary slip system, (1 $\bar{1}$ 2)[$\bar{1}$ 1 1] (SDV71), taken at 2 μm beam displacement, corresponding to 0.4 u/w and $\sim$ 2.2 % simple beam strain.

The CP size effect results in table 4.3 show that yield occurs at $\sim$ 0.06 u/w. At the point of yield, the average GND densities on the primary slip system is small in comparison to large strains. From this, it can be assumed that GND pinning of mobile dislocations has a much more significant contribution to microcantilever size effects at

larger plastic strains than they do at smaller plastic strains.

In literature, microcantilever size effects are often quantified by the variance of yield stress [260, 237, 203]. Using this definition, it is likely that any size effect caused by mobile dislocation pinning by GND densities is dominated by other mechanisms, such as the limitation of available sources, particularly as microcantilever depth sizes approaching 1 μm or lower. As beam size increases, e.g. depths $> 5\,\mu$m, source limitation becomes much less significant [197] (discussed in detail in section 2.6.7 on page 81), and mobile dislocation pinning from a density of GNDs at low plastic strains becomes more significant. Although for all simulated beam sizes, the increase in the measured yield stress due to GND pinning of mobile dislocations is quite small.

This provides a reason why the yield stress approaches bulk values at microcantilever depths $> 5\,\mu$m. However, from figure 4.35 and figure 4.37 we see that the GND densities increase with increasing strain. At 0.4 u/w, there is a significant difference in the GND density between the 3x18 μm and 5x30 μm microcantilever. This implies that a size effect in the work hardening regime should persist past microcantilever depths $> 5\,\mu$m, although the magnitude of this size effect is likely to drop off quickly with increased geometry size.

4.4.4 CP microcantilever size effect summary

A size dependent crystal plasticity UMAT was provided by Dunne et al. [178][238], and implemented within ABAQUS 6.14-2 commercial finite element software. Initial checks of the UMAT in section 4.3.5 discovered that there was a critical element size, below which the GND density would fall to zero resulting in a perfectly plastic response of that element. The effect of this was significant enough to reverse the size effect in two simulations in section 4.3. Therefore, a compromise had to be made between solution stability and mesh refinement. Consequentially, the microcantilever geometries used for section 4.4 could not be reduced much below 1 μm of width whilst keeping adequate

mesh refinement, since too many elements would be below the critical size.

Three equilateral prismatic microcantilever finite element models of geometry size, 5x30μm, 3x18μm, 1x6μm were simulated. Each microcantilever was displaced to the same strain, and the GND densities on the top twenty four slip systems were calculated for every increment. Work hardening within the UMAT was achieved by making the plastic velocity gradient dependent on a probability of pinning from a density of GNDs on the first twenty four BCC slip systems. An increase in strain gradient, increases the GND density, reducing the plastic velocity gradient; this relationship introduces size dependency into the UMAT. A modest size effect was obtained and the yield stresses were calculated using simple beam theory, results are given in table 4.3.

The size effect modelled was far weaker than that found experimentally. The relatively small contribution GNDs had to the microcantilever size effect was determined to be due to to the relatively small GND density present during yield. Yield typically occurs small strains, particularly in microcantilevers as stress is initially localised to the lower vertex at the fixed end. The magnitude of the hardening caused by GNDs at the point of yield was much lower than that at high strains. From these results it can be determined that the microcantilever size effect, when quantified by yield strength, is dominated other other mechanisms. However, the GND densities in the respective sized microcantilevers rapidly diverged and increased after $\sim 0.17\ {}^{u}/_{w}$ ($\sim$ 1 % simple beam strain), which is much higher strain than that at yield ($\sim$ 0.3%). Therefore the contribution GNDs had to the size effect became increasingly more significant during work hardening.

Beam depth /μm	Total GND density in representative element at $\sim$ 2.2 % strain /m^{-2}	Dislocation spacing /nm
5	3.1 x10^{14}	56
3	5.0 x10^{14}	44
1	1.2 x10^{15}	29

Table 4.6: GND density values for three different sized CP microcantilever beam widths (width:length of 1:6) taken at $\sim$ 2.2 % strain in a representative element (shown in figure 4.34). Table for comparison to literature.

The GND densities found in this investigation, summarised in table 4.6, showed reasonable agreement to those found experimentally. GND density measurements in single crystal copper microcantilevers by Armstrong (2009) [237] showed a maximum GND density of, 7.4 x 10^{15} m^{-2}, 9.2 x 10^{15} m^{-2} and 1.6 x 10^{14} m^{-2} for beam depths 1.6 μm, 3.4 μm and 15.3 μm, tested to a simple beam strain of 2.4, 2.1 and 2.9 respectively. These results are also in reasonable agreement the 3D DD simulations of Motz et al. (2008) [196] who found a dislocation pile-up spacing of 35 nm and 90 nm for rectangular beams of widths 0.5 μm and 1 μm.

4.5 Computational plasticity study conclusion

The work reported in this chapter proved that the pinning of mobile dislocations by a density of GNDs is not the dominant hardening mechanism at beam widths < 5 μm . By comparing this work with the DD simulations carried out by Tarleton et al. (2015) [197], it is clear that dislocation source limitation, the statistical variation in source strength, the statistical variation in source distribution, and the suppression of active sources caused by back-stress from soft-pile ups have a much greater influence on yield stress at this lengthscale; all of which cannot explicitly be modelled using computational plasticity models. However, it may be possible to empirically alter the constitutive equation for the plastic velocity gradient to match the experimentally observed results.

Chapter 5

5 Micromechanical study of proton irradiated ODS steels

Chapter 3 section 3.4.5 characterised the microcantilever size effect for the reference alloys and the in-house produced steel alloys, consolidated at 1150 $^{\circ}C$. It was found that as the beam depth was reduced below approximately 4.5 μm, the measured yield stress significantly diverged from near-macroscale values. A reduction in beam size also increased the scatter in yield stress; this was attributed to a natural statistical variation in source strength and distribution. The work reported in this chapter aims to investigate irradiation hardening in the in-house produced alloys, measured using nanoindentation and microcantilever bend tests.

In order to reduce the amount of scatter observed in the microcantilever tests, and to achieve a closest approximation possible to macroscale properties, microcantilevers needed be fabricated with beam depths greater than 4.5 μm. Due to this restriction, damage was introduced using proton irradiation, since this produced a much deeper damage layer than heavy ion irradiation, and was not subject to the long timescales and active sample handling involved with neutron irradiation.

5.1 Introducing damage

First wall structural materials in a commercial fusion reactor will be exposed to a 14.1 MeV neutron flux, which is projected to impart a displacement damage in excess of 150 dpa during an operating lifetime of 5 years [10] (section 2.1). Therefore, examining a candidate material's behaviour under irradiation is vital to assessing its viability for use in reactor components. Since an adequate fusion relevant neutron source has yet to be built, damage has to be introduced to test specimens through other means. Currently, this is most often achieved through ion irradiation, or fission produced neutrons. For reasons discussed above, neutron irradiation was not suitable for use in this project,

and heavy ion implantation could not produce the damage depth necessary for the fabrication of large microcantilevers. Protons are able to overcome some of the main drawbacks of heavy ion and neutron irradiation, i.e. lack of penetration, along with activation and long irradiation times respectively. At 2 MeV, protons have a penetration of between 15 μm and 25 μm in transition metals, but not enough energy to surmount the Coulomb barrier to produce activation.

Due to a high electronic energy loss, incident ions lose energy quickly. As a charge particle's energy decreases, its interaction cross-section increases, leading to reduction in the particle's mean free path. This gives rise to a spatial region just before the particle stops where more energy is dissipated, known as the Bragg peak (figure 5.3). High energy protons in matter give rise to a particularly characteristic damage profile, which is approximately flat before a well-defined deep Bragg peak. Damage is produced in small clusters via Rutherford scattering, in which the Coulomb charge field of proton and nucleus interact and permit an exchange of energy [261]. This results in several small widely spaced damage cascades and many isolated Frankel pairs [25]. In contrast, heavy ions and neutrons tend to produce damage in much larger clusters.

5.1.1 Proton irradiation at Surrey Ion Beam Centre

The proton irradiation of the in-house produced alloys was carried out at the Surrey Ion Beam Centre (University of Surrey, UK). Protons were accelerated through an electrostatic field to an energy of 2 MeV using a Van de Graaff accelerator. The irradiation area was originally designed for four inch silicon wafers but to increase the dose, a two inch aperture was used. The smaller irradiation area required the design and fabrication of a custom sample plate, shown in figure 5.1.

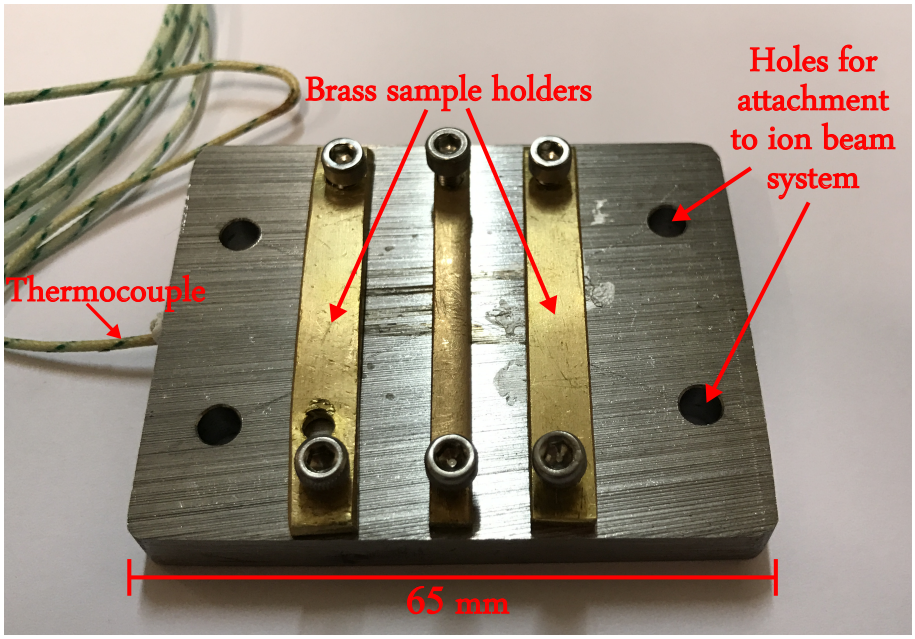


Figure 5.1: Sample plate used for Surrey proton irradiation.

Brass sample holders were used to mechanically attach specimens to the base plate, and conductive paint was applied under the specimens to prevent a build up of charge. The irradiation temperature was kept constant at 300 $°C$, measured using a thermocouple placed inside a deep drilled hole to the centre of the plate. Thermal contact was ensured by flooding the hole with thermally conductive ceramic-filled epoxy resin prior to insertion of the thermocouple. Irradiation dose was kept as homogeneous as possible across the irradiated area, through beam raster scanning. Fluence was measured using four Faraday cups attached to the rear of the aperture plate, and close enough to the aperture to be incorporated into the rastered scan. The total fluence over an irradiation time of 30 hours was 1.5 x10^{17} ions/cm^2.

The spatial distribution of damage into the sample was simulated using the Monte Carlo code SRIM 2008 (Stopping Range of Ions in Matter). As explained in section 2.2.1 (p14), coding errors, highlighted by Stoller et al. (2013) [47], necessitated the use of the Quick K-P energy calculation. Approximately 1 x10^5 2 MeV protons were simulated in an iron target using a displacement threshold energy of 40 eV and lattice

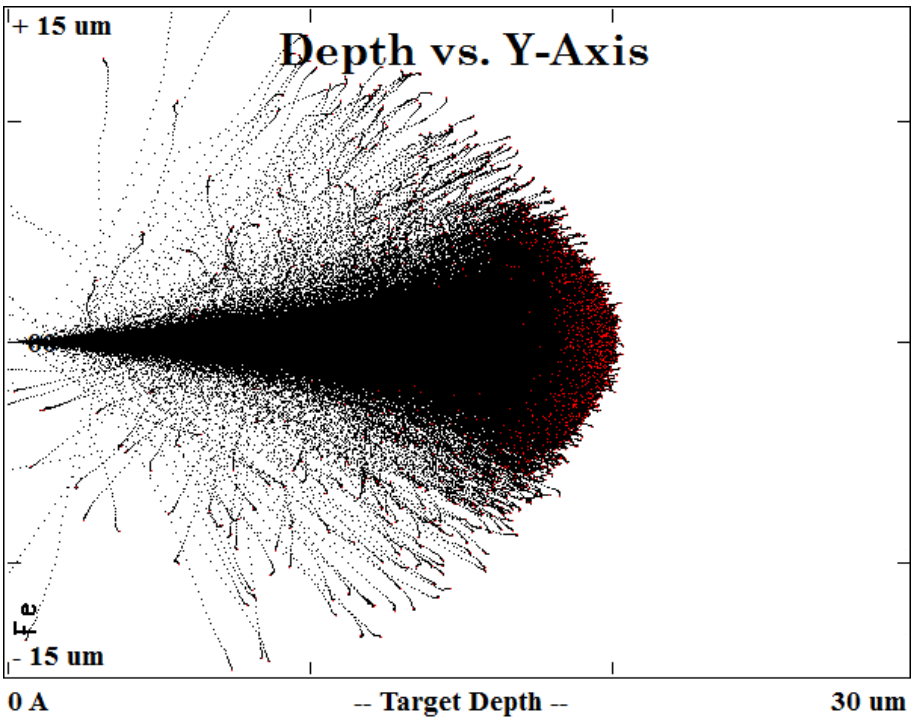


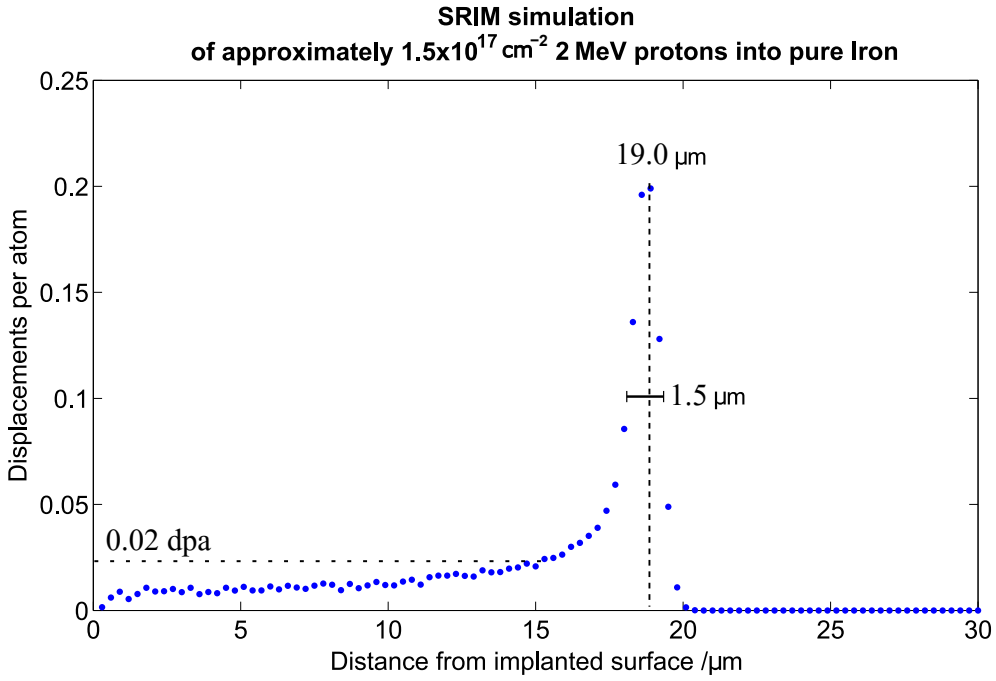
Figure 5.2: SRIM simulation of approximately 1 x10^5 2 MeV protons in iron.

binding energy of 0 eV [47], results are shown in figure 5.2.

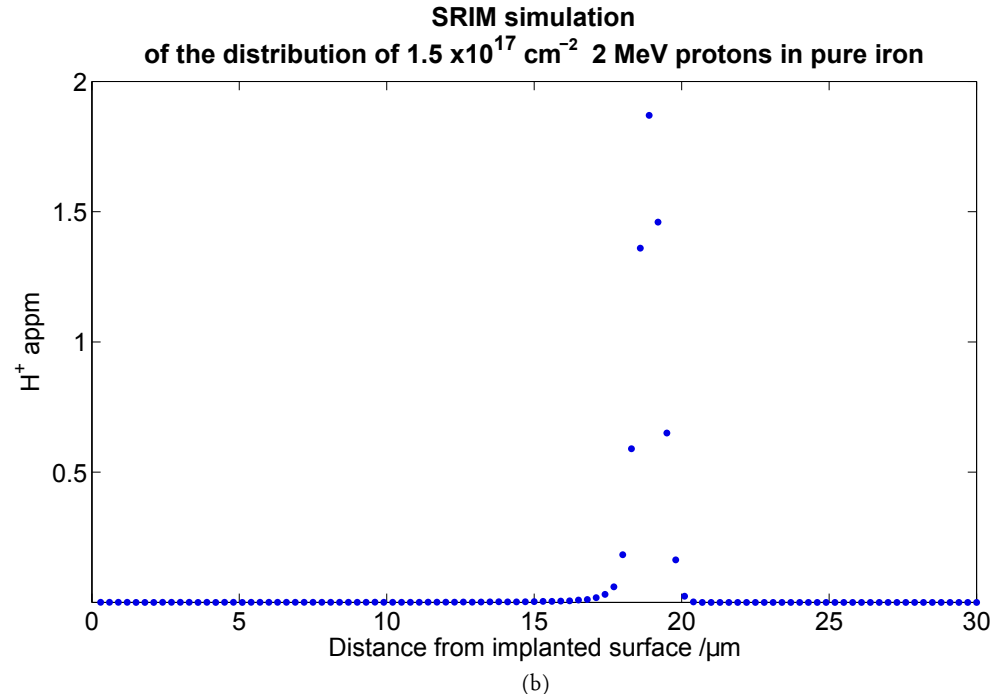
SRIM calculates damage per incident ion as a function of depth into sample, y, (in Angstrom layers). This allowed displacements per atom (dpa) to be calculated as a function of depth, y, by modifying equations 2.1 and 2.2 (p11), to give,

$$dpa(y) = \frac{\phi_T \nu(E_i, y)}{N} \tag{5.1}$$

where ϕ_T is the total fluence (ions per unit area). SRIM provides the value for $\nu(E_i, y)$, which is the displacements produced as a function of incident ion energy, E_i, and irradiation depth, y. N is the atomic density. SRIM assumes an amorphous target material, so crystallographic effects such as crowdion transfer and channeling are neglected from the calculation of $\nu(E_i, y)$. Figure 5.3 shows the displacement damage with respect to irradiation depth for 2 MeV protons in iron.



(a)



(b)

Figure 5.3: SRIM simulation of irradiation run at the University of Surrey, showing the penetration of 2 MeV protons in pure iron, the Bragg peak is at a depth of 19 μm from the surface. (a) Displacement damage. (b) Hydrogen concentration.

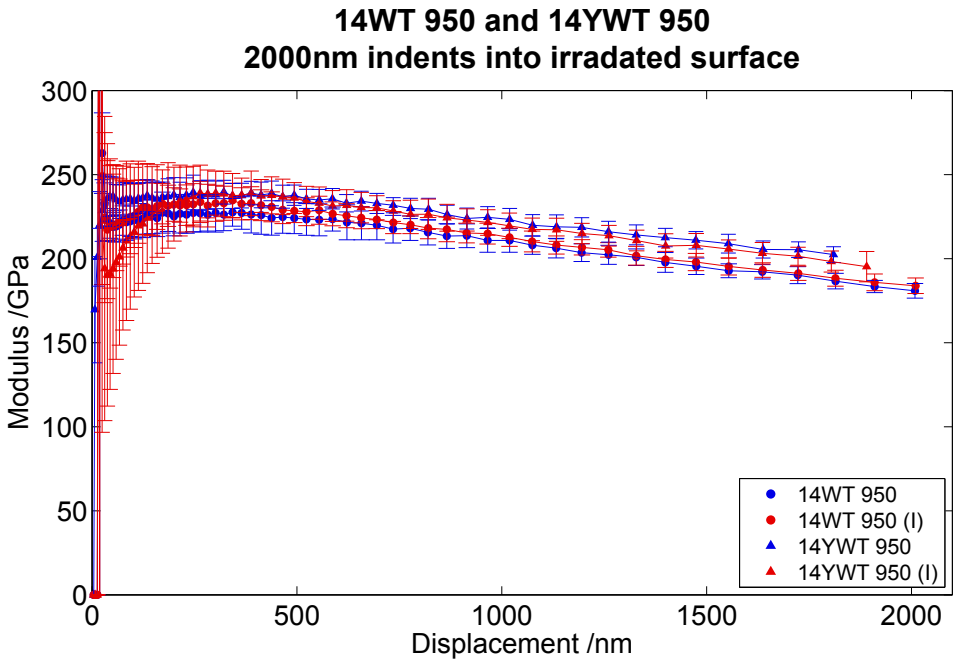
Figure 5.3(a) displays a damage profile that is characteristic of proton irradiation. A flat region of relatively constant damage is present from 0 to 15 μm depth, before a sharp and well defined Bragg peak from 15 to 20 μm depth. A peak damage of 0.2 dpa is observed at 19.0 μm depth, which was an order of magnitude higher than the damage at 15 μm depth of ~ 0.02 dpa. The Bragg peak was found to have a full width half maximum of approximately 1.5 μm. Figure 5.3(b) shows that almost all of the 2 MeV protons implanted into a pure iron specimen are stopped within approximately 17.5 μm and 20 μm irradiated depth.

5.2 Nanoindentation normal to irradiated layer

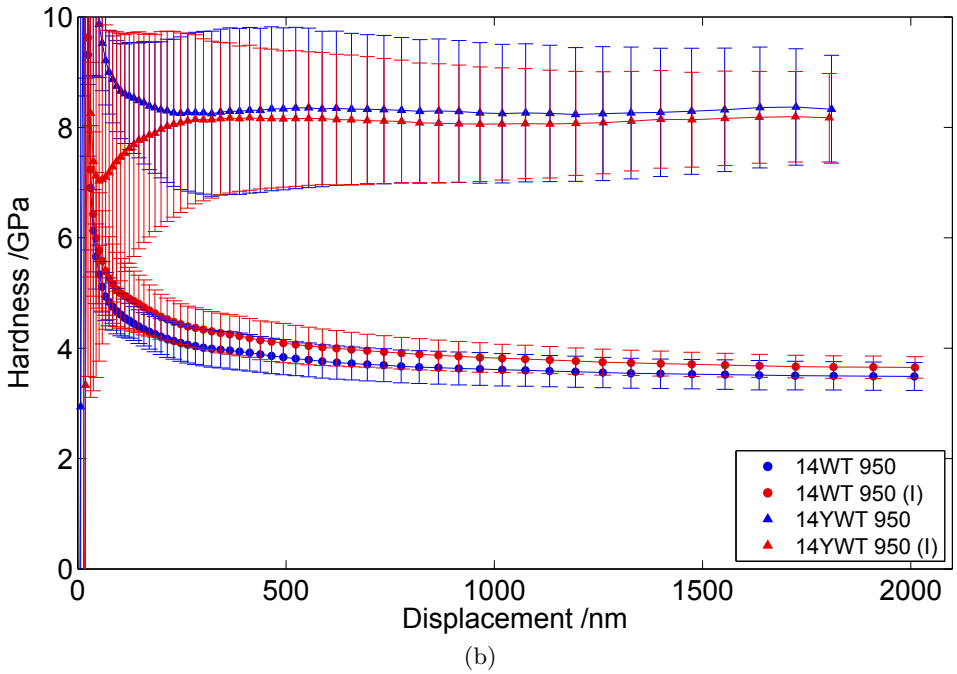
2 MeV proton irradiation at Surrey Ion Beam Centre produced a deep $\sim$ 20 μm layer of damage, with a Bragg peak at 19.0 μm. The damage produced however, was quite modest in comparison to heavy ion irradiation, approximately 0.01 - 0.02 dpa between the surface and 15 μm depth, and 0.2 dpa at the Bragg peak. As an initial investigation of the changes irradiation had on the mechanical properties of the in-house alloys, nanoindents, using a Berkovich tip geometry, were placed normal to the irradiated layer to a indentation depth of 2 μm, and the measured hardness was compared to their unirradiated counterparts.

Measurements of the modulus and hardness were made in an MTS Nanoindenter XP (MTS Nano Instruments, Oak Ridge, TN, USA) using a continuous stiffness measurement (CSM) system that used a 2 nm 45 Hz harmonic displacement, allowing the contact stiffness of the sample to be measured continuously during loading (described in section 2.6.2). Using a method similar to that described in section 2.6.1 (p53), the tip area coefficients were calculated from the average load-displacement data of sixteen 2 μm indents in fused silica. Then using the known area function and contact stiffness as a function of tip displacement, both modulus and hardness were also be calculated as a function of tip displacement.

5.2.1 Results for indentation normal to irradiated layer

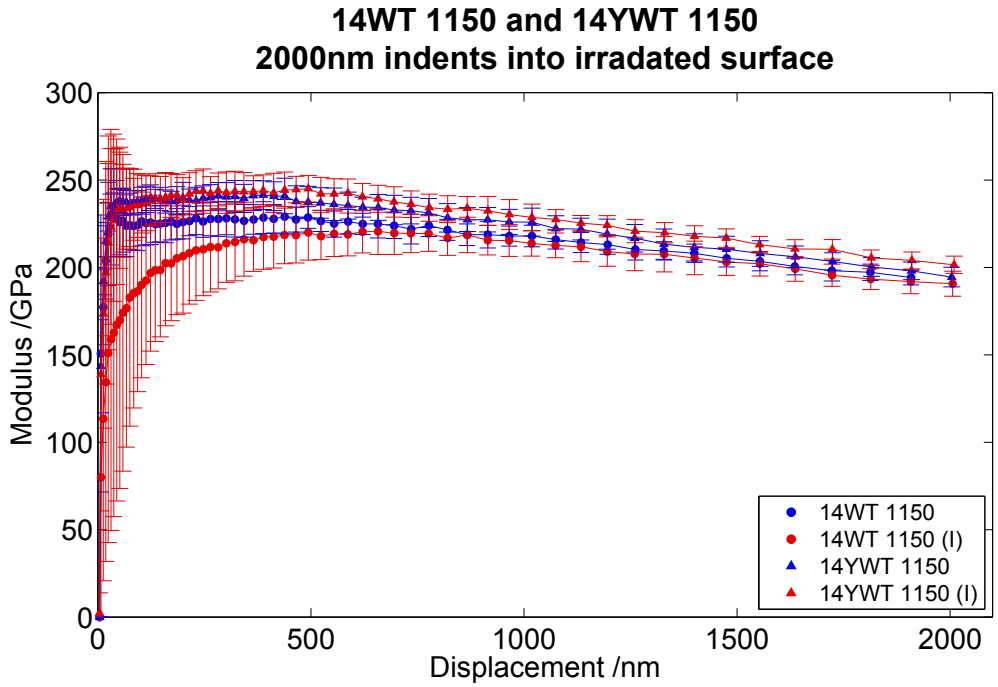


(a)

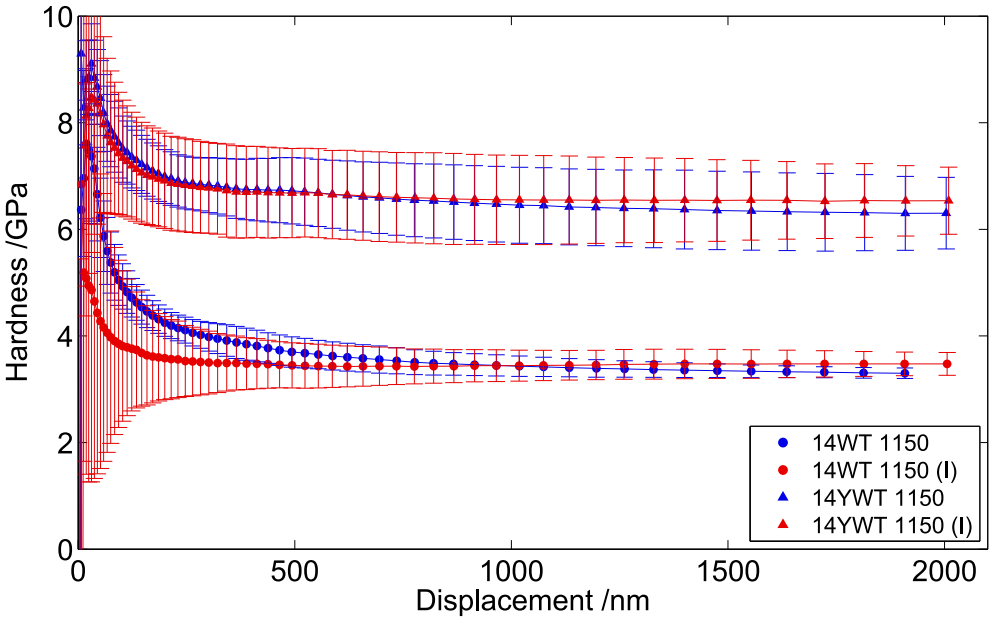


(b)

Figure 5.4: 14WT 950 and 14YWT 950 indents normal to the irradiated layer. Irradiated indents are shown in red. Bars depict $\pm$ 1σ (standard deviation).



(a)



(b)

Figure 5.5: 14WT 1150 and 14YWT 1150 indents normal to the irradiated layer. Irradiated indents are shown in red. Bars depict $\pm$ 1σ (standard deviation).

5.2.2 Result summary for indents normal to irradiated layer

Table 5.1 provides a summary of the results given in section 5.2.1.

Material	Unirradiated modulus /GPa (400 - 800 nm)	Irradiated modulus /GPa (400 - 800 nm)	Unirradiated hardness /GPa (1250 - 2000 nm)	Irradiated hardness /GPa (1250 - 2000 nm)
14WT 950	221.7 ± 9.1	225.9 ± 7.2	3.54 ± 0.27	3.73 ± 0.23
14YWT 950	234.6 ± 6.1	232.4 ± 9.0	8.28 ± 1.17	8.12 ± 0.91
14WT 1150	225.6 ± 7.2	219.0± 13.3	3.37 ± 0.14	3.47 ± 0.27
14YWT 1150	235.3 ± 8.3	240.4 ± 8.5	6.37 ± 0.72	6.54 ± 0.76

Table 5.1: Indents into unirradiated and irradiated surface (normal to irradiated surface) in the in-house produced material array. Results shown alongside ± 1σ (standard deviation).

As previously discussed in section 2.6.2, both the modulus and hardness should be invariant with respect to indentation depth for a uniform material (if excluding indentation size effects). This was the case for the measured hardness, after $\sim$ 150 nm where indentation size effects were significant. However, after being initially (approximately) flat, the modulus was measured to decrease at larger indentation depths. This was most likely caused by compliance of the sample mounting medium (hot wax), causing an apparent drop in contact stiffness under the high loads present for large Berkovich indentation in these materials (230 mN to 500 mN). For this reason, the modulus data summarised in table 5.1 was averaged between 400 nm and 800 nm displacement into sample. The hardness data was averaged between 1250 nm and 2000 nm, since this region was approximately invariant with indentation depth. There was also a noticeable increase in the standard deviation of hardness in the ODS variants; this will be discussed in detail in section 5.3.

Any irradiation hardening shown by the materials tested was insignificant, and was

within one standard deviation. 14YWT 950 showed possible softening, but again, this was well within one standard deviation, and not conclusive. This may have been due to a lack of irradiation damage close to the irradiated surface, which can be observed from the SRIM simulation in figure 5.3. The depth of the plastic zone under indenter tip can be approximated by five times the indent depth (for a Berkovich indent) [161]; this would suggest that for the first 200 - 500 nm of indent the damage levels examined were extremely low. The data from the SRIM simulation showed that as as the irradiation depth was increased from 0 to 2 μm, the irradiation damage increased from 0 to $\sim$ 0.01 dpa. This can possibly be observed as a slight increase in average hardness in 14WT 1150 and 14YWT 1150 after approximately 1000 nm. However, this is not observed in either 14WT 950 or 14YWT 950, and the results are not significant enough to be conclusive.

5.3 Nanoindentation across irradiated layer

In section 5.2, large 2000 nm indents were placed in the irradiated surface. No conclusive hardening was observed in any of the materials tested, which was attributed to the small damage levels found close to the surface. The SRIM simulation of protons in iron, figure 5.3, showed that the damage at the Bragg peak was an order of magnitude higher than that found at irradiation depths < 15 μm. To investigate whether the damage profile could be observed with nanoindentation, cross-sectional specimens were prepared and 250 nm deep indents were placed across the profile of the irradiated layer. The hardness as a function of irradiation depth could then be determined.

5.3.1 Method for nanoindentation of irradiated layer cross-section

To prepare the specimens for indentation, each sample was rotated 90° so that the cross-section of the irradiated layer was exposed, demonstrated in figure 5.7. The cross-sectional surface was then polished to a colloidal silica finish. A rounded edge is produced during polishing, partly from the impact of the sample's leading edge on the polishing medium, and partly from the impression the sample makes in the soft polishing pads used in the latter stages of polishing. As the sample moves over the polishing pad, the applied downwards force pushes the sample into the pad, rounding the edges, in particular, the leading edge.

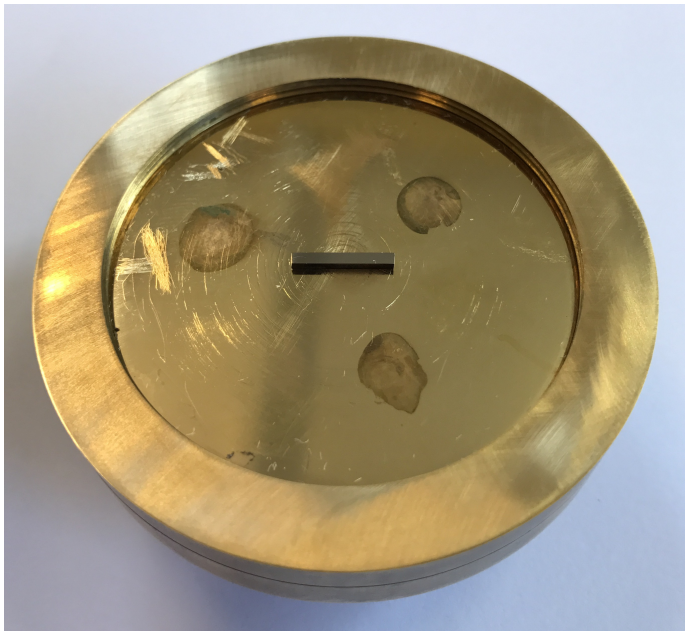


Figure 5.6: Polishing plate with ringed support.

Best efforts were made to reduce the fillet radius of the sample edge, i.e. to ensure a squared edge. Firstly, the polishing plate had an adjustable ringed support fitted to reduce the pressure exerted by the sample on the polishing pad, shown in figure 5.6. The downwards force on the polishing plate during each preparation stage was minimised, using only the weight of the polishing plate where possible. A PSU-M polishing pad (Kemet International Ltd, Maidstone, UK) was used for all stages of diamond polishing since this provided a firm lapping surface with minimal sample impression. Lastly, the specimen was polished so that the irradiated surface was always at the trailing edge.

A series of small Berkovich indents of 250 nm depth were made in an inclined array across the damage profile, demonstrated in figure 5.7. The indents were placed with a separations of 13 μm, so that their respective plastic zones could not interfere. A set of sixteen 250 nm calibration indents were performed after each array ($\sim$ 30 - 50) indents. Due to a small amount of rounding present, indents were not placed within 5 μm of the edge. Hardness values presented were averaged between 200 nm and 250 nm indentation depth. Results are given in section 5.3.2.

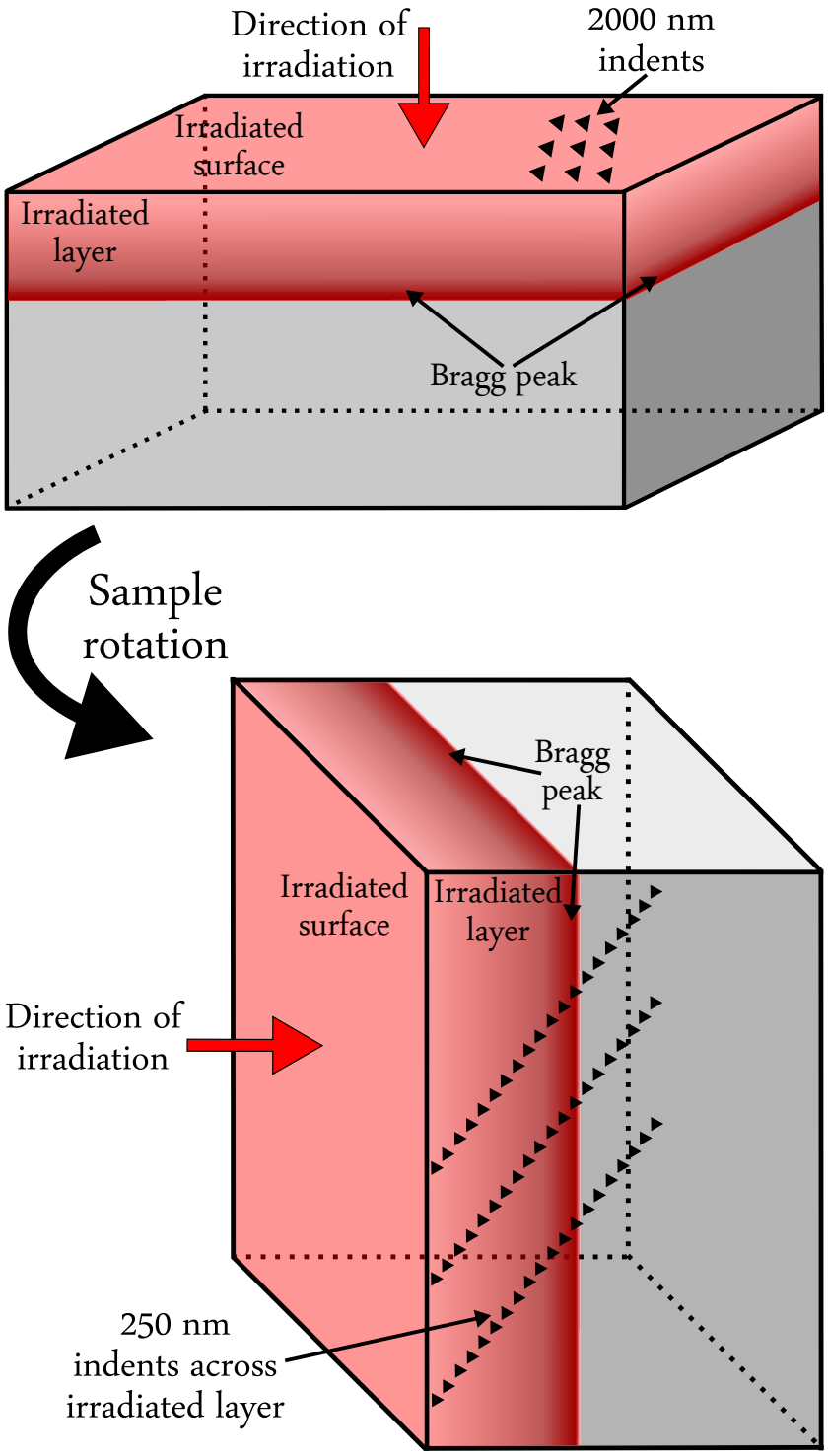
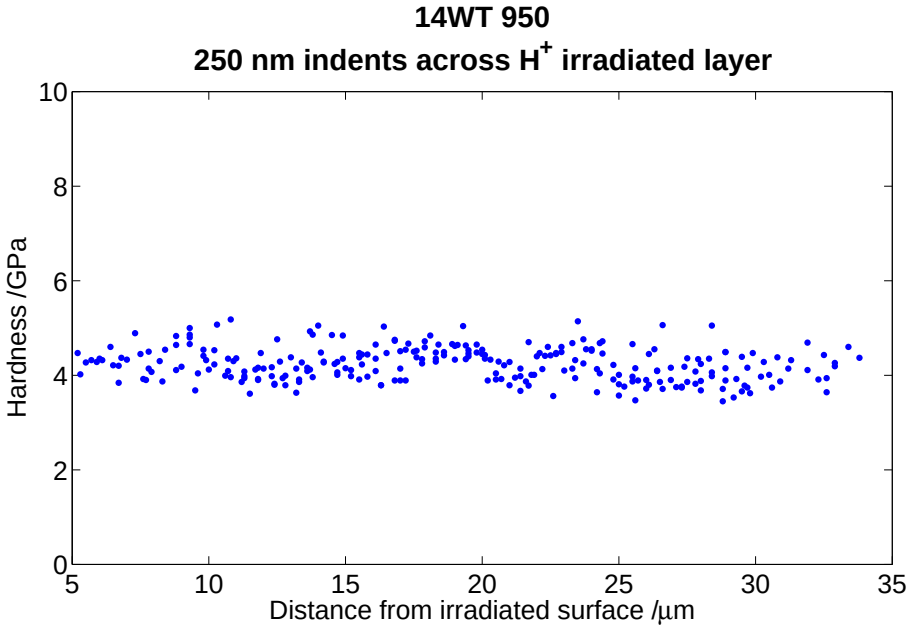
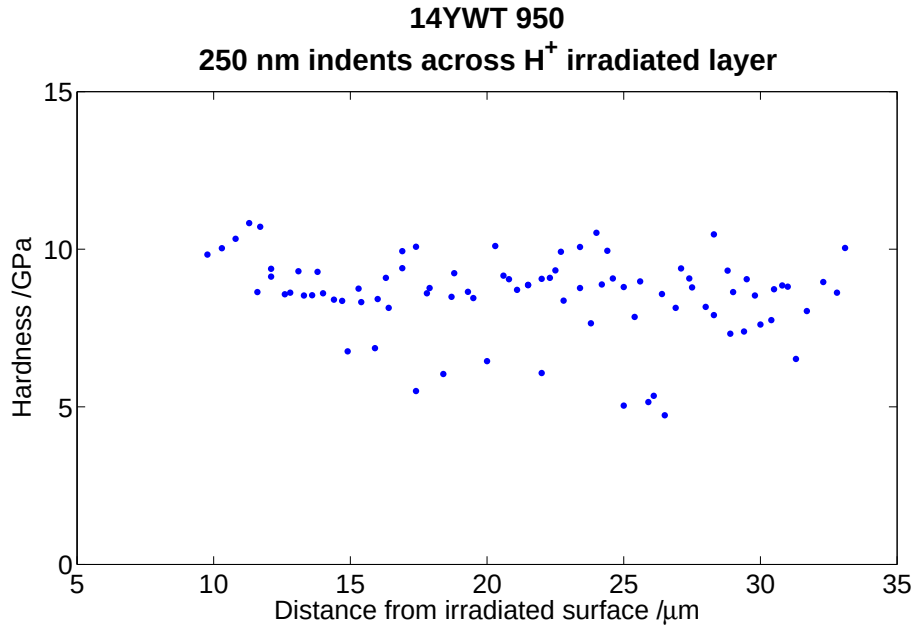


Figure 5.7: Schematic diagram of irradiated specimen, showing the two orientations of indents used. A gradient of red is used to represent the proton damage layer.

5.3.2 Results for nanoindentation of irradiated layer cross-sections

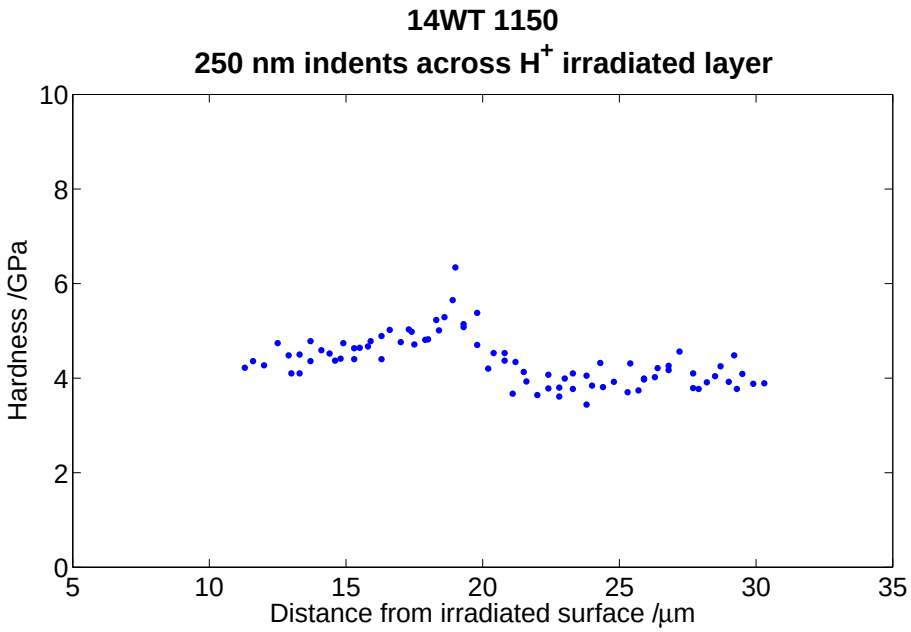


(a)

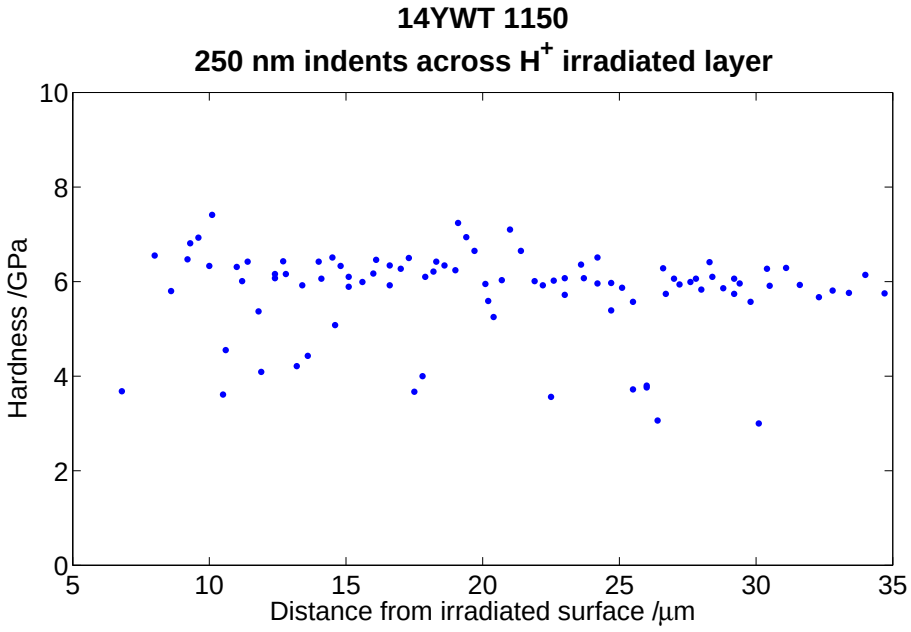


(b)

Figure 5.8: 250 nm indents examining the cross-section of the proton irradiated layer. (a) 14WT 950. (b) 14YWT 950.



(a)



(b)

Figure 5.9: 250 nm indents examining the cross-section of the proton irradiated layer. (a) 14WT 1150. (b) 14YWT 1150.

Results summary for nanoindentation of irradiated layer cross-section

Indentation hardness with respect to irradiation depth was measured across the irradiated layer, determined by SRIM simulation to be approximately 20 μm deep. Hardness values displayed in figures 5.8 and 5.9 were calculated from the average hardness between indentation depths of 200 nm to 250 nm. Table 5.2 summarises the indentation hardness measured across the irradiated layer. Average irradiated hardness was calculated for depths between 5 μm - 17 μm, corresponding to damage levels of 0.01 dpa - 0.04 dpa, this was to provide average hardness measurements and corresponding standard deviations across an approximately flat damage profile.

	Indents across the irradiated layer		Indents normal to irradiated surface	
Material	Unirradiated hardness /GPa (200 - 250 nm)	Irradiated hardness /GPa (200 - 250 nm) (0.01 - 0.02 dpa)	Unirradiated hardness /GPa (1250 - 2000 nm)	Irradiated hardness /GPa (1250 - 2000 nm)
14WT 950	4.13 ± 0.36 (> 20.5 μm)	4.28 ± 0.34 (< 17.0 μm)	3.54 ± 0.27	3.73 ± 0.23
14YWT 950	8.39 ± 1.33 (> 20.5 μm)	8.86 ± 1.11 (< 17.0 μm)	8.28 ± 1.17	8.12 ± 0.91
14WT 1150	4.00 ± 0.24 (> 20.5 μm)	4.60 ± 0.26 (< 17.0 μm)	3.37 ± 0.14	3.47 ± 0.27
14YWT 1150	5.67 ± 0.91 (> 20.5 μm)	5.78 ± 0.98 (< 17.0 μm)	6.37 ± 0.72	6.54 ± 0.76

Table 5.2: Summary table of hardness data from 250 nm deep indents placed across the irradiated layer., for comparison the hardness data from section 5.2.1 (table 5.1) is displayed alongside. For the indents placed across the irradiated layer, the unirradiated data shown was averaged for indents > 20.5 μm irradiation depth, and the irradiated (0.01 - 0.02 dpa) data was averaged for indents < 17.0 μm irradiation depth. Hardness and modulus of each indent was taken as an average between 200 - 250 nm indentation depth. Results are shown with $\pm$ 1σ (standard deviation).

5.3.3 Discussion for nanoindentation of irradiated layer cross-section

14WT 950 did not demonstrate any convincing irradiation hardening at depths corresponding to the lower damage levels (0 - 15 μm). A slight reduction in the scatter of the measured hardness was observed between $\sim$ 17 μm and 20 μm irradiation depth, correlating to the location of the Bragg peak. There was no observable change in hardness in higher bound of scatter at the Bragg peak; irradiation hardening only occurred in lower bound of scatter, i.e. softer indents. The hardness of the lower bound of scatter was 4.34 GPa at 19 μm irradiation depth, compared to an average of 3.73 GPa for the lower bound of scatter at a depth $^{\leq 17\,\mu\mathrm{m}}_{\geq 20\,\mu\mathrm{m}}$, equating to a radiation hardening of $\sim$ 0.6 GPa. Although the hardness increase at the Bragg peak in 14WT 950 was much less convincing than that shown by 14WT 1150, it was unlikely to be produced by a natural statistical variation due to the large number of indents made.

Irradiation hardening in 14WT 950 appeared to be suppressed, when compared that demonstrated by 14WT 1150. This suggests that 14WT 950 had an increased density of sink sites (particularly in the higher hardness scatter bound) that promoted the recombination of defects, thus reducing the effective damage in the specimen. This argument is further supported by the slight increase in hardness of 14WT 950 when compared to 14WT 1150. The increased number of sink sites in 14WT 950, could be due to the lower consolidation temperature, allowing for greater retention of the dislocation network and a slight reduction of the grain size (table 3.3), increasing the volume fraction of grain boundaries.

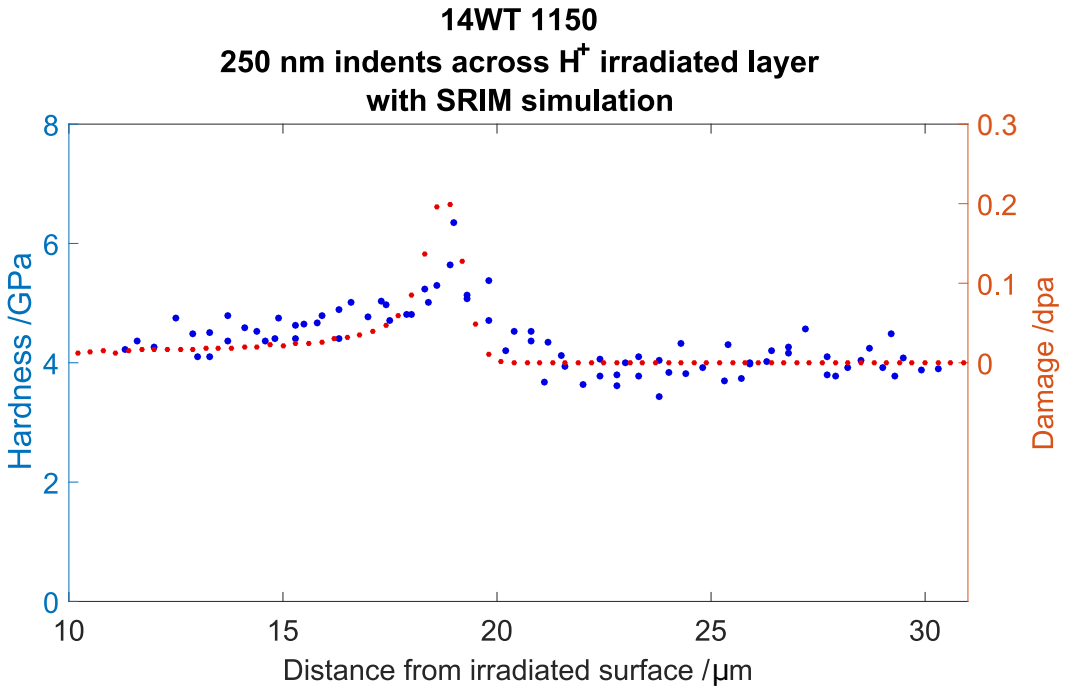


Figure 5.10: Hardness profile of indents across the irradiated layer in 14WT 1150 in comparison to the SRIM damage profile.

The graph of indentation hardness with respect to irradiation depth for 14WT 1150, figure 5.9(a), produced a profile that appears to correlate well with the proton damage profile calculated by SRIM. This correlation is displayed more clearly in figure 5.10. From table 5.2, 14WT 1150 gave an average unirradiated hardness of 4.00 GPa with a standard deviation of 0.24 GPa, this increased to 4.60 GPa for the region irradiated to 0.01 - 0.04 dpa. Hardness data clearly displayed the Bragg peak, determined to be at 19.0 μm irradiation depth. In comparison, the Bragg peak, calculated from SRIM, was at 18.9 μm. There was a small error in the measurement of the indent distance from irradiated surface, determined to be approximately $\pm$ 0.15 μm; however, this was small in comparison to the irradiated layer width, so was excluded from the graph. In addition to a small error in measurement, the slight discrepancy between the SRIM damage peak and peak measured using indent hardness could be due to crystallographic irradiation damage effects neglected by SRIM. The hardness at the Bragg peak was measured to

be 6.34 GPa at a corresponding damage of approximately 0.2 dpa.

In comparison, no discernible irradiation hardening was observed in either ODS alloy. This was most likely due the high density of additional sink sites provided by the oxide-matrix interface. The indents at $\sim$ 19 μm irradiation depth in 14YWT 1150 did measure a higher hardness than the modal value, the work reported in the following section (p261) argues that this was unlikely to be caused by irradiation hardening.

A large scatter was observed for both ODS alloys across the range of depths measured. The hardness distribution appeared to be bimodal, with the majority of the indents measured displaying a hardness close to the mean, and a small population having a hardness much closer to that expected for the their respective non-ODS alloy.

5.3.4 Investigation of bimodal nanoindentation hardness in ODS 14YWT

The bimodal variation in hardness, observed in both ODS alloys, was thought to be due to the microstructural heterogeneity of the two materials. Spatial variations in hardness can be produced by several types of microstructural heterogeneity in ODS alloys:

1. Heterogeneous grain morphology
2. Heterogeneity in local chemistry
3. Heterogeneity in oxide population

Work presented in the thesis by Burrows (2015) [208] also observed heterogeneous hardness distribution in the in-house produced ODS alloys. The author assumed that oxide density was homogeneous at the lengthscale of the 2000 nm indents and concluded that difference in hardness must be due to Hall-Petch strengthening in the fine grained regions.

The work reported in this section explores this further by using EBSD and energy-dispersive X-ray spectroscopy (EDX) to investigate variations in microstructure around specific indents made in 14YWT 1150 (from section 5.3.2). Since EBSD was not possible in 14YWT 950 (discussed further in section 3.2.3, p108), analysis was only carried on 14YWT 1150. The specific indent sites chosen for analysis are shown graphically in figure 5.11.

EDX is an analytical electron microscopy technique used to identify the spatial distribution of elemental components of a material. A full description of the technique is beyond the scope of this thesis, a comprehensive overview can be found in reference [262]. The EDX work in this thesis was carried out in a Zeiss Merlin SEM fitted with an X-Max^N 150 mm^2 EDS silicon drift detector produced by Oxford Instruments PLC. AZtecEnergy EDS software, also produced by Oxford Instruments PLC, was used for data acquisition and post-processing.

Results of EBSD and EDX analysis of 14YWT 1150 indents

Figure 5.11 graphically displays the indent sites chosen for each analysis technique. The specific sites are highlighted on the graph of hardness as a function of distance from irradiated surface for 14YWT 1150. The indents analysed were uniquely identified with numbers 1 through 11, and will be referred to as such throughout the discussion of the results. Indents 6 and 7 were investigated with both EBSD and EDX. It should be noted that the EBSD micrographs (figure 5.12) were recorded so that sample edge is at the top of the page, and the EDX maps (figures 5.13, 5.14, 5.15, 5.16 and 5.17) were recorded with the sample edge at the bottom of the page.

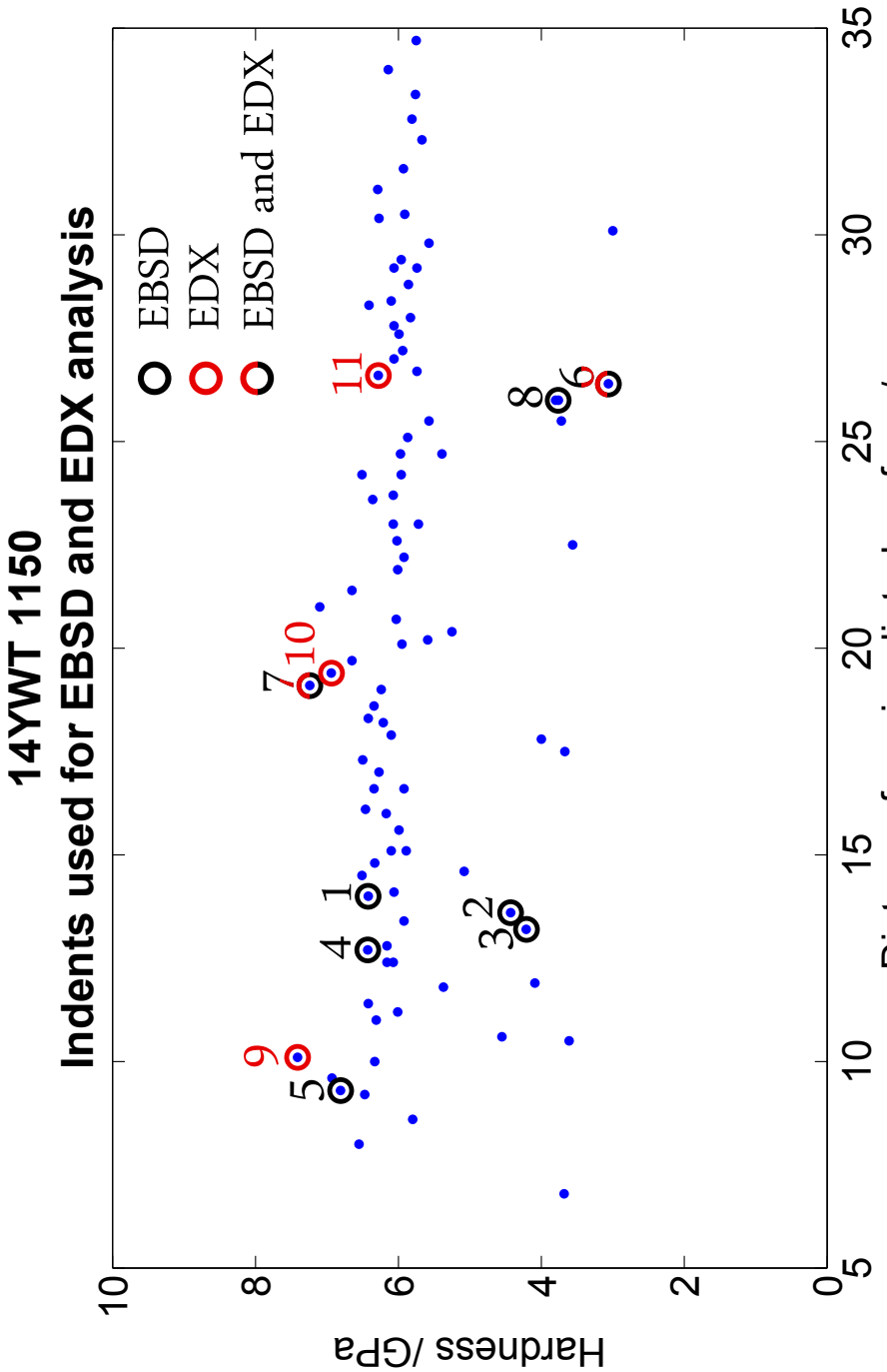


Figure 5.11: Hardness as a function of distance from the irradiated surface in 14YWT 1150, measured using Berkovich indents to a depth of 250 nm. Highlighted and numbered are the indent sites used for EBSD and EDX analysis.

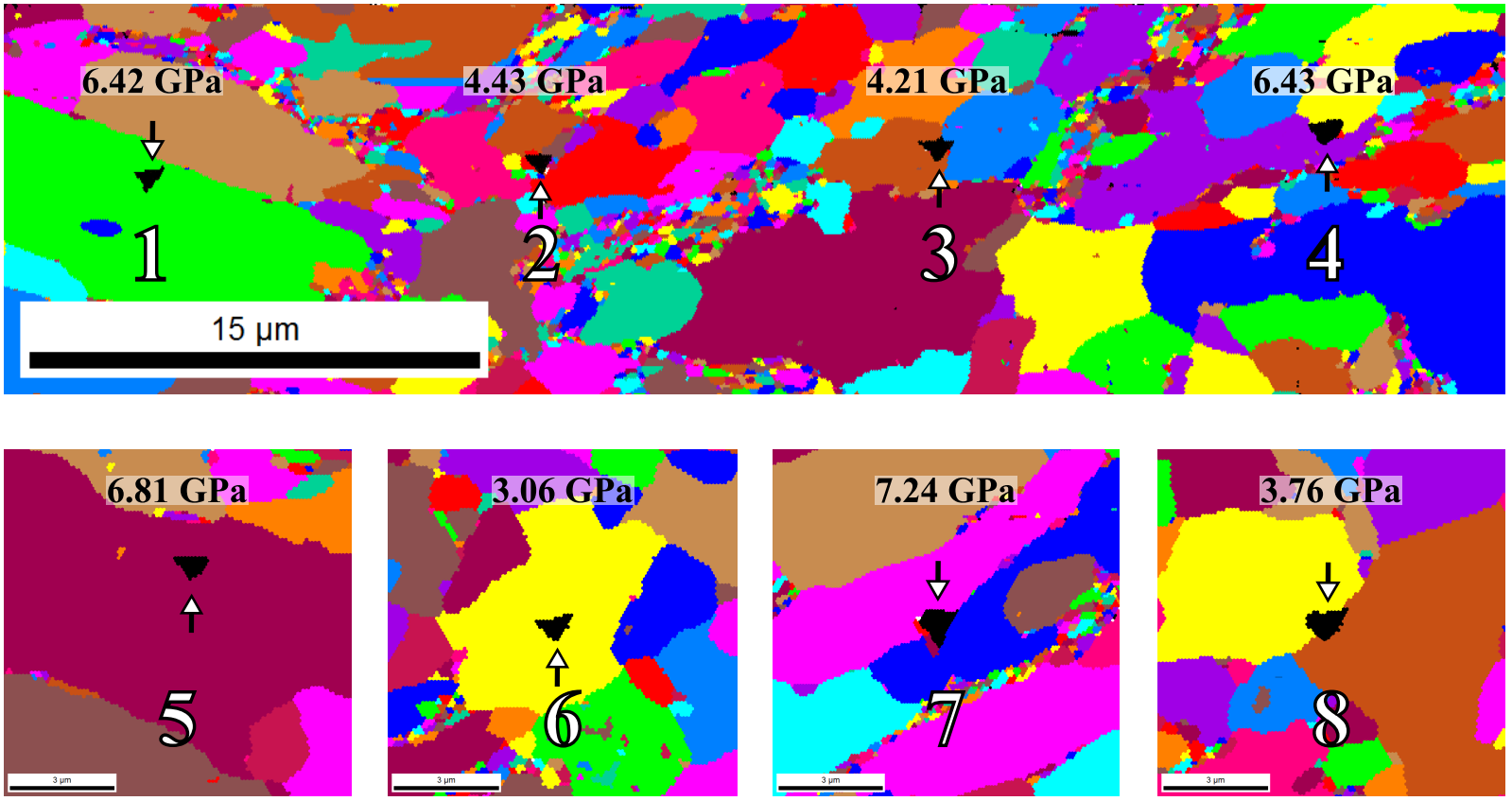


Figure 5.12: EBSD micrographs showing grain morphology around indent sites 1 to 8. Poorly indexed Kikuchi patterns are designated with a black pixel, thus indents are visible as black triangular shapes.

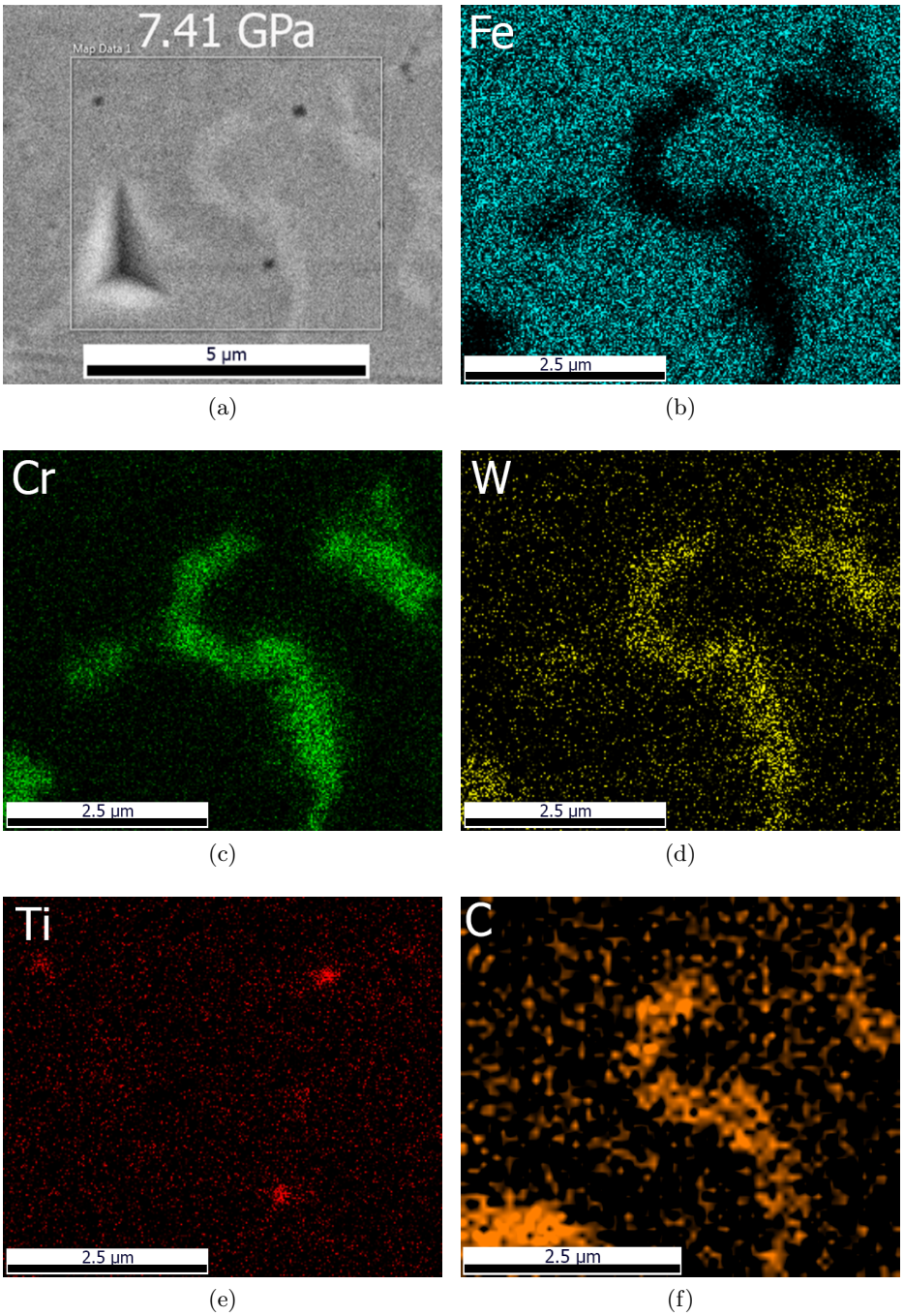
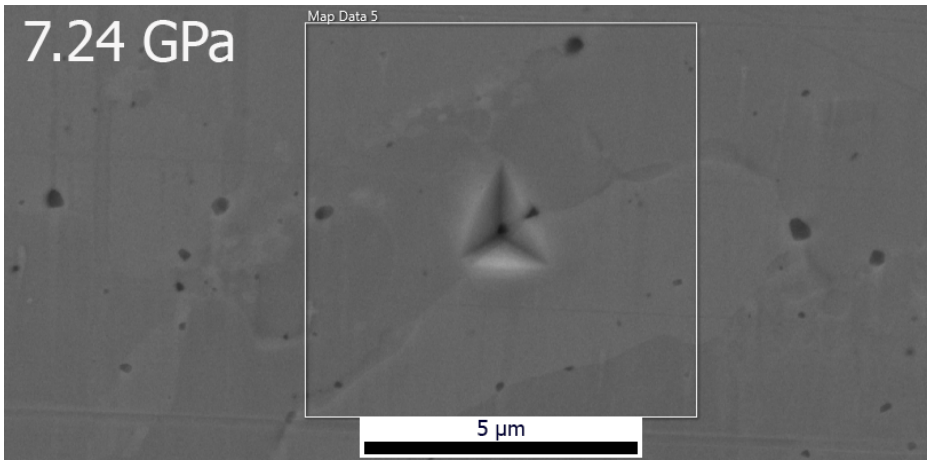
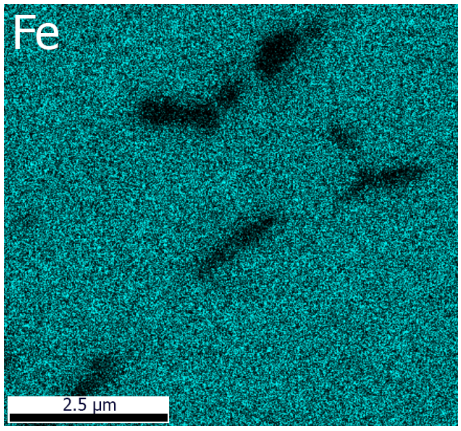


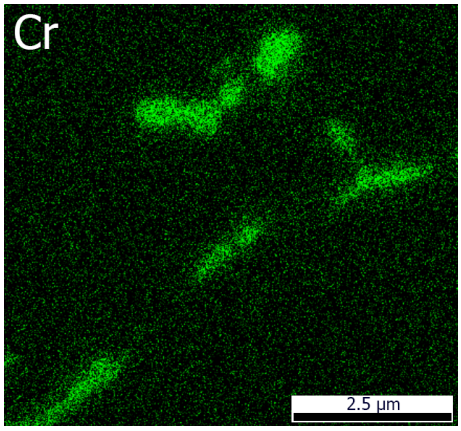
Figure 5.13: EDX element maps for indent site 9. (a) SEM image of indent site with bounding box for EDX scan highlighted in white.



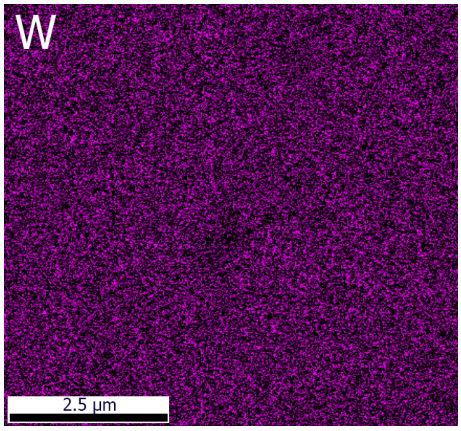
(a)



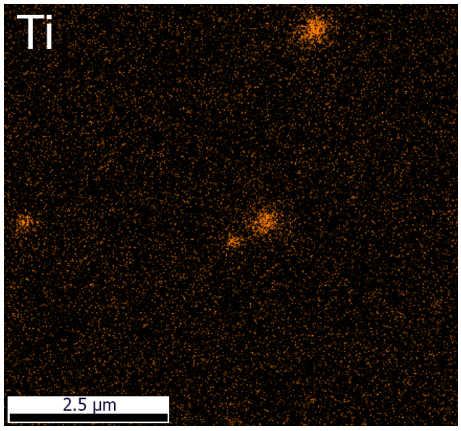
(b)



(c)

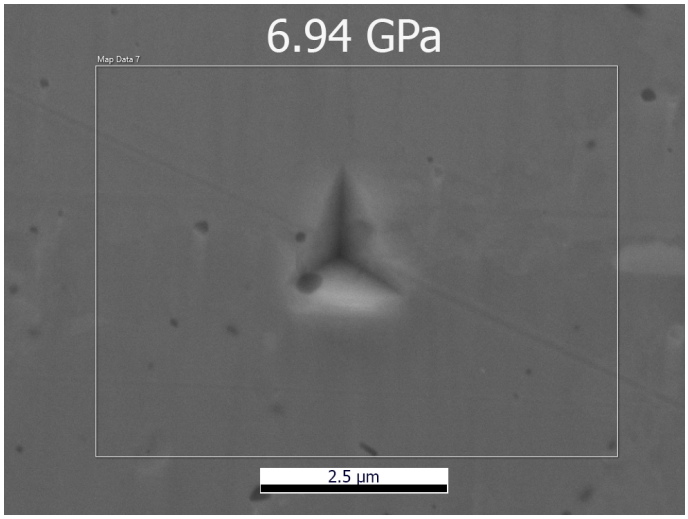


(d)

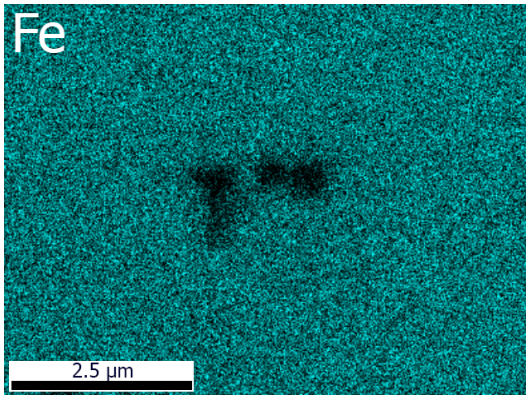


(e)

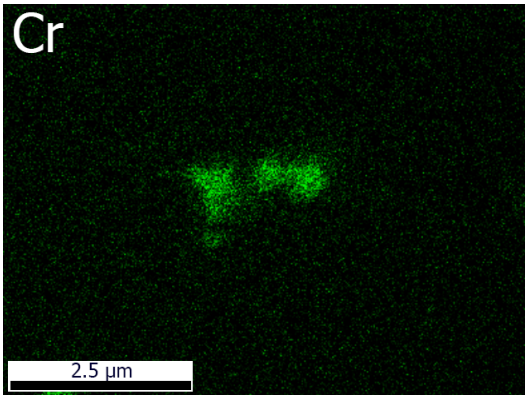
Figure 5.14: EDX element maps for indent site 7. (a) SEM image of indent site with bounding box for EDX scan highlighted in white.



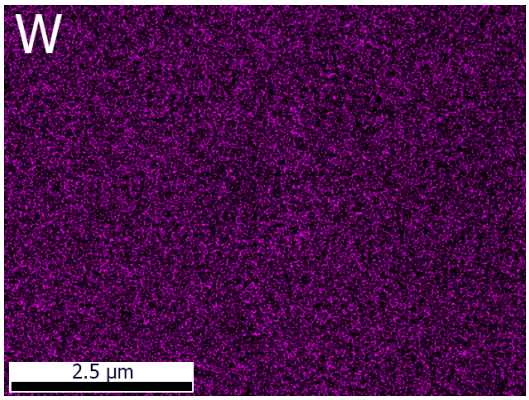
(a)



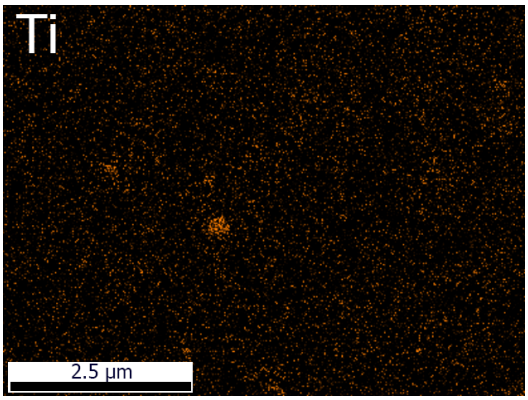
(b)



(c)

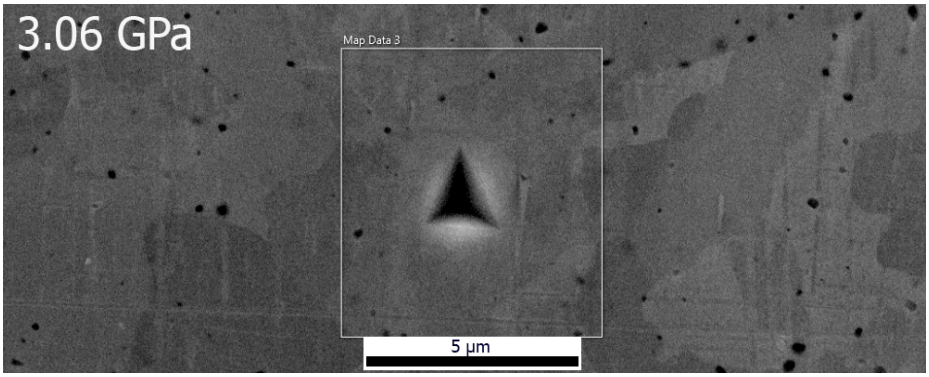


(d)

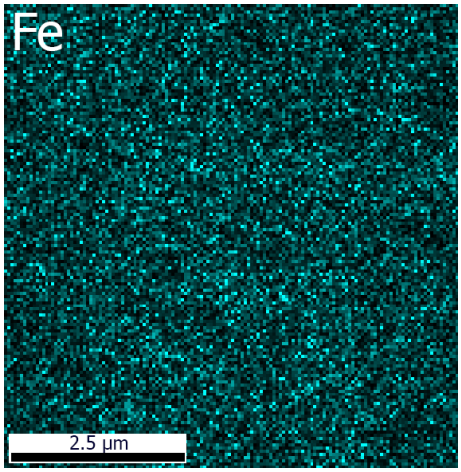


(e)

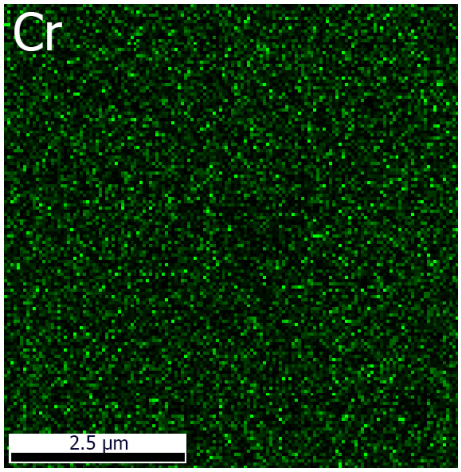
Figure 5.15: EDX element maps for indent site 10. (a) SEM image of indent site with bounding box for EDX scan highlighted in white.



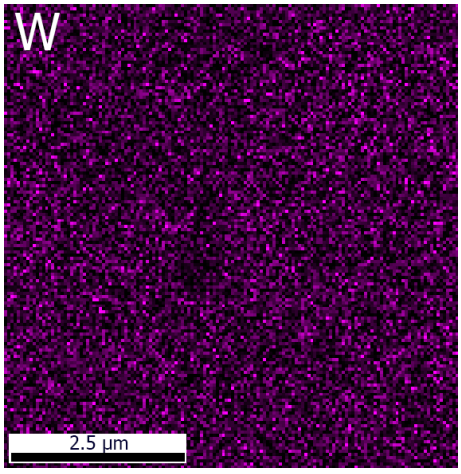
(a)



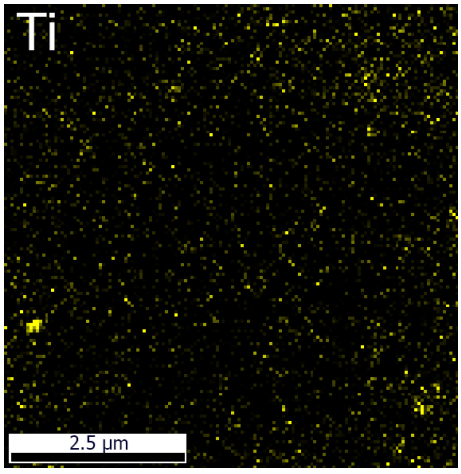
(b)



(c)

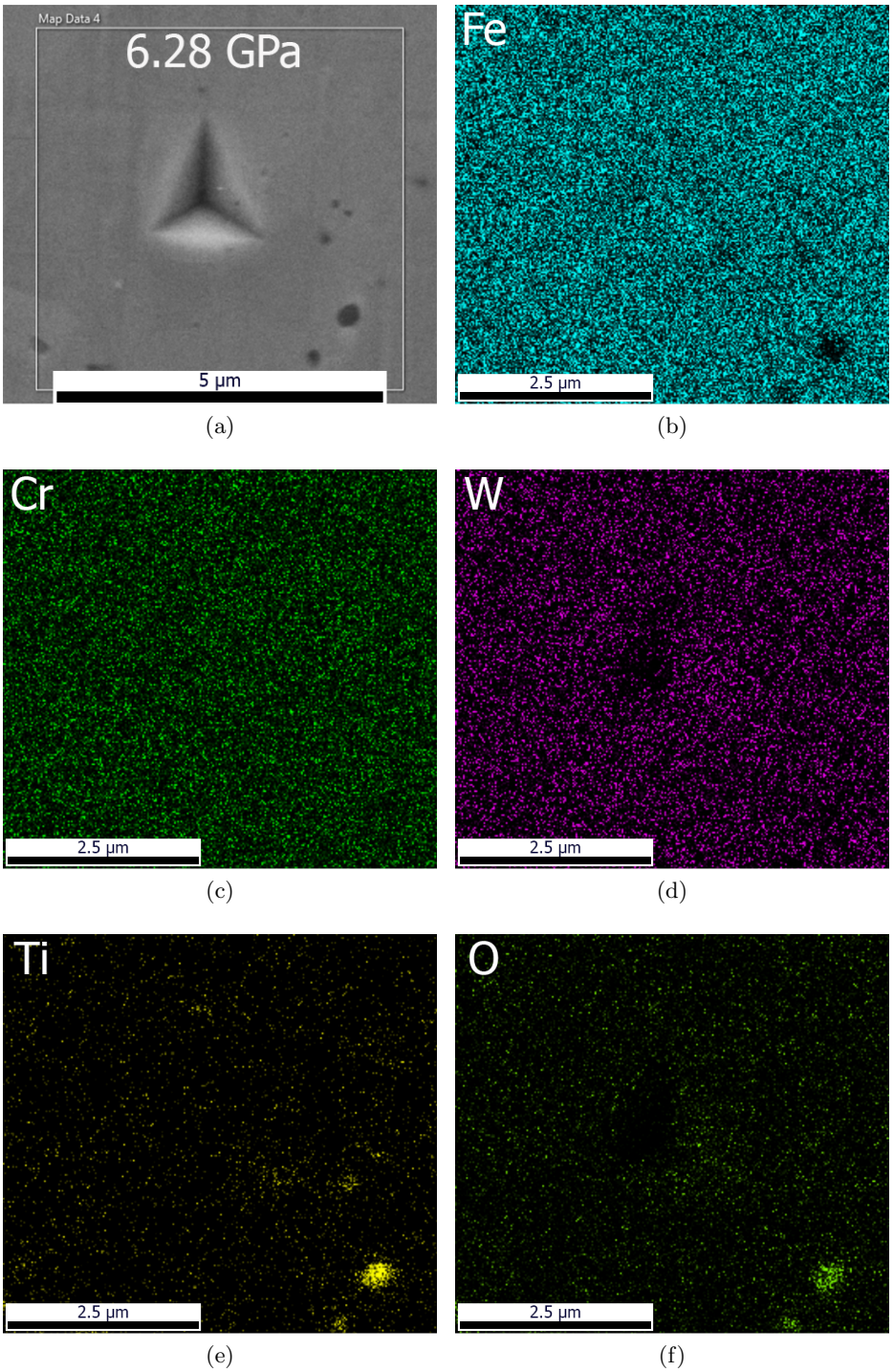


(d)



(e)

Figure 5.16: EDX element maps for indent site 6. (a) SEM image of indent site with bounding box for EDX scan highlighted in white.



(a) (b) (c) (d) (e) (f)

Figure 5.17: EDX element maps for indent site 11. (a) SEM image of indent site with bounding box for EDX scan highlighted in white.

Discussion of EBSD and EDX analysis on specific indents

Qualitative descriptions of the EBSD results for each indent is shown in table 5.3, alongside the corresponding distance from irradiated surface and indent hardness.

EBSD analysis of bimodal hardness in 14YWT 1150 indents			
Indent site	Distance from irradiated surface /μm	Hardness /GPa	Qualitative position w.r.t. grain morphology
1	14.0	6.42	Indent within a large grain, i.e. not on grain boundary
2	13.6	4.43	Indent on multiple grain boundaries
3	13.2	4.21	Indent on single grain boundary
4	12.7	6.43	Indent on single grain boundary
5	9.3	6.81	Indent within a large grain, i.e. not on grain boundary
6	26.4	3.06	Indent within a large grain, i.e. not on grain boundary
7	19.1	7.24	Indent on single grain boundary
8	26.0	3.76	Indent on single grain boundary

Table 5.3: Summary of EBSD characterisation of specific indent sites in 14YWT 1150.

From EBSD characterisation of indents 1 through 8 (indent I.D. defined in figure 5.11), it can be concluded that there was no correlation between indent location with respect to grain morphology, and indent hardness. The large EBSD scan of indents 1 through 4 demonstrates this quite clearly. Indents 2, 3 and 4 were positioned on grain boundaries, and indent 1 was positioned within the grain area, away from the grain boundary. If it were assumed that the bimodal hardness distribution was solely caused by Hall-Petch strengthening, then it would be expected that indent 1 would be much softer than 2, 3 and 4, with 2 being hardest due being placed on multiple grain

boundaries. However this was not the case, indents 1 and 4 were the hardest, with a hardness of 6.42 GPa and and 6.43 GPa respectively. Indent 2 (4.43 GPa) was only moderately harder than indent 3 (4.21 GPa).

The lack of correlation was further confirmed in the EBSD characterisation of indents 5 through 8. Indents 5 and 6 were both placed away from grain boundaries but the hardness of indent 5 was in the upper range of hardnesses measured, at 6.81 GPa, and indent 6 was the lowest, at 3.06 GPa. Conversely, indents 7 and 8 were both placed directly on grain boundaries; indent 7 had the second highest hardness measured, at 7.24 GPa, and indent 8 was much softer, with a hardness of 3.76 GPa.

While the Hall-Petch strengthening mostly likely had a modest effect on the overall measured hardness, it clearly was not the cause of the significant site-to-site hardness variations observed in the two ODS steels. Due to this, EDX analysis of specific indents was used to determine whether local variations in chemistry might be the cause of the bimodal hardness distribution. Table 5.4 gives a qualitative summary of these results.

EDX analysis of bimodal hardness in 14YWT 1150 indents			
Indent site	Distance from irradiated surface /μm	Hardness /GPa	Local chemistry around indent site
9	10.1	7.41	Tungsten/chromium carbides at and around indent site
7	19.1	7.24	Two titanium enriched (oxide) inclusions at indent site, one directly at centre of indent. Chromium enriched grain boundaries at indent site
10	19.4	6.94	Large titanium enriched (oxide) inclusion of centre at indent site. Chromium enrichment at indent site
6	26.4	3.06	Homogeneous local chemistry at indent
11	26.6	6.28	Homogeneous local chemistry at indent. Very large titanium oxide inclusion away from indent location allowing oxygen to be visable

Table 5.4: Summary of EDX analysis of specific indent sites in 14YWT 1150.

EDX elemental maps were created for indents 6, 7, 9, 10 and 11, of which both 6 and 7 also had been characterised using EBSD. Indents of particular interest were targeted for EDX analysis, i.e. indent 9, that displayed the highest hardness measured, 7.41 GPa; indent 7, situated at the Bragg peak, which had a hardness of 7.24 GPa; indent 10, also close to the Bragg peak, with a hardness of 6.94 GPa; indent 6, with the lowest hardness, 3.06 GPa and indent 11, that had a hardness of 6.28 GPa approximately equivalent to the modal hardness.

The elemental maps shown in figure 5.13, display large elongated areas, approximately 3 - 6 μm long, that were almost completely depleted of iron and enriched in

chromium, tungsten and carbon. The indent site lies directly on one of these areas, which was highly likely to be some form of tungsten/chromium carbide. This provides a good explanation for the seemingly anomalously high hardness at this indentation site.

Indent 7, at a distance from the irradiated surface of 19.1 μm (Bragg peak), initially appeared to show a small amount of irradiation hardening. However, EDX maps, in figure 5.14(e) show two small titanium enriched precipitates (likely to be TiO_2) at the indent site, with one directly at the centre of the indent; this provides and alternative explaination of the increased hardness. The presence of 10 - 100 nm TiO_2 precipitates in ODS Fe-Cr-Ti steels have been reported by many authors [263, 205, 264], and their presence in 14YWT 1150 in this work may be supported by the titanium map and corresponding oxygen map in figure 5.17(f). By observing the SEM micrograph in figure 5.14(a), the majority of the titanium precipitates (black speckles) are decorating grain boundaries, possibly providing grain boundary pinning during consolidation (EBSD map for indent 7 is provided in figure 5.12). In addition to titanium precipitates, the indent also appears to be placed on a chromium enriched region, most likely a carbide, decorating the grain boundary.

Indent 10, also close to the Bragg peak, initially appeared to show signs of irradiation hardening. Similarly to indent 7, figure 5.15(e) and (e) show that the indent was placed on a chromium-enriched area (carbide) and a large titanium enriched precipitate (TiO_2). The EDX maps in figures 5.14 and 5.15 provides good evidence that the high hardness measured for indents 7 and 10 was not due to irradiation hardening.

Although indent 11 had a measured hardness of over twice that of indent 6, these two indents appeared to show no differences in local chemistry. The conclusion of this work is that the bimodal hardness distribution is most likely due to heterogeneity in the nanoscale oxide population. Further supported by noting that the average hardness of the population of 'softer' indents in 14YWT 1150 was 3.80 GPa, compared to the

average unirradiated 2000 nm indent value of 3.37 GPa for 14WT 1150 (non ODS). This suggests that large regions of 14YWT 1150 were almost completely devoid of oxide particles, or the particles were too coarse to provide significant hardening. The population of 'softer' indents in 14YWT 950 gave a much higher average hardness of 5.86 GPa, compared to the average unirradiated 2000 nm indent value of 3.54 GPa in 14WT 950 (non ODS), suggesting that regions of 14YWT 950 experienced either a decreased oxide number density or oxide coarsening (or a combination of both). This conclusion will need to be supported by TEM or APT evidence.

Using TEM and APT, the thesis by Burrows (2015) [208] conversely reported a homogeneous oxide population in materials of the same composition, processing route, and producer (Dr. M. J. Gorley, Oxford Materials), but of a different batch to that used in this thesis. TEM and APT of 14YWT 950 and 1150, performed by Burrows (2015) [208], are shown in figures 3.3 and 3.4 (p100 and 101). If the conclusion of the work presented in this section is correct, then it suggests that either batch to batch variability is extremely significant, and/or the analysis by Burrows (2015) was not extensive enough to highlight the large-scale spatial variations in oxide population.

5.3.5 Summary of nanoindentation in the irradiated layer cross-section

A large number of 250 nm indents were placed across the 2 MeV proton irradiated layer in the in-house produced alloys. 14WT 1150 showed significant irradiation hardening both at the Bragg peak and the region of relatively constant damage. Hardness at the Bragg peak, with a damage of 0.2 dpa, was $\sim$ 2.4 GPa harder than unirradiated mean. For damage levels between 0.01 and 0.02 dpa the hardness was $\sim$ 0.6 GPa harder than the unirradiated mean. Slight irradiation hardening of the lower bound of scatter was observed in 14WT 950 between $\sim$ 17 μm and 20 μm irradiation depth, with $\sim$ 0.6 GPa of hardening at the Bragg peak for the lower bound of scatter. No significant hardening was observed for either ODS alloy, attributed to the additional sink sites provided by

the fine dispersion of oxides within these materials.

Similar evidence for the fine dispersion of oxides acting as effective sink sites can be observed in indentation hardness tests of helium implanted variants of the same in-house produced alloys by Burrows (2015) [208] (though a different batch to that used in this project). The average hardening effect, attributed to helium bubbles, was reduced from 1.6 GPa in 14WT 1150 to 0.6 GPa in (ODS) 14YWT 1150. Comparatively, helium implantation in 14WT 950 had a slightly smaller hardening effect to 14WT 1150 of 1.0 GPa, and helium implanted 14YWT 950 showed a reduction in hardness of -0.4 GPa compared to the unimplanted value. Burrows (2015) attributed the softening of 14YWT 950 to the complete enveloping of the small ($\sim$ 2 nm diameter) oxide particles by the helium bubbles, which acts to effectively remove the oxide particles from the system.

A bimodal distribution of hardness was observed in both ODS alloys, several hard indents had a hardness slightly higher than the average of the harder population of indents. EBSD and EDX analysis of specific indents was carried out to determine the cause of the bimodal hardness distribution. EBSD characterisation showed that Hall-Petch hardening was not the cause of the large variations in measured hardness. EDX analysis helped explain why several indents were measured with a hardness significantly higher than the average for the harder population of indents. It was seen that these specific indents appeared to be placed on what was most likely to be carbides and TiO_2 precipitates. However, from the EDX results it was concluded that the bimodal hardness was not caused by local variations in chemistry. Instead, heterogeneity in the nanoscale oxide population was likely to be the cause of the bimodal hardness distribution. TEM analysis of specific indents must be carried out in future work to confirm this.

The pronounced heterogeneity in the microstructure, and the subsequent mechanical response of the in-house produced ODS alloys makes them unsuitable for engineering or commercial use. This is because microstructural features, such as large carbides, are likely to lead to stress concentrations and possible areas for crack nucleation. Addition-

ally, the regions of reduced hardness will lead to local variations in deformation, making behaviour of engineering components fabricated from this material unpredictable and unsafe due to their variability. While the radiation resistance of the ODS RAF alloys investigated in this work looks promising, the microstructural heterogeneity will need to be addressed before considering them for use in plasma facing, or first wall structural components, in a prototype fusion reactor.

5.4 Microcantilevers in irradiated 14WT 1150 and 14YWT 1150

The work reported in this section aimed to investigate further the mechanical response of the in-house produced alloys to 2 MeV proton irradiation, by measuring the yield stress and elastic modulus for two sizes of microcantilevers. From nanoindentation across the irradiated layer in the in-house produced alloys (section 5.3), it was found that 14WT 1150 displayed the most significant irradiation hardening. Whereas, the hardening observed in 14WT 950 was not as significant, even at the Bragg peak. Both ODS variants showed no significant hardening. Therefore, microcantilevers studied in this section were only fabricated in the alloys consolidated at 1150 $^{\circ}C$.

It was found in chapter 3 section 3.4.5, that yield stress, measured from microcantilevers, significantly diverged from near-macroscale values as beam depth was reduced below approximately 4.5 μm. Therefore, in order to best approximate to a macroscale mechanical response, microcantilevers with depths greater than 4.5 μm were fabricated within the irradiated layer. In this section, beams of this size are referred to as 'large microcantilevers'.

In section 5.3.2, nanoindentation revealed a dramatic increase in hardness at the Bragg peak for 14WT 1150. Therefore, in addition to the large microcantilevers, several smaller microcantilevers where fabricated so that the central axis of the beams were situated along the Bragg peak, with a beam width of $\sim$ 1.5 μm, equal to the full width half maximum of the SRIM calculated Bragg peak (figure 5.3). In this section, these are referred to as 'small microcantilevers'.

5.4.1 Method used for the placement of microcantilevers in the irradiated layer

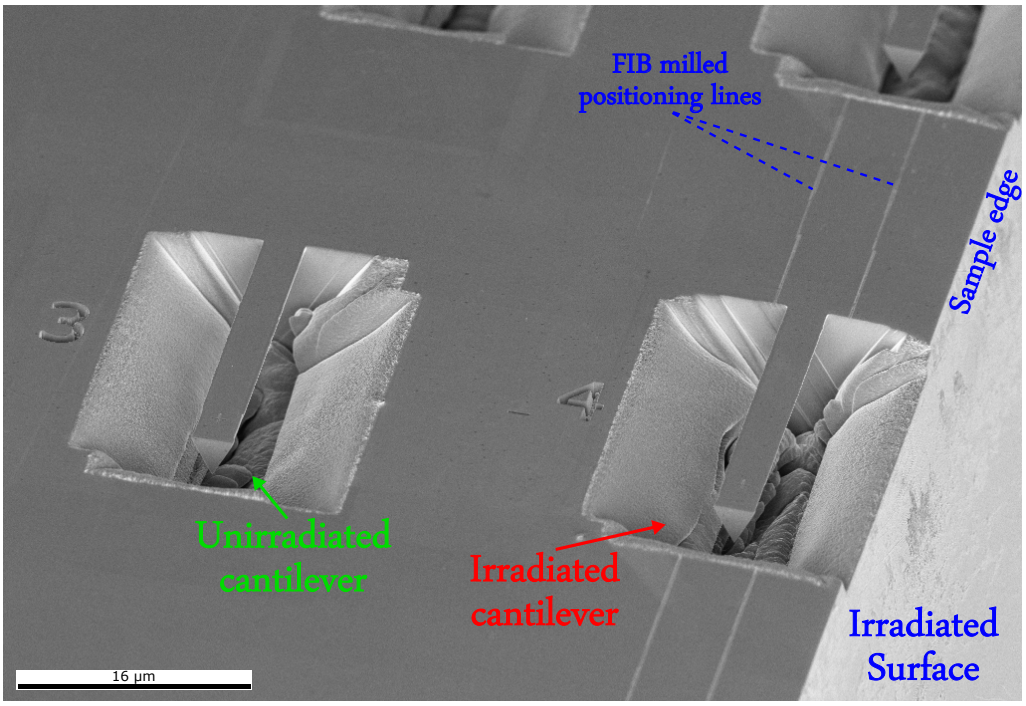


Figure 5.18: SEM micrograph of large microcantilevers in irradiated and unirradiated material, taken with the in-lens detector.

'Irradiated' microcantilevers were fabricated so that the beam axis was parallel to the irradiated surface, this ensured that the entire length of the beam was equivalently irradiated. In order to accurately place each beam at the same irradiation depth, two positioning lines were FIB milled parallel to the irradiated surface and at irradiation depths of 10.5 μm and 21.5 μm, as can be seen in figure 5.18. Two small ($\sim$ 5 μm) additional lines were milled at irradiation depths of 13.5 μm and 18.5 μm. These defined the width of the beam to be milled and were situated at position of the cantilever's free end. Initial trenches were aligned with the large positioning lines, and excess material was then milled away using progressively finer beam currents until the small lines defining the beam width were removed. A plan view of a finished large irradiated microcantilever is shown in figure 5.19.

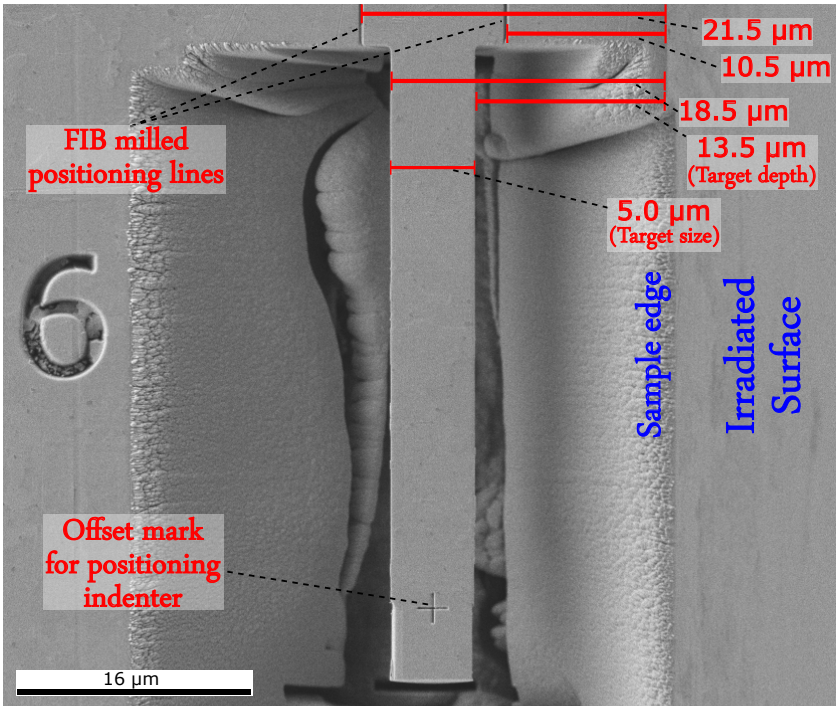


Figure 5.19: SEM micrograph with annotations showing target position and width in relation to the irradiated surface for the large irradiated microcantilevers.

A similar process was used to fabricate the small microcantilevers situated at the Bragg peak. To ensure that the plastic zone was localised at the Bragg peak, determined by nanoindentation to be at 19.0 μm, a small line, additional to the two lines defining the beam width, was milled at 19.0 μm prior to fabrication. The microcantilever was then milled from the surface, ensuring that this line was always central with respect to the beam. A plan view of a finished small irradiated microcantilever is shown in figure 5.20.

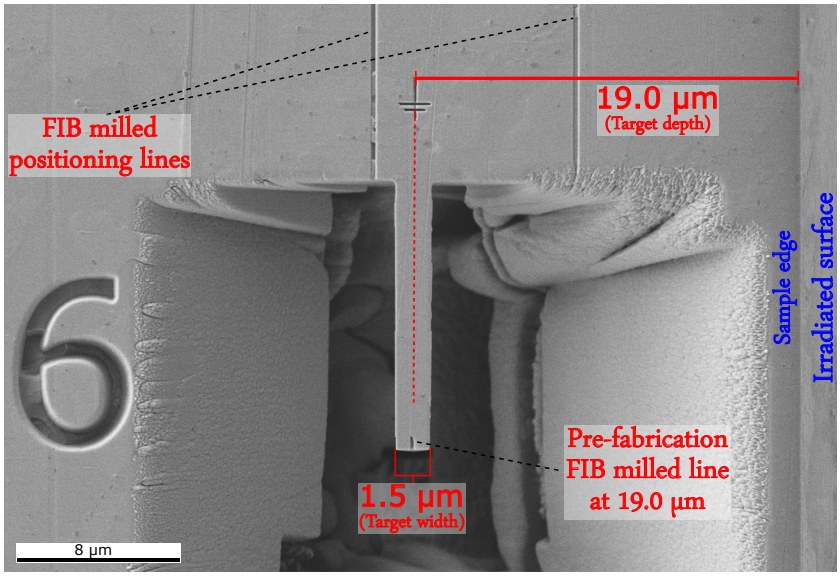


Figure 5.20: SEM micrograph with annotations showing target position and width in relation to the irradiated surface for the small irradiated microcantilevers positioned at the Bragg peak.

5.4.2 Results for irradiated microcantilevers

Load-displacement data was analysed using simple beam theory and finite element analysis (FEA). The method used for both of these analysis techniques is described in section 3.4.4. A graph of simple beam stress against simple beam strain is provided for each data set. Alongside each graph is a table detailing the moduli and yield stress calculated from simple beam theory and FEA for each microcantilever. Simple beam theory was used for a graphical interpretation of the data; for quantitative analysis, FEA was used.

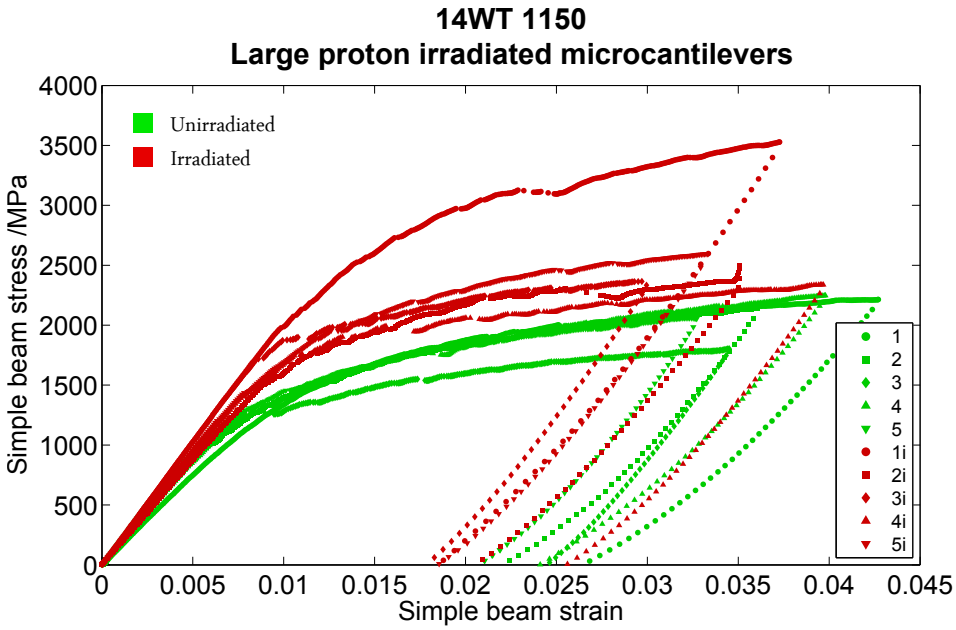


Figure 5.21: Irradiated and unirradiated large microcantilevers in 14WT 1150. Stress and strain were calculated using simple beam theory.

Cantilever I.D.	Cantilever depth /μm	Simple beam modulus /GPa	Simple beam yield stress /GPa	FEA Modulus /GPa	FEA Yield stress /GPa
1	4.86	151	1.04	177	0.64
2	5.22	177	0.97	207	0.56
3	5.11	191	0.80	221	0.48
4	4.83	175	1.00	203	0.65
5	5.25	200	0.86	231	0.52
1i	4.81	205	1.96	238	1.23
2i	5.36	175	1.44	204	0.96
3i	5.38	206	1.63	239	1.15
4i	5.16	184	1.43	215	1.05
5i	5.26	192	1.34	223	0.85
Unirradiated average	5.05	179	0.93	208	0.57
Irradiated average	5.19	192	1.56	224	1.05

Table 5.5: Summary table of results from the large irradiated and unirradiated microcantilevers fabricated in 14WT 1150. 'i' denotes irradiated beams.

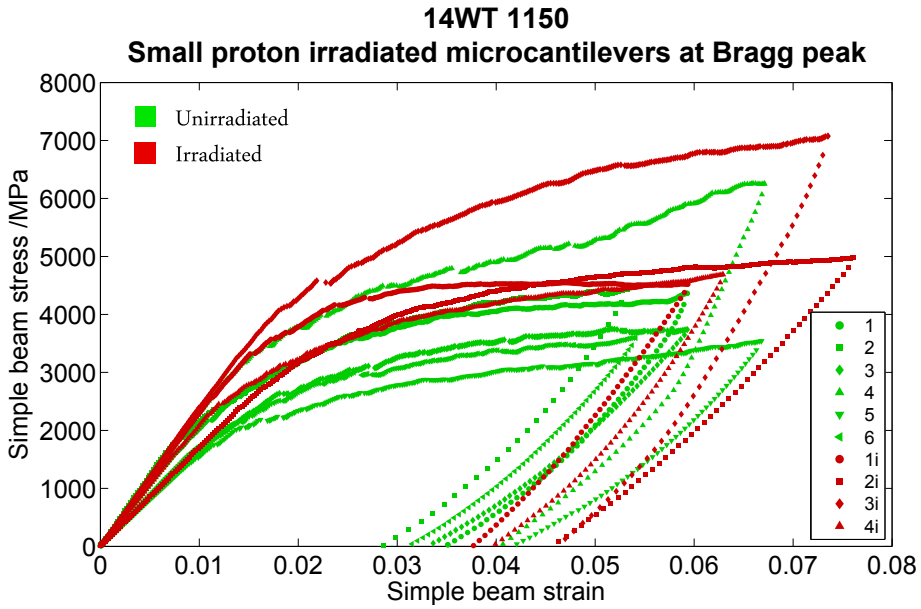


Figure 5.22: Irradiated and unirradiated small microcantilevers at the Bragg peak in 14WT 1150. Stress and strain were calculated using simple beam theory.

Cantilever I.D.	Cantilever depth /μm	Simple beam modulus /GPa	Simple beam yield stress /GPa	FEA Modulus /GPa	FEA Yield stress /GPa
1	1.79	214	1.97	251	1.17
2	1.80	246	1.84	287	1.02
3	1.74	164	1.99	192	1.19
4	1.55	232	2.89	273	1.74
5	1.87	160	1.64	190	1.05
6	1.84	179	1.71	209	1.05
1i	1.87	231	2.97	272	1.84
2i	1.76	171	2.76	204	1.74
3i	1.62	241	3.60	286	2.20
4i	1.77	215	2.29	254	1.75
Unirradiated average	1.76	199	2.00	234	1.20
Irradiated average	1.76	214	2.91	254	1.88

Table 5.6: Summary table of results from the small irradiated and unirradiated microcantilevers fabricated in 14WT 1150. 'i' denotes irradiated beams.

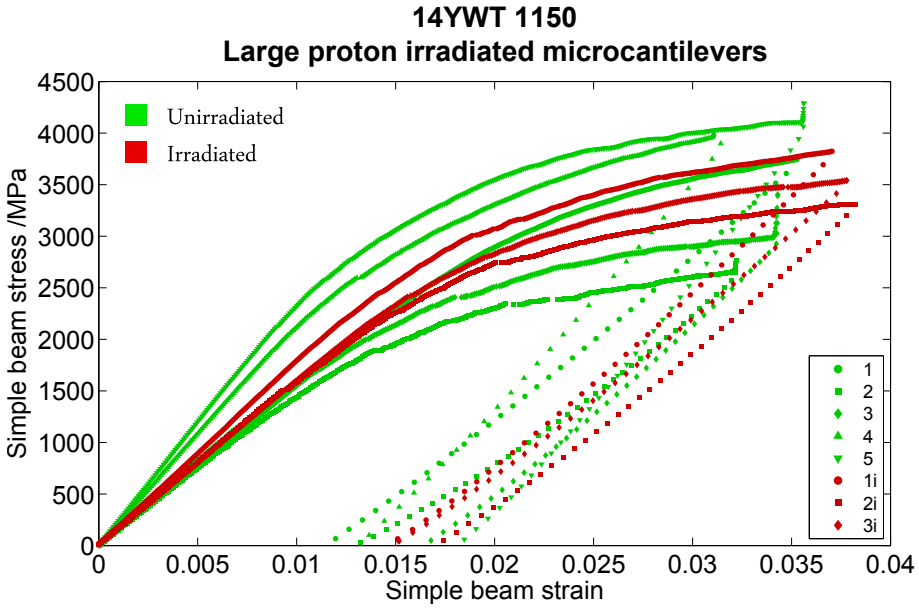


Figure 5.23: Irradiated and unirradiated large microcantilevers in 14YWT 1150. Stress and strain were calculated using simple beam theory.

Cantilever I.D.	Cantilever depth /μm	Simple beam modulus /GPa	Simple beam yield stress /GPa	FEA Modulus /GPa	FEA Yield stress /GPa
1	5.64	156	2.42	182	1.87
2	5.58	150	1.44	176	0.87
3	5.52	166	1.55	194	0.91
4	4.83	217	2.12	252	1.41
5	4.69	240	2.24	279	1.42
1i	5.53	179	2.26	209	1.62
2i	5.53	162	1.56	190	1.15
3i	5.93	161	2.21	188	1.56
Unirradiated average	5.25	186	1.95	216	1.30
Irradiated average	5.66	167	2.01	196	1.44

Table 5.7: Summary table of results from the large irradiated and unirradiated microcantilevers fabricated in 14YWT 1150. 'i' denotes irradiated beams.

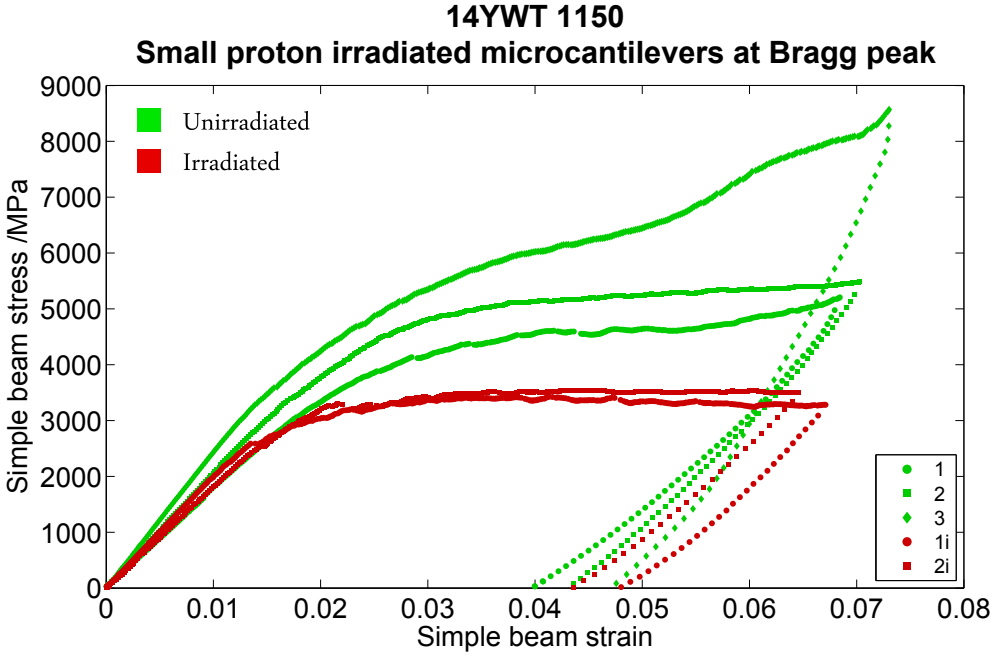


Figure 5.24: Irradiated and unirradiated small microcantilevers at the Bragg peak in 14YWT 1150. Stress and strain were calculated using simple beam theory.

Cantilever I.D.	Cantilever depth /μm	Simple beam modulus /GPa	Simple beam yield stress /GPa	FEA Modulus /GPa	FEA Yield stress /GPa
1	1.76	179	2.77	211	2.18
2	1.68	206	3.27	241	2.04
3	1.85	243	3.34	284	2.02
1i	1.65	201	2.34	235	1.49
2i	1.86	183	2.49	215	1.85
Unirradiated average	1.72	192	3.02	226	2.11
Irradiated average	1.76	192	2.42	225	1.67

Table 5.8: Summary table of results from the small irradiated and unirradiated microcantilevers fabricated in 14WT 1150. 'i' denotes irradiated beams.

5.4.3 Discussion of irradiated microcantilevers

The elastic moduli for all microcantilever specimens measured in this work agreed well with those measured in the characterisation of the microcantilever size effect in section 3.4.5. As expected, the scatter increased with deceasing beam size, but all measured values fell within the single crystal values for iron, between 129 GPa and 276 GPa [236]. This suggested that there was a relatively low error in the dimensional measurement of the beams.

14WT 1150 large and small microcantilevers

As with the cross-sectional nanoindentation of the irradiated layer, significant irradiation hardening was measured in microcantilevers fabricated in (non-ODS) 14WT 1150. The average yield stress for the large unirradiated microcantilevers was 0.57 GPa, which increased $\sim$ 0.5 GPa to 1.05 GPa for the irradiated specimens. The macroscale yield stress for 14WT 1150 was approximately 0.42 GPa, determined from four-point flexure tests of 14WT 950 (explained in detail in section 3.3.3 and 3.4.5). This suggested that there was an increase in apparent strength of $\sim$ 0.15 GPa in the large beams due to the size effect, with the unirradiated microcantilevers closely approximating the macroscale behaviour.

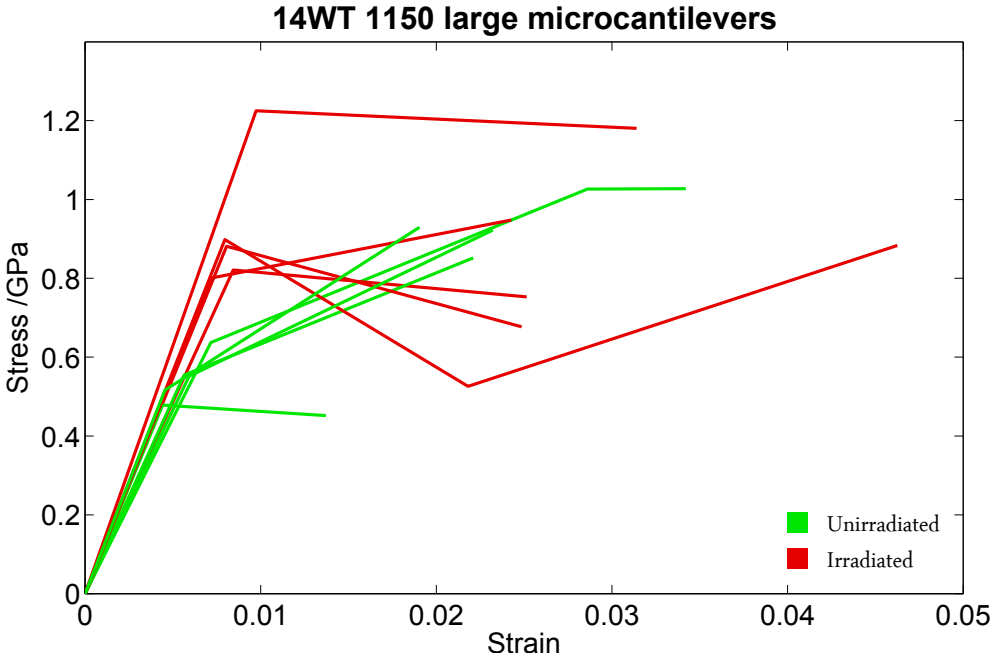


Figure 5.25: FEM matched stress-strain response of unirradiated and irradiated 14WT 1150 large microcantilevers. Irradiated beam centre at $\sim$ 0.026 dpa.

Figure 5.25 shows the FEM calculated stress-strain response of the 14WT 1150 large microcantilevers; demonstrating clear hardening of the yield stress in the irradiated beams. The full plastic response of the beams could not be modelled due to the failure of the model to match the experimental data at high plastic strains. Figure 5.25 only includes the flow stresses calculated at the matched points prior to the failure of the model.

The target depth for the large microcantilever beam centre was 16 μm, therefore the yield stress increase of $\sim$ 0.5 GPa was determined to be at a damage of $\sim$ 0.026 dpa. It should be noted that there was an order of magnitude variation in the damage with respect to the distance across the beam, e.g. the damage at 13.5 μm was 0.018 dpa, and 18.5 μm was 0.19 dpa.

Significant irradiation hardening was also observed in small 14WT 1150 microcantilevers at the Bragg peak. At a damage of 0.2 dpa, the unirradiated average yield stress was measured to be 1.20 GPa, which increased to 1.88 GPa for the irradiated

specimens. This equated to a yield stress increase of $\sim$ 0.7 GPa.

Comparison to 250 nm nanoindentation for 14WT 1150

Table 5.9, compares this section's microcantilever results in 14WT 1150 with the 250 nm indents across the irradiated layer, reported in section 5.3. First hardness values were converted to equivalent yield stresses using the Tabor approximation [165]; this states that indentation hardness is three times the yield stress. The hardness-derived, and the microcantilever derived yield stress values are both performed at test scales where size effects are expected to give rise to values higher than those for macroscale 'bulk' tests. Corrections were applied as follows:

1. For indentation data, the size effect corrections were evaluated by comparing the hardness at 250 nm with the average average hardness between 1250 - 2000 nm in figure 5.5(b). The increase in average hardness due to indentation size effects was determined to be 0.76 GPa, corresponding to a Tabor derived yield stress increase (due to size effects) of 0.25 GPa.

2. For microcantilever data, the size effect corrections were evaluated by comparing the average yield stress for the unirradiated beams with the macroscale four-point flexure tests from section 3.3.3. As discussed in section 3.3.3, data from the four-point flexure tests in 14WT 950 had to be used to provide bulk test values for 14WT 1150. Section 3.4.5 (p145) presents an argument as to why this was deemed a reasonable comparison. The yield stress increase due to size effects for large 14WT 1150 microcantilevers was measured to be 0.15 GPa. For small 14WT 1150 microcantilevers, 0.78 GPa.

The corrected yield stress, displayed in table 5.9, does not account for the possibility that size effect mechanisms were affected by irradiation induced defects. Similar to work in micropillars by Kiener et al (2011) [198] (discussed in section 2.6.8), it was likely that the mechanical hardening response of the large irradiated beams were largely dominated

by dislocation-defect interaction and any change in hardening due to size effects were negligible. However, for the smaller irradiated test geometries (e.g. small Bragg peak beams) it was possible that there was a reduction of the contribution size dependent mechanisms had to the overall mechanical response. If this was the case, there would be an increase in the corrected yield stress for these specimens.

	Yield stress /GPa		Yield increase due to size effects /GPa	Corrected yield stress /GPa		Irradiated $\Delta\sigma_y$ /GPa
	Unirr	Irr		Unirr	Irr	
14WT 1150 large beams	0.57	1.05	0.15	0.42	0.90	$\sim$ 0.5
250 nm indents at 0.026 dpa	1.33 (Tabor)	1.53 (Tabor)	0.25 (Tabor)	1.08 (Tabor)	1.28 (Tabor)	$\sim$ 0.2 (Tabor)
14WT 1150 small beams	1.20	1.88	0.78	0.42	1.10	$\sim$ 0.7
250 nm indents at 0.2 dpa	1.33 (Tabor)	2.11 (Tabor)	0.25 (Tabor)	1.08 (Tabor)	1.86 (Tabor)	$\sim$ 0.8 (Tabor)

Table 5.9: Comparison of 14WT 1150 microcantilever results with the 250 nm nanoindentation across irradiated layer in 14WT 1150. Nanoindentation hardness was converted to yield stress using the Tabor approximation. Magnitude of indent size effect was found from comparing the hardness at 250 nm with hardness average hardness between 1250 - 2000 nm in figure 5.5(b). Magnitude of microcantilever size effect was found by comparing the average yield stress in unirradiated beams with the macromechanical four-point flexure tests performed in section 3.3.3. Centre of the large beams was at 0.026 dpa, and the centre of the small beams was at 0.2 dpa.

For the large beams, the increase yield stress due to irradiation ($\sim$ 0.5 GPa) was more twice that derived from indentation data ($\sim$ 0.2 GPa). Conversely, the increase yield stress due to irradiation in the small beams ($\sim$ 0.7 GPa) was very close to that derived from indentation data ($\sim$ 0.8 GPa). However, the use of the Tabor approxima-

tion on indentation data greatly overestimated the yield stress for both sized beams. This discrepancy was most likely due to differences in stress states and work hardening behaviour of the two micromechanical testing methods. Also, the plastic zone of the large microcantilevers samples a dose that varied by an order of magnitude across the beam, resulting in differences in work hardening response across the beam itself. The accuracy of the Tabor approximation, although often useful, is questionable; since it assumes an average effective strain, however the stress state underneath an indent is complex so it is often unclear which regions are experiencing the strain. It also assumes that the work hardening response of the two testing methods are equivalent.

14YWT 1150 large microcantilevers

In the ODS variant, the large microcantilevers, with a beam centre damage of ~ 0.026 dpa, measured an average unirradiated yield stress of 1.30 GPa, which increased to 1.44 GPa for the irradiated specimens. Equating to an average yield stress increase of ~ 0.14 GPa. The macroscale yield stress, determined by four-point flexure tests, was 0.84 GPa. Although, the macroscale stress-strain response was very similar to ODS EUROFER that gave an average macroscale yield stress of 1.17 GPa.

There was a large scatter in yield stress, both in the large and small 14YWT 1150 microcantilevers. Data from the large irradiated microcantilevers fell completely within the scatter-range of the unirradiated beams. The presence of a large scatter in yield stress agreed well with what was observed in the characterisation of the microcantilever size effects in section 3.4.5, and the investigation of the bimodal hardness of 14YWT in section 5.3.4. In section 5.3.4, it was found that the large microstructural heterogeneity gives rise to local variations of hardness, which was most likely the cause the significant spread in yield stress found in this section.

A confident measurement of the irradiation hardening in 14YWT 1150 could not be made, since many more microcantilevers would be needed to give statistically sig-

nificant results, due to the large scatter. However, a reduction of irradiation hardening in 14YWT 1150 would be in good agreement with the nanoindentation results in section 5.3, which observed no appreciable hardening in 14YWT compared with significant hardening in 14WT 1150. Relevant literature also observes similar reductions in irradiation hardening with the addition of a fine dispersion of oxide precipitates. Tensile test specimens of 14WT and 14YWT were neutron irradiated in the HFIR at ORNL to 1.5 dpa at 300 $°C$ by McClintock et al. (2009) [138], results of which are shown in figure 2.19 (p47). In McClintock's room temperature tests, the irradiation hardening of 14YWT, measured from increase in yield stress, was reduced by 50 % comparison to the non-ODS variant 14WT; the yield stress hardening was 0.13 GPa (14YWT) and 0.25 GPa (14WT). The irradiation hardening measured in this section for 14WT ($\sim$ 0.5 GPa) was much higher than that measured by McClintock et al. but at a much lower dpa. This could be due to the post consolidation treatments carried out by the authors (inputting more sink sites), whereas the material in this thesis was used as-produced. Secondly, the dose rate used in this work was much higher than those used by McClintock. A similar hardening response (0.15 GPa) to that found by McClintock et al. was measured by 14YWT 1150 microcantilevers in this section.

14YWT 1150 small microcantilevers (at Bragg peak)

The problems associated with the microstructural heterogeneity in 14YWT 1150 were exacerbated as the sample size was decreased. The presence of irradiation effects could not be determined for small microcantilevers positioned at the Bragg peak, due to the lack of statistically significant results. Many more microcantilevers would need to be fabricated to extract meaningful data.

5.4.4 Summary for irradiated microcantilevers

Microcantilevers of two different sizes were milled in cross-sectional surfaces of a 2 MeV proton irradiated damage layer in the in-house produced alloy 14WT 1150, and its ODS counterpart, 14YWT 1150. Large microcantilevers with widths of approximately 5 μm were fabricated so that the beam centre was at a damage of approximately 0.026 dpa, with the inner edge of the beam close to the Bragg peak. Small microcantilevers with a beam width of 1.5 μm were also tested, fabricated to ensure that the beam centre was in-line with the Bragg peak, at a damage of 0.2 dpa.

Significant irradiation hardening was measured for both beam sizes in 14WT 1150. The average yield stress for the large unirradiated microcantilevers was measured to be 0.57 GPa, which increased $\sim$ 0.5 GPa to 1.05 GPa for the irradiated specimens. The yield stress measured from the large unirradiated microcantilevers showed good agreement with the macroscale yield of $\sim$ 0.42 GPa, determined from four-point bend tests; this demonstrated that very little size effects were present. The small microcantilevers, situated at the Bragg peak, measured an unirradiated average yield stress of 1.20 GPa, which increased $\sim$ 0.7 GPa to 1.88 GPa for the irradiated specimens. Comparison of the unirradiated beams to macroscale values suggests that there was an increase in strength of $\sim$ 0.75 GPa due to the microcantilever size effect.

The irradiation hardening, as measured by an increase in yield stress, appeared to be less significant in 14YWT 1150. Large microcantilevers measured an average unirradiated yield stress of 1.30 GPa, which showed a small average yield stress increase of 0.14 GPa to 1.44 GPa for the irradiated specimens. Although, the measured yield stress of the irradiated microcantilevers fell within the large scatter of the unirradiated specimens. A confident measurement of the irradiation hardening in 14YWT 1150 could not be made, since more microcantilevers would be needed to give statistically significant results due to the large scatter. However, a reduction of irradiation hardening in 14YWT 1150 would be in good agreement with the nanoindentation results presented

in section 5.3 and results from McClintock et al. (2009) [138].

The work in this section has demonstrated a method for extracting engineering relevant mechanical properties from shallow irradiated layers that closely approximate to the macroscale yield stress measured in the literature and section 3.3.3 of this thesis. This method required the use of high energy proton irradiation as a neutron surrogate, allowing for a much deeper damage layer. However, questions remain over how well protons can simulate neutron damage, with their widely spaced, small defect clusters.

Although 14YWT 1150 displayed a large amount of scatter in measured yield stress, both the method used for measuring irradiation hardening, and the mechanical response of 14YWT to irradiation showed great promise. Efforts should be made to reduce the heterogeneity of the microstructure, possibly with post-consolidation treatments, such as those explored by Lindau et al. (2005) [76] in ODS EUROFER and Hoelzer et al. (2016) [141] in 14YWT (described in section 2.5.3). After which, the method presented in this section should be repeated.

Chapter 6

6 Summary, conclusions and further work

6.1 Thesis aims

The primary aim of this thesis was to develop a method for extracting yield stress and elastic modulus data from shallow irradiated layers that closely approximated macroscale values. The novel approach was to use a size effect study to determine the geometry of microcantilever needed to approximate to macroscale mechanical behaviour, this data was then used to determine the ion irradiation conditions needed to fabricate microcantilevers of the appropriate size. Further aims of this thesis included:

- The cross-sectional micromechanical investigation of the proton damage profile using nanoindentation and microcantilevers.
- An investigation of the microcantilever size effect using a lengthscale dependent crystal plasticity model
- A method of using digital image correlation as a strain gauge in four-point flexure tests.

6.2 Summary of experimental chapters

Chapter 3

The work reported in chapter 3 introduced and characterised the materials used in this thesis. The grain morphology and distribution was measured using EBSD and found that the in-house produced alloys (used in the as-produced condition) each had a large size distribution of relatively equiaxed grains. RAF steels that were mechanically alloyed with yttrium oxide displayed a particularly heterogeneous bimodal grain size distribution. The macroscale mechanical behaviour was then characterised using a four-

point flexure test which used digital image correlation (DIC) as a strain gauge. DIC had to be performed on small 1 x 1 x 10 mm samples with microscale resolution, due to the small quantity of material produced by the HIPed powders. This required a specialist lens and a novel method for introducing speckle onto the imaged surface. The microcantilever size effects were then characterised. The results from the macroscale flexure tests were used to determine that the yield stress significantly diverged from bulk values at a beam depth of < 4.5 μm. Using knowledge of this, irradiation conditions could be determined.

Chapter 4

The work reported in chapter 4 simulated the size dependent behaviour of microcantilevers using a lengthscale dependent crystal plasticity UMAT, developed by Dunne et al. and implemented within ABAQUS 6.14-2 commercially available finite element software. The UMAT produced a lengthscale dependent response by making the increment in plastic strain dependent on the GND density. The simulation of the GND density evolution with increasing plastic strain allowed their contribution to the microcantilever size effect, through mobile dislocation pinning, to be determined. This novel approach to modelling size effects in three dimensional microcantilever finite element models, demonstrated that while it was possible to simulate a lengthscale dependent response, more mechanisms must be included in the constitutive equation for the plastic velocity gradient if simulations are to match the experimentally derived results in the previous section.

Chapter 5

The work reported in chapter 5 used micromechanical testing methods to examine the extent of irradiation hardening in the in-house produced alloys. 2 MeV proton irradiation was chosen to due to its deep penetration and relatively flat damage profile before a sharp Bragg peak. The large 2000 nm indents placed into the irradiated layer failed to

measure any significant irradiation hardening, attributed to the very small dose present near the irradiated surface.

Each specimen was rotated and polished to reveal the surface that contained a cross-section of the irradiated layer. Small 250 nm indents, placed across the irradiated layer, revealed a clear proton damage profile in the hardness data for 14WT 1150. The average unirradiated hardness was measured to be 4.00 GPa, this increased to 4.60 GPa for the region irradiated to 0.01 - 0.04 dpa, and 6.34 GPa at the Bragg peak (with a damage of 0.2 dpa). A modest amount of hardening, $\sim$ 0.6 GPa, was measured for the lower scatter bound of indents at the Bragg peak of 14WT 950. No appreciable hardening was observed in either 14YWT specimens, attributed to the fine dispersion of nanoscale oxides providing a high number density of defect sink sites. However, a large bimodal variation in hardness was measured in both of these alloys. This was investigated using EBSD and EDX, and was determined to be caused by a pronounced heterogeneity of the microstructure. While Hall-Petch strengthening and changes in the local chemistry had some effect on the measured hardness, the most likely cause of the large variation in local hardness was heterogeneity in the nanoscale oxide population.

Microcantilevers were fabricated out of the irradiated layer cross-section in 14WT 1150 and 14YWT 1150. Large microcantilevers with $\sim$ 5 μm beam depth were placed with their beam centre at $\sim$ 0.026 dpa, and small microcantilevers with $\sim$ 1.5 μm beam depth were placed with their beam centre at the Bragg peak, $\sim$ 0.2 dpa. Both the large and the small microcantilevers fabricated in 14WT 1150 displayed significant irradiation hardening. The average yield stress for the large unirradiated beams was measured to be 0.57 GPa, which increased to 1.05 GPa for the irradiated specimens, measuring a yield stress increase of $\sim$ 0.5 GPa. The macroscale yield stress, as measured by the four-point flexure tests, was 0.42 GPa, suggesting a modest size effect strength increase of $\sim$ 0.15 GPa was present at these large beam sizes. The small microcantilevers situated at the Bragg peak, measured the unirradiated average yield stress to be 1.20 GPa, which

increased to 1.88 GPa for the irradiated specimens, measuring a yield stress increase of $\sim$ 0.7 GPa. A size effect strength increase of $\sim$ 0.75 GPa was present at this beam size.

Irradiation hardening in ODS variant 14YWT 1150 appeared to be reduced. Large microcantilevers measured an average unirradiated yield stress of 1.30 GPa, which increased to 1.44 GPa for the irradiated specimens, measuring a yield stress increase of $\sim$ 0.15 GPa. Although, the measured yield stress of the irradiated microcantilevers fell within the large scatter of the unirradiated specimens. However, a confident measurement of the irradiation hardening in 14YWT 1150 could not be made, since more microcantilevers are needed to give statistically significant results due to the large scatter present, even for the large beams. A summary of the experimental results discussed in this thesis is shown in table 6.1.

	Average 250 nm indent hardness (0.01 - 0.02 dpa) /GPa		Yield stress small beams (0.2 dpa) /GPa		Yield stress large beams ($\sim$ 0.026 dpa) /GPa		Macroscale yield stress from flexure tests /GPa
	Unirr	Irr	Unirr	Irr	Unirr	Irr	
14WT 950	4.13 $\pm$ 0.36	4.28 $\pm$ 0.34	-	-	-	-	$0.421\ ^{+.35}_{-.32}$
14YWT 950	8.39 $\pm$ 1.33	8.86 $\pm$ 1.11	-	-	-	-	1344 (Fracture stress)
14WT 1150	4.00 $\pm$ 0.24	4.60 $\pm$ 0.26	1.20	1.88	0.57	1.05	-
14YWT 1150	5.67 $\pm$ 0.91	5.78 $\pm$ 0.98	2.11	1.67	1.30	1.44	$0.842\ ^{+.63}_{-.47}$

Table 6.1: Summary of experimental results discussed in this thesis

6.3 Thesis conclusion

This thesis successfully showed it is possible to extract a close approximation of the macroscale yield stress from shallow irradiated layers, providing that the irradiation condition is carefully chosen in response to known size dependent behaviour. Although the apparent reduction of irradiation hardening in ODS in-house produced alloys showed great promise, these alloys also displayed a large amount of scatter in measured hardness and yield stress, attributed the pronounced heterogeneity in the microstructure.

Alloys with such significant microstructural heterogeneity are not suitable for engineering or commercial use. This is because microstructural features, such as large carbides, are likely to lead to stress concentrations and possible areas for crack nucleation. Additionally, the regions of reduced hardness will lead to local variations in deformation, making the behaviour of engineering components fabricated from this material unpredictable and unsafe, due to their variability. Efforts should be made to reduce the heterogeneity of the microstructure, a possible route to explore is post-consolidation treatments, such as hot rolling then annealing. Although, this is likely to increase the average grain size and slightly coarsen the nanoscale oxides.

6.4 Further work

Further investigations specifically relating to the work in this thesis:

- More 14YWT 1150 microcantilevers need to be tested in order to fully and confidently evaluate the effect nanoscale oxides had on suppressing irradiation hardening in microcantilevers fabricated out of the proton irradiated cross-section.
- TEM investigation of the bimodal hardness of 14YWT to confirm heterogeneity in the oxide population.
- Exploration of post-consolidation treatments to decrease the microstructural heterogeneity.

- Increase the size of macromechanical flexure tests to provide greater strain resolution in digital image correlation.
- Add empirically derived terms to the constitutive equation for lengthscale dependent plastic strain to match experimentally observed results.

There is still a huge amount of research required in order for ODS RAF/M steels to be utilised in prototype fusion reactors. One of the primary areas of research, highlighted by this thesis, lies in the need to produce an alloy with a homogeneous microstructure, that is reproducible, reliable and cost-efficient on an industrial scale. Additional areas of research that are also needed to assess the capability of ODS RAF/M steels for engineering and commercial use:

- The continued evaluation of alloys under reactor relevant thermal and irradiation conditions, and the assessment of these properties over long lifecycles.
- The continued improvement of fracture toughness and DBTT, particularly when subjected to high irradiation doses.
- The continued assessment of helium trapping capabilities of nanoscale oxides, and the effects reactor relevant helium production, combined with the anticipated temperatures, have on the mechanical properties.

References

[1] Collins, M., et al. *Long-term Climate Change: Projections, Commitments and Irreversibility.* In *Climate Change 2013: The Physical Science Basis. Contribution of Working Group I to the Fifth Assessment Report of the Intergovernmental Panel on Climate Change*, chap. 12, 1029 – 1136. Cambridge University Press, 2013.

[2] The World Bank. *Fossil fuel energy consumption (% of total).*

[3] Duffy, D.M. *Fusion power: a challenge for materials science.* Philosophical Transactions of the Royal Society A: Mathematical, Physical and Engineering Sciences, 368(1923):3315, 2010.

[4] Schiller, P., et al. *Projected materials requirements for the next european torus and for longterm tokamak-based demo fusion devices.* Journal of Nuclear Materials, 155-157,(0):41, 1988.

[5] Bloom, E.E. *The challenge of developing structural materials for fusion power systems.* Journal of Nuclear Materials, 258-263(0):7, 1998.

[6] Goldston, R., et al. *A plan for the development of fusion energy.* Journal of fusion energy, 21(2):61, 2002.

[7] Moslang, A., et al. *Towards reduced activation structural materials data for fusion DEMO reactors.* Nuclear Fusion, 45(7):649, 2005.

[8] Zinkle, S.J., et al. *Designing Radiation Resistance in Materials for Fusion Energy.* Annu. Rev. Mater. Res, 44:241, 2014.

[9] Murty, K.L., et al. *Structural materials for Gen-IV nuclear reactors: Challenges and opportunities.* Journal of Nuclear Materials, 383(1):189, 2008.

[10] Zinkle, S.J., et al. *Materials challenges in nuclear energy.* Acta Materialia, 61(3):735, 2013.

[11] Zinkle, S.J., et al. *Structural materials for fission & fusion energy.* Materials Today, 12(11):12, 2009.

[12] Baluc, N., et al. *Status of R&D activities on materials for fusion power reactors.* Nuclear Fusion, 47(10):S696, 2007.

[13] Mandal, D., et al. *Synthesis & fabrication of lithium-titanate pebbles for ITER breeding blanket by solid state reaction & spherodization.* Fusion Engineering and Design, 85(5):819, 2010.

[14] *https://www.iter.org/album/Media/7 - Technical, ITER Organisation.*

[15] Ihli, T., et al. *Review of blanket designs for advanced fusion reactors.* Fusion Engineering and Design, 83(7):912, 2008.

[16] Ec.europa.eu. *European Commission - Research: Energy - Technology R&D.* 2016.

[17] Moriyama, H., et al. *Tritium recovery from liquid metals.* Fusion Engineering and Design, 28:226, 1995.

[18] Kurtz, R.J., et al. *Recent progress toward development of reduced activation ferritic/martensitic steels for fusion structural applications.* Journal of Nuclear Materials, 386-388(0):411, 2009.

[19] Raffray, A.R., et al. *High heat flux components – Readiness to proceed from near term fusion systems to power plants.* Fusion Engineering and Design, 85(1):93, 2009.

[20] Bolt, H., et al. *Materials for the plasma-facing components of fusion reactors.* Journal of Nuclear Materials, 329-333, P(0):66, 2004.

[21] Zinkle, S.J. *Advanced materials for fusion technology.* Fusion Engineering and Design, 74(1-4):31, 2005.

[22] Mansur, L.K. *Theory and experimental background on dimensional changes in irradiated alloys.* Journal of Nuclear Materials, 216(0):97, 1994.

[23] Odette, G.R., et al. *Irradiation-tolerant nanostructured ferritic alloys: Transforming helium from a liability to an asset.* JOM Journal of the Minerals, Metals and Materials Society, 62(9):84, 2010.

[24] Odette, G.R., et al. *Recent developments in irradiation-resistant steels.* Annu. Rev. Mater. Res., 38:471, 2008.

[25] Was, G.S. *Fundamentals of radiation materials science: metals and alloys.* Springer Verlag, 2007.

[26] Scott, P. *A review of irradiation assisted stress corrosion cracking.* Journal of Nuclear Materials, 211(2):101, 1994.

[27] Kenik, E.A., et al. *Radiation-induced grain boundary segregation and sensitization of a neutron-irradiated austenitic stainless steel.* Journal of Nuclear Materials, 183:145, 1991.

[28] Van der Schaaf, B., et al. *High dose, up to 80 dpa, mechanical properties of Eurofer 97.* Journal of Nuclear Materials, 386:236, 2009.

[29] Klueh, R.L., et al. *High-chromium ferritic and martensitic steels for nuclear applications*, vol. 3. Astm International, 2001.

[30] Meis, D.D., et al. *Application of Eurofer97 steels for demo divertor cassette irradiated at temperature below 350 C.* 2016.

[31] Klueh, R., et al. *Ferritic/martensitic steels - overview of recent results.* Journal of Nuclear Materials, 307:455, 2002.

[32] Klueh, R.L., et al. *Ferritic/martensitic steels: promises and problems.* Journal of Nuclear Materials, 191-194,(0):116, 1992.

[33] Grieveson, E.M., et al. *Investigation into irradiation effects in ODS steels using ion implantation and micromechanical testing.* 2013 IEEE 25th Symposium on, 2013.

[34] Gilbert, M.R., et al. *An integrated model for materials in a fusion power plant: transmutation, gas production, and helium embrittlement under neutron irradiation.* Nuclear Fusion, 52(8):083019, 2012.

[35] Gilbert, M.R., et al. *Neutron-induced dpa, transmutations, gas production, and helium embrittlement of fusion materials.* Journal of Nuclear Materials, 442(1):S755, 2013.

[36] Cottrell, G.A. *Void migration, coalescence and swelling in fusion materials.* Fusion Engineering and Design, 66-68(0):253, 2003.

[37] Kohyama, A., et al. *Low-activation ferritic and martensitic steels for fusion application.* Journal of Nuclear Materials, 233-237,(0):138, 1996.

[38] Baka, B., et al. *The influence of Helium bubbles on the critical resolved shear stress of dispersion strengthened alloys.* Journal of Nuclear Materials, 386-388(0):112, 2009.

[39] Ullmaier, H. *The influence of helium on the bulk properties of fusion reactor structural materials.* Nuclear Fusion, 24(8):1039, 2011.

[40] Brager, H.R., et al. *Development of reduced activation alloys for fusion service.* Journal of Nuclear Materials, 133-134(0):907, 1985.

[41] Boutard, J.L., et al. *Fissile core and Tritium-Breeding Blanket: structural materials and their requirements.* Comptes Rendus Physique, 9(3):287, 2008.

[42] Gilbert, M.R., et al. *Neutron-induced transmutation effects in W and W-alloys in a fusion environment.* Nuclear Fusion, 51(4):043005, 2011.

[43] Tanigawa, H., et al. *Technical issues related to the development of reduced-activation ferritic/martensitic steels as structural materials for a fusion blanket system.* Fusion Engineering and Design, 86(9-11):2549, 2011.

[44] Hishinuma, A., et al. *Current status and future R&D for reduced-activation ferritic/martensitic steels.* Journal of Nuclear Materials, 258:193, 1998.

[45] Klueh, R.L. *Reduced-activation steels: Future development for improved creep strength.* Journal of Nuclear Materials, 378(2):159, 2008.

[46] Kinchin, G.H., et al. *The displacement of atoms in solids by radiation.* Reports on progress in physics, 18(1):1 , 1955.

[47] Stoller, R.E., et al. *On the use of SRIM for computing radiation damage exposure.* Nuclear instruments and, 310:75 , 2013.

[48] Norgett, M.J., et al. *A proposed method of calculating displacement dose rates.* Nuclear Engineering and Design, 33(1):50 , 1975.

[49] Stoller, R.E., et al. *Recommendations on damage exposure units for ferritic steel embrittlement correlations.* Journal of Nuclear Materials, 186:203, 1992.

[50] Ziegler, J.F., et al. *SRIM - The stopping and range of ions in matter (2010).* Nuclear Instruments and Methods in Physics Research Section B: Beam Interactions with Materials and Atoms, 268(11):1818, 2010.

[51] Fischer, U., et al. *Transmutation behaviour of Eurofer under irradiation in the IFMIF test facility and fusion power reactors.* Journal of Nuclear Materials, 329:228, 2004.

[52] Singh, B.N., et al. *Aspects of microstructure evolution under cascade damage conditions.* Journal of Nuclear Materials, 25(1):107, 1997.

[53] Ukai, S., et al. *Perspective of ODS alloys application in nuclear environments.* Journal of Nuclear Materials, 307:749, 2002.

[54] Goshchitskii, B.N., et al. *Structure, radiation resistance and thermal creep of ODS ferritic steels.* Journal of Nuclear Materials, 307-311, P(0):783, 2002.

[55] Schilling, W., et al. *Recovery of irradiated and quenched metals.* Journal of Physics F: Metal Physics, 3(2):322, 1973.

[56] Schilling, W., et al. *Interpretation of defect reactions in irradiated metals by the one interstitial model.* No. CONF-751006–P1, 7(23), 1975.

[57] Kwapuliński, P., et al. *The kinetics of structural defect recovery in pure iron in the temperature interval 300 to 800 K.* physica status solidi (a), 88(2):561, 1985.

[58] Beeler, J.R. *Radiation effects computer experiments.* Elsevier, 2012.

[59] Borodin, V.A., et al. *The influence of dissociation of small helium-vacancy clusters on the growth of helium bubbles, the accumulation of helium at the grain boundaries and the kinetics of helium desorption from irradiated materials.* Journal of Nuclear Materials, 154(2-3):263, 1988.

[60] Klueh, R.L., et al. *Ferritic/martensitic steels for next-generation reactors.* Journal of Nuclear Materials, 371(1-3):37, 2007.

[61] Klueh, R.L. *Elevated temperature ferritic and martensitic steels and their application to future nuclear reactors.* International Materials Reviews, 50(5):287, 2005.

[62] Krivit, S.B., et al. *Nuclear energy encyclopedia: science, technology, and applications.* John Wiley & Sons, vol. 5 ed., 2011.

[63] Klueh, R.L., et al. *High-chromium Ferritic and Martensitic Steels for Nuclear Applications.* Astm International, vol.3 ed., 2001.

[64] Garner, F.A., et al. *Comparison of swelling and irradiation creep behavior of fcc-austenitic and bcc-ferritic/martensitic alloys at high neutron exposure.* Journal of Nuclear Materials, 276(1-3):123, 2000.

[65] Singh, B.N., et al. *Significant differences in defect accumulation behaviour between fcc and bcc crystals under cascade damage conditions.* Journal of Nuclear Materials, 226(3):277, 1995.

[66] Odette, G.R. *On mechanisms controlling swelling in ferritic and martensitic alloys.* Journal of Nuclear Materials, 155:921, 1988.

[67] Kimura, A., et al. *High resistance to helium embrittlement in reduced activation martensitic steels.* Journal of Nuclear Materials, 307:521, 2002.

[68] Kasada, R., et al. *Two-Step Recovery Process of Irradiation Hardening in 1% Ni Doped 9% Cr-2% W Martensitic Steel.* Effects of Radiation on Materials: 19th International Symposium, 2000.

[69] de Castro, V., et al. *In-situ Fe + Ion Irradiation of an Oxide Dispersion Strengthened Steel.* Journal of Physics: Conference Series, 522(1):012032, 2014.

[70] Lazauskas, T., et al. *Simulating radiation damage in a bcc Fe system with embedded yttria nanoparticles.* Journal of Nuclear Materials, 437(1):317, 2013.

[71] Wurster, S., et al. *Nanostructured metals under irradiation.* Scripta Materialia, 60(12):1083, 2009.

[72] Oksiuta, Z., et al. *Mechanical properties and thermal stability of nanostructured ODS RAF steels.* Mechanics of Materials, 67:15, 2013.

[73] Klueh, R.L., et al. *The development of ferritic steels for fast induced-radioactivity decay for fusion reactor applications.* Nuclear Engineering and Design. Fusion, 2(3):383, 1985.

[74] Ehrlich, K., et al. *The Development of Structural Materials for Reduced Long-Term Activation.* In *Effects of Radiation on Materials: 17th International Symposium*, 1109–1109–14. ASTM International, 100 Barr Harbor Drive, PO Box C700, West Conshohocken, PA 19428-2959, 1996.

[75] Van der Schaaf, B., et al. *The development of EUROFER reduced activation steel.* Fusion Engineering and Design, 69(1-4):197, 2003.

[76] Lindau, R., et al. *Present development status of EUROFER and ODS-EUROFER for application in blanket concepts.* Fusion Engineering and Design, 75:989, 2005.

[77] Klueh, R.L., et al. *Impurity effects on reduced-activation ferritic steels developed for fusion applications.* Journal of Nuclear Materials, 280(3):353, 2000.

[78] Toloczko, M.B., et al. *Irradiation creep and swelling of the US fusion heats of HT9 and 9Cr-1Mo to 208 dpa at 400C.* Journal of Nuclear Materials, 212-215:604, 1994.

[79] Gelles, D.S. *Microstructural development in reduced activation ferritic alloys irradiated to 200 dpa at 420C.* Journal of Nuclear Materials, 212-215:714, 1994.

[80] Singh, B.N., et al. *Radiation hardening revisited: role of intracascade clustering.* Journal of Nuclear Materials, 249(2-3):103, 1997.

[81] Hull, D., et al. *Introduction to dislocations.* Butterworth-Heinemann, 2011.

[82] Little, E.A. *Neutron-irradiation hardening in irons and ferritic steels.* International Metals Reviews, 21:1:25, 1976.

[83] K., L.M., et al. *Friction and source hardening in irradiated mild steel.* Scripta Metallurgica, 17(3):317, 1983.

[84] Victoria, M., et al. *The microstructure and associated tensile properties of irradiated fcc and bcc metals.* Journal of Nuclear Materials, 276(1):114, 2000.

[85] Gaganidze, E., et al. *Mechanical properties and TEM examination of RAFM steels irradiated up to 70 dpa in BOR-60.* Journal of Nuclear Materials, 417(1-3):93, 2011.

[86] Alamo, A., et al. *Mechanical properties of 9Cr martensitic steels and ODS-FeCr alloys after neutron irradiation at 325C up to 42dpa.* Journal of Nuclear Materials, 367:54, 2007.

[87] Lucon, E., et al. *Mechanical properties of the European reference RAFM steel (EUROFER97) before and after irradiation at 300C.* Journal of Nuclear Materials, 329:1078, 2004.

[88] Rensman, J.W. *NRG irradiation testing: report on 300 C and 60 C irradiated RAFM steels.* NRG report 68497, 2005.

[89] Gaganidze, E., et al. *Mechanical properties of reduced activation ferritic/martensitic steels after high dose neutron irradiation.* Proc. of 22st IAEA Fusion Energy Conference, 13–18, 2008.

[90] Klueh, R.L., et al. *Tensile properties of 9Cr-1MoVNb and 12Cr-1MoVW steels irradiated to 23 dpa at 390 to 550C.* Journal of Nuclear Materials, 182(0):230, 1991.

[91] Henry, J., et al. *Tensile and impact properties of 9Cr tempered martensitic steels and ODS-FeCr alloys irradiated in a fast reactor at 325C up to 78dpa.* Journal of Nuclear Materials, 417(1-3):99, 2010.

[92] Lucas, G.E. *The evolution of mechanical property change in irradiated austenitic stainless steels.* Journal of Nuclear Materials, 206(2-3):287, 1993.

[93] Hashimoto, N., et al. *Relationship between hardening and damage structure in austenitic stainless steel 316LN irradiated at low temperature in the HFIR.* Journal of Nuclear Materials, 273(1):95, 1999.

[94] Odette, G.R., et al. *Embrittlement of nuclear reactor pressure vessels.* JOM, 53(7):18, 2001.

[95] Xue, L. *Damage accumulation and fracture initiation in uncracked ductile solids subject to triaxial loading.* International Journal of Solids and Structures, 44(16):5163, 2007.

[96] Gaganidze, E., et al. *Post Irradiation Examination of RAF/M Steels After Fast Reactor Irradiation Up to 71 Dpa and< 340C (ARBOR 2): RAFM Steels: Metallurgical and Mechanical Characterisation*, vol. 7596. KIT Scientific Publishing, 2011.

[97] Gaganidze, E., et al. *Irradiation programme HFR phase IIb-SPICE. Impact testing on up to 16.3 dpa irradiated RAFM steels. Final report for task TW2-TTMS 001b-D05.* EURATOM, 39(37), 2008.

[98] Petersen, C., et al. *Mechanical properties of reduced activation ferritic/martensitic steels after European reactor irradiations.* 21th IAEA Fusion, 2006.

[99] Petersen, C., et al. *Impact property degradation of ferritic/martensitic steels after the fast reactor irradiation 'ARBOR 1'.* Journal of Nuclear, 367:544, 2007.

[100] Lindau, R., et al. *First results on the characterisation of the reduced-activation-ferritic-martensitic steel EUROFER.* Fusion Engineering and Design, 58:781, 2001.

[101] Armas, A.F., et al. *Mechanical and microstructural behaviour of isothermally and thermally fatigued ferritic/martensitic steels.* Journal of Nuclear Materials, 307-311,(0):509, 2002.

[102] Xiao, X., et al. *Coarsening behavior for M23C6 carbide in 12% Cr-reduced activation ferrite/martensite steel: experimental study combined with DICTRA simulation.* Journal of Materials Science, 48(16):5410, 2013.

[103] Klimiankou, M., et al. *Direct correlation between morphology of (Fe,Cr)23C6 precipitates and impact behavior of ODS steels.* Journal of Nuclear Materials, 367-370,(0):173, 2007.

[104] Lindau, R., et al. *Thermal and mechanical behaviour of the reduced-activation-ferritic-martensitic steel EUROFER.* Fusion Engineering and Design, 61-62(0):659, 2002.

[105] Di Maio, P.A., et al. *On the optimization of the first wall of the DEMO water-cooled lithium lead outboard breeding blanket equatorial module.* Fusion Engineering and Design, 109:335, 2016.

[106] Shao, S., et al. *Spiral Patterns of Dislocations at Nodes in (111) Semi-coherent FCC Interfaces.* Scientific Reports, 3(1):2448, 2013.

[107] Shao, S., et al. *Relaxation Mechanisms, Structure and Properties of Semi-Coherent Interfaces.* Metals, 5(4):1887, 2015.

[108] Dapeng, Z., et al. *ODS ferritic steel engineered with bimodal grain size for high strength and ductility.* Materials Letters, 65(11):1672, 2011.

[109] Oksiuta, Z., et al. *Development and characterisation of a new ODS ferritic steel for fusion reactor application.* Journal of Nuclear Materials, 393(1):114, 2009.

[110] Baluc, N., et al. *Review on the EFDA work programme on nano-structured ODS RAF steels.* Journal of Nuclear Materials, 417(1-3):149, 2011.

[111] Soni, P.R. *Mechanical alloying: fundamentals and applications.* Cambridge Int Science Publishing, 2000.

[112] Bhadeshia, H. *Recrystallisation of practical mechanically alloyed iron-base and nickel-base superalloys.* Materials Science and Engineering: A, A 223(1):64, 1997.

[113] Suryanarayana, C., et al. *The science and technology of mechanical alloying.* Materials Science and Engineering: A, 304:151, 2001.

[114] Jones, A.R. *Historical perspective-ODS alloy development.* Presenation, 2010.

[115] Ramar, A., et al. *Effect of mechanical alloying on the mechanical and microstructural properties of ODS EUROFER 97.* Fusion Engineering and Design, 82(15):2543, 2007.

[116] Suryanarayana, C. *Mechanical alloying and milling.* Progress in Materials Science, 46(1):1, 2001.

[117] Genes, D.S., et al. *Fabrication Technological Development of the Oxide Dispersion Strengthened Alloy MA957 I for Fast Reactor Applications.* U.S. Department of Energy, 2000.

[118] Ukai, S., et al. *Tube manufacturing and characterization of oxide dispersion strengthened ferritic steels.* Journal of Nuclear Materials, 283:702, 2000.

[119] Sundararajan, G., et al. *Development of 9Cr ferritic-martensitic and 18Cr ferritic oxide dispersion strengthened steels.* Current Science, 105(8), 2013.

[120] Alinger, M.J., et al. *The development and stability of Y-Ti-O nanoclusters in mechanically alloyed Fe-Cr based ferritic alloys.* Journal of Nuclear Materials, 329:382, 2004.

[121] Okuda, T., et al. *Dispersion behaviour of oxide particles in mechanically alloyed ODS steel.* Journal of materials science letters, 14(22):1600, 1995.

[122] Sakasegawa, H., et al. *Precipitation behavior of oxide particles in mechanically alloyed powder of oxide-dispersion-strengthened steel.* Journal of Alloys and Compounds, 452(1):2, 2008.

[123] Alinger, M.J., et al. *On the role of alloy composition and processing parameters in nanocluster formation and dispersion strengthening in nanostuctured ferritic alloys.* Acta Materialia, 57(2):392, 2009.

[124] Hin, C., et al. *Formation of Y 2 O 3 nanoclusters in nanostructured ferritic alloys during isothermal and anisothermal heat treatment: A kinetic Monte Carlo study.* Physical Review B, 80(13):134118, 2009.

[125] Barnard, L., et al. *An ab initio study of Ti-Y-O nanocluster energetics in nanostructured ferritic alloys.* Acta Materialia, 60(3):935, 2012.

[126] Hilger, I., et al. *The structural changes of Y2O3 in ferritic ODS alloys during milling.* Journal of Nuclear Materials, 447(1):242, 2014.

[127] Liu, T., et al. *Structure evolution of Y 2 O 3 nanoparticle/Fe composite during mechanical milling and annealing.* Progress in Natural Science: Materials International, 23:434, 2013.

[128] Parida, P.K., et al. *Structural studies of Y 2 O 3 dispersoids during mechanical milling and annealing in a Fe-15 Y 2 O 3 model ODS alloy.* Journal of Nuclear Materials, 441:331, 2013.

[129] Klueh, R.L., et al. *Oxide dispersion-strengthened steels: A comparison of some commercial and experimental alloys.* Journal of Nuclear Materials, 341(2):103, 2005.

[130] Kasada, R., et al. *Pre- and post-deformation microstructures of oxide dispersion strengthened ferritic steels.* Journal of Nuclear Materials, 367:222, 2007.

[131] Miller, M.K., et al. *Atom probe tomography of nanoscale particles in ODS ferritic alloys.* Materials Science and Engineering: A, 353(1):140, 2003.

[132] Klueh, R.L., et al. *Tensile and creep properties of an oxide dispersion-strengthened ferritic steel.* Journal of Nuclear Materials, 307:773, 2002.

[133] Kim, I.S., et al. *Defect and void evolution in oxide dispersion strengthened ferritic steels under 3.2 MeV Fe+ ion irradiation with simultaneous helium injection.* Journal of Nuclear Materials, 280(3):264, 2000.

[134] Larson, D.J., et al. *Three-dimensional atom probe observation of nanoscale titanium-oxygen clustering in an oxide-dispersion-strengthened Fe-12Cr-3W-0.4 Ti+ Y 2 O 3.* Scripta Materialia, 44(3):359, 2001.

[135] Miller, M.K., et al. *Advanced oxide dispersion strengthened and nanostructured ferritic alloys.* Materials Science and Technology, 29(10):1174, 2013.

[136] Hsiung, L.L., et al. *Formation mechanism and the role of nanoparticles in Fe-Cr ODS steels developed for radiation tolerance.* Physical Review B, 82(18):184103, 2010.

[137] Ukai, S., et al. *Nano-mesoscopic structure control in 9Cr-ODS ferritic steels.* Energy Materials: Materials Science and Engineering for Energy Systems, 2(1):26, 2007.

[138] McClintock, D.A., et al. *Mechanical properties of irradiated ODS-EUROFER and nanocluster strengthened 14YWT.* Journal of Nuclear Materials, 392(2):353, 2009.

[139] Sokolov, M.A., et al. *Fracture toughness and tensile properties of nano-structured ferritic steel 12YWT.* Journal of Nuclear Materials, 367:213, 2007.

[140] Byun, T.S., et al. *High temperature fracture characteristics of a nanostructured ferritic alloy (NFA).* Journal of Nuclear Materials, 407(2):78, 2010.

[141] Hoelzer, D.T., et al. *Influence of processing on the microstructure and mechanical properties of 14YWT.* Journal of Nuclear Materials, 471:251, 2016.

[142] Hoelzer, D.T., et al. *Joining of 14YWT and F82H by friction stir welding.* Journal of Nuclear Materials, 442(1):S529, 2013.

[143] Kim, J.H., et al. *Effect of milling temperature on nanoclusters and ultra fine grained microstructure of oxide dispersion strengthened steel.* Journal of Alloys and Compounds, 585:69, 2014.

[144] Hse. *Work with ionising radiation Work with ionising radiation Health and Safety Executive.* 2000.

[145] Gane, N., et al. *Microdeformation of Solids.* Journal of Applied Physics, 39(3):1432, 1968.

[146] Di Maio, D., et al. *Measuring fracture toughness of coatings using focused-ion-beam-machined microbeams.* J. Mater. Res, 20(2):299, 2005.

[147] Armstrong, D.E.J., et al. *Measuring anisotropy in Young's modulus of copper using microcantilever testing.* Journal of Materials Research, 24(11):3268, 2009.

[148] Gong, J., et al. *Investigation of elastic properties of single-crystal alpha-Ti using microcantilever beams.* Philosophical Magazine Letters, 90(7):503, 2010.

[149] Kiener, D., et al. *Determination of mechanical properties of copper at the micron scale.* Advanced Engineering Materials, 8(11):1119, 2006.

[150] Uchic, M.D., et al. *Sample dimensions influence strength and crystal plasticity.* Science, 305(5686):986, 2004.

[151] Uchic, M.D., et al. *Micro-compression testing of fcc metals: a selected overview of experiments and simulations.* JOM Journal of the Minerals, Metals and Materials Society, 61(3):36, 2009.

[152] Brinell, J.A. *Mémoire sur les épreaves á bille en acier, II.* Cong. Int. Methodes d'Essai, 1900.

[153] Sargent, P.M. *Thesis on nanoindentation.* Ph.D. thesis, University of Oxford, 1979.

[154] Pethicai, J.B., et al. *Hardness measurement at penetration depths as small as 20 nm.* Philosophical Magazine A, 48(4):593, 1983.

[155] Oliver, W.C., et al. *Improved technique for determining hardness and elastic modulus using load and displacement sensing indentation experiments.* Journal of materials research, 7(6):1564, 1992.

[156] Oliver, W.C., et al. *Measurement of hardness and elastic modulus by instrumented indentation: Advances in understanding and refinements to methodology.* Journal of materials research, 19(01):3, 2004.

[157] Strader, J.H., et al. *An experimental evaluation of the constant β relating the contact stiffness to the contact area in nanoindentation.* Philosophical Magazine, 86(33-35):5285, 2006.

[158] Beck, C.E., et al. *Correcting for contact area changes in nanoindentation using surface acoustic waves.* Scripta Materialia, 128:83, 2017.

[159] Li, X., et al. *A review of nanoindentation continuous stiffness measurement technique and its applications.* Materials Characterization, 48(1):11, 2002.

[160] Pethica, J.B., et al. *Tip surface interactions in STM and AFM.* Physica Scripta, T19A:61, 1987.

[161] Hosemann, P., et al. *Issues to consider using nano indentation on shallow ion beam irradiated materials.* Journal of Nuclear Materials, 425(1):136, 2012.

[162] Gouldstone, A., et al. *Indentation across size scales and disciplines: Recent developments in experimentation and modeling.* Acta Materialia, 55(12):4015, 2007.

[163] Hosemann, P., et al. *Nanoindentation on ion irradiated steels.* Journal of Nuclear Materials, 389(2):239, 2009.

[164] Yabuuchi, K., et al. *Evaluation of irradiation hardening of proton irradiated stainless steels by nanoindentation.* Journal of Nuclear Materials, 446(1):142, 2014.

[165] Tabor, D. *The hardness of metals.* Oxford university press, 2000.

[166] Cheng, Y.T., et al. *Scaling, dimensional analysis, and indentation measurements.* Materials Science and Engineering: R: Reports, 44(4):91, 2004.

[167] Sánchez-Martín, R., et al. *Measuring the critical resolved shear stresses in Mg alloys by instrumented nanoindentation.* Acta Materialia, 71:283, 2014.

[168] Britton, T.B., et al. *The effect of crystal orientation on the indentation response of commercially pure titanium: experiments and simulations.* Proceedings of the Royal Society A: Mathematical, Physical and Engineering Science, 466(2115):695, 2010.

[169] Zaafarani, N., et al. *Three-dimensional investigation of the texture and microstructure below a nanoindent in a Cu single crystal using 3D EBSD and crystal plasticity finite element simulations.* Acta Materialia, 54(7):1863, 2006.

[170] Dao, M., et al. *Computational modeling of the forward and reverse problems in instrumented sharp indentation.* Acta Materialia, 49(19):3899, 2001.

[171] Weihs, T., et al. *Mechanical deflection of cantilever microbeams: A new technique for testing the mechanical properties of thin films.* Journal of Materials Research, 3(05):31, 1988.

[172] Grivet, P., et al. *Ion microscopy: History and actual trends.* Annals of the New York Academy of Sciences, 306(1):158, 1978.

[173] Seliger, R., et al. *A high-intensity scanning ion probe with submicrometer spot size.* Applied Physics Letters, 34(5):310, 1979.

[174] McCarthy, J., et al. *FIB micromachined submicron thickness cantilevers for the study of thin film properties.* Thin Solid Films, 358(1):146, 2000.

[175] Rubanov, S., et al. *FIB-induced damage in silicon.* Journal of Microscopy, 214(3):213, 2004.

[176] Walker, J.F. *Surface damage of semiconductor TEM samples prepared by focused ion beams.* Inst. Phys. Conf., 157, 1997.

[177] Gong, J., et al. *Anisotropy in the plastic flow properties of single-crystal alpha-titanium determined from micro-cantilever beams.* Acta Materialia, 57(19):5693, 2009.

[178] Dunne, F.P.E., et al. *Lengthscale-dependent, elastically anisotropic, physically-based hcp crystal plasticity: Application to cold-dwell fatigue in Ti alloys.* International journal of plasticity, 23(6):1061, 2007.

[179] Taylor, G.F. *A Method of Drawing Metallic Filaments and a Discussion of their Properties and Uses.* Physical Review, 23(5):655, 1924.

[180] Brenner, S.S. *Tensile Strength of Whiskers.* Journal of Applied Physics, 27(12):1484, 1956.

[181] *Iron, http://www.goodfellow.com/E/Iron.html, online catalogue source supplier of research materials in small quantities, Goodfellow.*

[182] Gane, N. *The Direct Measurement of the Strength of Metals on a Sub-Micrometre Scale.* Proceedings of the royal society A: Mathematical, physical and engineering sciences, 317(1530), 1970.

[183] Pethica, J.B., et al. *Contact of characterised metal surfaces at very low loads: Deformation and adhesion.* Surface Science, 89(1):182, 1979.

[184] Mughrabi, H. *On the current understanding of strain gradient plasticity.* Materials Science and Engineering: A, 387:209, 2004.

[185] Nix, W.D., et al. *Indentation size effects in crystalline materials: a law for strain gradient plasticity.* Journal of the Mechanics and Physics of Solids, 46(3):411, 1998.

[186] Ashby, M.F. *The deformation of plastically non-homogeneous materials.* Philosophical Magazine, 21(170):399, 1970.

[187] Dimiduk, D.M., et al. *Size-affected single-slip behavior of pure nickel microcrystals.* Acta Materialia, 53(15):4065, 2005.

[188] Uchic, M.D., et al. *Plasticity of Micrometer-Scale Single Crystals in Compression.* Annual Review of Materials Research, 39(1):361, 2009.

[189] Kraft, O., et al. *Plasticity in Confined Dimensions.* Annual Review of Materials Research, 40(1):293, 2010.

[190] Greer, J.R., et al. *Plasticity in small-sized metallic systems: Intrinsic versus extrinsic size effect.* Progress in Materials Science, 56(6):654, 2011.

[191] Greer, J.R., et al. *Nanoscale gold pillars strengthened through dislocation starvation.* Physical Review B, 73(24):245410, 2006.

[192] Senger, J., et al. *Discrete dislocation simulations of the plasticity of micro-pillars under uniaxial loading.* Scripta Materialia, 58(7):587, 2008.

[193] Rao, S.I., et al. *Athermal mechanisms of size-dependent crystal flow gleaned from three-dimensional discrete dislocation simulations.* Acta Materialia, 56(13):3245, 2008.

[194] Girault, B., et al. *Strength effects in micropillars of a dispersion strengthened superalloy.* Advanced Engineering Materials, 12(5):385, 2010.

[195] Motz, C., et al. *Mechanical properties of micro-sized copper bending beams machined by the focused ion beam technique.* Acta Materialia, 53(15):4269, 2005.

[196] Motz, C., et al. *Micro-bending tests: A comparison between three-dimensional discrete dislocation dynamics simulations and experiments.* Acta Materialia, 56(9):1942, 2008.

[197] Tarleton, E., et al. *A discrete dislocation plasticity study of the micro-cantilever size effect.* Acta Materialia, 88:271, 2015.

[198] Kiener, D., et al. *In situ nano-compression testing of irradiated copper.* Nature materials, 10(8):608, 2011.

[199] Hardie, C.D., et al. *Mechanical properties and plasticity size effect of Fe-6%Cr irradiated by Fe ions and by neutrons.* Journal of Nuclear Materials, 482:236, 2016.

[200] Shim, S., et al. *Effects of focused ion beam milling on the compressive behavior of directionally solidified micropillars and the nanoindentation response of an electropolished surface.* Acta Materialia, 57(2):503, 2009.

[201] Halliday, F.M., et al. *Nanoindentation and micromechanical testing of iron-chromium alloys implanted with iron ions.* Advanced Materials, 59:304, 2009.

[202] Armstrong, D.E.J., et al. *Small-scale characterisation of irradiated nuclear materials: Part II nanoindentation and micro-cantilever testing of ion irradiated nuclear materials.* Journal of Nuclear Materials, 462:374, 2015.

[203] Hardie, C.D. *Micro-Mechanics of Irradiated Fe-Cr Alloys for Fusion Reactors.* Ph.D. thesis, University Of Oxford, 2013.

[204] Gaganidze, E., et al. *Assessment of neutron irradiation effects on RAFM steels.* Fusion Engineering and Design, 88(3):118, 2013.

[205] Williams, C.A. *Atomic scale characterisation of oxide dispersion stengthened steels for fusion applications.* Ph.D. thesis, University of Oxford, 2011.

[206] Klimiankou, M., et al. *HRTEM Study of yttrium oxide particles in ODS steels for fusion reactor application.* Journal of Crystal Growth, 249(1):381, 2003.

[207] Williams, C.A., et al. *Nanoscale characterisation of ODS-Eurofer 97 steel: An atom-probe tomography study.* Journal of Nuclear Materials, 400(1):37, 2010.

[208] Burrows, C. *The irradiation resistance of oxide dispersion strengthened streels.* Ph.D. thesis, University of Oxford, 2015.

[209] Gorley, M.J. *Powder processing of oxide dispersion strengthened alloys for nuclear applications.* Ph.D. thesis, University of Oxford, 2014.

[210] Engler, O., et al. *Introduction to texture analysis: macrotexture, microtexture, and orientation mapping.* CRC press, 2009.

[211] Schwartz, A.J., et al. *Electron backscatter diffraction in materials science.* Springer, 2009.

[212] Potts, P.J. *A Handbook of Silicate Rock Analysis.* Springer US, Boston, MA, 1992.

[213] Kuběna, I., et al. *Microstructural stability of ODS steels in cyclic loading.* Fatigue & Fracture of Engineering Materials & Structures, 38(8):936, 2015.

[214] Ji, G., et al. *Processing conditions, microstructure and mechanical properties of hetero-nanostructured ODS FeAl alloys produced by spark plasma sintering.* Materials Science and Engineering: A, 559:566, 2013.

[215] Hilger, I., et al. *Bimodal Grain Size Distribution of Nanostructured Ferritic ODS Fe-Cr Alloys.* Journal of the American Ceramic Society, 98(11):3576, 2015.

[216] Boulnat, X., et al. *Microstructure Evolution in Nano-reinforced Ferritic Steel Processed By Mechanical Alloying and Spark Plasma Sintering.* Metallurgical and Materials Transactions A, 45(3):1485, 2014.

[217] Hilger, I., et al. *Fabrication and characterization of oxide dispersion strengthened (ODS) 14Cr steels consolidated by means of hot isostatic pressing, hot extrusion and spark plasma sintering.* Journal of Nuclear Materials, 472:206, 2016.

[218] Pimentel, G., et al. *Role of strain heterogeneity on recrystallisation of oxide dispersion strengthened Fe-Cr-Al alloys for high-temperature applications.* Journal of Materials Science, 47(14):5605, 2012.

[219] Peters, W.H., et al. *Digital Imaging Techniques In Experimental Stress Analysis.* Optical Engineering, 21(3):213427, 1982.

[220] Peters, W.H., et al. *Application Of Digital Correlation Methods To Rigid Body Mechanics*. Optical Engineering, 22(6):226738, 1983.

[221] Sutton, M.A., et al. *Determination of displacements using an improved digital correlation method*. Image and vision computing, 1(3):133, 1983.

[222] Pan, B., et al. *Two-dimensional digital image correlation for in-plane displacement and strain measurement: a review*. Measurement Science and Technology, 20(6):062001, 2009.

[223] Sutton, M.A., et al. *Image correlation for shape, motion and deformation measurements: basic concepts, theory and applications*. Springer Science & Business Media, 2009.

[224] University College London. *Noise sources in a CCD*.

[225] Hammant, B. *The use of 4-point loading tests to determine mechanical properties*. Composites, 2(4):246, 1971.

[226] Gere, J.M., et al. *Mechanics of materials*. Nelson Education, 2012.

[227] Luzginova, N.V., et al. *Irradiation response of ODS Eurofer97 steel*. Journal of Nuclear Materials, 428(1-3):192, 2012.

[228] Ehrlich, K., et al. *Report of the IEA Workshop on Reduced Activation Ferritic/Martensitic Steels, Tokyo, Japan*. JAERI-Conference, 7, 2001.

[229] Jitsukawa, S., et al. *Irradiation effects on reduced activation ferritic/martensitic steels – tensile, impact, fatigue properties and modelling*. Nuclear Fusion, 49(11):115006, 2009.

[230] Kim, J.H., et al. *Tensile fracture characteristics of nanostructured ferritic alloy 14YWT*. Journal of Nuclear Materials, 407(3):143, 2010.

[231] Yagodzinskyy, Y., et al. *Hydrogen effects on tensile properties of EUROFER 97 and ODS-EUROFER steels*. Journal of Nuclear Materials, 444(1):435, 2014.

[232] Cambridge University Engineering Department. *Materials Data Book*. 2003.

[233] Yao, N. *Focused ion beam systems: basics and applications*. Cambridge University Press, 2007.

[234] *Agilent Nano Indenter G200 Data Sheet, http://literature.cdn.keysight.com/litweb/pdf/5990-4172EN.pdf*.

[235] Von Mises, R. *Göttinger nachrichten*. Math-Phys Klasse, 1913.

[236] Gilmore, C. *Materials science and engineering properties*. Nelson Education, 2014.

[237] Armstrong, D.E.J. *Measuring Elastic, Plastic and Fracture Properties using Micro-Cantilever Testing*. Ph.D. thesis, University of Oxford, 2009.

[238] Dunne, F.P.E., et al. *Crystal plasticity analysis of micro-deformation, lattice rotation and geometrically necessary dislocation density*. Proceedings of the Royal Society A: Mathematical, Physical and Engineering Sciences, 468(2145):2509, 2012.

[239] Pope, G.G. *A discrete element method for analysis of plane elasto-plastic strain problems.* 1st Conf Math Meth in Struct Mech, 1965.

[240] Kai, C.Y., et al. *The finite element method in structural and continuum mechanics, numerical solution of problems in structural and continuum mechanics.* London : McGraw-Hill, 1967.

[241] Dunne, F., et al. *Introduction to computational plasticity.* Oxford University Press, 2005.

[242] Bonet, J., et al. *Nonlinear continuum mechanics for finite element analysis.* Cambridge university press, 1997.

[243] Zienkiewicz, O.C., et al. *The finite element method for solid and structural mechanics.* Butterworth-heinemann, 2005.

[244] Zhu, J.Z., et al. *The finite element method: its basis and fundamentals.* Elsevier, 2013.

[245] Kiwanuka, R. *Micro-deformation and texture in engineering materials.* Ph.D. thesis, University of Oxford, 2013.

[246] Busso, E. *Gradient-dependent deformation of two-phase single crystals.* Journal of the Mechanics and Physics of Solids, 48(11):2333, 2000.

[247] Cottrell, A.H. *Dislocations and Plastic Flow in Crystals.* Clarendon Press, 1953.

[248] Seeger, A. *The generation of lattice defects by moving dislocations, and its application to the temperature dependence of the flow-stress of fcc crystals.* The London, Edinburgh, and Dublin Philosophical Magazine and Journal of Science, 46(382):1194, 1955.

[249] Gibbs, G.B. *Thermodynamic analysis of dislocation glide controlled by dispersed local obstacles.* Materials Science and Engineering, 4(6):313, 1969.

[250] Manonukul, A., et al. *Physically-based model for creep in nickel-base superalloy C263 both above and below the gamma solvus.* Acta Materialia, 50(11):2917, 2002.

[251] Nye, J.F. *Some geometrical relations in dislocated crystals.* Acta metallurgica, 1(2):153, 1953.

[252] Acharya, A. *Lattice incompatibility and a gradient theory of crystal plasticity.* Journal of the Mechanics and Physics of Solids, 48(8):1565, 2000.

[253] Gao, H., et al. *Geometrically necessary dislocation and size-dependent plasticity.* Scripta Materialia, 48(2):113, 2003.

[254] Kartal, M.E., et al. *Determination of sub-surface stresses at inclusions in single crystal superalloy using HR-EBSD, crystal plasticity and inverse eigenstrain analysis.* International Journal of Solids and Structures, 67(68):27, 2015.

[255] Smallman, R.E., et al. *Metals and materials: science, processes, applications.* Elsevier, 2013.

[256] Sweeney, C.A., et al. *The role of elastic anisotropy, length scale and crystallographic slip in fatigue crack nucleation.* Journal of the Mechanics and Physics of Solids, 61(5):1224, 2013.

[257] Watanabe, R. *Possible Slip Systems in Body Centered Cubic Iron.* Materials Transactions, Vol.47(No.8):1886, 2006.

[258] Evers, L. *Non-local crystal plasticity model with intrinsic SSD and GND effects.* Journal of the Mechanics and Physics of Solids, 52(10):2379, 2004.

[259] Abbott P. C. *Tricks of the Trade.* The Mathematica Journal, Wolfram Me(8(3)):383, 2002.

[260] Gong, J., et al. *A microcantilever investigation of size effect, solid-solution strengthening and second-phase strengthening for -a- prism slip in alpha-Ti.* Acta Materialia, 59(15):5970, 2011.

[261] Olesen, H.L. *Radiation Effects on Electronic Systems.* Plenum Press, 1966.

[262] Briefings, E.K. *Energy Dispersive Spectroscopy.* John Wiley & Sons, 2nd ed., 2015.

[263] Miller, M.K., et al. *Stability of ferritic MA/ODS alloys at high temperatures.* Intermetallics, 13(3-4):387, 2005.

[264] Ukai, S., et al. *Development of 9Cr-ODS Martensitic Steel Claddings for Fuel Pins by means of Ferrite to Austenite Phase Transformation.* Journal of Nuclear Science and Technology, 39(7):778, 2002.